Heterometallacrowns as High-Spin Molecules

Dissertation

zur Erlangung
„Doktor der Naturwissenschaften"
im Promotionsfach Chemie

am Fachbereich Chemie, Pharmazie und Geowissenschaften der Johannes Gutenberg-Universität Mainz

vorgelegt von

Peter Happ
geb. in Fulda

April 2014

Tag der mündlichen Prüfung: 06.08.2014

Erklärung

Die vorliegende Arbeit wurde in der Zeit von Januar 2011 bis April 2014 unter Anleitung von Frau Prof. Dr. Eva Rentschler im Institut für Anorganische und Analytische Chemie der Johannes Gutenberg-Universität Mainz angefertigt.

Ich erkläre hiermit, dass ich die vorliegende Arbeit selbstständig und ohne fremde Hilfe verfasst habe. Alle verwendeten Quellen und Hilfsmittel sind vollständig angegeben.

Mainz, April 2014

Acknowledgement

I am grateful to the German National Academic Foundation (Studienstiftung des deutschen Volkes) and the Graduate School of Excellence “Material Science in Mainz” (MAINZ) for their financial support.

Chapter 2 has already been published as a paper in the Journal Dalton Transaction and is reproduced with permission from the Royal Society of Chemistry.

P. Happ, E. Rentschler, Enforcement of ahigh-spin ground state for the first 3d hetero-metallic 12-metallacrown-4 complex, Dalton Trans. 2014, 43, 15308-15312

DOI: 10.1039/C4DT02275K

Some results and figures of Chapter 3 have been published in the Journal Coordination Chemistry Reviews and is reproduced with permission from Elsevier.

P. Happ, C. Plenk, E. Rentschler, Review-Artikel, 12-MC-4 metallacrowns as versatile tools for SMM research, Coord. Chem. Rev., 2015, 289-290, 238-260

DOI: 10.1016/j.ccr.2014.11.012

Contents

1 Introduction

The present Ph.D. thesis deals with the fusion of two complementary topics in current coordination chemistry. While the magneto-chemical aspect of single-molecule magnetism represents the effect- and function-oriented component, its purposeful realization via accordingly designed metallacrown complexes characterizes the synthetic task. This chapter gives a brief introduction to the basics of both topics and outlines current challenges in the respective fields of research. Subsequently, the reasons for the choice of the target to equip the distinguished compound class of 12-MC-4 metallacrowns with the feature of single-molecule magnetic behavior are elucidated.

1.1 Single-molecule magnets (SMMs)

Since the discovery of the slow relaxation of magnetization and the appearance of a magnetic hysteresis below a certain blocking temperature for the paradigmatic Mn_{12}[1] cluster in 1993,[2,3] the vision of discrete magnets with molecular-scale dimensions and the associated occurrence of observable quantum phenomena has intensively spurred magnetochemical research.[4–11] A plethora of future applications of the so-called single-molecule magnets has hence been envisioned which range from more conventional usages like magnetic refrigeration via the magnetocaloric effect or high-density data storage based on the orientation of the magnetic moment to the utilization of their quantum size effects for the processing of information in molecular spintronic devices and quantum computers.[12–19] Merging their magnetic properties with other features and effects, single-molecule magnets hold out the prospect of their incorporation into various multifunctional materials.[20–27] Even if they will not find their way into mass products for daily life, at least specialized applications can be expected with high probability in a world of growing complexity and demand for subtle individual solutions. However, the enormous importance of molecular magnetic research in general and the investigation of single-molecule magnetism in particular for the extension of the scope of knowledge concerning the magnetic principles and interaction mechanisms in matter is beyond question. Therefore, this field of research has already and will further on directly or indirectly facilitate also tangible present and future yields. Here, the advantages of the bottom-up approach in molecular magnetism consist in its foundation on well defined and easily modifiable structures which enable the synergetic cycle of synthesis, analysis, deduction of magneto-structural correlations and enhanced design.[28]

The simplified common model for the explanation of the origins of single-molecule magnetic behavior is based on a molecule in its spin ground state S which features a magnetic anisotropy and therefore has an energetic preference of certain possible spin

orientations with different projections on the specified axis already in the absence of an external magnetic field.[7,29] Here, the anisotropy arises from the weak interaction of the spin with its environment and is mediated by the spin-orbit coupling.[30] Consequently, the general degeneracy of the M_S sublevels which characterize thee different orientations of the spin vanishes and the extent of the axial zero-field splitting is described via the parameter D. For a strictly axial anisotropy, the degeneracy is maintained for the M_S states which only differ in their sign or, to be more illustrative, for corresponding orientations of the spin component parallel and antiparallel to the specified axis. Although reversed configurations are discussed for current examples of mononuclear Co(II) single-molecule magnets,[31–34] the preference of the orientation of the spin with large projections along the specified axis (easy axis) and corresponding high modulus values of the M_S quantum numbers is assumed in the common model concept. The sign of the zero-field splitting parameter D is defined negative for this case by convention.

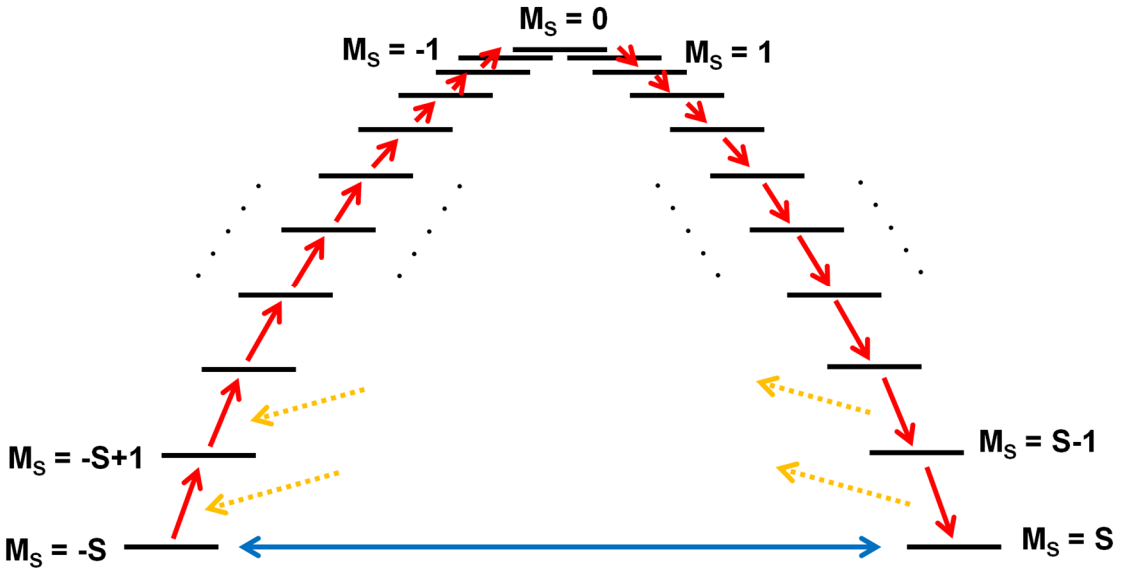

Figure 1 Generalized energy level diagram of the M_S states of the spin ground state of an SMM and with depicted relaxation pathways of quantum tunneling (blue) and Orbach process (red) via phonon exchange with the lattice (yellow).

At very low temperatures only the two degenerated lowest lying M_S states are populated with equal occupancy for an ensemble of molecules in the absence of an applied magnetic field. Turning on an external field along the specified axis, the degeneracy of the associated M_S levels also vanishes due to the Zeeman effect and the states with negative quantum numbers are lowered in energy whereas those with positive sign are elevated due to the positive or negative projection of the magnetic moment on direction of the external field. Therefore, the majority of molecules exists in the state with the highest negative M_s value after the corresponding equilibrium has been reached and an over-all magnetization can be detected. When the field is switched off again, the ensemble has to return into the equilibrium with a parity population of the redegenerated pair of lowest-

lying states with the highest M_S values. The corresponding decrease of the magnetization follows an exponential decay law (1) with a relaxation time τ. Depending on its magnitude, the value of τ at a certain temperature and field strength can be obtained from ac-susceptibility measurements with an oscillating applied magnetic field or from time dependent static dc-magnetization data.

$$\boldsymbol{M_z(t) = M_z(0) \cdot \exp(-t/\tau)} \quad (1)$$

Here, the relaxation rate τ^{-1} is effected by different mechanisms which can be split into spin-lattice relaxation processes via spin-phonon interactions and quantum tunneling. While for the interpretation of the dynamic magnetism of lanthanide and mononuclear transition metal ion based SMMs the Raman and direct process have gained importance, the features of the slow relaxation of magnetization have been discussed as a dominant interplay of quantum tunneling and the successive passing through intermediate M_S states via the absorption and emission of phonons for the early multinuclear transition metal complexes. Due to the non-degeneracy of these levels, the latter so-called Orbach process is tantamount with the overcoming of an energy barrier and the temperature dependence of its relaxation rate can therefore be expressed by the Arrhenius equation (2).

$$\boldsymbol{\tau^{-1} = \tau_0^{-1} \cdot \exp(-U/kT)} \quad (2)$$

The height of the corresponding anisotropy barrier U to magnetization reversal (3/4) is proportional to the zero-field splitting parameter D as well as the to the square of the spin ground state S for integer spins and the spin ground state reduced by ¼ for Kramer's systems, respectively. Performing a linear regression of the experimental data from the Arrhenius plot of the natural logarithm of the relaxation time versus the reciprocal temperature, the values of the effective energy barrier U_{eff} and the attempt relaxation time τ_0 are commonly obtained from the high temperature range according to the linearized form of (2).

$$\boldsymbol{U = -D \cdot S^2} \quad (3)$$

$$\boldsymbol{U = -D \cdot (S^2 - ¼)} \quad (4)$$

By contrast, the quantum tunneling through this potential energy barrier is independent from temperature and is mediated by hyperfine, intermolecular dipolar interactions and a transversal anisotropy which is characterized by the parameter E. The latter source holds however not validity for the facilitation of quantum tunneling for non-integer spins. Evidence for the occurrence of this relaxation process is given by a temperature-independent relaxation time regime in the low temperature range of the Arrhenius plot and by the stepwise change of the magnetization in the hysteresis curves of SMMs due to the enforced degeneration of different M_S states under the influence of the magnetic

field. The direct process describes the immediate transition between two states by the exchange of a phonon of suitable energy with the lattice whereas the Raman mechanism involves the promotion into a virtual state via the absorption of one phonon and the instantaneous decay into the target state under emission of another phonon.[35,36] Both processes cause curvature in the Arrhenius plot as they scale linearly with and are a power function with power factors between 1 and 9 of the temperature, respectively.[37]

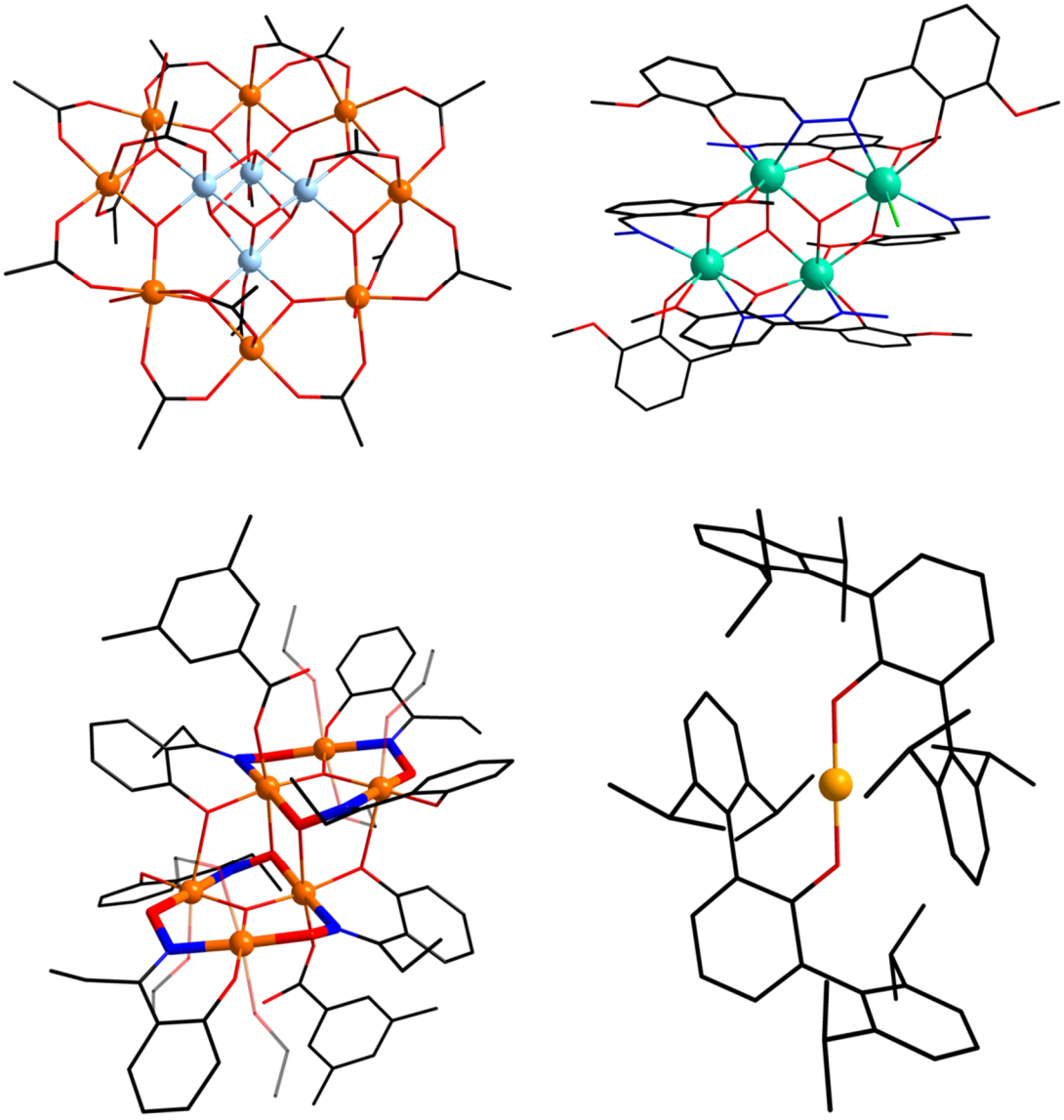

Figure 2 Prominent examples of complexes with SMM behavior: Mn_{12}[1] (top left), Mn_6[49] (down left), Dy_4[53] (top right) and Fe_1[53] (down right); color code: green - Dy(III), yellow - Fe(II), light blue - Mn(IV), orange - Mn(III), red - O, dark blue - N, black - C.

According to the equations (3) and (4) for the height of the anisotropy barrier, the attempts to increase the latter aimed at the simultaneous enhancement of the axial anisotropy and the spin ground state by a raise of the number of single-ion contributions in the

early years of single-molecule magnet research. Although corresponding clusters of high nuclearity could be synthesized, the obtained energy barrier of 60-64 K for Mn_{12} could not be exceeded significantly in this way[38–42] as both essential parameters revealed to be strongly correlated with each other causing a so-called anisotropy dilution.[43–47] By contrast, the purposeful synthetic fine-tuning of the magnetic properties of known finite compounds via their molecular configuration yielded a new record energy barrier of 86 K for a member of the family of Mn_6 complexes based on salicylaldoxime derivatives in 2007.[48,49] A new massive impulse was given to this field of research by the incorporation of lanthanide ions into SMMs.[50,51] Here, the involvement of f-electrons potentially provides a large spin, a large unquenched orbital moment, strong spin-orbit coupling and a resultant high single-ion magnetic anisotropy as valuable contributions for a high energy barrier to magnetization reversal.[52] Though, the inner character of the 4f magnetic orbitals and the corresponding weak covalence of the coordinative bonds hamper the purposeful shaping of the coordination sphere as well as a targeted synthetic integration of the rare earth metal ions into designed magnetic coupling schemes. In spite of the introduction of simple rough guidelines for the triggering of high anisotropy barriers in mononuclear compounds via tailored ligand fields, the complexity of the electronic structure and the challenging synthetic handling creates especially the realization of multinuclear lanthanide ion based SMMs in general a mixture of determination via elaborate ligands and serendipity. Nevertheless, a tetranuclear dysprosium complex took over the record by an energy barrier of 170 K in 2009 and since then rare earth metal clusters have dominated the high-performance section.[51,53] Especially SMMs based on a single, virtually magnetically isolated metal ion, which are sometimes referred to as single-ion magnets (SIMs), have been established by examples of lanthanide compounds and have yielded remarkable capability.[54–57] So, the hitherto highest energy barrier at all of 938 K was for instance generated by a mononuclear heteroleptic phthalocyanato double-decker terbium sandwich complex.[58] These results moreover reflect the general development of an increased focus on finite nuclearity and the emphasized significance of the magnetic anisotropy in the research on single-molecule magnets. Accordingly, the issue of slow relaxation of the magnetization based on a single metal center has currently developed into a hot topic for transition metals because corresponding molecules exceeded the energy barriers of comparable conventional multinuclear clusters with respective peak values of exceptional 260 K for a mononuclear Fe(II) complex[36,59] and 96 K for a cobalt dimer.[60] Furthermore, the transition metal based SMMs feature the advantage of a more targeted and versatile synthetic modifiability of the crucial shape of their coordination sphere over the lanthanide containing pendants. Besides some rare examples of mononuclear Mn(III)[61–63] and Fe(III)[24] complexes, Fe(II) and Co(II) ions dominate the respective research results as they can feature very strong spin-orbit coupling as effective source for magnetic anisotropy. While the Fe(II) containing examples also require the installation of special electronic

configurations via elaborate ligand systems,[36,64–66] Co(II) complexes with SMM behavior based on a virtually magnetically isolated metal ion can be obtained for different donor atoms, coordination numbers and sphere geometries from relative simple synthetic approaches.[27,31-34,67–75]

In spite of the great potential of this structural flexibility, this plurality of single-molecule magnets based on just one Co(II) ion hitherto lacks a comprehensive model for the reasons of the slowed relaxation and the interplay of involved processes. The occurrence of special effects like the coexistence and transfer of multiple relaxation pathways by the enforcement of an applied static magnetic field additionally reveal further concealed interesting features despite the evadable simplicity of these systems.[74] Simultaneously, the still remaining incompleteness of the understanding of these actually simplest examples points out the demand for further investigations of multinuclear clusters and possibly provides new aspects for their development potential. Similar issues can be claimed for the other transition metal ions and especially for the increasing number of lanthanide ion based compounds which show a slow relaxation of magnetization.[36,5152,] Consequently, the guidelines for the rational design of high-performance single-molecule magnets are still under permanent improvement alongside the extension of the scope of respective knowledge. Besides the developments of the core research, the fulfillment of essential requirements for possible future applications is already approached. Here, the deposition of the SMMs on surfaces as a necessary precondition of an addressability for preparative and readout procedures receives increasing attention because the complex interactions of both components often causes the loss of the intended properties and the control of the orientation of the SMMs still represents a demanding task.[76–79] Moreover, the purposeful linkage of molecular magnets with each other[14,80–86] and the attachment of moieties for the response on complementary external stimuli[20,22,23,25] represent interesting current challenges of the research on single-molecule magnets.

1.2 Metallacrowns (MCs)

Comprising the multiple cyclic repetition of the characteristic sequence [M-O-N-], the first examples of metallacrown complexes were discovered in 1989[87–89] and named in the style of their organic pendants, the crown ethers, and their corresponding coronates which had attained the Nobel Prize two years before.[90–92] In the following years, the concept of the metallacrown analogy was spread in different ring sizes like 9-MC-3,[93–100] 12-MC-4,[101–117] 15-MC-5[118–121] and 18-MC-6[122,123] across the periodic table of the elements by examples of cluster based on various hydroxylamine,[107,112,114] oxime,[94–100,104,110,116,117,122,123] hydroxamic acid,[93,102,108,111,115,118–121] nitrosyl[106] and nitrite[101,109] ligands as well as their combinations.[103,105,113] Consequently, a specific no-

menclature with the general formula (5) was developed on the basis of the naming of the organic crown ethers.[124,125]

$$\boldsymbol{M'(Ox)X_x\left[12-MC_{M(Ox)N(L)}-4\right]Y_y} \quad (5)$$

Here, the central guest ion M' with its oxidation state as well as the attached anions X are prefixed to a bracket which contains the letters MC for metallacrown embedded into the total number of all atoms and the amount of oxygen donor atoms in the characteristic cyclic host. The type of ring metal ion with its oxidation state and the substitute of the second virtual methylene unit arising from a ligand with short name L are added as subscript to the initials of the compound class. After the bracket, the bound uncharged secondary ligands at the peripheral ring are added.

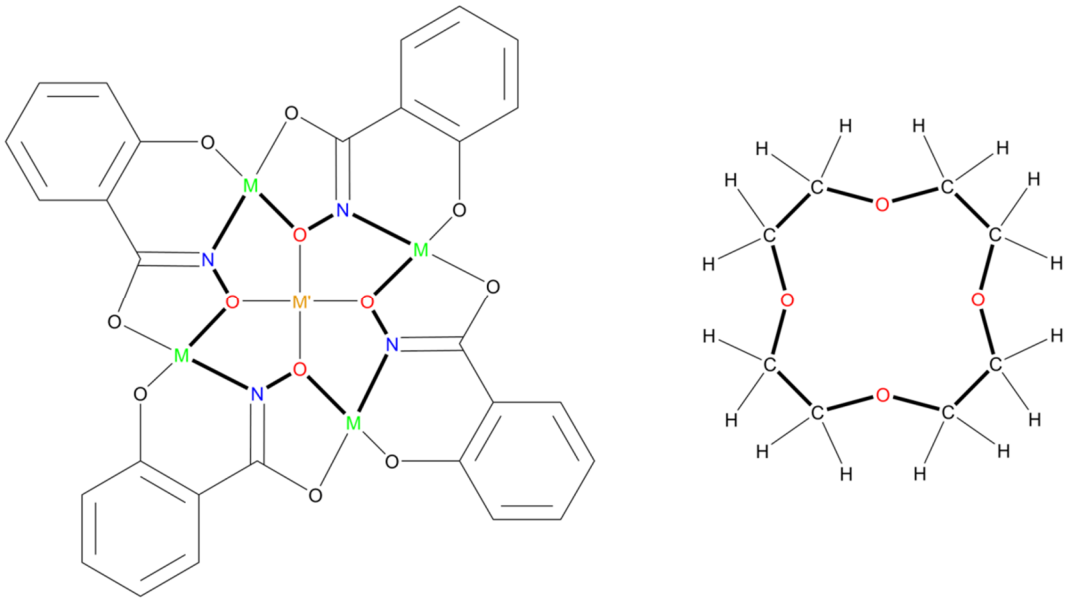

Figure 3 Structural analogy of an inorganic 12-MC-4 metallacrown complex (left) and an organic 12-C-4 crown ether molecule (right); color code: orange - central guest ion, green - ring metal ions, red - oxygen donor atoms in the characteristic cyclic host, blue - nitrogen, black - peripheral oxygen atoms / carbon and hydrogen atoms.

Moreover, the concept was also transferred to derivatives with modified repetition units like [M-N-N-] for aza-,[126–137] [M-O-C-N-] for expanded[138–143] and [M-N-C-N-] for expanded aza-metallacrowns.[144–150] Due to their unique properties, metallacrowns have found widespread application in various fields of research like catalysis,[151–153] modeling of active sites in enzymes,[154] bioactivity,[155,156] magnetic resonance imaging,[157] one- and multidimensional solids,[158–162] molecular recognition,[163–165] near-infrared luminescence[115] and single-molecule magnetism.[116,166]

The compounds based on the pioneering ligands salicylhydroxamic (H_3Shi) acid hold a paradigmatic significance as they represent the basis for the establishment of this compound class and significantly enabled the extraction of its distinguished features.[87–89,93,102,111,118,152,154,156,167–176] Here, the expansion of the simple structural towards a functional analogy to the organic crownethers was targeted in the early days of metallacrown chemistry. However, the essential integrity in solution which could not be taken for granted due to the partial exchange of covalent by coordinative bonds as constituting interactions of the cyclic scaffold had to be ensured previously. First of all, the reliability of the evolution of the 12-MC-4 type as dominating structural pattern for the salicylhydroximate ligand was ascertained by many examples of different metal species in spite of the finite ligand size and can be rationalized by the angle of 90° between both metal binding moieties. By contrast, ligands like 2-pilolinhydroxamic acid with an increased corresponding angle of 108° prefer the formation of extended 15-MC-5 type clusters.

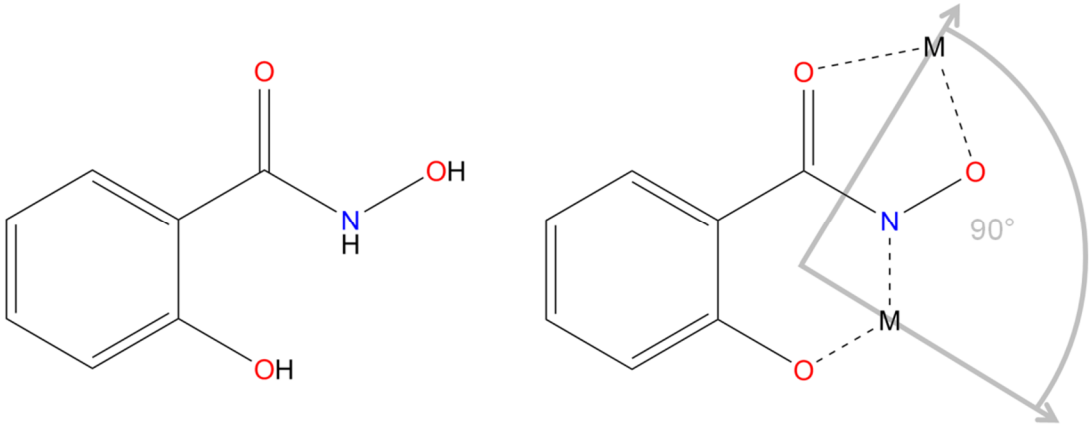

Figure 4 Structural formula of salicylhydroxamic acid (left) and its characteristic binding in 12-MC-4 metallacoronates (right); color code: orange - central guest ion, green - ring metal ions, red - oxygen, blue - nitrogen, black - carbon.

In manifold experimental setups, the integrity of the basic metallacrown motif and the absence of main ligand exchange were then verified whereas the bridging and secondary ligands can easily undergo substitution.[93,102,169,170] Finally, a strong dependence on the presence of respective anions was observed concerning the selectivity towards different central guest ions as the principal feature of the organic crown ethers and hence the host-guest behavior of the metallacrowns was described by the term ion-pair selectivity. The stability constants of the cyclic inorganic scaffolds in general exceed the corresponding values of their organic pendants due to the additional counter charges and the higher degree of rigid preorganization of the donor atoms[124,125] Nevertheless, the complexation of different cations at the core of the cluster requires an adaption of the cavity

sizes and the arrangement of the hydroximate oxygen donor atoms which is achieved via a flexible variation of the molecular configuration of the cyclic scaffold.[169]

Heterometallic metallacoronates of the 12-MC-4 motif are hitherto limited to manganese based complexes with one or two alkali[170,172] or alkaline earth[154] metal guest ions, a sodium centered gallium metallacryptand[102] and a zinc sandwich cluster with an encapsulated terbium ion.[115] A pure transition metal based metallacrown with another transition metal at its core has not been reported for this compound class to date. By contrast, a great number of heterometallic 15-MC-5 metallacoronates which comprise copper,[119,153,157,160,165,166,177–189] nickel[120,121] and zinc[121] in the cyclic host have already been discovered. Due to the enlarged cavity size, especially lanthanide ions[120,121,153,157,160,165,166, 177–189,] are the most common guest ions but also alkali (earth), transition metal, lead[120,182] and uranium[119] ions can be encapsulated. Another striking point which contradicts the widespread existence of such complexes for metal ions across the periodic table of the elements represents the just weakly developed metallacrown chemistry of cobalt. While in general the corresponding examples in literature are limited to some 9-MC-3 compounds[97,190,191], few derivatives of one basic inverse 12-MC-4 molecule[192,193] and some aza-metallacrowns,[127–130] cobalt complexes based on the pioneering ligand salicylhydroxamic acid have not yet been reported at all although they had already been predicted in the early days of metallacrown chemistry.[89]

1.3 Metallacrown based single-molecule magnets

Metallacrowns have proven to unit a combination of several properties in a unique way which creates them a potentially powerful tool to face various current issues of single-molecule magnet research. In summary, metallacrowns in general and the established 12-MC-4 complexes based on salicylhydroxamic acid in particular feature the most singular dualism between the reliability of their cyclic host on the one hand and the versatility concerning the encapsulated central guest ion, the molecular configuration as well as the kind of secondary and bridging ligands on the other hand.[124] While the aspect of their integrity represents an essential requirement for their varied application via the deposition on surfaces or the incorporation into functional materials, the flexibility as key feature allows for a targeted synthetic engineering of the magnetic properties of the metallacoronates and facilitates the control of their interaction with various other compounds and environments. These general sources of capability can be utilized by a development of specified strategies which match the respective addressed issue. Hence, the magnetic core features can be adapted by a manipulation of the coupling scheme via a purposeful positioning of suitable metal species in the cavity and the surrounding scaffold as well as by an adjustment of the anisotropy via the shaping of the individual coordination spheres and the overall molecular configuration with the help of peripheral

interactions, secondary and bridging ligands. Moreover, the introduction of multifunctional bridging and secondary ligands facilitates the linkage among the complexes, with additional receptor molecules as well as surfaces of substrates and can simultaneously serve as communication interface for magnetic and other interactions between the so associated components. An alternative pathway to achieve the latter targets is provided by a direct integration of additional functional groups at the periphery of the metallacrown main ligands. Due to the reliable evolution of the metallacrowns in the style of a powerful synthetic protocol, this proceeding should be compatible with a wide range of attached moieties. Furthermore, metallacoronates have revealed their potential to function as supramolecular ligands by the complexation of additional cation via a suitable arrangement of their peripheral donor atoms which is facilitated by the flexible adaption of the molecular configuration.[169] The advancement of this option holds out the prospect for a purposeful expansion of these complexes. Hence, the dualism of reliability and versatility predestines metallacrowns and especially the 12-MC-4 type for their application in magneto-chemical research and provide uniquely targeted pathways for the realization of advanced approaches to the progress of single-molecule magnetism.

However, only one example of a transition metal based 12-MC-4 coronate with single-molecule magnetic behavior is hitherto reported in literature. So, the pioneering compound $Mn(II)(OAc)_2[12\text{-}MC_{Mn(III)N(Shi)}\text{-}4](DMF)_6 \cdot 2DMF$ features an energy barrier of 21K to magnetization reversal.[87,194] A main source for this lack consists in the preference of the mutual cancelation of spins by the arrangement of coupling pathways within the intrinsic connectivity pattern for the most common case of antiferromagnetic interactions.[161] This finding remains also valid for the aforementioned heterovalent manganese cluster but is compensated by the consequence of another structural characteristic of the previous 12-MC-4 complexes. The anisotropic structure in the form of a planar disc shape is accompanied by an accordant combination of the single-ion contributions of the magnetic anisotropy due to the nearly parallel alignment of the Jahn-Teller-axis of the trivalent manganese ions in the ring.[194] Exhibiting a slow relaxation of magnetization reversal, the presence of metal ions with high single-ion anisotropy is also most likely the decisive factor in a Gd_8 cluster with 12-MC-4 subunit which embraces four hydroxide ions at its core[116] and a vacant aza-12-MC-4 cobalt complex.[130] By contrast, the 9-MC-3 motif represents a deserve building unit in the development of transition metal based SMMs[195–197] and is for example also contained in the family of Mn_6 clusters of salicylaldoxime[48,198–200] derivatives featuring the former record holder of the highest anisotropy barrier.[49] However, the beneficial increased spin ground state here originates from a completely different connectivity pattern due to the absence of a central magnetic guest ion and the occasion of ferromagnetic interactions. At the same time, the reported single-molecule magnets for the larger 15-MC-5[166] complexes, the non-classical 14-MC-5 type[201–203] and multinuclear, metallacrown related heterometal-

lic Mn_xLn_y clusters[204,205] certainly gain from the single-ion contributions to the overall spin and magnetic anisotropy of incorporated lanthanide ions.

This thesis summarizes two novel complementary strategies and their present results to overcome the intrinsic handicap of the connectivity pattern of the magnetic interaction pathways in 12-MC-4 metallacoronates for the creation of single-molecule magnets by the utilization of the exceptional dualism of reliability and versatility of the corresponding salicylhydroxamic acid based complexes. Therefore, it provides targeted access to these unique advantages of metallacrowns for the investigation, optimization and application of single-molecule magnets.

The first approach respects the given connectivity pattern of the magnetic coupling pathways and intends to turn its intrinsic features into an advantage for the establishment of a high-spin ground state. For that purpose, a more parallel alignment of the spins in the peripheral ring is planned to be enforced in spite of expected antiferromagnetic exchange interactions via an emphasis of the coupling pathways between the central guest ion and the individual metal ions in the cyclic host versus the magnetic interaction within the ring. Therefore, a Cu(II) ion which is capable for the occurrence of strong magnetic interactions is scheduled as magnetic director at the core of the complex whereas metal ions with large spin contributions like Fe(III) are placed in the surrounding scaffold of the designed heterometallic high-spin metallacrown.

The second strategy corresponds to the current trend in this field of research to yield, analyze and optimize single-molecule magnetic behavior based on a virtually magnetic isolated metal ion. Having gotten hold of the first examples of cobalt metallacrowns of salicylhydroxamic acid, the potential of these Co(II)[12-$MC_{Co(III)N(Shi)}$-4] complexes to feature single-molecule magnetism depending on the central Co(II) guest ion is investigated. The diamagnetic nature of the Co(III) ions in the cyclic host avoids the above-mentioned problematic coupling scheme and shields the encapsulated guest ion at the core from unintended magnetic interactions. Moreover, the flexibility of the molecular configuration of this scaffold enables the crucial modification of the coordination sphere of the central Co(II) ion by the exchange secondary and bridging ligands as well as by the attachment of additional cations at the periphery of the complex. Due to the high sensitivity of divalent high-spin cobalt ions, the shape and the composition of this coordinative environment are assigned to the role of an interface for the synthetic tuning of the magnetism of the virtually magnetically isolated Co(II) guest ion at the core of the single-molecular magnet based on a heterovalent cobalt metallacrown.

The detailed concepts of both strategies, their already attained results and the corresponding discussions are presented in the following chapters in the form of manuscripts for publications with attached further experimental details, data, illustrations and addi-

tional remarks as supplementary information. At the date of the submission of this thesis, the manuscripts concerning the heterometallic metallacrowns has been sent to publishers and is under review whereas the treatise on the heterovalent cobalt metallacrowns will be rearranged into a communication and the body of a focused review article due to short occasions.

1.4 References

[1] T. Lis, *Acta Cryst. B Struct Crystallogr Cryst Chem*, **1980,** *9*, 2042

[2] R. Sessoli, D. Gatteschi, A. Caneschi and M.A. Novak, *Nature*, **1993,** *6442*, 141

[3] R. Sessoli, H.Lien Tsai, A.R. Schake, S. Wang, J.B. Vincent, K. Folting et al., *J. Am. Chem. Soc.*, **1993,** *5*, 1804

[4] D. Gatteschi, R. Sessoli and A. Cornia, *Chem. Commun*, **2000,** *9*, 725

[5] G. Christou, *Polyhedron*, **2005,** *16-17*, 2065

[6] S. Accorsi, A.-L. Barra, A. Caneschi, G. Chastanet, A. Cornia, A.C. Fabretti et al., *J. Am. Chem. Soc.*, **2006,** *14*, 4742

[7] D. Gatteschi, R. Sessoli, J. Villain, *Molecular Nanomagnets*, **2006**, Oxford University Press (Mesoscopic physics and nanotechnology, 5)

[8] R. Winpenny, *Single-Molecule Magnets and Related Phenomena*, 2006, Springer-Verlag (Structure and Bonding)

[9] A.J. Tasiopoulos and S.P. Perlepes, *Dalton Trans*, **2008,** *41*, 5537

[10] M. Murrie, *Chem. Soc. Rev.*, **2010,** *6*, 1986

[11] D. Gatteschi, M. Fittipaldi, C. Sangregorio and L. Sorace, *Angew. Chem. Int. Ed.*, **2012,** *20*, 4792

[12] G. Christou, D. Gatteschi, D.N. Hendrickson and R. Sessoli, *MRS Bull.*, **2000,** *11*, 66

[13] M.N. Leuenberger and D. Loss, *Nature*, **2001,** *6830*, 789

[14] W. Wernsdorfer, N. Aliaga-Alcalde, D.N. Hendrickson and G. Christou, *Nature*, **2002,** *6879*, 406

[15] A. Ardavan, O. Rival, J. Morton, S. Blundell, A. Tyryshkin, G. Timco and R. Winpenny, *Phys. Rev. Lett.*, **2007,** *5*

[16] M. Manoli, R.D. L. Johnstone, S. Parsons, M. Murrie, M. Affronte, M. Evangelisti and E.K. Brechin, *Angew. Chem. Int. Ed.*, **2007,** *24*, 4456

[17] L. Bogani and W. Wernsdorfer, *Nat Mater*, **2008,** *3*, 179

[18] M. Mannini, F. Pineider, C. Danieli, F. Totti, L. Sorace, P. Sainctavit et al., *Nature*, **2010,** *7322*, 417

[19] B. Luo, J. Liu, J.-T. Lü, J.-H. Gao and K.-L. Yao, *Sci. Rep.*, **2014**

[20] H. Hiraga, H. Miyasaka, K. Nakata, T. Kajiwara, S. Takaishi, Y. Oshima et al., *Inorg. Chem.*, **2007,** *23*, 9661

[21] Y. Bi, X.-T. Wang, W. Liao, X. Wang, R. Deng, H. Zhang and S. Gao, *Inorg. Chem.*, **2009,** *24*, 11743

[22] M. Morimoto, H. Miyasaka, M. Yamashita and M. Irie, *J. Am. Chem. Soc.*, **2009,** *28*, 9823

[23] M. Gonidec, F. Luis, À. Vílchez, J. Esquena, D.B. Amabilino and J. Veciana, *Angew. Chem. Int. Ed.*, **2010,** *9*, 1623

[24] S. Mossin, B.L. Tran, D. Adhikari, M. Pink, F.W. Heinemann, J. Sutter et al., *J. Am. Chem. Soc.*, **2012,** *33*, 13651

[25] R. Ababei, C. Pichon, O. Roubeau, Y.-G. Li, N. Bréfuel, L. Buisson et al., *J. Am. Chem. Soc.*, **2013,** *39*, 14840

[26] K. Yamashita, R. Miyazaki, Y. Kataoka, T. Nakanishi, Y. Hasegawa, M. Nakano et al., *Dalton Trans.*, **2013,** *6*, 1987

[27] D.-K. Cao, J.-Q. Feng, M. Ren, Y.-W. Gu, Y. Song and M.D. Ward, *Chem. Commun.*, **2013,** *78*, 8863

[28] M. Verdaguer, *Polyhedron*, **2001,** *11-14*, 1115

[29] D. Gatteschi and R. Sessoli, *Angew. Chem. Int. Ed.*, **2003,** *3*, 268

[30] R. Boča, *Coordination Chemistry Reviews*, **2004,** *9-10*, 757

[31] W. Huang, T. Liu, D. Wu, J. Cheng, Z.W. Ouyang and C. Duan, *Dalton Trans.*, **2013,** *43*, 15326

[32] J. Vallejo, I. Castro, R. Ruiz-García, J. Cano, M. Julve, F. Lloret et al., *J. Am. Chem. Soc.*, **2012,** *38*, 15704

[33] J.M. Zadrozny, J. Liu, N.A. Piro, C.J. Chang, S. Hill and J.R. Long, *Chem. Commun.*, **2012,** *33*, 3927

[34] E. Colacio, J. Ruiz, E. Ruiz, E. Cremades, J. Krzystek, S. Carretta et al., *Angew. Chem.*, **2013,** *35*, 9300

[35] R.L. Carlin, *Magnetochemistry*, **1986**, Berlin, Springer Verlag

[36] J.M. Zadrozny, M. Atanasov, A.M. Bryan, C.-Y. Lin, B.D. Rekken, P.P. Power et al., *Chem. Sci.*, **2012,** *1*, 125

[37] K.N. Shrivastava, *phys. stat. sol. (b)*, **1983,** *2*, 437

[38] M. Murugesu, M. Habrych, W. Wernsdorfer, K.A. Abboud and G. Christou, *J. Am. Chem. Soc.*, **2004,** *15*, 4766

[39] M. Murugesu, J. Raftery, W. Wernsdorfer, G. Christou and E.K. Brechin, *Inorg. Chem*, **2004,** *14*, 4203

[40] A.J. Tasiopoulos, A. Vinslava, W. Wernsdorfer, K.A. Abboud and G. Christou, *Angew. Chem.*, **2004,** *16*, 2169

[41] A.M. Ako, I.J. Hewitt, V. Mereacre, R. Clérac, W. Wernsdorfer, C.E. Anson and A.K. Powell, *Angew. Chem. Int. Ed.*, **2006,** *30*, 4926

[42] M. Manoli, R. Inglis, M.J. Manos, V. Nastopoulos, W. Wernsdorfer, E.K. Brechin and A.J. Tasiopoulos, *Angew. Chem*, **2011**, n/a

[43] G. Aromí and E.K. Brechin, *Synthesis of 3d Metallic Single-Molecule Magnets*, **2006**, In: Richard Winpenny: *Single-Molecule Magnets and Related Phenomena*, Bd. 122, Springer-Verlag (Structure and Bonding), 1

[44] E. Ruiz, J. Cirera, J. Cano, S. Alvarez, C. Loose and J. Kortus, *Chem. Commun.*, **2007,** *1*, 52

[45] O. Waldmann, *Inorg. Chem.*, **2007,** *24*, 10035

[46] S. Hill, S. Datta, J. Liu, R. Inglis, C.J. Milios, P.L. Feng et al., *Dalton Trans.*, **2010,** *20*, 4693

[47] F. Neese and D.A. Pantazis, *Faraday Discuss.*, **2010**, 229

[48] C.J. Milios, R. Inglis, R. Bagai, W. Wernsdorfer, A. Collins, S. Moggach et al., *Chem. Commun.*, **2007,** *33*, 3476

[49] C.J. Milios, A. Vinslava, W. Wernsdorfer, S. Moggach, S. Parsons, S.P. Perlepes et al., *J. Am. Chem. Soc.*, **2007,** *10*, 2754

[50] R.J. Blagg, C.A. Muryn, E.J. L. McInnes, F. Tuna and R.E. P. Winpenny, *Angew. Chem. Int. Ed*, **2011,** *29*, 6530

[51] D.N. Woodruff, R.E. P. Winpenny and R.A. Layfield, *Chem. Rev.*, **2013,** *7*, 5110

[52] J.D. Rinehart and J.R. Long, *Chem. Sci.*, **2011,** *11*, 2078

[53] P.-H. Lin, T.J. Burchell, L. Ungur, L.F. Chibotaru, W. Wernsdorfer and M. Murugesu, *Angewandte Chemie*, **2009,** *50*, 9653

[54] N. Ishikawa, M. Sugita, T. Ishikawa, S.-y. Koshihara and Y. Kaizu, *J. Am. Chem. Soc.*, **2003,** *29*, 8694

[55] N. Ishikawa, *Polyhedron*, **2007,** *9-11*, 2147

[56] P.-E. Car, M. Perfetti, M. Mannini, A. Favre, A. Caneschi and R. Sessoli, *Chem. Commun.*, **2011,** *13*, 3751

[57] K. Katoh, H. Isshiki, T. Komeda and M. Yamashita, *Coordination Chemistry Reviews*, **2011,** *17-18*, 2124

[58] C.R. Ganivet, B. Ballesteros, G. de la Torre, J.M. Clemente-Juan, E. Coronado and T. Torres, *Chem. Eur. J.*, **2013,** *4*, 1457

[59] C. Ni and P.P. Power, *Chem. Commun.*, **2009,** *37*, 5543

[60] D. Yoshihara, S. Karasawa and N. Koga, *J. Am. Chem. Soc.*, **2008,** *32*, 10460

[61] A. Grigoropoulos, M. Pissas, P. Papatolis, V. Psycharis, P. Kyritsis and Y. Sanakis, *Inorg. Chem.*, **2013,** *22*, 12869

[62] R. Ishikawa, R. Miyamoto, H. Nojiri, B.K. Breedlove and M. Yamashita, *Inorg. Chem.*, **2013,** *15*, 8300

[63] J. Vallejo, A. Pascual-Álvarez, J. Cano, I. Castro, M. Julve, F. Lloret et al., *Angew. Chem. Int. Ed.*, **2013,** *52*, 14075

[64] D.E. Freedman, W.Hill Harman, T.David Harris, G.J. Long, C.J. Chang and J.R. Long, *J. Am. Chem. Soc*, **2010,** *4*, 1224

[65] W.Hill Harman, T.David Harris, D.E. Freedman, H. Fong, A. Chang, J.D. Rinehart et al., *J. Am. Chem. Soc.*, **2010,** *51*, 18115

[66] P.-H. Lin, N.C. Smythe, S.I. Gorelsky, S. Maguire, N.J. Henson, I. Korobkov et al., *J. Am. Chem. Soc.*, **2011,** *40*, 15806

[67] J.M. Zadrozny and J.R. Long, *J. Am. Chem. Soc.*, **2011,** *51*, 20732

[68] T. Jurca, A. Farghal, P.-H. Lin, I. Korobkov, M. Murugesu and D.S. Richeson, *J. Am. Chem. Soc*, **2011,** *40*, 15814

[69] A. Buchholz, A.O. Eseola and W. Plass, *Comptes Rendus Chimie*, **2012,** *10*, 929

[70] V. Chandrasekhar, A. Dey, A.J. Mota and E. Colacio, *Inorg. Chem.*, **2013,** *8*, 4554

[71] D. Wu, X. Zhang, P. Huang, W. Huang, M. Ruan and Z.W. Ouyang, *Inorg. Chem.*, **2013,** *19*, 10976

[72] F. Yang, Q. Zhou, Y. Zhang, G. Zeng, G. Li, Z. Shi et al., *Chem. Commun.*, **2013,** *46*, 5289

[73] Y.-Y. Zhu, C. Cui, Y.-Q. Zhang, J.-H. Jia, X. Guo, C. Gao et al., *Chem. Sci.*, **2013,** *4*, 1802

[74] R. Boča, J. Miklovič and J. Titiš, *Inorg. Chem.*, **2014,** *5*, 2367

[75] A. Eichhöfer, Y. Lan, V. Mereacre, T. Bodenstein and F. Weigend, *Inorg. Chem.*, **2014,** *4*, 1962

[76] A. Naitabdi, J.-P. Bucher, P. Gerbier, P. Rabu and M. Drillon, *Adv. Mater.*, **2005,** *13*, 1612

[77] R.V. Martínez, F. García, R. García, E. Coronado, A. Forment-Aliaga, F.M. Romero and S. Tatay, *Adv. Mater.*, **2007,** *2*, 291

[78] A. Cornia, M. Mannini, P. Sainctavit and R. Sessoli, *Chem. Soc. Rev*, **2011,** *6*, 3076

[79] M.Jesus Rodriguez-Douton, M. Mannini, L. Armelao, A.-L. Barra, E. Tancini, R. Sessoli and A. Cornia, *Chem. Commun.*, **2011,** *5*, 1467

[80] S. Hill, *Science*, **2003,** *5647*, 1015

[81] R. Tiron, W. Wernsdorfer, D. Foguet-Albiol, N. Aliaga-Alcalde and G. Christou, *Phys. Rev. Lett.*, **2003,** *22*

[82] K. Bernot, L. Bogani, A. Caneschi, D. Gatteschi and R. Sessoli, *J. Am. Chem. Soc.*, **2006,** *24*, 7947

[83] H. Miyasaka and M. Yamashita, *Dalton Trans.*, **2007,** *4*, 399

[84] M. Murrie and D.J. Price, *Annu. Rep. Prog. Chem., Sect. A: Inorg. Chem.*, **2007**, 20

[85] E. Pardo, R. Ruiz-García, J. Cano, X. Ottenwaelder, R. Lescouëzec, Y. Journaux et al., *Dalton Trans.*, **2008,** *21*, 2780

[86] H. Miyasaka, M. Julve, M. Yamashita and R. Clérac, *Inorg. Chem.*, **2009,** *8*, 3420

[87] M.Soo Lah and V.L. Pecoraro, *J. Am. Chem. Soc*, **1989,** *18*, 7258

[88] V.L. Pecoraro, *Inorganica Chimica Acta*, **1989,** *2*, 171

[89] M.Soo Lah, M.L. Kirk, W. Hatfield and V.L. Pecoraro, *J. Chem. Soc., Chem. Commun*, **1989,** *21*, 1606

[90] C.J. Pedersen, *Angew. Chem. Int. Ed. Engl.*, **1988,** *8*, 1021

[91] J.-M. Lehn, *Angew. Chem. Int. Ed. Engl.*, **1988,** *1*, 89

[92] D.J. Cram, *Angew. Chem. Int. Ed. Engl.*, **1988,** *8*, 1009

[93] B.R. Gibney, A.J. Stemmler, S. Pilotek, J.W. Kampf and V.L. Pecoraro, *Inorg. Chem.*, **1993,** *26*, 6008

[94] P. Chaudhuri, M. Hess, E. Rentschler, T. Weyhermüller and U. Flörke, *New J. Chem.*, **1998,** *6*, 553

[95] M. Kim and F.P. Gabbai, *Dalton Trans.*, **2004,** *20*, 3403

[96] C. Papatriantafyllopoulou, G. Aromi, A.J. Tasiopoulos, V. Nastopoulos, C.P. Raptopoulou, S.J. Teat et al., *Eur. J. Inorg. Chem.*, **2007,** *18*, 2761

[97] C.P. Raptopoulou and V. Psycharis, *Inorganic Chemistry Communications*, **2008,** *10*, 1194

[98] A. Audhya, K. Bhattacharya, M. Maity and M. Chaudhury, *Inorg. Chem.*, **2010,** *11*, 5009

[99] A. Audhya, M. Maity, K. Bhattacharya, R. Clérac and M. Chaudhury, *Inorg. Chem*, **2010,** *19*, 9026

[100] J. Esteban, M. Font-Bardia and A. Escuer, *Eur. J. Inorg. Chem.*, **2013,** *30*, 5274

[101] G. Bombieri, G. Bruno, M. Cusumano and G. Guglielmo, *Acta Crystallogr C Cryst Struct Commun*, **1984,** *3*, 409

[102] M.Soo Lah, B.R. Gibney, D.L. Tierney, J.E. Penner-Hahn and V.L. Pecoraro, *J. Am. Chem. Soc*, **1993,** *13*, 5857

[103] G. Psomas, C. Dendrinou-Samara, M. Alexiou, A. Tsohos, C.P. Raptopoulou, A. Terzis and D.P. Kessissoglou, *Inorg. Chem*, **1998,** *26*, 6556

[104] E. Colacio, C. López-Magaña, V. McKee and A. Romerosa, *J. Chem. Soc., Dalton Trans.*, **1999,** *17*, 2923

[105] G. Psomas, A.J. Stemmler, C. Dendrinou-Samara, J.J. Bodwin, M. Schneider, M. Alexiou et al., *Inorg. Chem*, **2001,** *7*, 1562

[106] S.D. Kirik, R.F. Mulagaleev and A.I. Blokhin, *Acta Crystallogr C Cryst Struct Commun*, **2005,** *10*, m445

[107] S. Jana, R. Fröhlich, A. Hepp and N.W. Mitzel, *Organometallics*, **2008,** *6*, 1348

[108] M. Tegoni, M. Remelli, D. Bacco, L. Marchiò and F. Dallavalle, *Dalton Trans*, **2008,** *20*, 2693

[109] O.N. Shishilov, T.A. Stromnova, A.V. Churakov, L.G. Kuz'mina and J.A.K Howard, *Journal of Organometallic Chemistry*, **2009,** *9-10*, 1453

[110] J. Kübel, P.J. W. Elder, H.A. Jenkins and I. Vargas-Baca, *Dalton Trans.*, **2010,** *46*, 11126

[111] X.-J. Zhao, Q.-F. Zhang, D.-C. Li, J.-M. Dou and D.-Q. Wang, *Journal of Organometallic Chemistry*, **2010,** *18*, 2134

[112] M. Ullrich, R.J. F. Berger, C. Lustig, R. Fröhlich and N.W. Mitzel, *Eur. J. Inorg. Chem.*, **2006,** *21*, 4219

[113] M. Alexiou, C. Dendrinou-Samara, C.P. Raptopoulou, A. Terzis and D.P. Kessissoglou, *Inorg. Chem*, **2002,** *18*, 4732

[114] M. Ullrich, R.J. F. Berger, S. Jana, T. Pape, R. Fröhlich and N.W. Mitzel, *Dalton Trans.*, **2011,** *5*, 1144

[115] J. Jankolovits, C.M. Andolina, J.W. Kampf, K.N. Raymond and V.L. Pecoraro, *Angew. Chem. Int. Ed.*, **2011,** *41*, 9660

[116] M. Fang, H. Zhao, A.V. Prosvirin, D. Pinkowicz, B. Zhao, P. Cheng et al., *Dalton Trans.*, **2013,** *41*, 14693

[117] M. Hołyńska and M. Korabik, *Eur. J. Inorg. Chem.*, **2013,** *31*, 5469

[118] D.P. Kessisoglou, J. Kampf and V.L. Pecoraro, *Polyhedron*, **1994,** *9*, 1379

[119] A.J. Stemmler, J.W. Kampf and V.L. Pecoraro, *Angew. Chem. Int. Ed. Engl*, **1996,** *2324*, 2841

[120] S.Hamed Seda, J. Janczak and J. Lisowski, *Inorganic Chemistry Communications*, **2006,** *8*, 792

[121] J. Jankolovits, J.W. Kampf and V.L. Pecoraro, *Polyhedron*, **2013**, 491

[122] T. Afrati, C. Dendrinou-Samara, C.M. Zaleski, J.W. Kampf, V.L. Pecoraro and D.P. Kessissoglou, *Inorganic Chemistry Communications*, **2005,** *12*, 1173

[123] S.O. Baumann, M. Bendova, H. Fric, M. Puchberger, C. Visinescu and U. Schubert, *Eur. J. Inorg. Chem.*, **2009,** *22*, 3333

[124] V.L. Pecoraro, A.J. Stemmler, B.R. Gibney, J.J. Bodwin, H. Wang, J.W. Kampf and A. Barwinski, *Metallacrowns: A New Class of Molecular Recognition Agents*, 1996, In: K.D. Karli: *Progress in Inorganic Chemistry*, Bd. 45. John Wiley & Sons, Inc (Progress in Inorganic Chemistry), 83

[125] G. Mezei, C.M. Zaleski and V.L. Pecoraro, *Chem. Rev*, **2007,** *11*, 4933

[126] G.Attilio Ardizzoia, M.Angela Angaroni, G. La Monica, F. Cariati, S. Cenini, M. Moret and N. Masciocchi, *Inorg. Chem*, **1991,** *23*, 4347

[127] I. Kim, B. Kwak and M. Soo Lah, *Inorganica Chimica Acta*, **2001,** *1-2*, 12

[128] S. Lin, S.-X. Liu, J.-Q. Huang and C.-C. Lin, *J. Chem. Soc., Dalton Trans.*, **2002,** *8*, 1595

[129] J.Ivar van der Vlugt, S. Demeshko, S. Dechert and F. Meyer, *Inorg. Chem.*, **2008,** *5*, 1576

[130] D. Wu, D. Guo, Y. Song, W. Huang, C. Duan, Q. Meng and O. Sato, *Inorg. Chem.*, **2009,** *3*, 854

[131] L.F. Jones, C.A. Kilner and M.A. Halcrow, *Chem. Eur. J.*, **2009,** *18*, 4667

[132] Y. Chen, J. Dou, D. Zhang and D. Li, *Solid State Sciences*, **2010,** *4*, 461

[133] C. Chen, H. Qiu and W. Chen, *Inorg. Chem*, **2011**, 110727131033083

[134] G.-J. Chen, C.-Y. Gao, W. Gu, X. Liu, S.-P. Yan, J.-L. Tian and D.-Z. Liao, *Z. anorg. allg. Chem.*, **2011,** *3-4*, 374

[135] E.V. Govor, A.B. Lysenko, D. Quiñonero, E.B. Rusanov, A.N. Chernega, J. Moellmer et al., *Chem. Commun.*, **2011,** *6*, 1764

[136] A.A. Mohamed, S. Ricci, A. Burini, R. Galassi, C. Santini, G.M. Chiarella et al., *Inorg. Chem.*, **2011,** *3*, 1014

[137] D. Zhang, Y. Chen, Q. Zhao and Y. Wu, *Z. anorg. allg. Chem*, **2011,** *9*, 1175

[138] A.J. Blake, R.O. Gould, C.M. Grant, P.E. Y. Milne, D. Reed and R.E. P. Winpenny, *Angew. Chem. Int. Ed. Engl.*, **1994,** *2*, 195

[139] R.W. Saalfrank, S. Trummer, U. Reimann, M.M. Chowdhry, F. Hampel and O. Waldmann, *Angew. Chem. Int. Ed.*, **2000,** *19*, 3492

[140] H. Piotrowski, K. Polborn, G. Hilt and K. Severin, *J. Am. Chem. Soc.*, **2001,** *11*, 2699

[141] M.-L. Lehaire, R. Scopelliti, H. Piotrowski and K. Severin, *Angewandte Chemie International Edition*, **2002,** *8*, 1419

[142] Z. Grote, R. Scopelliti and K. Severin, *Angew. Chem. Int. Ed.*, **2003,** *32*, 3821

[143] T. Brasey, R. Scopelliti and K. Severin, *Inorg. Chem.*, **2005,** *2*, 160

[144] N. Masciocchi, E. Corradi, M. Moret, G.Attilio Ardizzoia, A. Maspero, G. La Monica and A. Sironi, *Inorg. Chem.*, **1997,** *24*, 5648

[145] K. Yamanari, I. Fukuda, T. Kawamoto, Y. Kushi, A. Fuyuhiro, N. Kubota et al., *Inorg. Chem.*, **1998,** *21*, 5611

[146] R.H. Fish, *Coordination Chemistry Reviews*, **1999**, 569

[147] P. Annen, S. Schildberg and W.S. Sheldrick, *Inorganica Chimica Acta*, **2000,** *1-2*, 115

[148] J. Omata, T. Ishida, D. Hashizume, F. Iwasaki and T. Nogami, *Inorg. Chem.*, **2001,** *16*, 3954

[149] K. Yamanari, R. Ito, S. Yamamoto, T. Konno, A. Fuyuhiro, K. Fujioka and R. Arakawa, *Inorg. Chem.*, **2002,** *25*, 6824

[150] N. Shan, S.J. Vickers, H. Adams, M.D. Ward and J.A. Thomas, *Angew. Chem. Int. Ed.*, **2004,** *30*, 3938

[151] M. Paz Muñoz, B. Martín-Matute, C. Fernández-Rivas, D.J. Cárdenas and A.M. Echavarren, *Adv. Synth. Catal.*, **2001,** *4*, 338

[152] T.K. Si, S. Chakraborty, A.K. Mukherjee, M.G.B Drew and R. Bhattacharyya, *Polyhedron*, **2008,** *11*, 2233

[153] J.T. Grant, J. Jankolovits and V.L. Pecoraro, *Inorg. Chem*, **2012**, 120502154627002

[154] E.S. Koumousi, S. Mukherjee, C.M. Beavers, S.J. Teat, G. Christou and T.C. Stamatatos, *Chem. Commun.*, **2011,** *39*, 11128

[155] I. Tsivikas, M. Alexiou, A.A. Pantazaki, C. Dendrinou-Samara, D.A. Kyriakidis and D.P. Kessissoglou, *Bioinorganic Chemistry and Applications*, **2003,** *1*, 85

[156] C. Dendrinou-Samara, A.N. Papadopoulos, D.A. Malamatari, A. Tarushi, C.P. Raptopoulou, A. Terzis et al., *Journal of Inorganic Biochemistry*, **2005,** *3*, 864

[157] A.J. Stemmler, J.W. Kampf, M.L. Kirk, B.H. Atasi and V.L. Pecoraro, *Inorg. Chem*, **1999,** *12*, 2807

[158] J.J. Bodwin and V.L. Pecoraro, *Inorg. Chem*, **2000,** *16*, 3434

[159] J.J. Bodwin, A.D. Cutland, R.G. Malkani and V.L. Pecoraro, *Coordination Chemistry Reviews*, **2001**, 489

[160] A.D. Cutland-Van Noord, J.W. Kampf and V.L. Pecoraro, *Angew. Chem*, **2002,** *24*, 4861

[161] A.B. Lago, J. Pasán, L. Cañadillas-Delgado, O. Fabelo, F.J. M. Casado, M. Julve et al., *New J. Chem*, **2011,** *9*, 1817

[162] C. McDonald, T. Whyte, S.M. Taylor, S. Sanz, E.K. Brechin, D. Gaynor and L.F. Jones, *CrystEngComm*, **2013,** *34*, 6672

[163] C.-S. Lim, A.Cutland van Noord, J.W. Kampf and V.L. Pecoraro, *Eur. J. Inorg. Chem*, **2007,** *10*, 1347

[164] C.-S. Lim, J.W. Kampf and V.L. Pecoraro, *Inorg. Chem*, **2009,** *12*, 5224

[165] C.-S. Lim, J. Jankolovits, P. Zhao, J.W. Kampf and V.L. Pecoraro, *Inorg. Chem*, **2011**, 110503091349087

[166] C.M. Zaleski, E.C. Depperman, J.W. Kampf, M.L. Kirk and V.L. Pecoraro, *Inorg. Chem*, **2006,** *25*, 10022

[167] M.Soo Lah and V. Pecoraro, *Comments on Inorg. Chem*, **1990,** *2*, 59

[168] M.Soo Lah and V.L. Pecoraro, *Inorg. Chem*, **1991,** *5*, 878

[169] B.R. Gibney, D.P. Kessissoglou, J.W. Kampf and V.L. Pecoraro, *Inorg. Chem*, **1994,** *22*, 4840

[170] B.R. Gibney, H. Wang, J.W. Kampf and V.L. Pecoraro, *Inorg. Chem*, **1996,** *21*, 6184

[171] C. Dendrinou-Samara, G. Psomas, L. Iordanidis, V. Tangoulis and D.P. Kessissoglou, *Chem. Eur. J*, **2001,** *23*, 5041

[172] D.P. Kessissoglou, J.J. Bodwin, J. Kampf, C. Dendrinou-Samara and V.L. Pecoraro, *Inorganica Chimica Acta*, **2002,** *1*, 73

[173] C. Dendrinou-Samara, L. Alevizopoulou, L. Iordanidis, E. Samaras and D.P. Kessissoglou, *Journal of Inorganic Biochemistry*, **2002,** *1-2*, 89

[174] B. Emerich, M. Smith, M. Zeller and C.M. Zaleski, *J Chem Crystallogr*, **2010,** *9*, 769

[175] B.R. Tigyer, M. Zeller and C.M. Zaleski, *Acta Crystallogr E Struct Rep Online*, **2011,** *8*, m1041

[176] J. Herring, M. Zeller and C.M. Zaleski, *Acta Crystallogr E Struct Rep Online*, **2011,** *4*, m419

[177] A.J. Stemmler, A. Barwinski, M.J. Baldwin, V. Young and V.L. Pecoraro, *J. Am. Chem. Soc*, **1996,** *47*, 11962

[178] A.D. Cutland, R.G. Malkani, J.W. Kampf and V.L. Pecoraro, *Angew. Chem. Int. Ed.*, **2000,** *15*, 2689

[179] A.D. Cutland, J.A. Halfen, J.W. Kampf and V.L. Pecoraro, *J. Am. Chem. Soc*, **2001,** *25*, 6211

[180] T.N. Parac-Vogt, A. Pacco, P. Nockemann, S. Laurent, R.N. Muller, M. Wickleder et al., *Chem. Eur. J*, **2006,** *1*, 204

[181] C.M. Zaleski, A.D. Cutland-Van Noord, J.W. Kampf and V.L. Pecoraro, *Crystal Growth & Design*, **2007,** *6*, 1098

[182] S.Hamed Seda, J. Janczak and J. Lisowski, *Eur. J. Inorg. Chem*, **2007,** *19*, 3015

[183] G. Mezei, J.W. Kampf, S. Pan, K.R. Poeppelmeier, B. Watkins and V.L. Pecoraro, *Chem. Commun.*, **2007,** *11*, 1148

[184] E.V. Govor, A.B. Lysenko, A.N. Chernega, J.A.K Howard, A.A. Mokhir, J. Sieler and K.V. Domasevitch, *Polyhedron*, **2008,** *11*, 2349

[185] M. Tegoni, M. Tropiano and L. Marchiò, *Dalton Trans*, **2009,** *34*, 6705

[186] J. Jankolovits, J.W. Kampf, S. Maldonado and V.L. Pecoraro, *Chem. Eur. J*, **2010,** *23*, 6786

[187] C.-S.Lim Jeff W. Kampf and Vincent L. Pecoraro Joseph Jankolovits, *Z. Naturforsch.*, **2010,** *65b*, 263

[188] C.M. Zaleski, C.-S. Lim, A.D. Cutland-Van Noord, J.W. Kampf and V.L. Pecoraro, *Inorg. Chem*, **2011,** *16*, 7707

[189] A.V. Pavlishchuk, S.V. Kolotilov, M. Zeller, L.K. Thompson and A.W. Addison, *Inorg. Chem.*, **2014**, 140114140153006

[190] G. Vlahopoulou, A. Escuer, M. Font-Bardia and T. Calvet, *Inorganic Chemistry Communications*, **2012**, 78

[191] A. Kaza, P. Jensen, J. Clegg, A.F. Masters, T. Maschmeyer and A.K.L Yuen, *Polyhedron*, **2013**, 909

[192] T.C. Stamatatos, C. Papatriantafyllopoulou, E. Katsoulakou, C.P. Raptopoulou and S.P. Perlepes, *Polyhedron*, **2007,** *9-11*, 1830

[193] T.C. Stamatatos, S. Dionyssopoulou, G. Efthymiou, P. Kyritsis, C.P. Raptopoulou, A. Terzis et al., *Inorg. Chem.*, **2005,** *10*, 3374

[194] C.M. Zaleski, S. Tricard, E.C. Depperman, W. Wernsdorfer, T. Mallah, M.L. Kirk and V.L. Pecoraro, *Inorg. Chem*, **2011,** *22*, 11348

[195] T.C. Stamatatos, D. Foguet-Albiol, S.-C. Lee, C.C. Stoumpos, C.P. Raptopoulou, A. Terzis et al., *J. Am. Chem. Soc*, **2007,** *30*, 9484

[196] R. Inglis, S.M. Taylor, L.F. Jones, G.S. Papaefstathiou, S.P. Perlepes, S. Datta et al., *Dalton Trans.*, **2009,** *42*, 9157

[197] S. Wang, L. Kong, H. Yang, Z. He, Z. Jiang, D. Li et al., *Inorg. Chem*, **2011**, 110303113001003

[198] C.J. Milios, A. Vinslava, P.A. Wood, S. Parsons, W. Wernsdorfer, G. Christou et al., *J. Am. Chem. Soc.*, **2007,** *1*, 8

[199] A.-R. Tomsa, J. Martínez-Lillo, Y. Li, L.-M. Chamoreau, K. Boubekeur, F. Farias et al., *Chem. Commun*, **2010,** *28*, 5106

[200] P.L. Feng and D.N. Hendrickson, *Inorg. Chem.*, **2010,** *14*, 6393

[201] T.T. Boron, J.W. Kampf and V.L. Pecoraro, *Inorg. Chem*, **2010,** *20*, 9104

[202] F. Cao, S. Wang, D. Li, S. Zeng, M. Niu, Y. Song and J. Dou, *Inorg. Chem.*, **2013,** *19*, 10747

[203] A. Deb, T.T. Boron, M. Itou, Y. Sakurai, T. Mallah, V.L. Pecoraro and J.E. Penner-Hahn, *J. Am. Chem. Soc.*, **2014**, 140320133230001

[204] C.M. Zaleski, E.C. Depperman, J.W. Kampf, M.L. Kirk and V.L. Pecoraro, *Angew. Chem. Int. Ed*, **2004,** *30*, 3912

[205] C.M. Zaleski, J.W. Kampf, T. Mallah, M.L. Kirk and V.L. Pecoraro, *Inorg. Chem*, **2007,** *6*, 1954

2 Heterovalent Metallacrowns

Enforcing a high-spin ground state for a 12-metallacrown-4 complex via a heterometallic magnetic director approach

Peter Happ and Eva Rentschler

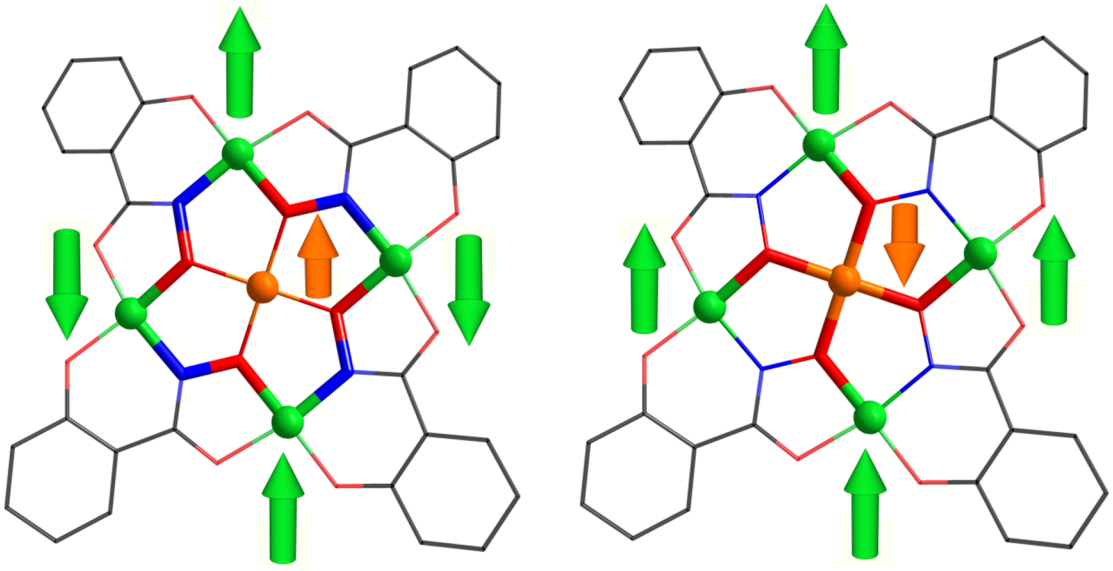

Applying a novel magnetic director approach, we have realized Cu(II)$(DMF)_2Cl_2$[12-$MC_{Fe(III)N(Shi)}$-4]$(DMF)_4 \cdot 2DMF$ as the first heterometallic transition metal 12-MC-4 complex in order to equip this type of compound with a high-spin ground state.

2.1 Abstract

Applying a novel magnetic director approach, we have realized Cu(II)$(DMF)_2Cl_2$[12-$MC_{Fe(III)N(Shi)}$-4]$(DMF)_4 \cdot 2DMF$ as the first heterometallic transition metal 12-MC-4 complex in order to equip this type of compound with a high-spin ground state. Synthesis was planed extracting basic principles of the magnetic interplay in corresponding homometallic compounds. The high spin ground state is realized as the central guest ion accomplishes its anticipated role as a magnetic director enforcing an appropriate spin topology.

2.2 Introduction

The quest for novel single-molecule magnets is one of the most powerful driving forces in coordination chemistry research.[1-4] Since the discovery of the phenomenon in 1993, [5,6] different approaches have been pursued in order to comply with the two essential requirements of a high-spin ground state and an axial magnetic anisotropy.[7] Attempts to raise these simultaneously by increasing the nuclearity,[8-10] revealed both parameters to be strongly correlated.[11-13] Current synthetic efforts focus on an increased anisotropy and are, hence, mostly geared towards the incorporation of lanthanide ions into new complexes[14-16] and/or the geometric and electronic optimization of SMMs identified already. [17-22] However, only a few rare approaches are based on a purposeful design of definite, novel target molecules and usually demand the establishment of advanced, determining ligands with various sets of donor atoms.[23,24]

Metallacrowns represent a promising class of compounds for the generation, engineering and further application of new single-molecule magnets, as they have proven most singularly to combine the features of synthetic reliability, stability of their basic scaffold, structural versatility, and facile functionalization.[25-27] In spite of the finite ligand size, salicylhydroxamic acid (H_3Shi) especially reliably creates the 12-MC-4 structural motif with four metal centers in the cyclic host and an encapsulated guest ion at its core (Fig. 1).[28-32] The complex Mn(II)$(OAc)_2$[12-$MC_{Mn(III)N(Shi)}$-4]$(DMF)_6$ has already been reported to reveal SMM behavior. In that case, the occurrence of an energy barrier to magnetization reversal has been attributed particularly to the combination of single-ion anisotropy contributions, which are promoted by the planar linkage of the spin carriers in the characteristic configuration.[33] However, 12-MC-4 clusters, in general, lack a high-spin ground state because the nearly complete mutual compensation of the spins via antiferromagnetic interactions is facilitated by the geometric arrangement of the coupling pathways.[33-35]

Therefore, we present here the first achievements of a complementary approach which respects the basic motif of the metallacrowns as an established class of complexes and realizes the enforcement of an increased spin ground state by a purposeful placement of

different metal ions in a designed target molecule. It, therefore, holds out the prospect of a uniquely rational access to novel and versatile single-molecule magnets based on high-spin metallacrowns. Featuring the most singular dualism of adaptability and stability, the upgrade of 12-MC-4 metallacrowns with advanced magnetic properties would create them powerful tools to face current challenges of magneto-chemical research. Particularly, the deposition on surfaces and the incorporation into functional materials and devices represent promising scopes in that respect.[36-39]

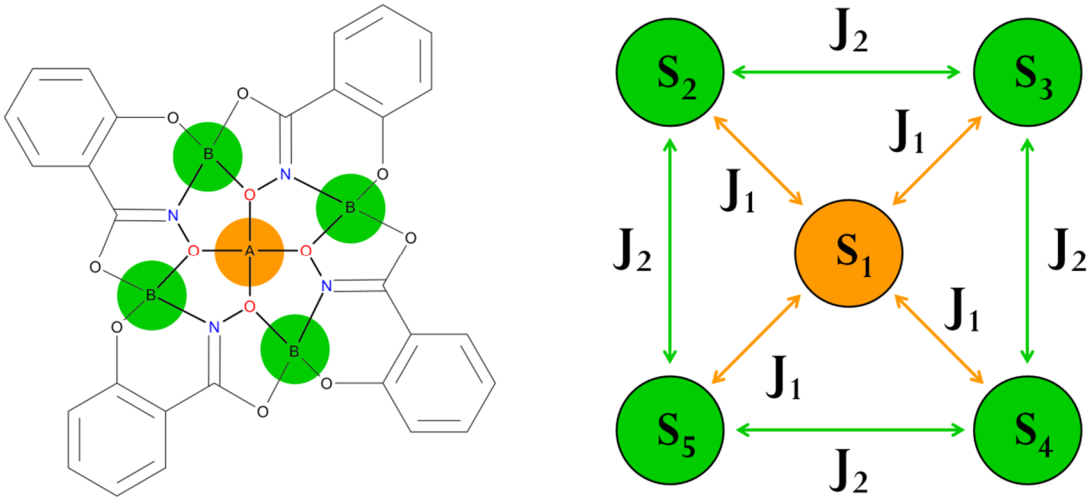

Fig.1 Basic 12-MC-4 motif with different metal-binding sites at the core (orange) and in the surrounding scaffold (green), and a corresponding idealized square magnetic model with a radial (J_1) and tangential (J_2) coupling constant.

As we are working in the field of metallacrown chemistry, we have been looking for a way to join the synthetic reliability of the characteristic structural motif with the insight into the intramolecular magnetic interplay in order to equip these complexes of distinguished features with a high-spin ground state. The interpretation of the magnetic properties of the homometallic metallacrown $(HNEt_3)_2Cu(II)[12\text{-}MC_{Cu(II)N(Shi)}\text{-}4]$ **1** in this article, demonstrates the reasonable application of the idealized square planar coupling scheme that is performed by default for 12-MC-4 type compounds in a paradigmatic way.[33-35,40-44] In this instance, the number of distinct coupling constants is reduced to one parameter J_1 for the radial interactions between the guest metal ion and the spin centers in the cyclic host, and another parameter J_2 for the tangential interactions within the peripheral ring (Fig. 1). As will be discussed in more detail below, this arrangement of coupling pathways and spins favors their mutual cancellation in the frequent case of antiferromagnetic interactions overall.

Nevertheless, the square magnetic model also comprises a star-shaped subpattern and a large number of examples of the latter structure type featuring a high-spin ground state in spite of antiferromagnetic interactions have been reported.[45-50] We, therefore,

developed the strategy to turn the square coupling scheme of the metallacrown into a dominantly star-shaped one by emphasizing the radial interactions via a deliberate placement of different metal ions inside the various binding sites. Concerning the spin topology of the ground state, this means the enforcement of a shift in the spectrum of possible orientations between the extremes of an antiparallel and a parallel alignment of the magnetic moments in the cyclic scaffold (Fig. S7). To that effect, a Cu(II) guest ion was intended to function as the central magnetic director, because its natural magnetic orbital dx^2-y^2 points directly towards basal donor atoms and can, consequently, induce extraordinary strong antiferromagnetic exchange interactions in an appropriate arrangement.[51-53] This holds especially for 12-MC-4 metallacrowns, as we have deduced from the magnetic behavior of **1** in accordance with similar compounds in literature. [35,40-44] Moreover, the range of the cavity size and the in plane position of the radial linking oxygen donor atoms appeared most promising for the aforementioned type of complex, which has been established as the predominant supramolecular assembly of the pioneering ligand salicylhydroxamic acid.[29-31,54-56] The design of the target molecule was completed by the placement of Fe(III) ions inside the cyclic periphery. These also provide high single-ion spin contributions as suitable sets of magnetic orbitals for the exchange interactions in the targeted cluster Cu(II)[12-$MC_{Fe(III)N(Shi)}$-4]. Furthermore, the coupling constants reported for the salicylhydroxamic acid-based metallacrown Fe(III)$(OAc)_3$[12-$MC_{Fe(III)N(Shi)}$-4]$(MeOH)_3$ are smaller by magnitudes than those for the homometallic copper metallacrowns such as **1**.[57] The quantitative evaluation of the interplay between radial and tangential exchange interactions performed is dealt with in the course of the interpretation of the experimental magnetic data, which have been obtained for the successfully synthesized compound Cu(II)$(DMF)_2Cl_2$[12-$MC_{Fe(III)N(Shi)}$-4]$(DMF)_4$·2DMF (**2)**.

The homometallic complex $(HNEt_3)_2$Cu(II)[12-$MC_{Cu(II)N(Shi)}$-4] (**1)** and the heterometallic compound Cu(II)$(DMF)_2Cl_2$[12-$MC_{Fe(III)N(Shi)}$-4]$(DMF)_4$·2DMF (**2)** have been prepared by reactions of salicylhydroxamic acid with the corresponding metal chloride salts in the presence of amine bases in methanol and dimethylformamide, respectively. Pursuing the positioning of the different metal ions for **2** outlined, a preferential formation of the cyclic scaffold by Fe(III) ions was anticipated due to the extraordinary affinity of the hydroxamic acid moiety towards this specie.[58-60] The encapsulation of the Cu(II) ion inside the core was, on the contrary, promoted by a waiver of potential bridging polydentate ligands in order to keep the number of pre-oriented donor atoms low, and to facilitate a flexible adaption of the cavity size via the overall molecular configuration. The successful synthesis of both compounds has been verified by various characerization methods like X-ray crystallography, elemental analysis, infrared spectroscopy, UV-Vis spectroscopy, atomic absorption spectroscopy, mößbauer spectroscopy and ESI-mass spectrometry.

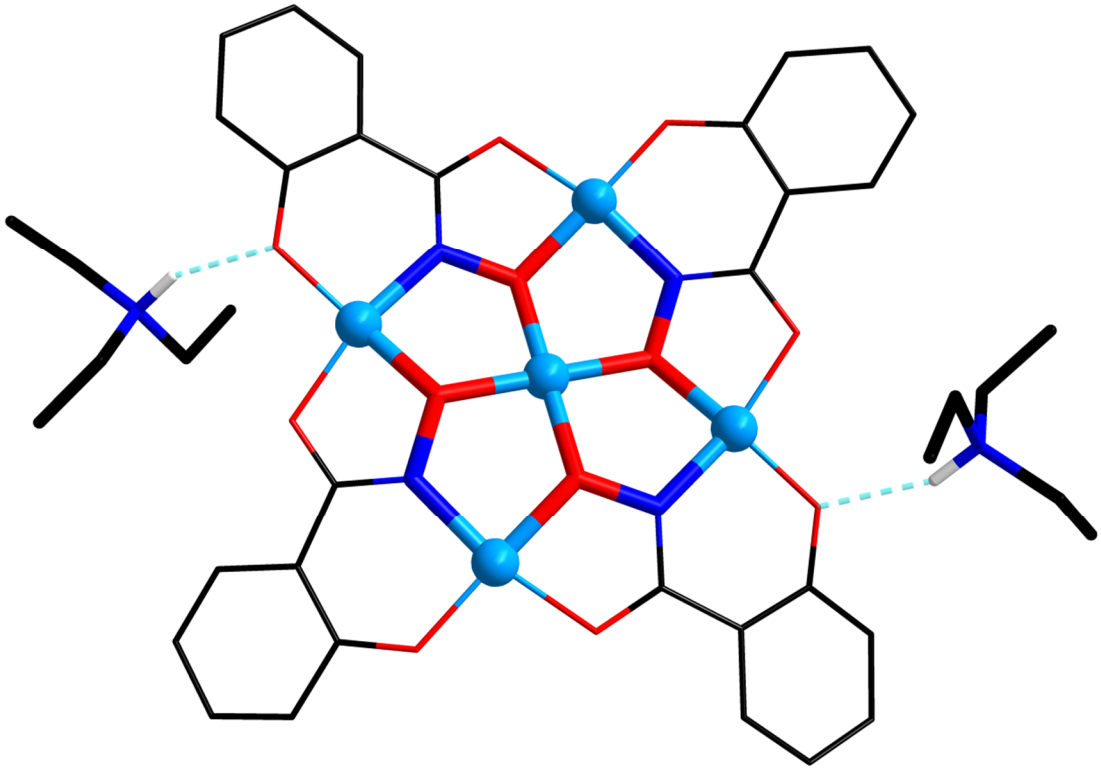

Fig. 2 Molecular structure of $(HNEt_3)_2Cu(II)[12\text{-}MC_{Cu(II)N(Shi)}\text{-}4]$ in crystals of **1**; color scheme: light blue outlined - Cu(II), red - O, dark blue - N, and black - C.

The crystal structure of **1** contains the well-known pentanuclear complex dianion $Cu(II)[12\text{-}MC_{Cu(II)N(Shi)}\text{-}4]^{2-}$ (Fig. 2, S1).[29,56] Four of the Cu(II) ions are linked by the same number of threefold deprotonated salicylhydroxamic acid molecules forming the cyclic host of the metallacrown with the characteristic repetition unit [Cu-O-N-]. Thus, each ligand binds one metal center via its hydroximate group, while the iminophenolate functionality associated is coordinated with a different copper ion of the metallamacrocycle. As every copper ion of this peripheral scaffold is bound by the complementary moieties of two adjacent salicylhydroximates, a succession of five- and six-membered chelate rings is observed. The fifth Cu(II) ion resides in the inner cavity on a center of inversion and is surrounded by the hydroximate oxygen donor atoms, which point towards the inside of the complex. Although all metal centers adopt a square planar coordination sphere, the overall molecule does not feature perfect planarity. By contrast, a so-called ‘sofa-configuration’ is present, because both adjacent ligands of the asymmetric unit are tilted slightly out of the plane of the metal ions in a different orientation and are symmetrically related to the salicylhydroximates in the opposite half of the molecule by the center of inversion. As has been described previously for similar compounds, the metallacrown is disordered over two positions about the central guest ion in a refined ratio of 86:14.[29,56] The triethyl ammonium ions interact via hydrogen bonding with two phenolate oxygen atoms (carbonyl oxygen atoms for the minority orientation) on oppo-

site sides of the periphery of the 12-MC-4 cluster. The metallacrown dianions in the crystals of **1** overlap like bricks in the ‘a’ direction, forming triethyl ammonium-flanked chains. These are aligned towards layers along the ‘c’ axis (Fig. S2), which are alternately stacked in the ‘b’ direction, with opposite inclination of the chains (Fig. S3). Crystal structure information, and selected interatomic distances and angles are provided in Tables S1, S2 and S3 of the ESI, and are given in proper places for the discussion of the magneto-structural correlations.

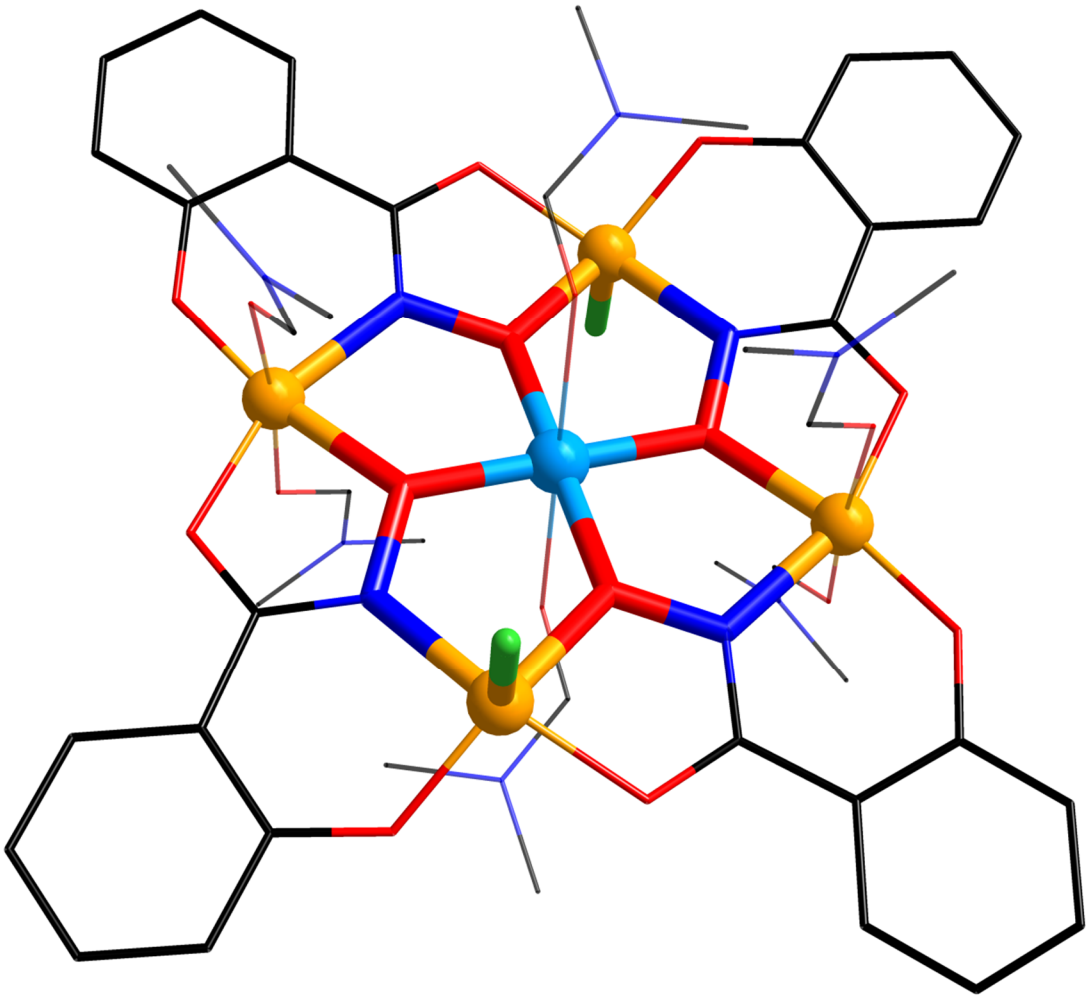

Fig. 3 Molecular structure of Cu(II)$(DMF)_2Cl_2$[12-$MC_{Fe(III)N(Shi)}$-4]$(DMF)_4$ in crystals of **2**; colour scheme: light blue - Cu(II), yellow - Fe(III), green - Cl, red - O, dark blue - N, black - C.

The neutral molecules in the crystal structure of compound **2** also obey the regular 12-MC-4 constitution, which has been described in detail for **1** (Fig 3, S4). However, the cyclic host comprises four Fe(III) ions while a Cu(II) ion is encapsulated inside the core of the complex. Due to the centrosymmetry of the metallacrown, two of the iron ions on opposite sides of the ring are surrounded by a square pyramidal coordination sphere

with a chloride counter ion on the apical position ($\tau = 0.058$). [61] On the contrary, a pair of transoid dimethylformamide secondary ligands each completes the distorted octahedral environment of the remaining Fe(III) ions and likewise delimits the distinguished axis of the strongly Jahn-Teller elongated octahedron around the central copper ion. The planarity of the basic motif is again slightly perturbed as the adjacent salicylhydroximate main ligands of the asymmetric unit are tilted out of the plane of the metal ions in opposite directions.

The complex is also disordered over two positions about the copper ion on the center of inversion but the extent is significantly lower with a rate of above 97% for the majority orientation. Additionally, two disordered dimethylformamide solvent molecules per metallacrown fill the space between adjacent complexes. The latter are packed towards layers in the plane, which is spanned by the 'a+c' and 'a+b' vector (Fig S4). The dimethylformamide ligands project into the interspace between the layers. Crystal structure information, selected interatomic distances and angles are listed in tables S1, S2 and S3. Moreover, the relevant parameters are picked in the course of the discussion of the magnetic data.

The magnetic properties of **1** according to a $\chi_M T$ vs. T plot are depicted in figure 4. At room temperature the experimental $\chi_M T$ value of 1.00 $cm^3\ K\ mol^{-1}$ is distinctly lower than the calculated spin-only value of 1.88 $cm^3\ K\ mol^{-1}$ for five uncoupled Cu(II) ions with S = ½ and g = 2.0. Decreasing the temperature, the $\chi_M T$ values decline with continuously increasing slop until an inflection point is reached slightly above 100 K. Both observations already indicate a favoritism of low spin states due to strong antiferromagnetic interactions between the metal ions. Below 100 K, the slope decreases and the data reveal a plateau at 0.44 $cm^3\ K\ mol^{-1}$ between 40 and 10 K. Anticipating an usually slightly raised g-factor for copper compounds, this feature gives evidence for an isolated S = ½ spin ground state. The $\chi_M T$ values finally decrease again for very low temperatures. Due to the shortest distance of only 6.05 Å for Cu(II) ions of different metallacrowns within the chains along the a axis and 6.92 Å between the chains in c direction, the latter might be attributed to intermolecular antiferromagnetic interactions.

The interpretation of the magnetic data was performed via the idealized square coupling scheme (Fig.1), which has been frequently applied for 12-MC-4 compounds in literature.[33-35,40-44] Hence, only two different coupling constants for radial and tangential exchange interactions have been introduced into the following isotropic spin-Hamiltonian according to the Heisenberg-Dirac-van-Vleck model.

$$\hat{H} = -2J_1\left(\hat{S}_1\hat{S}_2 + \hat{S}_1\hat{S}_3 + \hat{S}_1\hat{S}_4 + \hat{S}_1\hat{S}_5\right)$$
$$- 2J_2(\hat{S}_2\hat{S}_3 + \hat{S}_3\hat{S}_4 + \hat{S}_4\hat{S}_5 + \hat{S}_2\hat{S}_5)$$

In spite of the lack of an exact C_4 symmetry, this simplification is justified by the conformity of the relevant structural parameters. The distances of the central Cu(II) ion and the two crystallographically distinguished hydroximate oxygen atoms for instance both amount to 1.90 Å while the bond lengths of these donor atoms to the adjacent copper ions in the periphery measure 1.91 and 1.90 Å. Moreover, the spanned angles between the guest ion, the linking oxygens atoms and the metal centers in the host hardly differ with 116.8 and 117.6° respectively. Within the cyclic scaffold, the distances between the Cu(II) ions also resemble each other accounting for 4.58 and 4.61 Å.

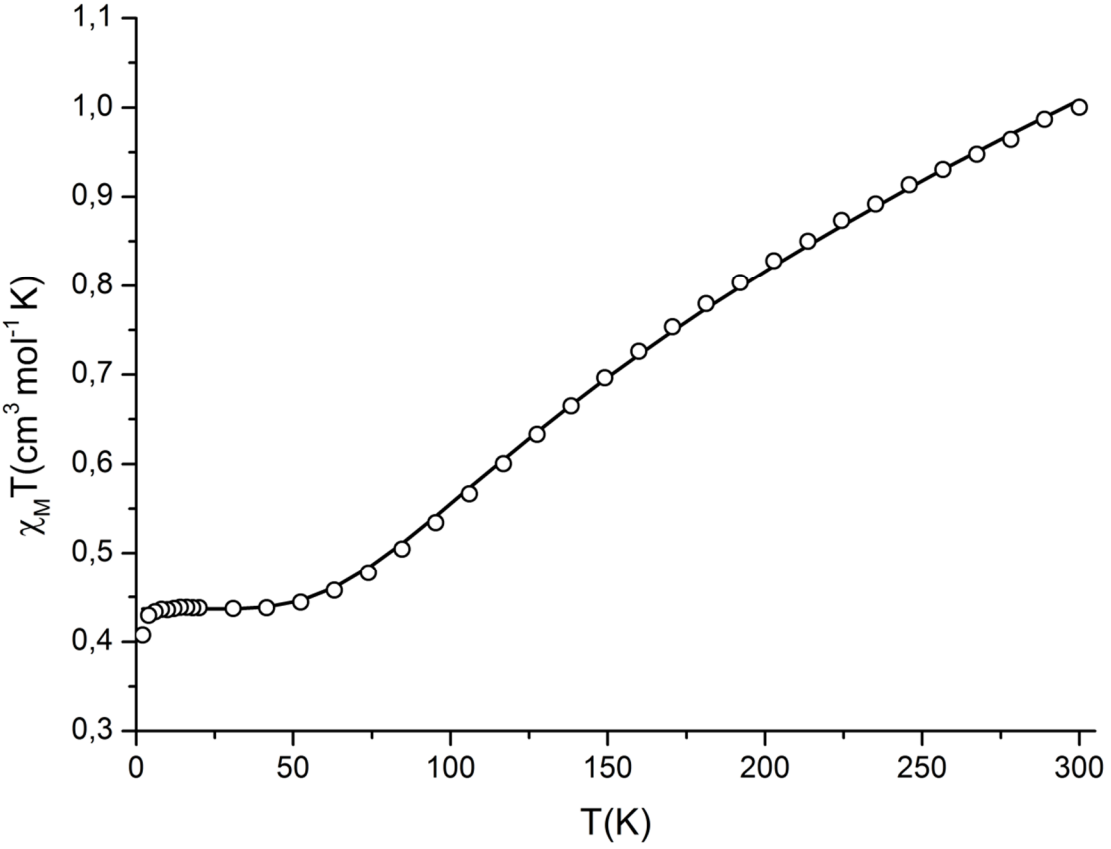

Fig.4 Temperature dependence of the $\chi_M T$ product ($\chi_M T$ vs. T plot) for experimental susceptibility data of compound **1**; the solid line refers to the best fit of the experimental data according to an idealized square magnetic model.

The best fit result of g = 2.16, J_1 = -155.2 cm^{-1} and J_2 = -92.3 cm^{-1} is in good accordance with the reported values for comparable compounds and implies strong antiferromagnetic coupling for both interaction pathways.[35,40,42-44] However, the radial interaction via the single hydroximate oxygen atom clearly exceeds the tangential coupling through the diatomic N-O bridge. According to the corresponding energy level diagram (Fig. S10), the low-spin ground state of S = 1/2 is well separated from two excited S = 1/2 states by

125.8 and 184.5 cm^{-1} and from the lowest lying S = 3/2 high-spin state by 213.8 cm^{-1}. The analyses of the magnetization measurements confirm this finding as they match the anticipated Brillouin function for an isolated spin ground state (Fig. S8, S9). A parallel alignment of the peripheral spins like in antiferromagnetically coupled star shaped molecules is hence not accomplished. As it has been demonstrated previously, the relative energies of the spin states are linear functions of the ratio between the radial and the tangential coupling constants J_1/J_2 for the here applied model (Fig. S11).[35] Thus, below the threshold of $J_1/J_2 = 1$ an S = ½ ground state representing the case of an alternating spin topology in the cyclic scaffold is adopted whereas the parallel alignment of the peripheral spins opposite to the central spin is achieved above the limit of $J_1/J_2 = 4$ (Fig. S12). Between those extremes of dominating tangential or radial exchange coupling and specifically for the here analyzed compound **1** ($J_1/J_2 = 1.68$), another S = 1/2 spin state holds the lowest energy (Fig. S13). Therefore, the enforcement of a high-spin ground state via superior radial magnetic interactions reveals to be hindered by the geometric arrangement of the coupling pathways (Fig. S14).

Based on the insight into the magnetic interactions of homometallic 12-MC-4 compounds like **1**, an evaluation of the spin state energies in correlation with the ratio between radial and tangential coupling has been performed for the Cu(II)[12-$MC_{Fe(III)N(Shi)}$-4] target molecule within the range of of the idealized square magnetic model. The number of states significantly increases from 10 to 286 due to the placement of S = 5/2 spins in the sites at the periphery (Fig. S15). Starting from superior tangential coupling, an S = ½ state is lowest in energy, which represents the extreme of an alternating spin topology within the cyclic host. Between ratios of $J_1/J_2 = 1$ and 4, again a different S = ½ state takes over. Proceeding towards relatively stronger radial interactions, the value of the spin ground state increases continuously from S = 3/2 at the threshold of $J_1/J_2 = 4$ in steps of 1 for every raise of the ratio by 2 until the other extreme of a parallel aligned spin orientation in the ring with S = 19/2 is reached at the limit of $J_1/J_2 = 20$ (Fig. S16). These considerations on the one hand stress the need for distinctly superior radial magnetic interactions. But on the other hand, high-spin ground states are already achieved via the magnetic director approach in spite of the geometric hindrance for ratios between radial and tangential interaction which are significantly lower than the demanded threshold for the completely parallel alignment of the peripheral spins (Fig. S17).

The magnetic data of the synthesized compound **2** are presented according to a $\chi_M T$ vs. T plot in figure 5. At room temperature, the experimental $\chi_M T$ value of 17.12 cm^3 K mol^{-1} resembles the expected spin-only value of 17.88 cm^3 K mol^{-1} for four non-interacting Fe(III) ions with S = 5/2 and one Cu(II) ions with S = ½ at a g-factor of g = 2.0. Cooling down the sample, the $\chi_M T$ values increase until a maximum of 22.45 cm^3 K mol^{-1} is reached close to 40 K. This feature indicates an energetic preference of higher

spin states by strong intramolecular magnetic interactions. For lower temperatures, the $\chi_M T$ values decrease with rising slope. Due to the distances of 7.10 and 7.42 Å between Fe(III) ions of different metallacrowns within the layers, the relevance of intermolecular magnetic interactions for the magnetic properties of compound **2** at very low temperature cannot be excluded. Moreover, the influence of magnetic anisotropy has to be taken into considerations as significant zero field splitting parameters D have been reported for square pyramidal coordinated Fe(III) ions.[62-64]

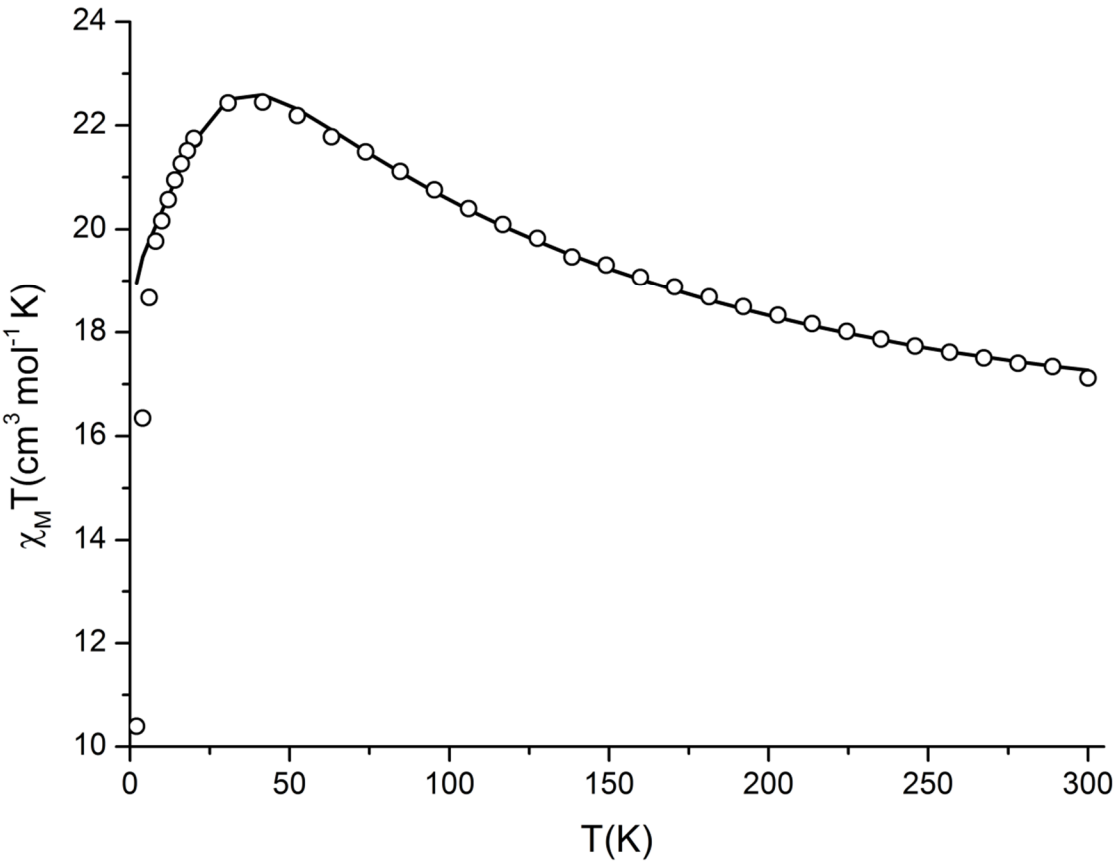

Fig. 5 Temperature dependence of the $\chi_M T$ product ($\chi_M T$ vs. T plot) for experimental susceptibility data of compound **2**; the solid line refers to the best fit of the experimental data according to an idealized square magnetic model.

Although the deviation of the metallacrown from C_4 symmetry is directly obvious from the different coordination numbers and secondary ligands of the crystallographically distinct Fe(III) ions, the interpretation of the magnetic data has again been performed via an idealized square coupling scheme. This proceeding is supported by the comparison of the relevant structural parameters. For instance, the interatomic distances along the radial interaction pathways show nearly identical values. So, the bond lengths between the Cu(II) ion and the hydroximate oxygen atoms account for 1.91 and 1.92 Å. The distance between the latter and the Fe(III) ion in the square pyramidal coordination sphere is with 1.99 Å only slightly smaller than the value of 2.01 Å for the counterpart

of the six-fold coordinated metal ion. Additionally, the corresponding angles moreover measure 123.6 and 124.1°, respectively. Concerning the tangential coupling, the two distinguishable distances between the peripheral iron centers strongly resemble each other with 4.88 and 4.89 Å. This kind of simplification has furthermore been applied successfully for a very similar case of a pseudo-symmetrical iron cluster in literature.[59]

Thus, the optimized coupling constant for the interaction between the Cu(II) ion in the core with S = ½ and the peripheral Fe(III) ions of the cyclic host with S = 5/2 amounts to J_1 = -49.2 cm-1 while J_2 = -3.8 cm-1 was obtained as best fit results for the exchange interaction in the ring due to the square magnetic model at a g-factor of g = 2.03. Setting up the energy diagram based on these values, an S = 11/2 state is lowest in energy due to the ratio of J_1/J_2 = 12.9 (Fig. S20) but it is closely accompanied by a S = 13/2 and a S = 9/2 state only 3.3 and 4.2 cm^{-1} above, respectively (Fig. S21). Despite of the limitations of the applied model, its significance is underlined by the simulation of the temperature dependent magnetization data using the optimized fit parameters, which matches the measured data comparatively well (Fig. S18). A fitting according to the Brillouin function of an isolated spin ground state was not performed due to the anticipated near excited states, which might be the reason besides magnetic anisotropy for the missing superimposition of the measured values towards a master curve in the plot of the reduced magnetization versus the field-temperature ratio (Fig. S19). The achievement of a high-spin ground state is therefore decidedly confirmed by both types of magnetic measurements.

Although the behavior of the sample under a dynamic magnetic field was analyzed, no evidence of SMM characteristics could be observed even with an additional static field. A discussion of the reasons for this demands a more detailed investigation of the lowest lying states, which has to be performed by elaborate methods because of their weak energetic separation. The successful establishment of a high-spin ground state will now allow achieving the features of single-molecule magnetism by a synthetic fine adjustment via the engineering of secondary ligands, coordination geometries and the molecular configuration in analogy to the family of star-shaped Fe_4 clusters.[65-66]

2.3 Conclusions

Inspired by the insight into the interplay of the magnetic interactions in the compound $(HNEt_3)_2$Cu(II)[12-$MC_{Cu(II)N(Shi)}$-4] and related complexes in literature, a strategy to overcome the nearly complete cancellation of the spins in 12-MC-4 metallacrowns was devolved that respects their basic structural motif, considers the frequent occurrence of antiferromagnetic coupling and utilizes their advantageous features. The herein presented magnetic director approach is aimed at the enforcement of a high-spin ground state via dominating radial magnetic interactions. For that purpose, a copper-centered iron

metallacrown was designed as a target molecule and realized through the compound $Cu(II)(DMF)_2Cl_2[12\text{-}MC_{Fe(III)N(Shi)}\text{-}4](DMF)_4$ x 2 DMF. Indeed, the magnetic data of this first example of a transition metal-based heterometallic 12-MC-4 metallacrown prove the presence of a high-spin ground state. Therefore, the novel magnetic director approach has revealed its potential to join the established, distinguished features of 12-MC-4 metallacrowns, such as stability of the basic scaffold, structural versatility and facile functionalization with advanced magnetic features in a singularly targeted way. It represents hence a suitable strategy to develop those compounds for their application in magneto-chemical issues.

Elaborate investigations, including XMCD measurements, are in progress in order to refine the magnetic model of the novel heterometallic compound. Moreover, synthetic experiments are currently being performed which aim at the further engineering of the magnetic properties via the substitution of secondary ligands.

2.4 Acknowledgement

We are grateful to Regine Jung-Pothmann for the collection of the X-ray diffraction data. Andre Lohse is acknowledged for preparative assistance. We thank Vadim Ksenofontov for performing and fitting the Mößbauer measurements. Peter Happ is recipient of a fellowship through the Excellence Initiative (DFG/GSC 266). Furthermore, he is grateful to the German National Academic Foundation (Studienstiftung des deutschen Volkes) for financial support.

2.5 Notes

Electronic Supplementary Information (ESI) available: [Experimetal details; synthesis; X-ray crystallography - crytal structure information (Tab. S1), selected interatomic distances and angles (Tab. S2-3), numbering schemes with thermal ellipsoids (Fig. S1, S4), packing diagramms (Fig. S2-3, S5-6); magnetism - energy level diagrams (Fig. S10-13, S15-17, S20-21), magetization curves (Fig. S8-9, S18-19), spin topology illustrations (Fig. S7, S14); elemental analysis - data; infrared spectroscopy - data; UV-Vis spectroscopy - data, spectra (Fig. S22-23); atomic absorption spectroscopy - data; mößbauer spectroscopy - data, spectrum (Fig. S24), ESI-mass spectrometry - data].

Crystal data. 1 $C_{40}H_{48}Cu_5N_6O_{12}$, M = 1122.58, monoclinic, a = 9.5697(7), b = 18.8080(13), c = 11.8032(9) Å, α = 90, β = 107.039(2), γ = 90°, U = 2031.2(3) Å^3, T = 173 K, space group $P2_1/c$ (no.14), Z = 2, 19690 reflections measured, 4967 unique (R_{int} = 0.0825) which were used in all calculations. The final $wR(F^2)$ was 0.0795 (all data). **2** $C_{52}H_{72}Cl_2CuFe_4N_{12}O_{20}$, M = 1543.04, triclinic, a = 11.7510(5), b = 12.8013(5), c = 12.8605(5) Å, α = 96.9260(10), β = 111.4130(10), γ = 110.2760(10)°, U = 1620.39(11)

Å³, T = 173 K, space group P-1 (no.2), Z = 1, 35651 reflections measured, 7811 unique (R_{int} = 0.0466) which were used in all calculations. The final wR(F^2) was 0.0779 (all data). CCDC 984042 and 984043.

2.6 References

[1] D. Gatteschi, R. Sessoli and A. Cornia, *Chem. Commun*, **2000**, *9*, 725

[2] G. Christou, *Polyhedron*, **2005**, *16-17*, 2065

[3] A.J. Tasiopoulos and S.P. Perlepes, *Dalton Trans*, **2008**, *41*, 5537

[4] M. Murrie, *Chem. Soc. Rev.*, **2010**, *6*, 1986

[5] R. Sessoli, H.Lien Tsai, A.R. Schake, S. Wang, J.B. Vincent, K. Folting et al., *J. Am. Chem. Soc.*, **1993**, *5*, 1804

[6] R. Sessoli, D. Gatteschi, A. Caneschi and M.A. Novak, *Nature*, **1993**, *6442*, 141

[7] D. Gatteschi and R. Sessoli, *Angew. Chem. Int. Ed.*, **2003**, *3*, 268

[8] M. Murugesu, J. Raftery, W. Wernsdorfer, G. Christou and E.K. Brechin, *Inorg. Chem*, **2004**, *14*, 4203

[9] M. Murugesu, M. Habrych, W. Wernsdorfer, K.A. Abboud and G. Christou, *J. Am. Chem. Soc.*, **2004**, *15*, 4766

[10] A.M. Ako, I.J. Hewitt, V. Mereacre, R. Clérac, W. Wernsdorfer, C.E. Anson and A.K. Powell, *Angew. Chem. Int. Ed.*, **2006**, *30*, 4926

[11] E. Ruiz, J. Cirera, J. Cano, S. Alvarez, C. Loose and J. Kortus, *Chem. Commun.*, **2007**, *1*, 52

[12] O. Waldmann, *Inorg. Chem.*, **2007**, *24*, 10035

[13] S. Hill, S. Datta, J. Liu, R. Inglis, C.J. Milios, P.L. Feng et al., *Dalton Trans.*, **2010**, *20*, 4693

[14] P.-H. Lin, T.J. Burchell, L. Ungur, L.F. Chibotaru, W. Wernsdorfer and M. Murugesu, *Angewandte Chemie*, **2009**, *50*, 9653

[15] R.J. Blagg, C.A. Muryn, E.J. L. McInnes, F. Tuna and R.E. P. Winpenny, *Angew. Chem. Int. Ed*, **2011**, *29*, 6530

[16] D.N. Woodruff, R.E. P. Winpenny and R.A. Layfield, *Chem. Rev.*, **2013**, *7*, 5110

[17] T.C. Stamatatos, D. Foguet-Albiol, S.-C. Lee, C.C. Stoumpos, C.P. Raptopoulou, A. Terzis et al., *J. Am. Chem. Soc*, **2007**, *30*, 9484

[18] C.J. Milios, A. Vinslava, P.A. Wood, S. Parsons, W. Wernsdorfer, G. Christou et al., *J. Am. Chem. Soc.*, **2007**, *1*, 8

[19] C.J. Milios, S. Piligkos and E.K. Brechin, *Dalton Trans.*, **2008**, *14*, 1809

[20] R. Bagai and G. Christou, *Chem. Soc. Rev.*, **2009**, *4*, 1011

[21] R. Inglis, S.M. Taylor, L.F. Jones, G.S. Papaefstathiou, S.P. Perlepes, S. Datta et al., *Dalton Trans.*, **2009**, *42*, 9157

[22] H.L. C. Feltham, R. Clérac, L. Ungur, L.F. Chibotaru, A.K. Powell and S. Brooker, *Inorg. Chem.*, **2013**, *6*, 3236

[23] T. Glaser, M. Heidemeier, T. Weyhermüller, R.-D. Hoffmann, H. Rupp and P. Müller, *Angew. Chem.*, **2006**, *36*, 6179

[24] T. Glaser, *Chem. Commun.*, 2010, **1**, 116

[25] V.L. Pecoraro, A.J. Stemmler, B.R. Gibney, J.J. Bodwin, H. Wang, J.W. Kampf and A. Barwinski, *Metallacrowns: A New Class of Molecular Recognition Agents*, **1996**, In: Kenneth D. Karlin: *Progress in Inorganic Chemistry*, Bd. 45, John Wiley & Sons, Inc (Progress in Inorganic Chemistry), 83

[26] J.J. Bodwin, A.D. Cutland, R.G. Malkani and V.L. Pecoraro, *Coordination Chemistry Reviews*, **2001**, 489

[27] G. Mezei, C.M. Zaleski and V.L. Pecoraro, *Chem. Rev*, **2007**, *11*, 4933

[28] M.Soo Lah and V. Pecoraro, *Comments on Inorg. Chem*, **1990**, *2*, 59

[29] B.R. Gibney, D.P. Kessissoglou, J.W. Kampf and V.L. Pecoraro, *Inorg. Chem*, **1994**, *22*, 4840

[30] B.R. Gibney, H. Wang, J.W. Kampf and V.L. Pecoraro, *Inorg. Chem*, **1996**, *21*, 6184

[31] D.P. Kessissoglou, J.J. Bodwin, J. Kampf, C. Dendrinou-Samara and V.L. Pecoraro, *Inorganica Chimica Acta*, **2002**, *1*, 73

[32] E.S. Koumousi, S. Mukherjee, C.M. Beavers, S.J. Teat, G. Christou and T.C. Stamatatos, *Chem. Commun.*, **2011**, *39*, 11128

[33] C.M. Zaleski, S. Tricard, E.C. Depperman, W. Wernsdorfer, T. Mallah, M.L. Kirk and V.L. Pecoraro, *Inorg. Chem*, **2011**, *22*, 11348

[34] Z. Chen, M. Jia, Z. Zhang and F. Liang, *Crystal Growth & Design*, **2010**, *11*, 4806

[35] A.B. Lago, J. Pasán, L. Cañadillas-Delgado, O. Fabelo, F.J. M. Casado, M. Julve et al., *New J. Chem*, **2011**, *9*, 1817

[36] M. Cavallini, J. Gomez-Segura, D. Ruiz-Molina, M. Massi, C. Albonetti, C. Rovira et al., *Angew. Chem.*, **2005**, *6*, 910

[37] L. Bogani and W. Wernsdorfer, *Nat Mater*, **2008**, *3*, 179

[38] M. Mannini, F. Pineider, C. Danieli, F. Totti, L. Sorace, P. Sainctavit et al., *Nature*, **2010**, *7322*, 417

[39] K. Katoh, H. Isshiki, T. Komeda and M. Yamashita, *Coord. Chem. Rev.*, **2011**, *17-18*, 2124

[40] Y. Song, *Inorganica Chimica Acta*, **2000**, *2*, 135

[41] J. Legendziewicz, M. Puchalska, Z. Ciunik and W. Wojciechowski, *Polyhedron*, **2007**, *6*, 1331

[42] A.V. Pavlishchuk, S.V. Kolotilov, M. Zeller, O.V. Shvets, I.O. Fritsky, S.E. Lofland et al., *Eur. J. Inorg. Chem*, **2011**, *31*, 4826

[43] A.V. Pavlishchuk, S.V. Kolotilov, M. Zeller, L.K. Thompson, I.O. Fritsky, A.W. Addison and A.D. Hunter, *Eur. J. Inorg. Chem*, **2010**, *30*, 4851

[44] C. McDonald, T. Whyte, S.M. Taylor, S. Sanz, E.K. Brechin, D. Gaynor and L.F. Jones, *CrystEngComm*, **2013**, *34*, 6672

[45] A.L. Barra, A. Caneschi, A. Cornia, F. de Fabrizi Biani, D. Gatteschi, C. Sangregorio et al., *J. Am. Chem. Soc*, **1999**, *22*, 5302

[46] A. Cornia, A.C. Fabretti, P. Garrisi, C. Mortalò, D. Bonacchi, D. Gatteschi et al., *Angew. Chem. Int. Ed.*, **2004**, *9*, 1136

[47] R.W. Saalfrank, A. Scheurer, I. Bernt, F.W. Heinemann, A.V. Postnikov, V. Schünemann et al., *Dalton Trans.*, **2006**, *23*, 2865

[48] S. Khanra, K. Kuepper, M. Prinz, M. Raekers, S. Voget, A.V. Postnikov et al., *Inorg. Chem.*, **2008**, *11*, 4605

[49] C. Schlegel, E. Burzurí, F. Luis, F. Moro, M. Manoli, E.K. Brechin et al., *Chem. Eur. J*, **2010**, *33*, 10178

[50] L.J. Batchelor, M. Sander, F. Tuna, M. Helliwell, F. Moro, J. van Slageren et al., *Dalton Trans*, **2011**, *40*, 5278

[51] O. Kahn, *Molecular Magnetism, **1993***, Wiley VCH

[52] E. Ruiz, P. Alemany, S. Alvarez and J. Cano, *J. Am. Chem. Soc.*, **1997**, *6*, 1297

[53] P. Chaudhuri, *Coordination Chemistry Reviews*, **2003**, *1-2*, 143

[54] M.Soo Lah and V.L. Pecoraro, *J. Am. Chem. Soc*, **1989**, *18*, 7258

[55] A.J. Stemmler, J.W. Kampf and V.L. Pecoraro, *Angew. Chem. Int. Ed. Engl*, **1996**, *2324*, 2841

[56] J. Herring, M. Zeller and C.M. Zaleski, *Acta Crystallogr E Struct Rep Online*, **2011**, *4*, m419

[57] M.Soo Lah, M.L. Kirk, W. Hatfield and V.L. Pecoraro, *J. Chem. Soc., Chem. Commun*, **1989**, *21*, 1606

[58] B. Kurzak, H. Kozłowski and E. Farkas, *Coordination Chemistry Reviews*, **1992**, *2*, 169

[59] R. Codd, *Coordination Chemistry Reviews*, **2008**, *12-14*, 1387

[60 J.F. Liebman, Z. Rappoport, *The chemistry of hydroxylamines, oximes and hydroxamic acids*, **2009**, Wiley (Patai Series: the chemistry of functional groups)

[61] A.W. Addison, T.Nageswara Rao, J. Reedijk, J. van Rijn and G.C. Verschoor, *J. Chem. Soc., Dalton Trans.*, **1984**, *7*, 1349

[62] C. Belle, I. Gautier-Luneau, G. Gellon, J.-L. Pierre, I. Morgenstern-Badarau and E. Saint-Aman, *J. Chem. Soc., Dalton Trans.*, **1997**, *19*, 3543

[63] N. Madhu, J.-K. Tang, I.J. Hewitt, R. Clérac, W. Wernsdorfer, J. van Slageren et al., *Polyhedron*, **2005**, *16-17*, 2864

[64] C. Mukherjee, A. Stammler, H. Bögge and T. Glaser, *Chem. Eur. J.*, **2010**, *33*, 10137

[65] S. Accorsi, A.-L. Barra, A. Caneschi, G. Chastanet, A. Cornia, A.C. Fabretti et al., *J. Am. Chem. Soc.*, **2006**, *14*, 4742

[66] L. Gregoli, C. Danieli, A.-L. Barra, P. Neugebauer, G. Pellegrino, G. Poneti et al., *Chem. Eur. J.*, **2009**, *26*, 6456

2.7 Supplementary Information

2.7.1 Experimental Section

All chemicals were reagent grade and were used without further purification.

X-ray diffraction data for the structure analyses were collected from suitable crystals of **1** and **2** on a Bruker SMART 3-circle diffractometer with an APEX II CCD detector and Oxford cooling system using graphite-monochromated Mo-Kα radiation (λ = 0.71073 Å) at -100°C.

Magnetic data were obtained from polycrystalline samples on a Quantum Design MPMS XL SQUID magnetometer equipped with a 7 T magnet. Temperature dependent susceptibility was measured from 2 to 300 K at an applied field of 1 T. Magnetization data were collected in a range between 2 and 10 K up to a field of 7 T.

C, H and N elemental analyses were carried out on a Foss Heraeus Vario EL at the Institute of Organic Chemistry at the Johannes Gutenberg University Mainz.

Infrared absorption spectra were recorded at room temperature in a range of 400-4000 cm^{-1} on a JASCO FT/IR-4200 spectrometer using KBr pellets.

UV-Vis absorption measurements were performed between 210 and 1000 nm for a 0.2 and 0.01 mM solution of **1** in MeOH and between 250 and 1000 nm for a 0.002 mM solution of **2** in $CHCl_3$ on a JASCO V-570 UV/Vis/NIR spectrophotometer.

Atomic absorption spectroscopy was carried out on a PerkinElmer 5100 ZL spectrometer.

The ^{57}Fe Mössbauer spectrum was recorded in transmission geometry with a ^{57}Co(Rh) source kept at room temperature and a conventional spectrometer operating in the constant-acceleration mode. Previously, the powdered sample had been hermetically enclosed in the sample holder made of acryl.

ESI mass spectra were obtained in the positive ion mode from a Waters Q-ToF-ULTIMA 3 with LockSpray source at the Institute of Organic Chemistry at the Johannes Gutenberg University Mainz.

2.7.2 Synthesis

$(HNEt_3)_2$Cu(II)[12-MC$_{Cu(II)N(Shi)}$-4] (1)

$CuCl_2$ (0.168 g, 1.25 mmol) and salicylhydroxamic acid (0.153 g, 1 mmol) were dissolved in 20 ml of methanol and a solution of triethylamine (0.304 g, 3 mmol) in 10 ml of methanol was added. The dark green reaction mixture was stirred for 16 h and than filtered. Dark green crystals suitable for X-ray diffraction analysis were obtained from the filtrate by slow evaporation after two days.

Yield: 0.185 g (66%)

$Cu(II)(DMF)_2Cl_2[12\text{-}MC_{Fe(III)N(Shi)}\text{-}4](DMF)_4 \cdot 2\ DMF$ (2)

$CuCl_2$ (0.269 g, 2 mmol) and salicylhydroxamic acid (0.153 g, 1 mmol) were dissolved in 10 ml of dimethylformamide and a solution of triethanolamine (0.373 g, 2.5 mmol) in 10 ml of dimethylformamide was added. By addition of a solution of $FeCl_2 \cdot 4H_2O$ (0.199 g, 1 mmol) in 10 ml of dimethylformamide, the dark green reaction mixture immediately turned dark red. It was stirred for 16 h and than filtered. Dark red crystals suitable for X-ray diffraction analysis were obtained from the filtrate by slow evaporation after one month.

Yield: 0.126 g (33%)

2.7.3 X-ray Crystallography

A semi-empirical absorption correction of the obtained X-ray diffraction data was performed with MULABS.[1,2] The structures were solved by direct methods with the help of the program SIR97[3] and all non-hydrogen atoms were refined by full-matrix least squares methods on F^2 with anisotropic displacement parameters using SHELXL-97.[4] All carbon bound hydrogen atoms were placed on geometrically calculated positions and refined according to the riding model with a uniform value of U_{iso}. The nitrogen bound hydrogen of the triethylammonium moiety of **1** was located and refined according to the riding model.

Compound	**1**	**2**
Formula	$C_{40}H_{48}Cu_5N_6O_{12}$	$C_{52}H_{72}Cl_2CuFe_4N_{12}O_{20}$
Formula weight	1122.58	1543.04
T/K	173	173
Wavelength/Å	0.71073	0.71073
Crystal system	Monoclinic	Triclinic
Space group	P21/c	P-1
a/Å	9.5697(7)	11.7510(5)
b/Å	18.8080(13)	12.8013(5)
c/Å	11.8032(9)	12.8605(5)
α/°		96.926(1)
β/°	107.039(2)	111.413 (1)
γ/°		110.276 (1)
V/Å^3	2031.2(3)	1620.39 (11)
Z	2	1
δ_{calcd}/gcm^{-3}	1.835	1.581
μ/mm^{-1}	2.648	1.359
Crystal size/mm	0.47 × 0.45 × 0.24	0.30 × 0.21 × 0.08
θ_{max}/°	28.14	28.00
Reflns. collected	19690	35651
Indep. Reflns (Rint)	4967(0.0825)	7811(0.0466)
Data/restrains/parameters	4967/47/350	7811/70/478
Goof on F^2	1.021	0.963
R_1, wR_2 (I>2σ(I))	0.0343	0.0300
	0.0758	0.0735
R_1, wR_2 (all data)	0.0476	0.0444
	0.0795	0.0779
Largest diff. peak and hole/e Å^{-3}	0.529/-0.547	0.598/-0.354

Table S1 Crystallographic data and refinement parameters for the crystal structures of **1** and **2**

1		**2**	
Cu1–O1	1.896(2)	Cu1–O1	1.9155(12)
Cu1–O4	1.8996(19)	Cu1–O4	1.9114(12)
Cu2–O1	1.9032(19)	Cu1–O9	2.7166(18)
Cu2–O2	1.964(2)	Fe1–O1	1.9907(13)
Cu2–O6*	1.871(2)	Fe1–O2	1.9692(14)
Cu2–N2*	1.926(2)	Fe1–O6*	1.8635(13)
Cu3–O3	1.8999(19)	Fe1–N2*	2.0521(15)
Cu3–O4	1.907(2)	Fe1–Cl1	2.2473(6)
Cu3–O5	1.940(2)	Fe2–O3	1.8706(13)
Cu3–N1	1.913(3)	Fe2–O4	2.0094(12)
		Fe2–O5	1.9976(13)
Cu1···Cu2	3.2502(4)	Fe2–O7	2.0997(14)
Cu1···Cu3	3.2421(3)	Fe2–O8	2.0964(14)
Cu2···Cu3	4.5758(5)	Fe2–N1	2.0741(15)
Cu3···Cu2i	4.6057(6)		
		Fe1···Fe2	4.8905(4)
N3–H3N	0.91(3)	Fe1···Cu1	3.4503(3)
N3···O3	2.815(3)	Fe2···Fe1i	4.8759(4)
H3N···O3	1.96(3)	Fe2···Cu1	3.4556(3)

Table S2 Selected interatomic distances (Å) in the crystal structures of **1** and **2**

1		**2**	
Cu1–O1–Cu2	117.62 (10)	Cu1–O1–Fe1	124.07(6)
Cu1–O4–Cu3	116.81 (10)	Cu1–O4–Fe2	123.59(6)
O1–Cu1–O4	91.90(8)	O1–Cu1–O4	90.53(5)
O1–Cu1–O4*	88.10(8)	O1–Cu1– O4*	89.47(5)
O1–Cu2–O2	80.10(8)	O1–Cu1–O9	96.53(5)
O1–Cu2–N2*	88.77(10)	O1*–Cu1–O9	83.47(5)
O2–Cu2– O6*	98.15(8)	O4–Cu1–O9	92.68(5)
O6*–Cu2–N2*	92.98(11)	O4*–Cu1–O9	87.32(5)
O3–Cu3–O5	98.87(8)	O1–Fe1–O2	76.97(5)
O3–Cu3–N1	93.05(9)	O1–Fe1–N2*	83.51(5)
O4–Cu3–O5	81.20(8)	O1–Fe1–Cl1	105.35(4)
O4–Cu3–N1	91.52(10)	O2–Fe1–O6*	95.39(6)
		O2–Fe1–Cl1	104.03(5)
		O6*–Fe1–N2*	86.81(6)
		O6*–Fe1–Cl1	109.41(5)
		N2*–Fe1–Cl1	104.62(5)
		O3–Fe2–O5	112.06(6)
		O3–Fe2–O7	88.50(6)
		O3–Fe2–O8	90.90(6)
		O3–Fe2–N1	87.18(6)
		O4–Fe2–O5	77.48(5)
		O4–Fe2–O7	89.52(5)
		O4–Fe2–O8	92.11(6)
		O4–Fe2–N1	83.49(5)
		O5–Fe2–O7	89.03(6)
		O5–Fe2–O8	85.35(6)
		O7–Fe2– N1	95.79(6)
		O8–Fe2–N1	90.47(6)

Table S3 Selected bond angles (°) in the crystal structures of **1** and **2**

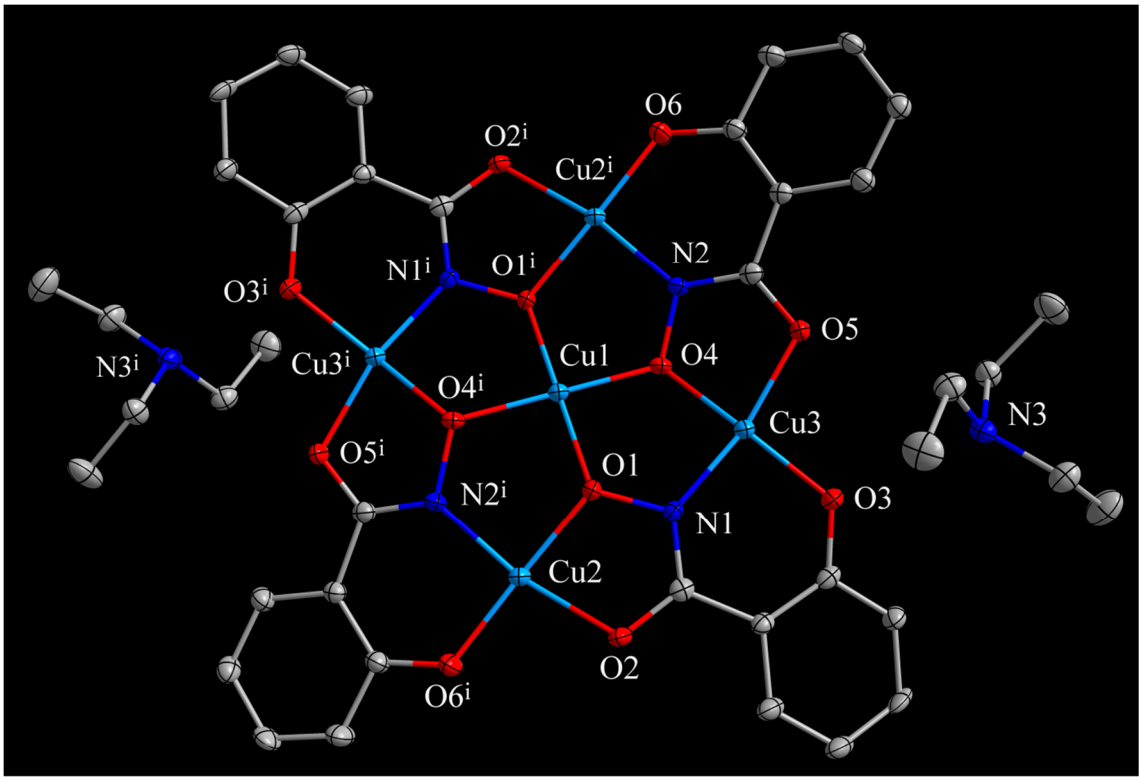

Figure S1 Molecular structure of $(HNEt_3)_2Cu(II)[12\text{-}MC_{Cu(II)N(Shi)}\text{-}4]$ in crystals of **1** with numbering scheme and thermal ellipsoids at 50% probability level; color scheme: light blue - Cu(II), red - O, dark blue - N, grey - C

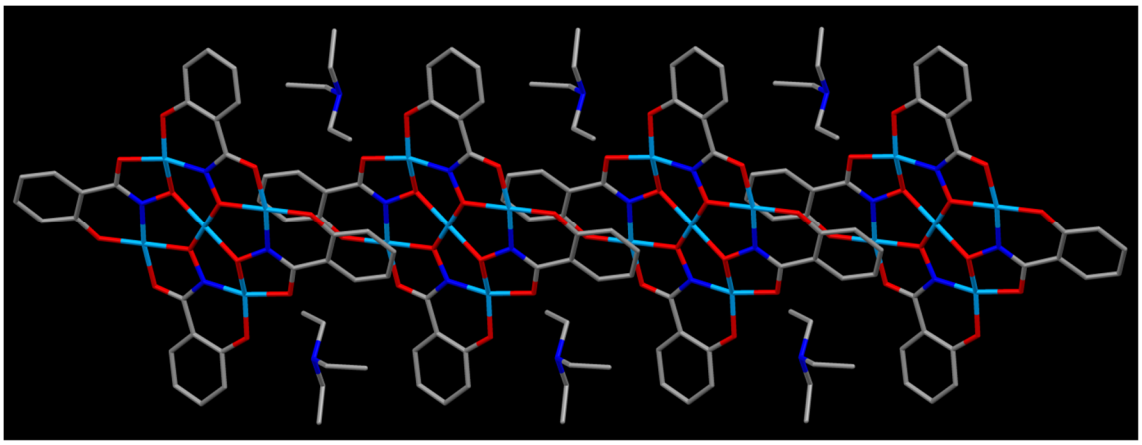

Figure S2 Packing of the $(HNEt_3)_2Cu(II)[12\text{-}MC_{Cu(II)N(Shi)}\text{-}4]$ units towards chains along the a axis in the crystal structure of **1**; view on the ac plane in b direction; color scheme: light blue - Cu(II), red - O, dark blue - N, grey - C

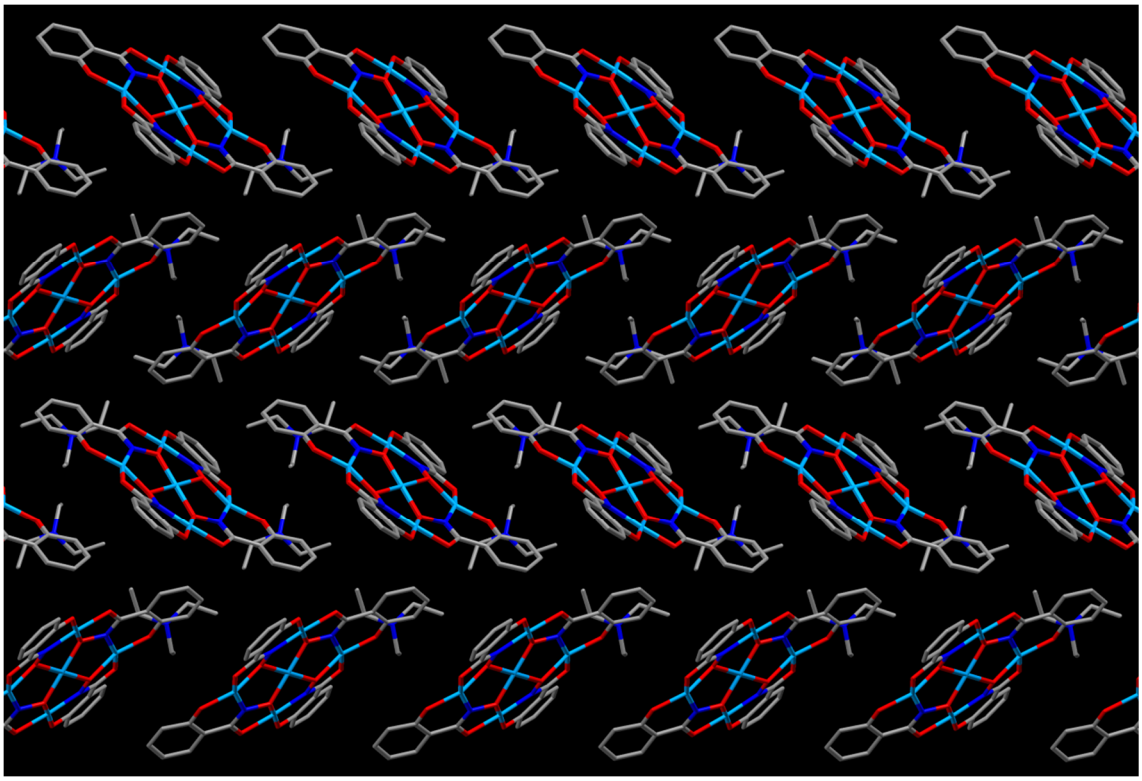

Figure S3 Packing of the chains towards layers along the c axis and stacking of these layers in b direction in the crystal structure of **1**; view on the bc plane along the a direction; color scheme: light blue - Cu(II), red - O, dark blue - N, grey - C

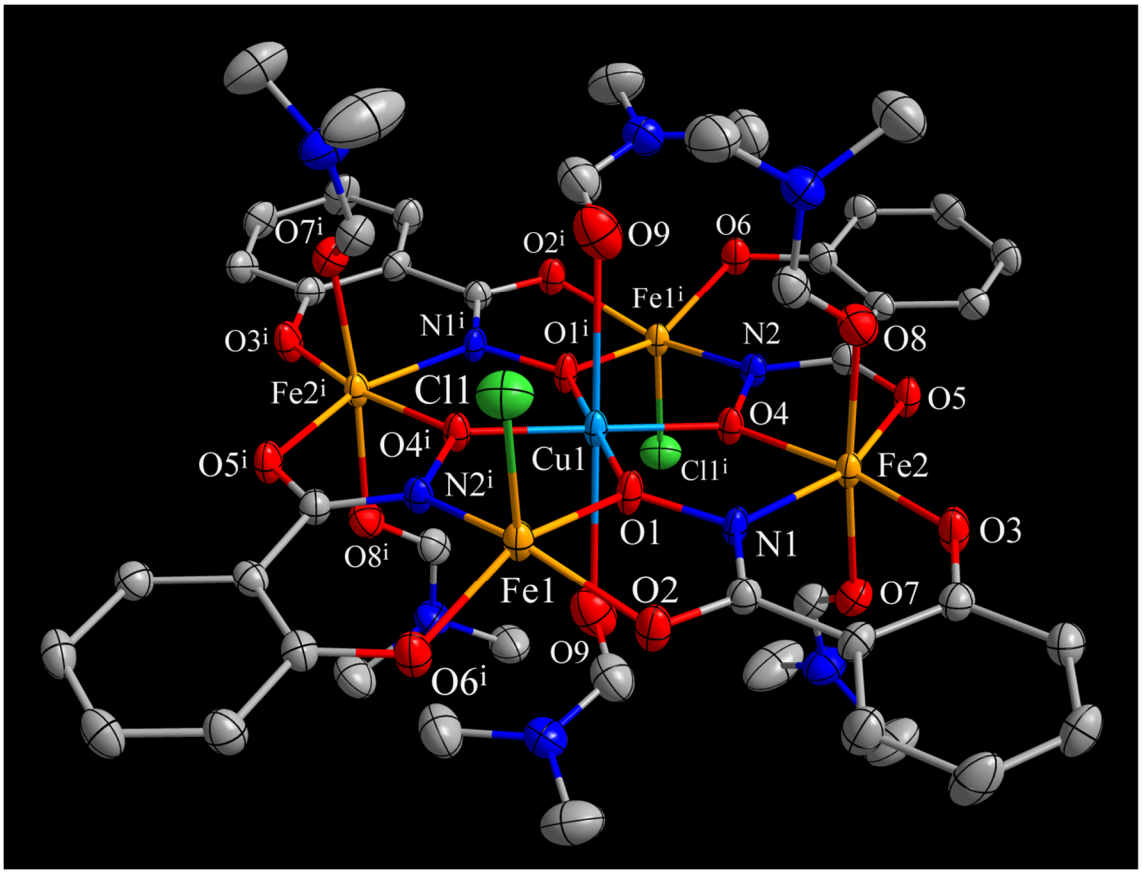

Figure S4 Molecular structure of Cu(II)(DMF)$_2$Cl$_2$[12-MC$_{Fe(III)N(Shi)}$-4](DMF)$_4$ in crystals of **2** with numbering scheme and thermal ellipsoids at 50% probability level; color scheme: light blue - Cu(II), yellow - Fe(III), green - Cl, red - O, dark blue - N, grey - C

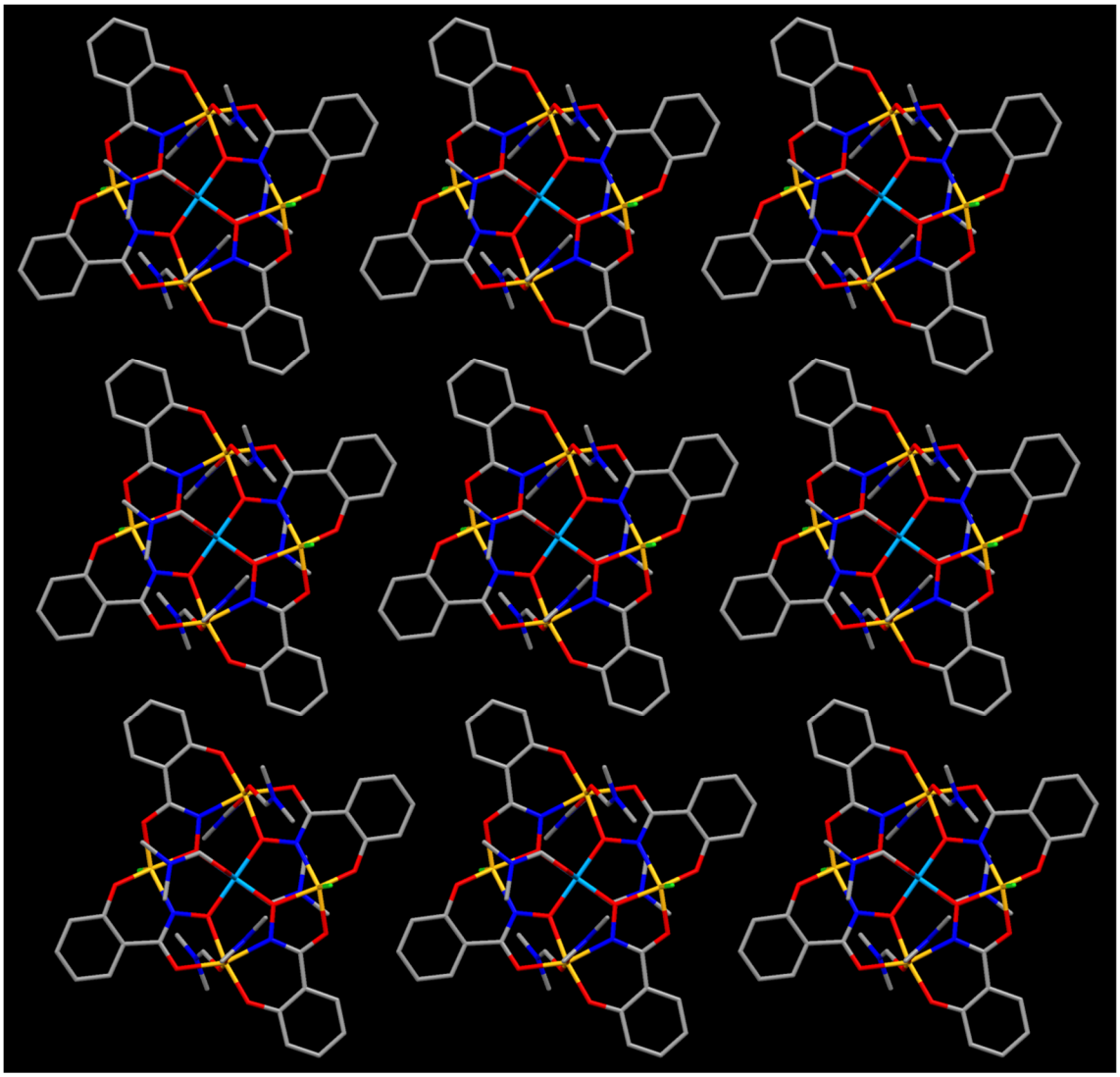

Figure S5 packing of the Cu(II)$(DMF)_2Cl_2$[12-$MC_{Fe(III)N(Shi)}$-4]$(DMF)_4$ units in the plane spanned by the a+b and a+c vector in the crystal structure of **2**; color scheme: light blue - Cu(II), yellow - Fe(III), green - Cl, red - O, dark blue - N, grey - C

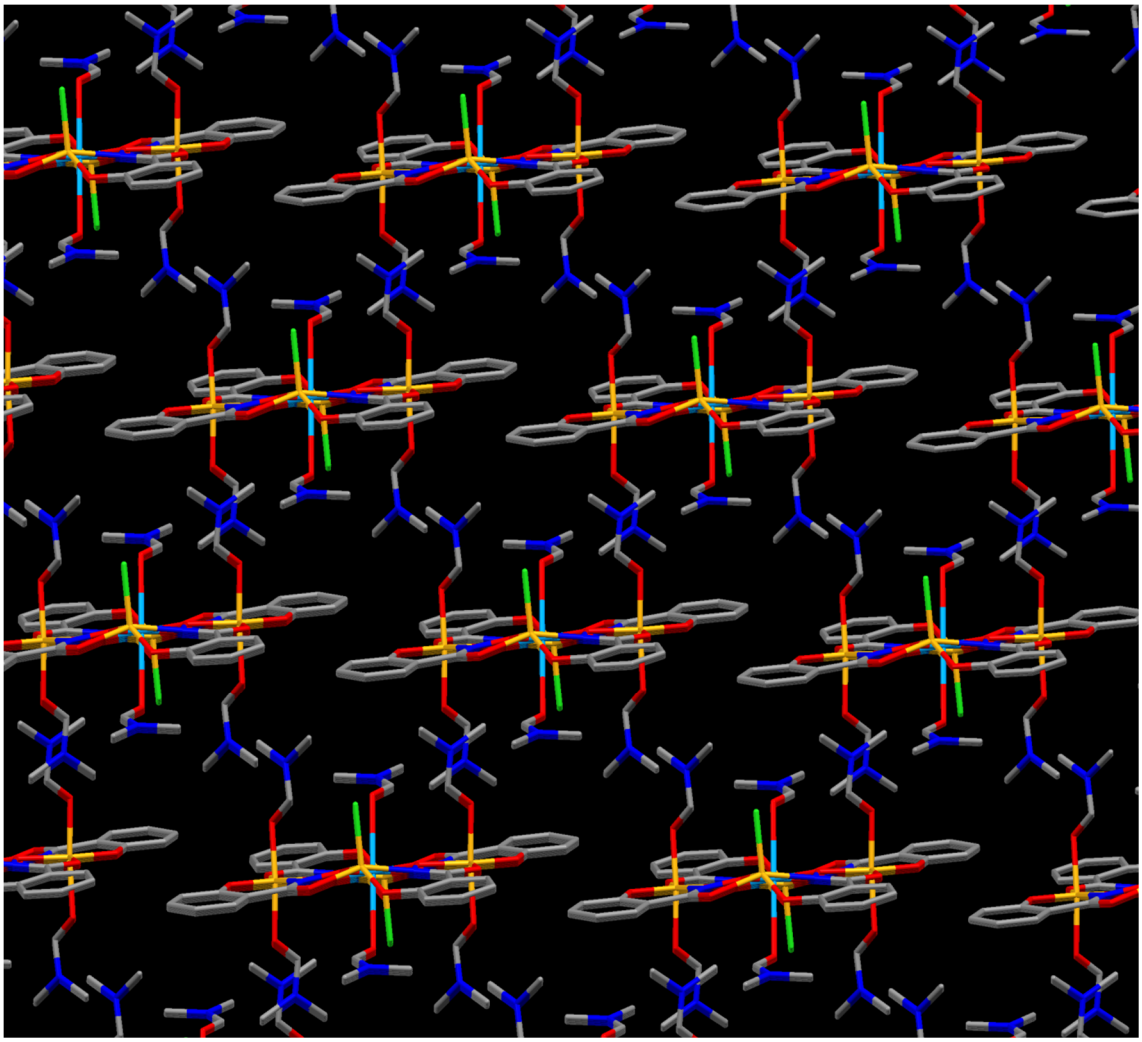

Figure S6 Stacking of the layers in the crystal structure of **2**; color scheme: light blue - Cu(II), yellow - Fe(III), green - Cl, red - O, dark blue - N, grey - C

2.7.4 Magnetism

In the course of the data processing of all magnetic measurements, diamagnetic corrections were applied for the holder as well as for the intrinsic contributions of atoms and moieties with the help of Pascal's constants.[5] The fitting of the temperature dependent susceptibility data was performed with the help of the program CLUMAG[6] using the χT vs. T plot of the measured data above 10 K. Model simulations and the simulation of the magnetization data of **2** were carried out via the software package FIT-MART.[7]

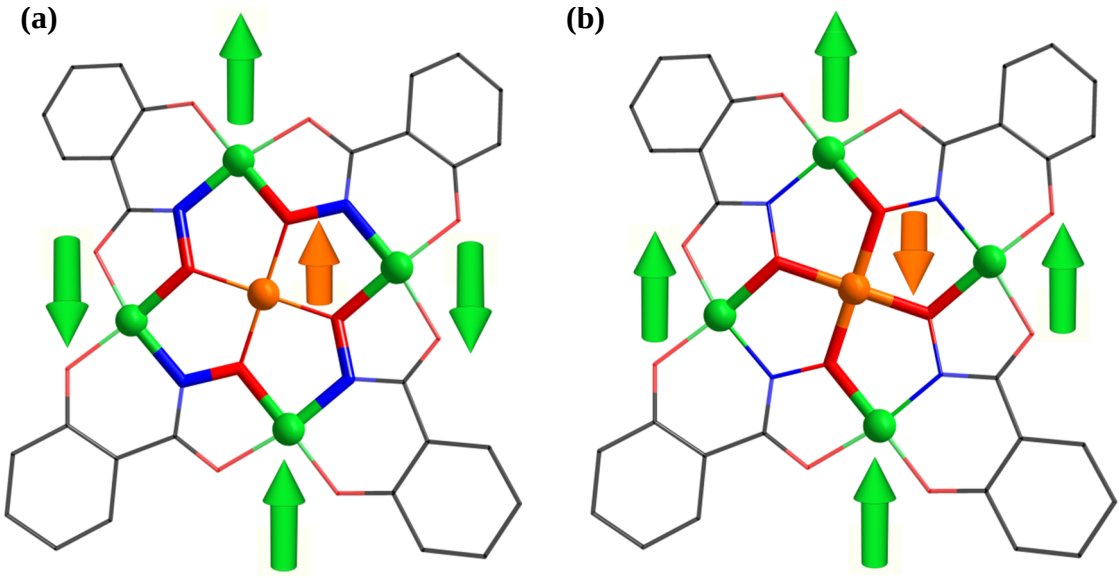

Figure S7 Schematic drawing of an alternating and parallel aligned spin topology for the cyclic host of a 12-MC-4 metallacrown as extreme cases of dominantly tangential (a) and radial (b) antiferromagnetic interactions; the respective superior coupling pathways are graphically highlighted

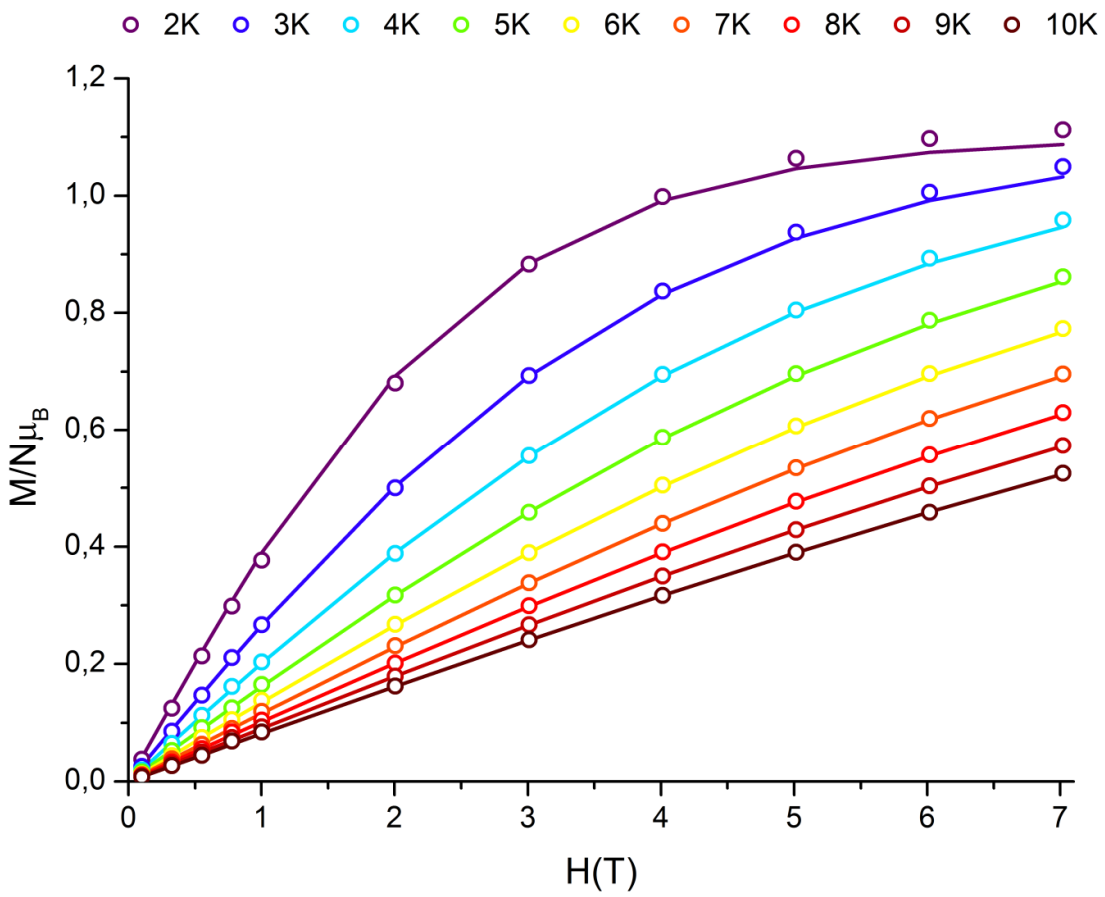

Figure S8 Field dependence of the reduced magnetization ($M/N\mu_B$ vs. H plot) of **1** for different temperatures between 2 and 10 K; solid lines represent simulations according to the Broillouin function for an isolated S = ½ ground state and a g-factor of g = 2.2

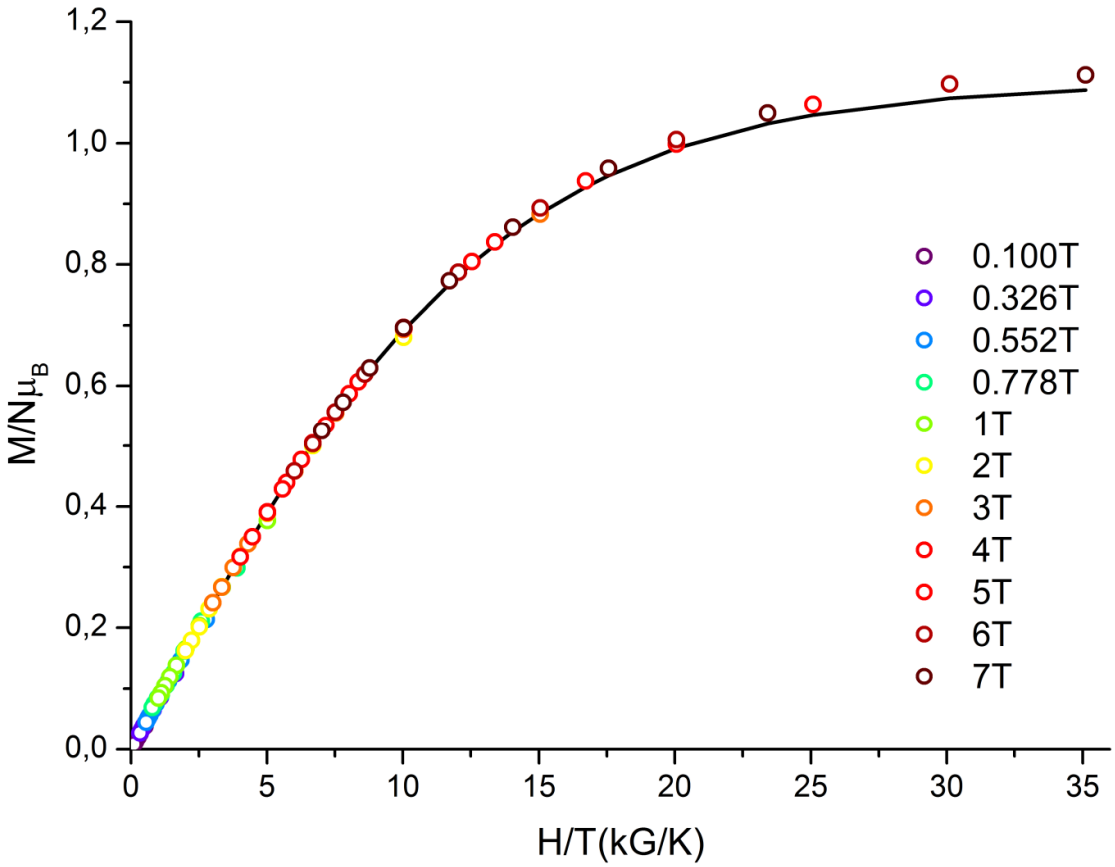

Figure S9 Field-temperature ratio dependence of the reduced magnetization ($M/N\mu_B$ vs. H/T plot) of **1** at temperatures between 2 and 10 K for applied magnetic field from 0.1 to 7 T; the solid line represents the simulated master curve according to the Broillouin function for an isolated S = ½ spin ground state and a g-factor of g = 2.2

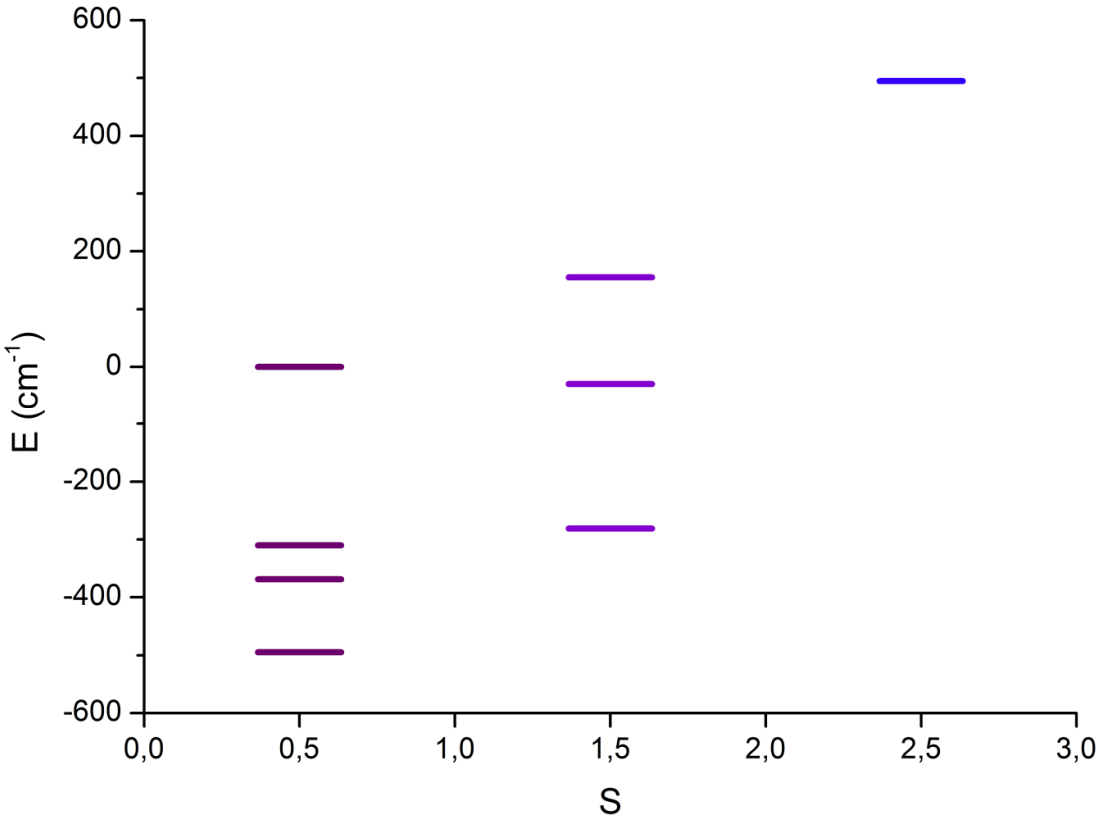

Figure S10 Energy level diagram of the spin states of the Cu(II)[12-MC$_{Cu(II)N(Shi)}$-4]$^{2-}$ complex in **1** according to the best fit result of the temperature dependence of the χ_MT product (χ_MT vs. T plot; Fig. 4) for an idealized square magnetic model using an isotropic Heisenberg Hamiltonian

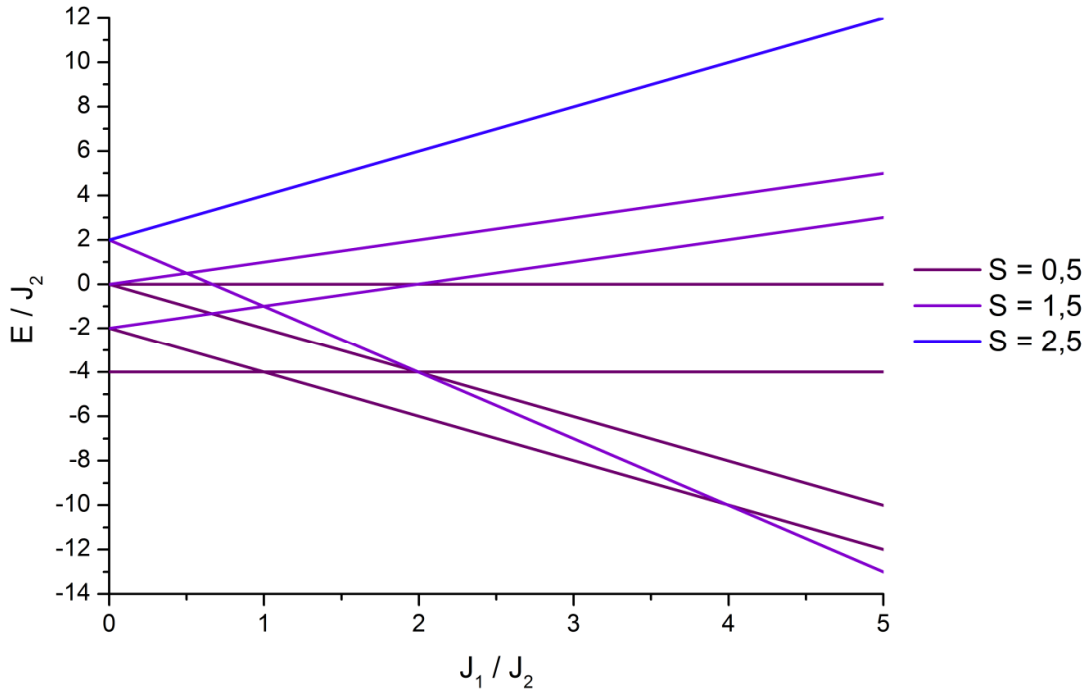

Figure S11 Coupling constants ratio dependent normalized energy level diagram of an idealized square magnetic model for a generalized Cu(II)[12-$MC_{Cu(II)N(Shi)}$-4]$^{2-}$ complex with radial (J_1) and tangential (J_2) antiferromagnetic interactions according to an isotropic Heisenberg Hamiltonian

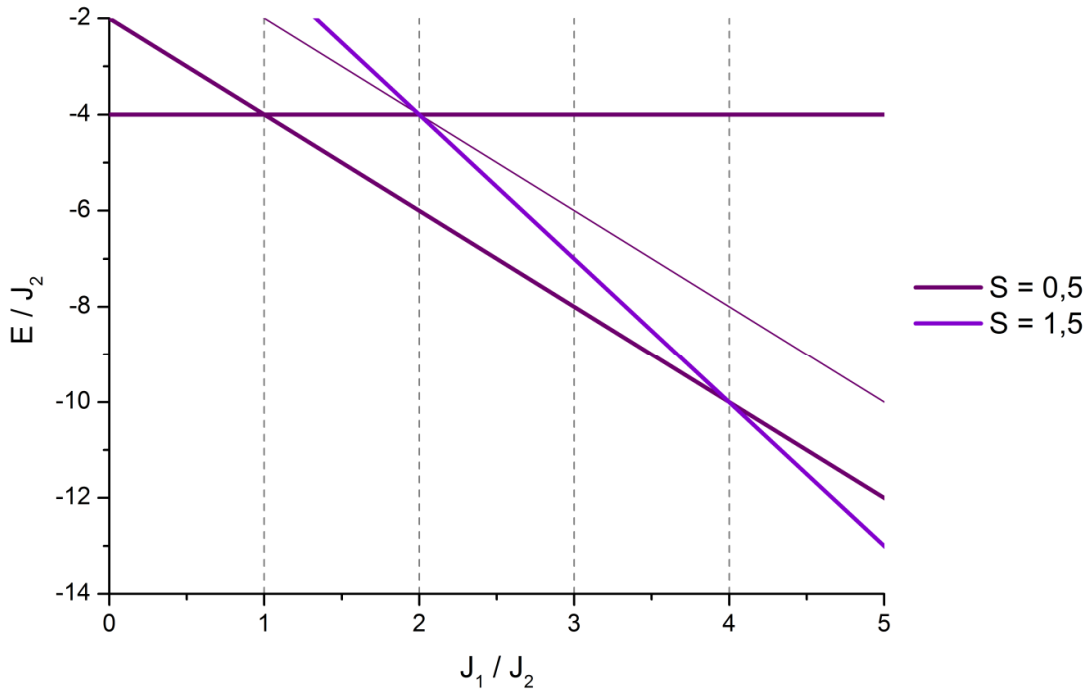

Figure S12 Coupling constants ratio dependent normalized energy level diagram of an idealized square magnetic model for a generalized Cu(II)[12-$MC_{Cu(II)N(Shi)}$-4]$^{2-}$ complex with radial (J_1) and tangential (J_2) antiferromagnetic interactions according to an isotropic Heisenberg Hamiltonian with special focus on the spin ground states; occurring spin ground states are highlighted

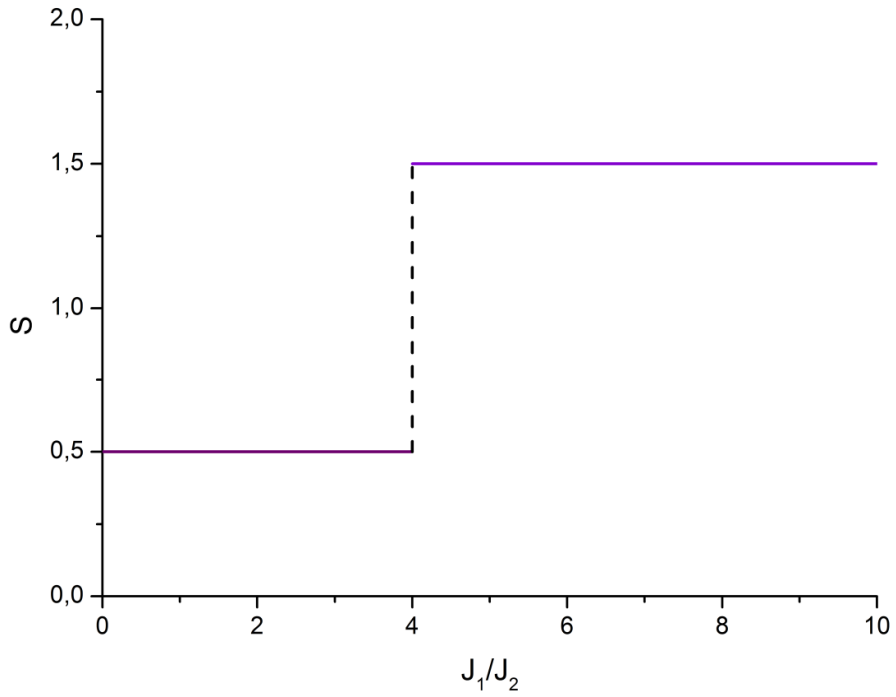

Figure S13 Coupling constants ratio dependence of the value of the spin ground state of an idealized square magnetic model for a generalized Cu(II)[12-MC$_{Cu(II)N(Shi)}$-4]$^{2-}$ complex with radial (J_1) and tangential (J_2) antiferromagnetic interactions according to an isotropic Heisenberg Hamiltonian

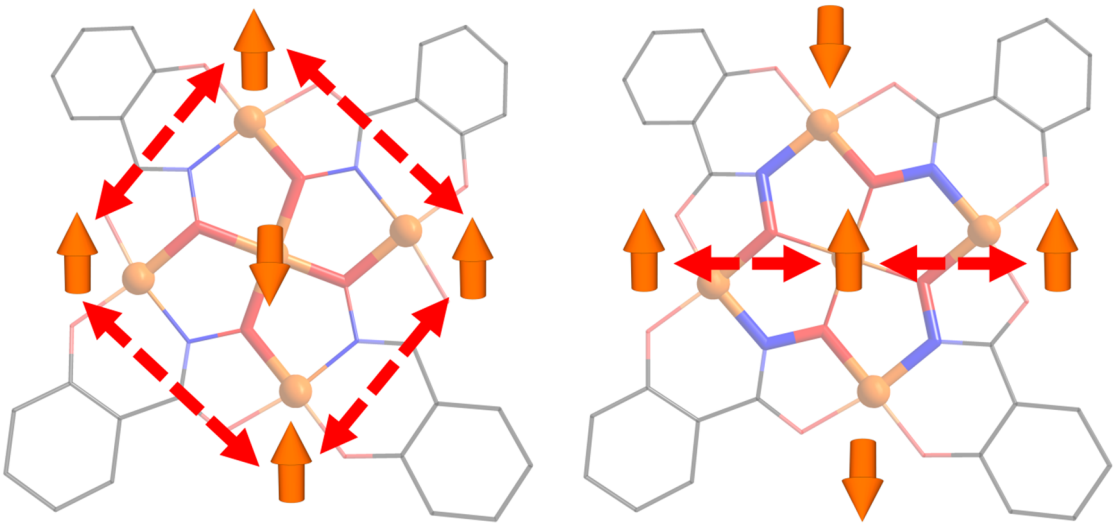

Figure S14 Illustrative visualization of the geometric hindrance from the manipulation of the spin ground state of a 12-MC-4 complex via a central magnetic director approach by a comparison of the spin topologies of the cyclic scaffold for both extreme cases of dominantly radial (a) and tangential (b) antiferromagnetic interactions; assuming the paradigm of a homometallic metallacrown with all spin centers S = ½ and identical, antiferromagnetic coupling constants J_1 and J_2, every parallel alignment of spins (red arrow) means an energetic penalty relative to an antiparallel orientation; the handicap of the intended high-spin state can be illustrated by simply counting the penalties for the parallel aligned (4) and alternating (2) spin topology in the ring

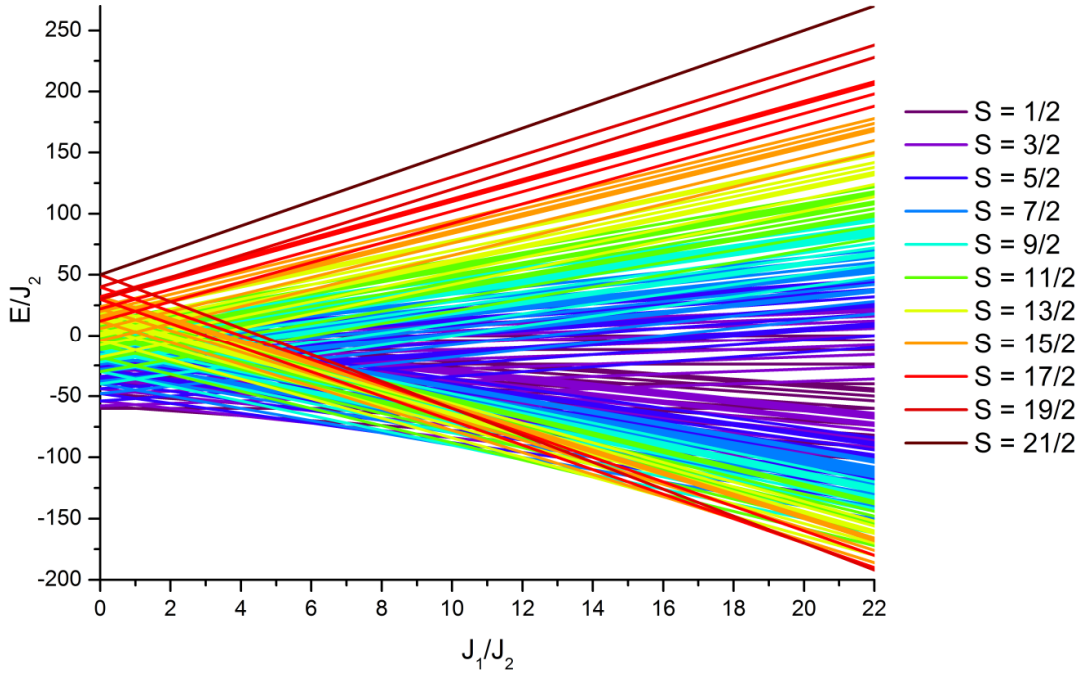

Figure S15 Coupling constants ratio dependent normalized energy level diagram of an idealized square magnetic model for a generalized Cu(II)[12-$MC_{Fe(III)N(Shi)}$-4] complex with radial (J_1) and tangential (J_2) antiferromagnetic interactions according to an isotropic Heisenberg Hamiltonian

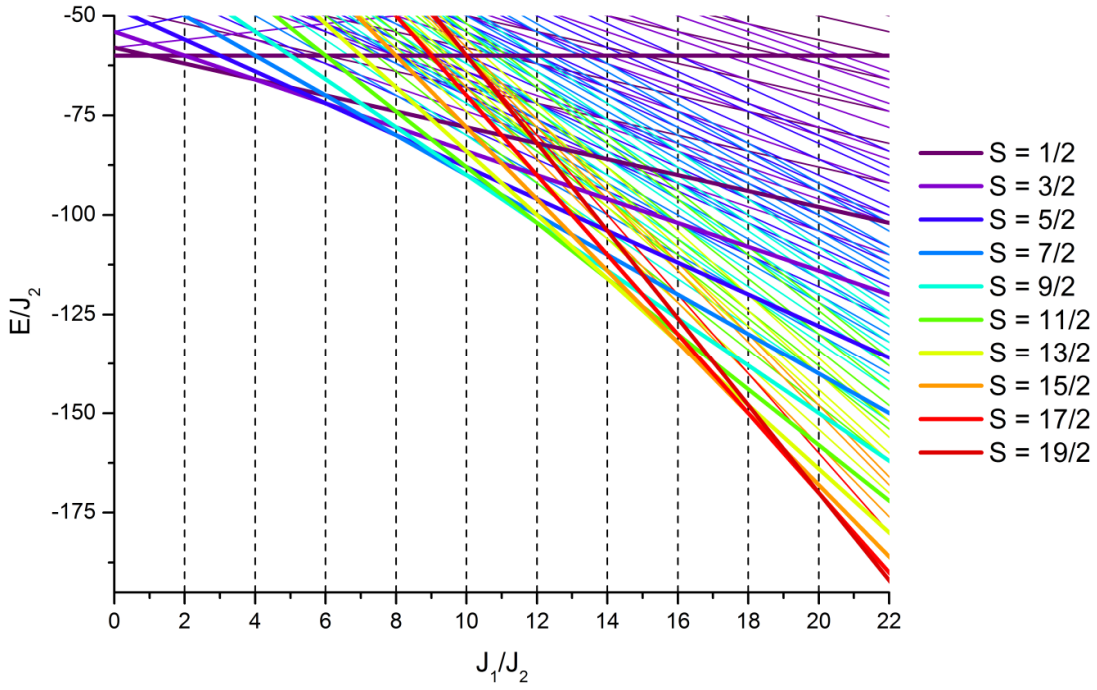

Figure S16 Coupling constants ratio dependent normalized energy level diagram of an idealized square magnetic model for a generalized Cu(II)[12-MC$_{Fe(III)N(Shi)}$-4] complex with radial (J_1) and tangential (J_2) antiferromagnetic interactions according to an isotropic Heisenberg Hamiltonian with special focus on the spin ground states; occurring spin ground states are highlighted

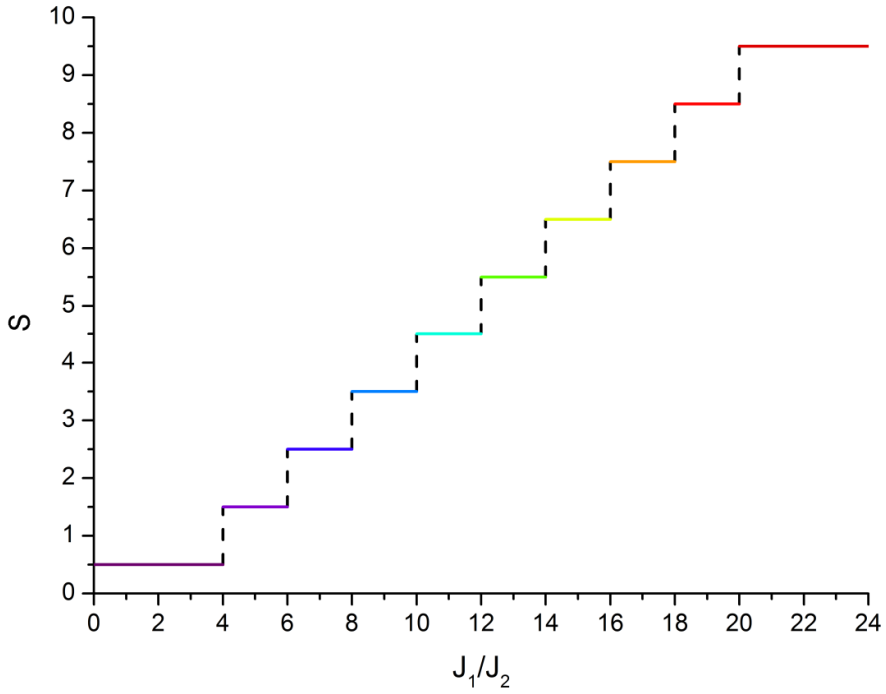

Figure S17 Coupling constants ratio dependence of the value of the spin ground state of an idealized square magnetic model for a generalized Cu(II)[12-$MC_{Fe(III)N(Shi)}$-4]$^{2-}$ complex with radial (J_1) and tangential (J_2) antiferromagnetic interactions according to an isotropic Heisenberg Hamiltonian

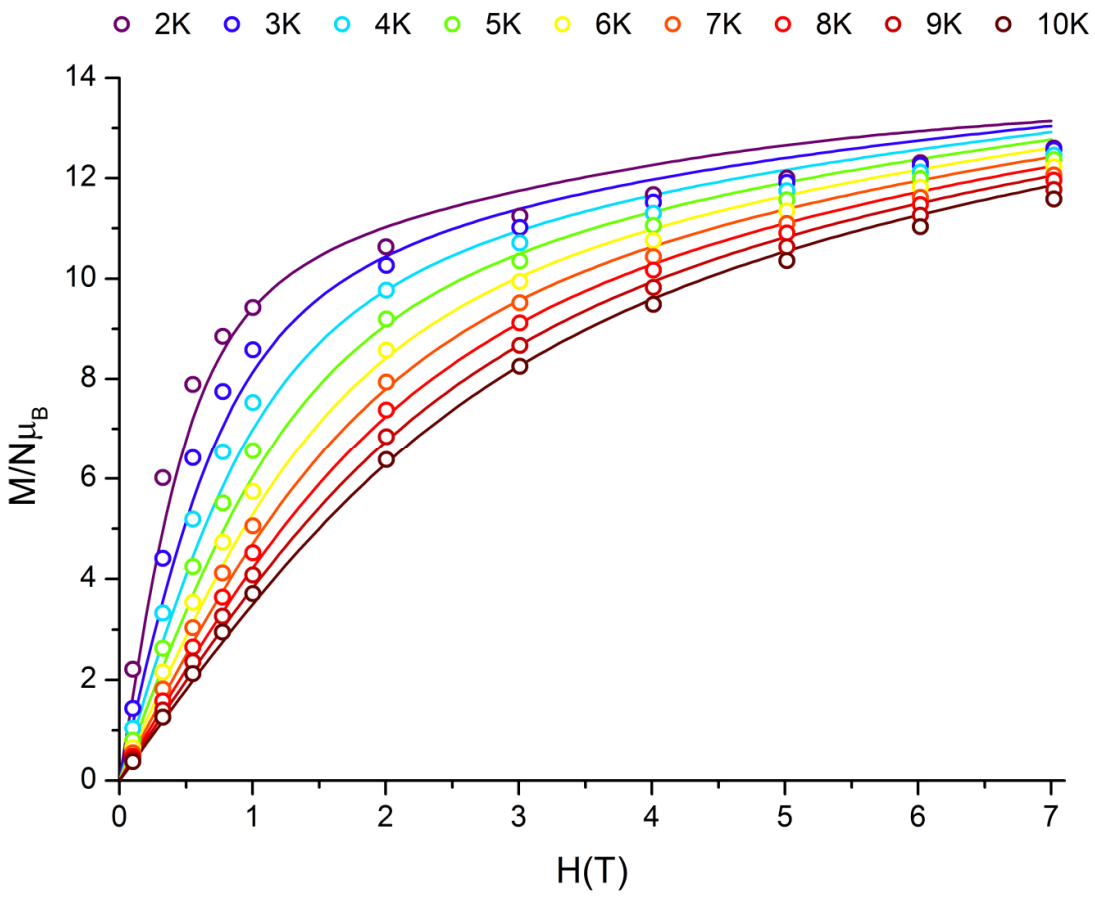

Figure S18 Field dependence of the reduced magnetization ($M/N\mu_B$ vs. H plot) of **2** for different temperatures between 2 and 10 K; solid lines represent simulations according to the best fit result of the temperature dependence of the $\chi_M T$ product ($\chi_M T$ vs. T plot; Fig. 5) for an idealized square magnetic model

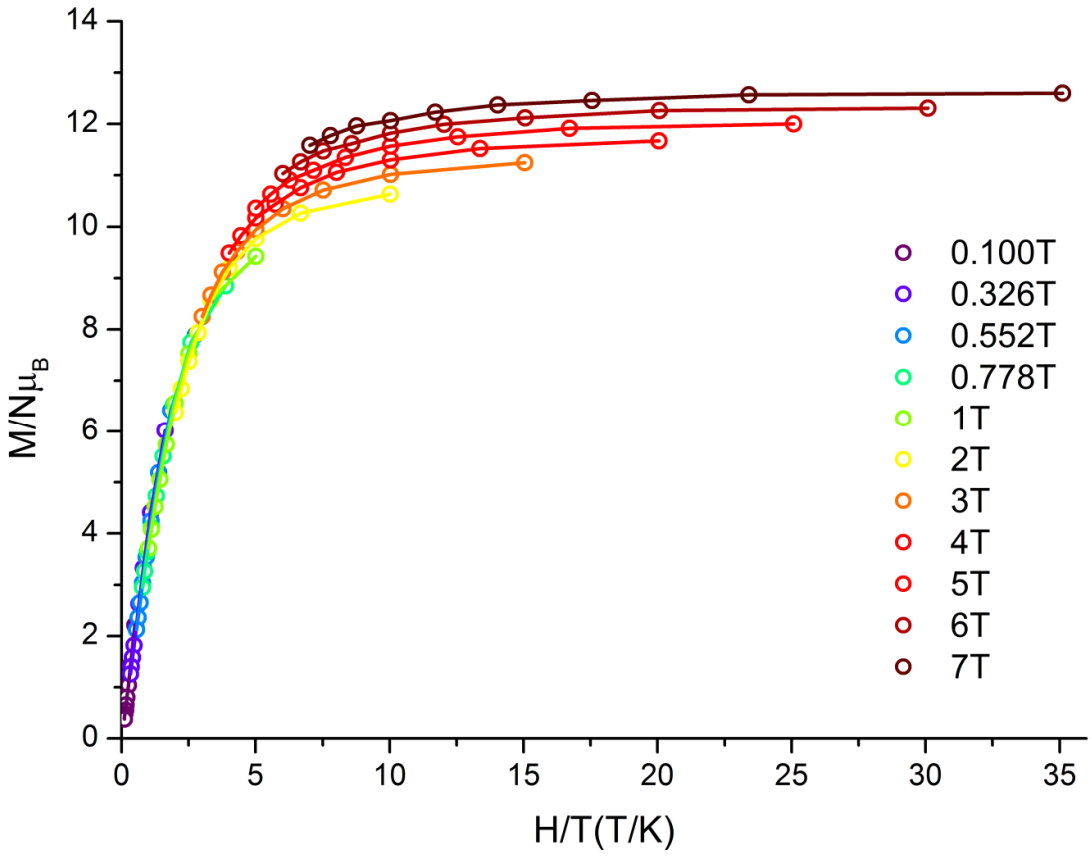

Figure S19 Field-temperature ratio dependence of the reduced magnetization ($M/N\mu_B$ vs. H/T plot) of **2** at temperatures between 2 and 10 K for applied magnetic field from 0.1 to 7 T; the solid lines are guidelines for the eyes

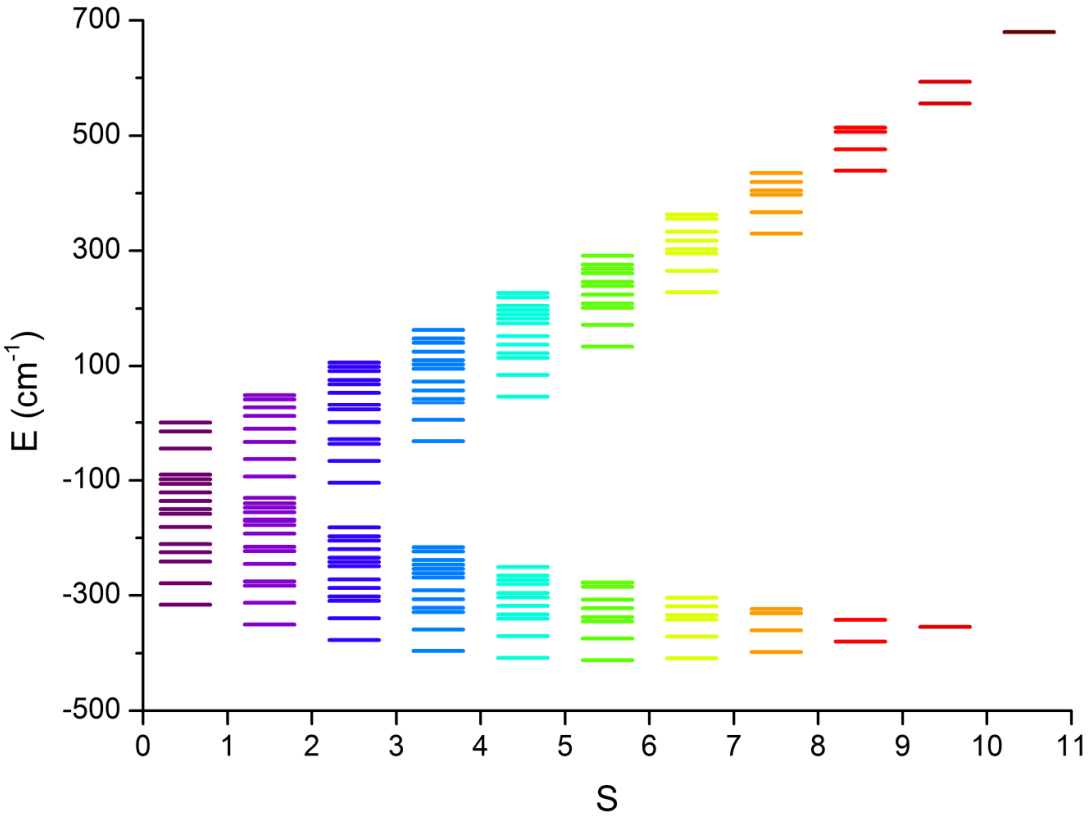

Figure S20 Energy level diagram of the spin states of the $Cu(DMF)_2Cl_2[12\text{-}MC_{Fe(III)N(Shi)}\text{-}4](DMF)_4$ complex in **2** according to the best fit result of the temperature dependence of the $\chi_M T$ product ($\chi_M T$ vs. T plot; Fig. 5) for an idealized square magnetic model using an isotropic Heisenberg Hamiltonian

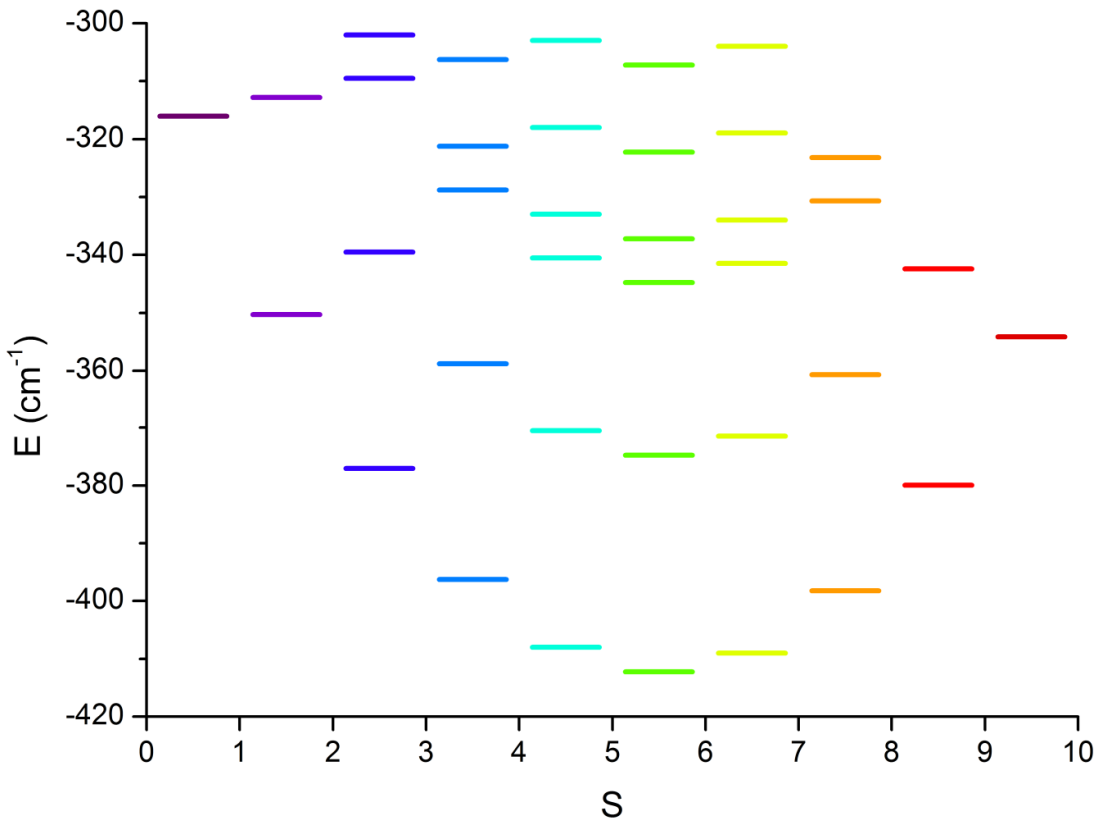

Figure S21 Energy level diagram of the spin states of the Cu(II)(DMF)$_2$Cl$_2$[12-MC$_{Fe(III)N(Shi)}$-4](DMF)$_4$ complex in **2** according to the best fit result of the temperature dependence of the χ_MT product (χ_MT vs. T plot; Fig. 5) for an idealized square magnetic model using an isotropic Heisenberg Hamiltonian with focus on the lowest lying states

2.7.5 Elemental Analysis

1: Found: C, 42.92; H, 4.47; N, 7.35. Calc. for $C_{40}H_{48}Cu_5N_6O_{12}$: C, 42.80; H, 4.31; N, 7.49%

2: Found: C, 40.48; H, 4.60; N, 10.96. Calc. for $C_{52}H_{72}Cl_2Cu_1Fe_4N_{12}O_{20}$: C, 40.48; H, 4.70; N, 10.89%

2.7.6 Infrared Absorption Spectroscopy

1: ν_{max}/cm^{-1}

3136w, 3025w, 2980m, 2942w, 2882w, 2737w, 2678w, 1597s ($\nu(C=N)_{Shi}$), 1565vs, 1523s, 1466m, 1433m, 1386s, 1321s, 1253s ($\nu(N-O)_{Shi}$), 1175w, 1152m, 1093m, 1065w, 1029m, 1020m, 943s, 852m, 795w, 755s, 688s, 654s, 580m, 545w, 509w, 475m, 454w, 424m

2: ν_{max}/cm^{-1}

3146br, 3059w, 2929m, 2864w, 2806w, 1647vs ($\nu(C=O)_{DMF}$), 1595s ($\nu(C=N)_{Shi}$), 1561s, 1492vs, 1427s, 1383s, 1316s, 1258s ($\nu(N-O)_{Shi}$), 1156m, 1145w, 1117w, 1100m, 1063w, 1034w, 1010m, 935s, 865s, 774w, 758s, 684s, 649s, 634w, 578w, 541w, 503w, 463m

The assignment of characteristic bands was performed via a comparison with reported data for similar salicylhydroxamic acid based metallacrowns.[8-13]

2.7.7 UV-Vis Absorption Spectroscopy

1: λ_{max}(MeOH)/nm 216 (ε/dm³ mol^{-1} cm^{-1} 110000), 236 (85000), 318 (29200), 616 (711)

2: λ_{max}($CHCl_3$)/nm 296 (ε/dm³ mol^{-1} cm^{-1} 48200), 472 (18400)

The band at 616 nm for **1** represents a copper centered d-d transition[14] whereas the light absorption by **2** at 472 nm is characteristic for a ligand-to-metal charge-transfer (LMCT) in hydroxamate iron complexes.[15-18] By comparison with the measured absorption maxima of the free main ligand salicylhydroxamic acid at 300 and 236 nm, the bands at 318, 236 of **1** and 296 nm of **2** can be assigned to excitations within the delocalized π-system of chelating hydroximate.

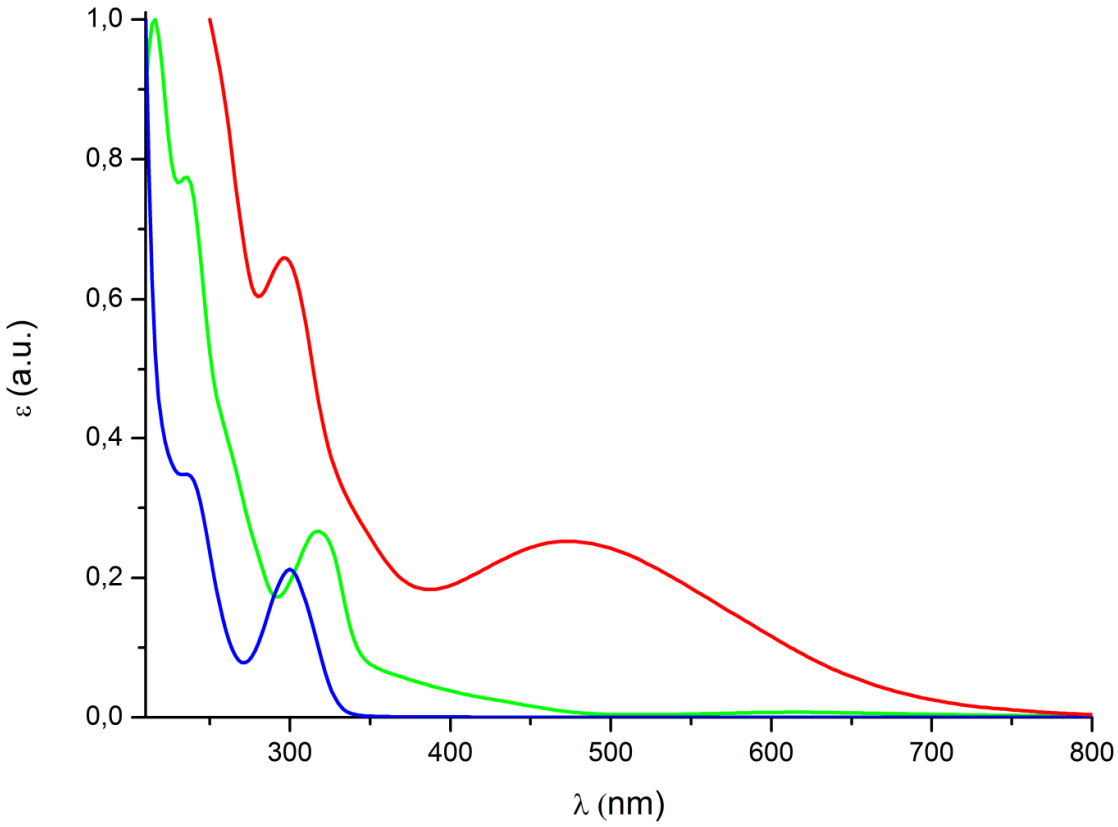

Figure S22 Normalized UV-Vis spectra of **1** in MeOH (green), **2** in $CHCl_3$ (red) and H_3Shi in MeOH (blue)

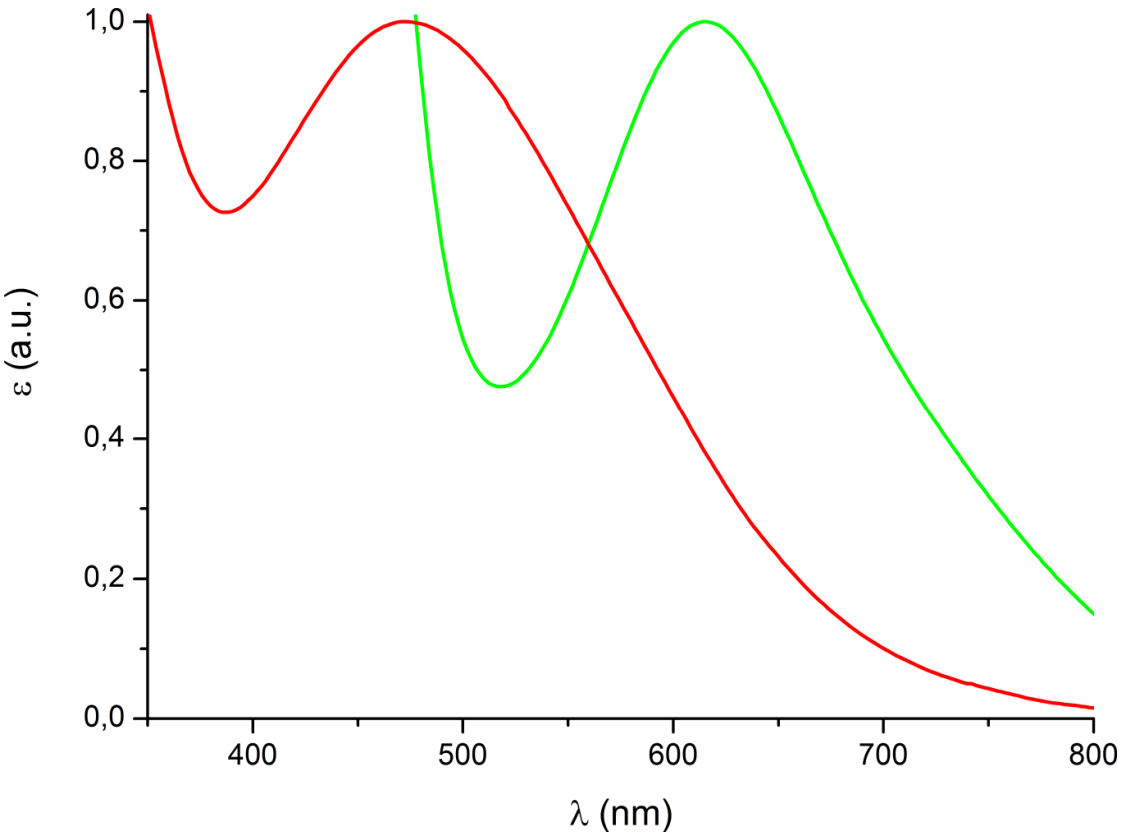

Figure S23 Normalized extract of the UV-Vis spectra of **1** in MeOH (green) and **2** in $CHCl_3$ (red)

2.7.8 Atomic Absorption Spectroscopy

2: Found: ratio Cu:Fe, 1:4.15. Calc. for $C_{52}H_{72}Cl_2Cu_1Fe_4N_{12}O_{20}$: ratio Cu:Fe, 1:4

2.7.9 Mößbauer Spectroscopy

The evaluation of the ^{57}Fe Mößbauer spectrum was performed with the help of the RECOIL 1.03 fit routine.[19] The optimized reasonable fit results of an applied two-site model for the isomer shift (δ_{IS}), quadrupole splitting (ΔE_Q), Lorentzian line width (Γ) and the area ratio (A) are given below.

2: doublet 1: δ_{IS} 0.4343 mm s^{-1}, ΔE_Q 1.816 mm s^{-1}, Γ 0.179 mm s^{-1}, A 49.8%

doublet 2: δ_{IS} 0.3336 mm s^{-1}, ΔE_Q 1.108 mm s^{-1}, Γ 0.181 mm s^{-1}, A 50.2%

The spectrum exhibits the presence of two distinct iron species, which are comprised in the compound with same quantity and both reveal typical values of the isomer shift for high-spin Fe(III) ions. Furthermore, the quite distinct quadrupol splittings match the inhomogeneous arrangement of donor atoms in coordination spheres. Hence, the wider doublet might moreover be attributed to the five-fold coordinated iron ion with the apical chloro ligand.

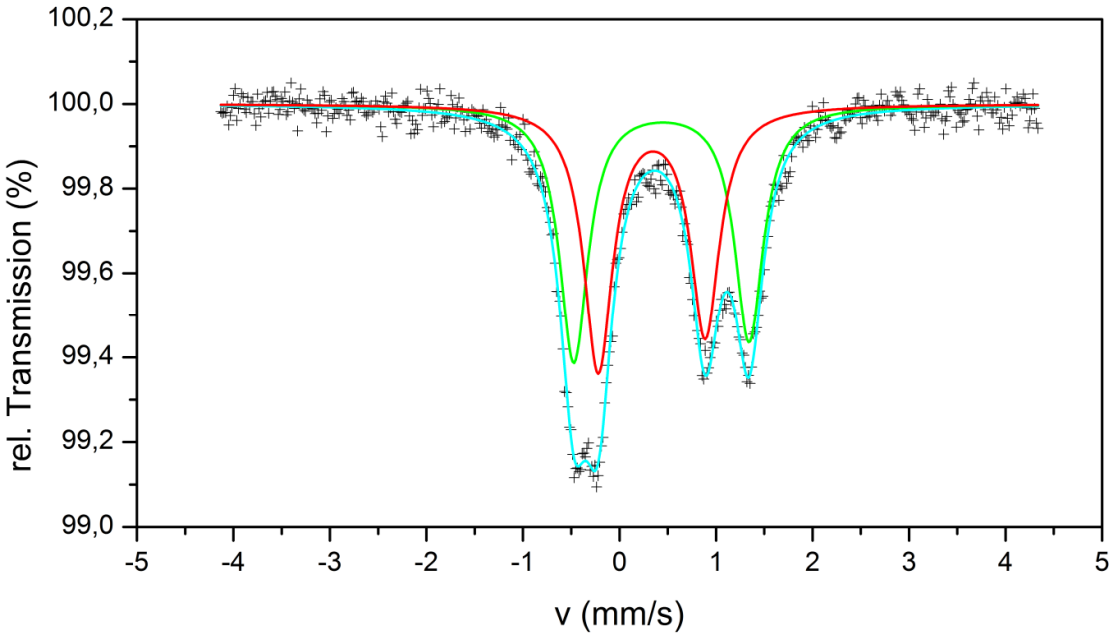

Figure S24 Mößbauer spectrum of **2**; solid lines represent the result of the entire fit (cyan), the fit for doublet 1 (green) and doublet 2 (red)

2.7.10 ESI Mass Spectrometry

1: m/z(MeCN)

920 $\{(Cu(II)[12\text{-}MC_{Cu(II)N(Shi)}\text{-}4])H_3\}^+$

1021 $\{(Cu(II)[12\text{-}MC_{Cu(II)N(Shi)}\text{-}4])(HNEt_3)H_2\}^+$

1122 $\{(Cu(II)[12\text{-}MC_{Cu(II)N(Shi)}\text{-}4])(HNEt_3)_2H\}^+$

1225 $\{(Cu(II)[12\text{-}MC_{Cu(II)N(Shi)}\text{-}4])(HNEt_3)_3\}^+$

1583 $\{(Cu(II)[12\text{-}MC_{Cu(II)N(Shi)}\text{-}4])_3(HNEt_3)_4H_4\}^{2+}$

1942 $\{(Cu(II)[12\text{-}MC_{Cu(II)N(Shi)}\text{-}4])_2(HNEt_3)H_4\}^+$

2043 $\{(Cu(II)[12\text{-}MC_{Cu(II)N(Shi)}\text{-}4])_2(HNEt_3)_2H_3\}^+$

1: m/z(MeOH)

942 $\{(Cu(II)[12\text{-}MC_{Cu(II)N(Shi)}\text{-}4])NaH_2\}^+$

964 $\{(Cu(II)[12\text{-}MC_{Cu(II)N(Shi)}\text{-}4])Na_2H\}^+$

1021$\{(Cu(II)[12\text{-}MC_{Cu(II)N(Shi)}\text{-}4])(HNEt_3)H_2\}^+$

1043 $\{(Cu(II)[12\text{-}MC_{Cu(II)N(Shi)}\text{-}4])(HNEt_3)NaH\}^+$

1122 $\{(Cu(II)[12\text{-}MC_{Cu(II)N(Shi)}\text{-}4])\ (HNEt_3)_2H\}^+$

1583$\{(Cu(II)[12\text{-}MC_{Cu(II)N(Shi)}\text{-}4])(HNEt_3)_4H_4\}^{2+}$

2: m/z(DMF:MeCN/1:1)

1126 $\{(Cu(II)(Cl)_2[12\text{-}MC_{Fe(III)N(Shi)}\text{-}4](DMF)_2)Na\}^+$

1141 $\{Cu(II)Cl[12\text{-}MC_{Fe(III)N(Shi)}\text{-}4](DMF)_3\}^+$

2.7.11 References

[1] A.L. Spek, *Acta Crystallogr D Biol Crystallogr*, 2009, **2**, 148

[2] R.H. Blessing, *Acta Crystallogr A Found Crystallogr*, 1995, **1**, 33

[3] A. Altomare, M.Cristina Burla, M. Camalli, G.Luca Cascarano, C. Giacovazzo, A. Guagliardi et al., *J Appl Crystallogr*, 1999, **1**, 115

[4] G.M. Sheldrick, *Acta Crystallogr A Found Crystallogr*, 2008, **1**, 112

[5] G.A. Bain and J.F. Berry, *J. Chem. Educ.*, 2008, **4**, 532

[6] D. Gatteschi and L. Pardi, *Gazz. Chim. Ital.*, 1993, **123**, 231

[7] L. Engelhardt, S.C. Garland, C. Rainey and R.A. Freeman, *arXiv:1305.0238 [cond-mat.str-el]*

[*8*] C. Dendrinou-Samara, G. Psomas, L. Iordanidis, V. Tangoulis and D.P. Kessissoglou, *Chem. Eur. J*, 2001, **23**, 5041

[9] G. Psomas, A.J. Stemmler, C. Dendrinou-Samara, J.J. Bodwin, M. Schneider, M. Alexiou et al., *Inorg. Chem*, 2001, **7**, 1562

[10] D.P. Kessissoglou, J.J. Bodwin, J. Kampf, C. Dendrinou-Samara and V.L. Pecoraro, *Inorganica Chimica Acta*, 2002, **1**, 73

[11] C. Dendrinou-Samara, L. Alevizopoulou, L. Iordanidis, E. Samaras and D.P. Kessissoglou, *Journal of Inorganic Biochemistry*, 2002, **1-2**, 89

[12] M. Alexiou, I. Tsivikas, C. Dendrinou-Samara, A.A. Pantazaki, P. Trikalitis, N. Lalioti et al., *Journal of Inorganic Biochemistry*, 2003, **3-4**, 256

[13 C. Dendrinou-Samara, A.N. Papadopoulos, D.A. Malamatari, A. Tarushi, C.P. Raptopoulou, A. Terzis et al., *Journal of Inorganic Biochemistry*, 2005, **3**, 864

[14] B.R. Gibney, D.P. Kessissoglou, J.W. Kampf and V.L. Pecoraro, *Inorg. Chem*, 1994, **22**, 4840

[15] E. Farkas, E. Kozma, M. Petho, K.M. Herlihy and G. Micera, *Polyhedron*, 1998, **19**, 3331–3342

[16] C. Mulcahy, K.A. Krot, D.M. Griffith, K.Yu Suponitsky, Z.A. Starikova and C.J. Marmion, *Eur. J. Inorg. Chem.*, 2007, **10**, 1373

[17] E. Farkas, D. Bátka, H. Csóka and N.V. Nagy, *Bioinorganic Chemistry and Applications*, 2007, **17**, 1

[18] S. Dhungana, J.M. Harrington, P. Gebhardt, U. Möllmann and A.L. Crumbliss, *Inorg. Chem.*, 2007, **20**, 8362

[19] K. Lagarec and D. Rancourt, *Nuclear Instruments and Methods in Physics Research Section B: Beam Interactions with Materials and Atoms*, 1997, **2**, 266

3 Heterovalent Cobalt Metallacrowns

A systematic interface to the SMM features based on a single Co(II) ion – the first cobalt metallacrowns of salicylhydroxamic acid

Peter Happ and Eva Rentschler

3.1 Abstract

The first examples of cobalt metallacrowns based on the pioneering ligand salicylhydroxamic acid have been synthesized and their rich chemistry has been investigated by a series of eight corresponding compounds which have been characterized by X-ray crystal structure analysis, one- and two-dimensional ^{1}H-NMR spectroscopy, mass spectrometry, UV-Vis spectroscopy, IR spectroscopy and static as well as dynamic magnetic measurements. Due to the high flexibility of the molecular configuration of the Co(III) containing cyclic host, a most singular structural diversity with various coordination environments of the central divalent cobalt guest ion is generated in dependence of the presence of different peripherally attached additional cations, secondary and bridging ligands. Moreover, single-molecule magnetic behaviour has been observed for three members of the novel Co(II)[12-MC$_{Co(III)N(Shi)}$-4] coronates featuring increasing energy barriers of up to 79 K along the distortion pathway from an octahedral to a trigonal prismatic shape of the coordination sphere of the magnetically virtually isolated high-spin Co(II) ion. Hence, the dualism of the reliability and indicated controllable versatility of these cobalt metallacrowns creates them a powerful synthetic interface for a further systematic investigation and optimization of the SMM features based on a single Co(II) ion as a current hot topic in magnetochemistry

3.2 Introduction

While complexes of high nuclearity had been in the focus of single-molecule magnet research in its early days,[1–4] later efforts in this field mainly targeted finite clusters and the fine tuning of their magnetic properties.[5–12] Due to the strong dependence between the value of the spin ground state and the axial magnetic anisotropy,[13–16] the attempts to enhance both of these essential parameters for SMM behaviour simultaneously with the number of single-ion contributions did not yield higher energy barriers to magnetization reversal. First advances were rather attained via the subtle synthetic modification of the magnetic interactions in the deserved family of finite Mn_6 clusters.[16,17] However, appreciable progress could not be achieved until lanthanide ions were incorporated into the SMM complexes.[18–21] A milestone was reached in 2003 when a terbium phthalocyaninato double-decker sandwich complex was discovered which revealed single-molecule magnetism based on just one single metal ion and represents in a most paradigmatic way the rising importance of the engineering of the magnetic anisotropy in this field of research.[22–24] Accordingly, a corresponding derivative currently holds the record energy barrier of 938 K.[25] Depending on the electronic configuration of the respective lanthanide ion, the distribution of the f-electrons is often highly anisotropic in the m_J microstates of the spin-orbit coupled ground state and hence an increased magnetic anisotropy can be triggered by a complementary ligand field.[26] However, the highly

polarized bonding due to the inner character of the valence orbitals provides only few selectivity for the shape of the coordination sphere. The targeted synthetic realization of precise and varied geometries hence requires the determining influence of large restrictive ligand systems. Providing more advantageous coordinative properties, complexes with SMM behaviour based on a single 3d metal ion have also yielded remarkable energy barriers up to 260K.[27] Besides a few examples of Fe(III)[28] and Mn(III)[29–31] this scientific realm is dominated by Co(II) and Fe(II) compounds because they are especially capable for a just partially quenched first-order orbital angular momentum as an effective source of magnetic anisotropy. While the later demands for an enforcement of special electronic configurations via elaborate ligands,[27,32–35] mononuclear Co(II) SMMs can be achieved with less synthetic efforts and in a greater variety of coordination spheres. Hence, corresponding complexes with trigonal-planar,[35] tetrahedral,[36–41] square-pyramidal,[42,43] distorted octahedral[44–47] and distorted trigonal prismatic[48] arrangement of nitrogen, oxygen, phosphorus, sulphur and halide donor atoms have been discovered. Recently, the impressive value of 109 K has been reported for the height of the anisotropy barrier to magnetization reversal of a mixed valent $Co(II)Co(III)_3$ complex which demonstrates the promising potential of this class of compounds to attain high-performance single-molecule magnets.[48] In that respect, the high sensitivity of the magnetic properties of divalent high-spin cobalt ions to different coordination spheres in combination with its marked flexibility to adopt them in a wide range simultaneously creates capabilities and challenges.[41] However, a comprehensive model of the reasons for the slowed relaxation and detailed general view of the interplay of different relaxation mechanisms as well as an explicit set of guidelines for the design of novel complexes with optimized energy barrier has not yet been extracted from the great variety of mononuclear Co(II) SMMs. In analogy to the prolific family of salicylaldoxime based Mn_6-clusters,[6,7,17,49] a basic complex type which features a reliably recurring structural motif and simultaneously provides the opportunities for versatile synthetic modifications in fine and large scale would afford an invaluable foundation for a systematic experimental investigation of this magneto-structurally correlated issue. Metallacrowns represent an established class of compounds which unify these opposing requirements in a most singular way and can be obtained without elaborate preliminary synthetic effort.[50,51] Especially, the 12-MC-4 complexes built by salicylhydroxamic acid have proven to combine a reasonable and reliable self-assembly of their cyclic host on the on hand with a flexible adaption of their molecular configuration and cavity size as well as a facile exchange of the central guest ion, bridging and secondary ligands on the other hand.[52–59] Therefore, the supramolecular metallacrown scaffold provides an ideal tuning workshop for the static and dynamic magnetic properties of an encapsulated Co(II) ion at its core. However, cobalt metallacrowns are very rare compounds in general[60–62] and hitherto no complex of the ligand salicylhydroxamic acid with the aforementioned

metal ion has been described in literature although their accessibility were already predicted in the first days of metallacrown research.[63]

Getting hold of the first two examples of salicylhydroxamic acid based cobalt metallacrowns, we recognized the potential of a rich chemistry as both complexes differed in their unique structural features from each other and the corresponding coronates of other transition metals from literature in spite of similar reagents and reaction conditions. Hence, we enlarged the scope to a series of eight compounds and discovered the slow magnetic relaxation of three novel single-molecule magnets among the Co(II)[12-$MC_{Co(III)N(Shi)}$-4] clusters based on the Co(II) high-spin guest ion at the core of the Co(III) comprising cyclic host. The dualism of supramolecular preorganization and enhanced structural flexibility of the molecular configuration of the surrounding scaffold allows for a large and fine scale manipulation of the coordination sphere and the correlated magnetic properties of the central divalent cobalt ion via synthetic tools like bridging and secondary ligands as well as peripheral attached cations. Therefore, we have established the foundations of a synthetic interface to the static and dynamic magnetic features based on a single Co(II) ion. It enables a systematic experimental investigation and optimization of the underlying causes and involved processes of the slowed relaxation in order to find a comprehensive model for this current hot topic in magnetochemistry.

3.3 Experimental section

Materials and methods

All chemicals were reagent grade and were used without further purification.

X-ray diffraction data for the structure analyses were collected from suitable crystals of **1**·3MeCN, **3**·7MeCN, **4**·3MeCN·H_2O, **5**·3.5MeOH·H_2O, **6**·2.75 MeOH, **7**·5.5MeOH·H_2O and **8**·5.75MeOH on a Bruker SMART 3-circle diffractometer with an APEX II CCD detector and Oxford cooling system using graphite-monochromated Mo-Kα radiation (λ = 0.71073 Å) at -100°C. Corresponding data of (**2**)$_3$·H_2Sal·2$OCMe_2$·H_2O were obtained from a Stoe IPDS 2T at -80°C with Oxford Cryostream using graphite-monochromated Mo-Kα radiation (λ = 0.71073 Å). Semi-empirical absorption corrections of the data from the Bruker SMART diffractometer were performed with MULABS[64,65] or SADABS.[66] The data from the Stoe IPDS 2T were corrected by the integration method. A first solution of the structures was computed by direct methods with the help of the program SIR97.[67] The subsequent refinement of the models was conducted via full-matrix least squares methods on F^2 with anisotropic displacement parameters for all non-hydrogen atoms with SHELXL-2013.[68] Moreover, the accomplishment of the refinement was supported by the representation of molecular graphics and difference Fourier maps via the programs Olex2,[69] Mercury

3.3[70] and ORTEP-3.[71] Graphics and compilations of the experimental data and parameters of the obtained models for publication were issued using the programs Diamond 3.2[72] and publCIF 1.9.16.[73]

Magnetic data were collected from ground and restrained polycrystalline samples on a Quantum Design MPMS XL SQUID magnetometer equipped with a 7 T magnet. Temperature dependent susceptibility was measured in a range from 2 to 300 K at an applied field of 0.1 T. Magnetization data were collected at temperatures between 2 and 10 K using magnetic fields up to 7 T. Diamagnetic corrections of the dc magnetic data were performed for the matrix and the intrinsic contributions of atoms and moieties of the samples with the help of Pascal's constants.[74] In- and out-of-phase ac susceptibility measurements were conducted in the presence and absence of a static magnetic field of up to 0.7 T at different temperatures below 15 K for frequencies between 1 and 1000 Hz. The fitting of the magnetization data was carried out with the help of the program PHI.[75]

C, H and N elemental analyses were obtained from a Foss Heraeus Vario EL at the Institute of Organic Chemistry at the Johannes Gutenberg University Mainz. ^{1}H and ^{1}H-^{1}H COSY nuclear magnetic resonance spectroscopic measurements were performed on a Bruker DRX 400 of solutions in deuterated dichlormethane and chloroform. The solvents were used as internal standards and the spectra are scaled in respect of the standard reference tetrametyhlsilan. The spectra analysis was conducted with the help of the MesTreNova 6.0.2 software.[76]

Infrared absorption spectra in a range of 400-4000 cm^{-1} were recorded at room temperature on a JASCO FT/IR-4200 spectrometer using KBr pellets. UV-Vis absorption measurements were performed between 250 and 1000 nm for solutions in $CHCl_3$ with concentrations between 0.2 and 0.01 mM on a JASCO V-570 UV/Vis/NIR spectrophotometer. ESI mass spectra were carried out in the positive ion mode from a Waters Q-ToF-ULTIMA 3 with LockSpray source at the Institute of Organic Chemistry at the Johannes Gutenberg University Mainz.

3.4 Synthesis

Precursor $[Co(II)_2(H_2O)(Piv)_4(HPiv)_4]$

The precursor compound $[Co(II)_2(H_2O)(Piv)_4(HPiv)_4]$ was prepared as described previously.[77]

$[Co_5(Shi)_3(Piv)_5(Pip)_4(OH)(H_2O)]$ (1)

A suspension of salicylhydroxamic acid (0.077 g, 0.5 mmol) in acetonitrile (10 mL) was added to a mixture of $[Co(II)_2(H_2O)(Piv)_4(HPiv)_4]$ (0.474 g, 0.5 mmol / 1.0 mmol based

on cobalt) and acetonitrile (10 ml). Piperidine (0.255 g, 3 mmol) was dissolved in acetonitrile (10 ml) and the solution was added to the reaction mixture. The resultant dark brown solution was stirred for 18 h at room temperature and filtered afterwards. Suitable crystals for X-ray structure analysis of **1**·3MeCN were obtained from the filtrate by slow evaporation of the solvent after one month. For further analysis, the product was washed with cold acetonitrile and dried under vacuum. Elemental analysis – Found: C, 48.44; H, 6.65; N, 6.29 .Calc. for $C_{66}H_{104}Co_5N_7O_{21}$ (**1**): C, 48.74; H, 6.45, 6.03. Yield: 29%

[12-MC$_{Co(III)N(Shi)}$-4](Py)$_8$ (2)

A suspension of salicylhydroxamic acid (0.230 g, 1.5 mmol) in acetone (10 mL) was added to a mixture of [Co(II)$_2$(H$_2$O)(Piv)$_4$(HPiv)$_4$] (0.474 g, 0.5 mmol / 1.0 mmol based on cobalt) and acetone (10 ml). Pyridine (0.712 g, 9 mmol) was dissolved in acetone (10 ml) and the solution was added to the reaction mixture. The resultant dark green brown solution was stirred for 18 h at room temperature and filtered afterwards. Suitable crystals for X-ray structure analysis of (**2**)$_3$·H$_2$Sal·2OCMe$_2$·H$_2$O were obtained from the filtrate by slow evaporation of the solvent after one month. For further analysis, the product was washed with cold acetone and dried under vacuum. Elemental analysis – Found: C, 54.79; H, 4.60.; N, 10,06 Calc. for $C_{223}H_{208}Co_{12}N_{36}O_{48}$ ((**2**)$_3$·H$_2$Sal·4OCMe$_2$·5H$_2$O): C, 55.03; H, 4.31, 10.36. Yield: 24%

Co(II)(Boa)$_2$[12-MC$_{Co(III)N(Shi)}$-4](Pip)$_6$ (3)

A suspension of salicylhydroxamic acid (0.230 g, 0.5 mmol) in acetonitrile (10 mL) was added to a mixture of [Co(II)$_2$(H$_2$O)(Piv)$_4$(HPiv)$_4$] (0.474 g, 0.5 mmol / 1.0 mmol based on cobalt) and acetonitrile (10 ml). Piperidine (1.021 g, 12 mmol) was dissolved in acetonitrile (10 ml) and the solution was added to the reaction mixture. The resultant dark orange brown solution was stirred for 18 h at room temperature and filtered afterwards. Suitable crystals for X-ray structure analysis of **3**·7MeCN and crystals of a byproduct were obtained from the filtrate by slow evaporation of the solvent after two month.

(HPip)(Piv)[Li[Co(II)(μ$_2$-Piv)$_2$(Piv)[12-MC$_{Co(III)N(Shi)}$-4](Pip)$_5$]]$_2$ (4)

A solution of piperidine (0.511 g / 6 mmol) in acetonitrile (10 mL) was added to a mixture of [Co(II)$_2$(H$_2$O)(Piv)$_4$(HPiv)$_4$] (0.474 g, 0.5 mmol / 1.0 mmol based on cobalt) and salicylhydroxamic acid (0.153 g, 1 mmol) in acetonitrile (10 ml). A suspension of lithium chloride (0.042 g, 1 mmol) in acetonitrile (10 mL) was added to the reaction mixture. The resultant dark orange brown solution was stirred for 18 h at room temperature and filtered afterwards. Suitable crystals for X-ray structure analysis of **4**·3MeCN·H$_2$O were obtained by slow evaporation of the solvent after two weeks. For further analysis, the product was washed with cold acetonitrile and dried under vacuum. Elemental anal-

ysis - Found: C, 50.46; H, 6.76; N, 8.21. Calc. for $C_{152}H_{228}Co_{10}Li_2N_{22}O_{39}$ (**4**·3MeCN·H_2O): C, 50.84; H, 6.40; N, 8.58%. Yield: 22%

Co(II)(Boa)(Piv)[12-$MC_{Co(III)N(Shi)}$-4](Morph)$_5$(MeOH) (5)

2-Benzoxazolinone (0.270 g, 2 mmol) and morpholine (0.784 g, 9 mmol) were dissolved in methanol (10 mL) and were added to a solution of [$Co(II)_2(H_2O)(Piv)_4(HPiv)_4$] (0.474 g, 0.5 mmol / 1.0 mmol based on cobalt) in methanol (10 mL). Salicylhydroxamic acid (0.230 g, 1.5 mmol) was dissolved in methanol (10 ml) and the solution was added to the reaction mixture. The resultant dark brown solution was stirred for 18 h at room temperature and filtered afterwards. Suitable crystals for X-ray structure analysis of **5**·3.5MeOH·H_2O were obtained from the filtrate by slow evaporation of the solvent after two weeks. For further analysis, the product was washed with cold methanol and dried under vacuum. Elemental analysis - Found: C, 44.58; H, 5.23; N, 8.47. Calc. for $C_{64.5}H_{94}Co_5N_{10}O_{26.5}$ (**5**·3.5MeOH·H_2O): C, 44.83; H, 5.48; N, 8.11% Yield: 55%

Co(II)(Piv)$_2$[12-$MC_{Co(III)N(Shi)}$-4](Py)$_6$ (6)
(Co(II)Co(III)(Py)$_3$(Piv)$_2$)Co(II)(NO_2)(Piv)(Shi)[12-$MC_{Co(III)N(Shi)}$-4](Py)$_4$ (7)

A solution of salicylhydroxamic acid (0.077 g, 0.5 mmol) in methanol (10 mL) was added to a mixture of [$Co(II)_2(H_2O)(Piv)_4(HPiv)_4$] (0.474 g, 0.5 mmol / 1.0 mmol based on cobalt) and methanol (10 ml). Pyridine (0.237 g, 3 mmol) was dissolved in methanol (10 ml) and the solution was added to the reaction mixture. The resultant dark brown solution was stirred for 18 h at room temperature and filtered afterwards. Suitable crystals for X-ray structure analysis of both products as **6**·2.75 MeOH and **7**·5.5MeOH·H_2O evolved simultaneously and with similar shape from the filtrate in the course of the slow evaporation of the solvent after one month.

Co(II)(NO_2)(Piv)[12-$MC_{Co(III)N(Shi)}$-4](Pic)$_6$ (8)

A solution of salicylhydroxamic acid (0.077 g, 0.5 mmol) in methanol (10 mL) was added to a mixture of [$Co(II)_2(H_2O)(Piv)_4(HPiv)_4$] (0.474 g, 0.5 mmol / 1.0 mmol based on cobalt) and methanol (10 ml). 3-Picoline (0.273 g, 3 mmol) was dissolved in methanol (10 ml) and the solution was added to the reaction mixture. The resultant dark brown solution was stirred for 18 h at room temperature and filtered afterwards. Suitable crystals for X-ray structure analysis of **8**·5.75MeOH were obtained from the filtrate by slow evaporation of the solvent. For further analysis, the product was washed with cold methanol and dried under vacuum. Elemental analysis - Found: C, 51.19; H, 4.65; N, 9.53. Calc. for $C_{70}H_{71}Co_5N_{11}O_{17}$ (**8**·1MeOH): C, 51.48; H, 4.38; N, 9.43% Yield: 28%

3.5 Results and Discussion

For simplicity, the results and discussion will be referred to the cobalt complexes with their associated number codes in spite of additional solvent molecules in the corresponding samples as they represent the central subject of this article and account for the major source of response for most of the different applied characterization methods. Otherwise the solvents will be directly addressed in proper places. Information on the number of solvent molecules in the crystal structure and in the dried polycrystalline powder state which was the basis of all other analyses are available at the description of the synthetic procedure and the results of the elemental analysis in the experimental section.

3.5.1 Synthesis

As we had found a pathway to synthesize cobalt metallacrowns with salicylhydroxamic acid by treating $[Co(II)_2(H_2O)(Piv)_4(HPiv)_4]$ with this ligand and an additional amine, we obtained the first two examples **2** and **6** which featured very different structures in spite of the similar reaction conditions. Hence, we anticipated a rich chemistry for this class of novel compounds and continued our synthetic efforts by altering solvents and amine ligands. Moreover, we detected during the characterization of **6**, that the sample contained the byproduct **7** and were even able to determine the molecular structure of the later. Therefore, we managed to synthesize the nearly isostructural, pure compound **8** by replacing the pyridine with 3-picoline. Utilizing the combination of salicylhydroxamic acid, piperidine and cobalt pivalate in different ratios with acetonitrile as solvent, we obtained a most singular series of complexes **1**, **3** and **4** which roughly reflects the proportion of applied reactants within the supramolecular composition of the products (Fig. S1). However, **4** crystallized parallel to another byproduct for which only very bad X-ray diffraction data could be obtained indicating a cobalt 12-MC-4 molecular structure with coordinated pipderidine carbamate. The knowledge of the molecular structure of **4** was nevertheless of great value in the process of the sharpening of the synthetic focus because simultaneously with the growth of the variety the single-molecule magnetic of the metallacoronates was discovered. As this property was based on the central Co(II) guest ion and revealed to be highly sensitive to the shape of the coordination sphere of the later, its manipulation via the choice of suitable additives became the dominant motivation of synthesis. Here, the bridging 2-benzoxazolinonate ligand (Boa^-) in **4** as an unscheduled rearrangement product of salicylhydroxamic acid with a weakly binding carbonyl oxygen donor atom introduced the opportunity to enforce a distortion of the geometry by the insertion of an elongated bond. Its purposeful addition into later synthetic experiments yielded the complex **5** and marked the first successful targeted step to set up a tuning workshop for the magnetic properties of the encapsulated Co(II) guest ion at the core of the flexible cobalt metallacrown host.

The large number of incorporated rearrangement and decomposition products of salicylhydroxamic acid within its cobalt complexes represents a remarkable aspect concerning the synthesis. Besides the aforementioned 2-benzoxazoline, salicylic acid and nitrite anions were contained in the crystal structures of **3**·7MeCN, (**2**)$_3$·H$_2$Sal·2OCMe$_2$·H$_2$O and **7**·5.5MeOH·H$_2$O, **8**·5.75MeOH. Although all of these secondary supramolecular building units can be simply rationalized and similar findings are known from literature,[78,79] the frequency of their occurrence suggests the assumption that their evolution is promoted by the presence of the cobalt ions.

3.5.2 Crystal structures

The assignment of oxidation states was performed with the help of charge balance considerations, the comparison of bond lengths and angles as well as the evaluation of the octahedricity of the coordination spheres. A quantified confirmation of the respective results was accomplished by Bond Valence Sum (BVS)[80-82] and Continuous Shape Measures (CShM) calculations.[83–85] The BVS analysis was additionally used to determine the protonation state of the oxygen ligands in **1**·3MeCN.[86,87] Selected details about bond length, angles and the performed calculations will be given in the course of the discussion. A full summary of the crystallographic data and refinement parameter is also available as from the supplementary information (Tab. 1, 2).

The naming of the metallacrown compounds, the labelling of the orientation modes of the bridging ligands and the numbering of the atoms and ions, which is illustrated in the supplementary information, was carried out in the style of the established nomenclature.[50] Moreover, the distinction of a lower and higher priority face is also sometimes used for descriptions when the central Co(II) ion is displaced out of the least square plane of the cyclic host. Here, the side which faces the elevated guest ion is assigned to the higher priority. Furthermore, the ligands are classified concerning their function within the complexes (Fig. S2). The term “main ligand” refers to salicylhydroxamic acid and its trianion as it is essential for the formation of the charactistic constitution motif of the metallacrowns. “Bridging ligands” are simultaneously attached to a ring metal center and the Co(II) ion at the core of the complex whereas “secondary ligands” saturate the remaining binding sites at a single metal ion. All structures comprise disordered ligands and/or solvent molecules. These were treated via two-site models and in rare cases for pivalate ligands with a nearly circular distribution of the electron density of the tert-butyl group via three-site models with restrained distances and restrained or constrained anisotrpic displacement parameters (ADPs). The structure of (**2**)$_3$·H$_2$Sal·2OCMe$_2$·H$_2$O contains large cavities with diffuse solvent molecules which had to be treated partially by the SQUEEZE routine.[65] Carbon bond hydrogen atoms were in general located in calculated positions and refined according to the riding model. By contrast, nitrogen and oxygen bond hydrogen atoms of non-disordered ligands

apart from the water and hydroxid ligand in **1**·3MeCN were refined in the semi-free procedure according to the riding model. Non-carbon bond hydrogen atoms of solvent molecules were placed in calculated positions and their orientation was partially adjusted according to hydrogen bonding considerations.

General constitution motif of Co(II)[12-MC$_{Co(III)N(Shi)}$-4] coronates

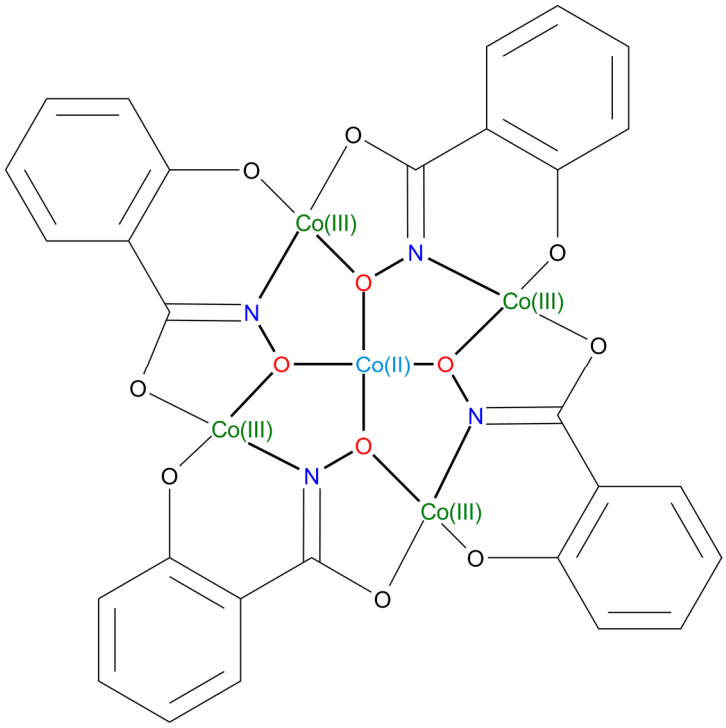

Scheme 1 General constitution motif of Co(II)[12-MCCo(III)N(Shi)-4] coronates; color code: green - Co(III), light blue - Co(II), red - O, dark blue - N, black - C

The constitution of the complexes **3, 4, 5, 6, 7, 8** features the classic 12-MC-4 motif with the regular, cyclic succession of the [M-O-N-] repetition unit which arises from the linkage of four Co(III) ions by four salicylhydroximate ligands (Shi^{3-}). Here, each of the four metal ions is coordinated by the hydroximate moiety of one main ligand and the iminophenolate group of the adjacent trianion forming a five- and a six-membered chelate ring (Scheme 1). As the cobalt ions of the cyclic host adopt the oxidation state of +III, their coordination spheres strictly obey octahedral geometry and the remaining two coordination sites are saturated by amines, methanol or anionic bridging ligands. By contrast, a Co(II) ion is chelated by the four inwards pointing hydroximate oxygen donor atoms at the core of the complex and its coordination sphere is strongly depending on the correlated interplay of the configuration of the cyclic scaffold, the type and the relative position of the bridging and secondary ligands. In respect of these features, the novel class of compounds reveals great differences from the salicylhydroxamic acid based metallacrowns known in literature. Due to this singularity and the tremendous

influence on the magnetic properties, these aspects will be discussed in detail for each complex below.

$[Co_5(Shi)_3(Piv)_5(Pip)_4(OH)(H_2O)]$ (1)

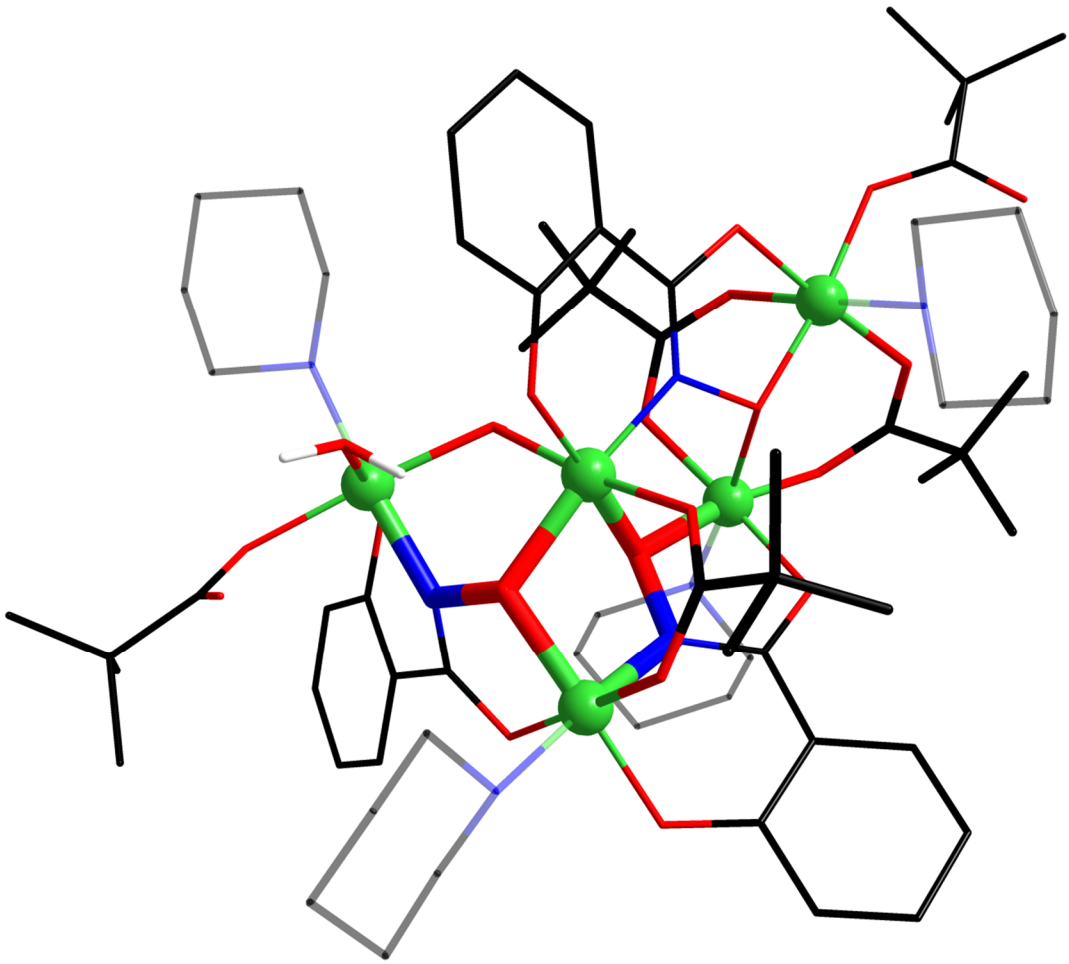

Figure 1 Molecular structure of **1;** color code: green - Co(III), red - O, dark blue - N, black - C

The molecular structure of **1** does not match the above outlined general motif of the cobalt metallacoronates in its full extent (Fig. 1, S3; Tab. S3, S4). However, it comprises a substructure with the constitutional features of a metallacrown fragment as well as an attached cobalt dimer that can be derived from the applied precursor compound. All contained cobalt ions adopt the oxidation state +III and their corresponding strictly octahedral coordination spheres contradict the asymmetric structure of the whole complex. The metallacrown fragment comprises the virtual guest ion Co4 and three ring metal ions Co1, Co2 and Co3, which are linked by two salicylhydroximate ligands in the normal metallacrown binding mode. However, they coordinate to the intermediate cobalt ion Co2 in cis fashion. Its remaining coordination sites are occupied by a piperidine ligand and a pivalate anion, which binds to the virtual guest ion Co4 via the second ox-

ygen donor atom. By contrast, the pivalate at the terminal end of the metallacrown fragment Co3 provides only one donor atom for a coordinative bond while the carbonyl type oxygen functions as acceptor atom in a hydrogen bond with a water ligand in cis position. Besides another piperidine ligand, a hydroxid ion additionally links the dangling tail of the ring with the virtual guest ion. Here, the assignment of the water O21 and hydroxid O20 ligand has been performed in respect of the coordination mode, bond lengths, hydrogen bonding considerations and the BVS calculations. The Co(III) ion at the opposite end of the metallacrown fragment Co1 is simultaneously involved in the reagent related dimer unit. Hence, it is bridged to a fifth cobalt ion Co5 via two pivalate ligands. The linkage between both assumed fragments is additionally promoted by another salicylhydroximate, which coordinates to the virtual guest ion Co4 via its iminophenolate and to the pheripheral metal center of the dimer via its hydroximate group. In analogy to the binding mode of the main ligand in the metallacrowns, the hydroximate oxygen donor atom also binds to the cobalt ion Co1, which participates in both subunits. Moreover the octahedral coordination sphere of the latter is completed by another piperidine molecule, while a pair of hydrogen bonded pivalate and piperidine ligands coordinates to the peripheral cobalt ion Co5. The complexes are closely packed in the bc plane, whereas the layers are separated by acetonitrile solvent molecules residing in the cavities of the interspace.

[12-MC$_{Co(III)N(Shi)}$-4](Py)$_8$ (2)

The asymmetric unit of (**2**)$_3$·H$_2$Sal·2OCMe$_2$·H$_2$O comprises three complexes [12-MC$_{Co(III)N(Shi)}$-4](Py)$_8$ **2** with identical constitution, pseudo-C_2 symmetry and chirality (Fig. 2, S4). Therefore, a general description of the general molecular structure is given at that point. Individual deviations in interatomic distances and angles are available from the supplementary information (Fig. S5, S6; Tab. S5-S10). The complexes can be classified as vacant reverse metallacrowns and consequently they do not obey the outlined general coronate pattern. The cyclic host is also composed by four Co(III) ions and four linking salicylhydroximate ligands. However, two of the main ligands bind with the same bidental moiety to each of the metal centres while both remaining coordination sites of the octahedrons are occupied by pyridine ligands. Therefore, the two cobalt ions on opposite sides of the metallacrown are involved in two five-membered chelate rings with the hydroximate moieties whereas the two other Co(III) ions are each coordinated by two iminophenolate groups forming six-membered chelate rings. Hence, [Co-O-N-] and reverse [Co-N-O-] repetition units alternate along the twelve-membered ring. Except for one Co(III) ion (Co2) with transoid arrangement of both iminophenolate moieties, all ring metal ions adopt the so-called propeller configuration with a cis orientation of the attached main ligands and can be assigned to the same chiral descriptor. Consequently, both salicylhydroximate ligands which connect the three centers of chirality are perpendicularly tilted out of the least square plane of the metal ions in

opposite direction. The configuration of the whole molecule adopts pseudo-C_2 symmetry and the corresponding pseudo-rotation axis defined by the position vectors of the two cobalt ions which participate in the six-membered chelate rings comprising the iminophenolate groups. Moreover, the overall shape of the metallacrowns is highly anisotropic even the least square plane of the metal ions as the average distance between the Co(III) ions on the pseudo-rotation axis accounts for 7.27 Å and 5.38 Å for the remaining pair of metal centers.

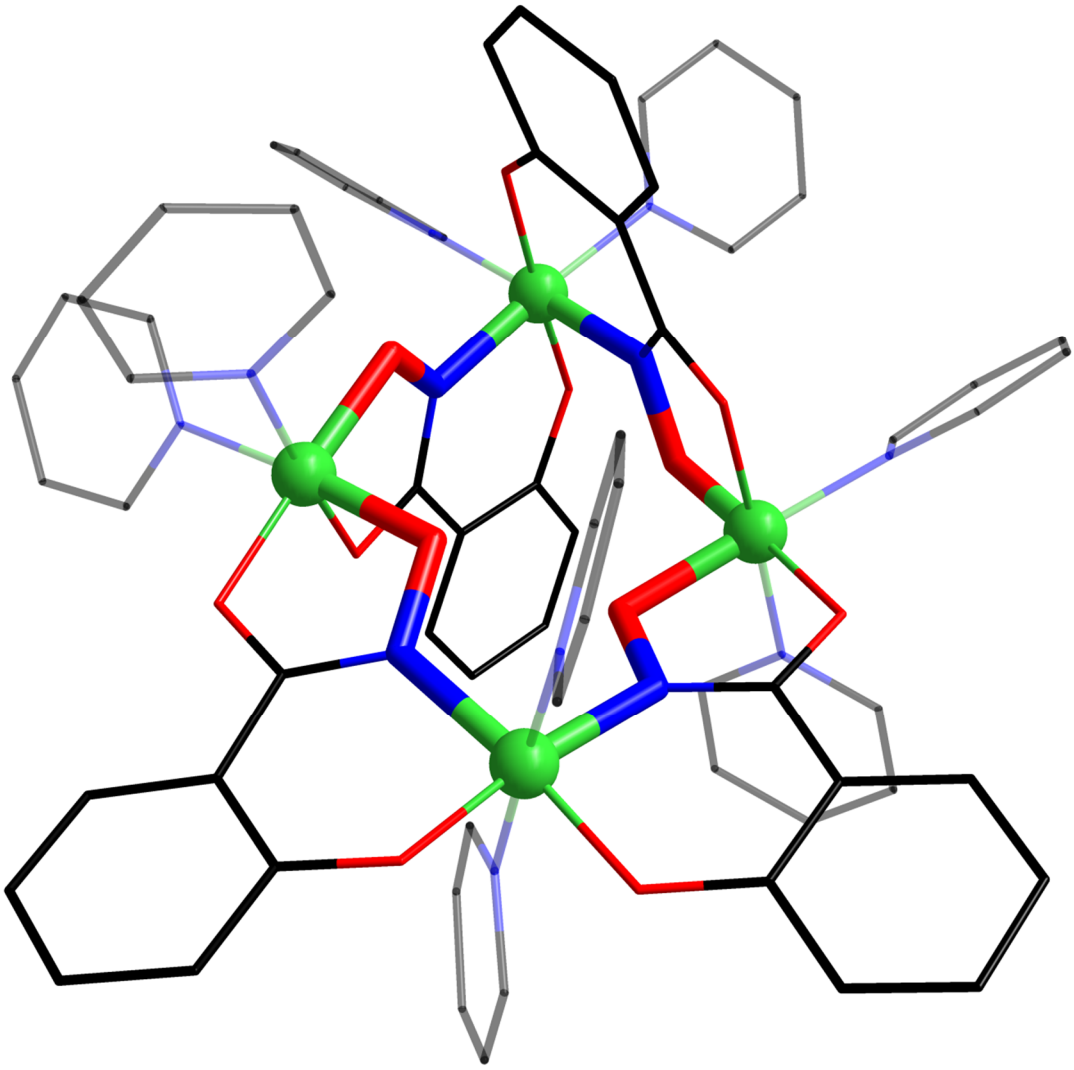

Figure 2 Molecular structure of **2;** color code: green - Co(III), red - O, dark blue - N, black - C

In the crystal structure of $(\mathbf{2})_3 \cdot H_2Sal \cdot 2OCMe_2 \cdot H_2O$, three of the individual but isostructural complexes are assembled around a water molecule in a star-shaped way. Here, the peripheral phenolate oxygen atoms at the Co(III) ions with planar configuration Co2 serve as acceptors of hydrogen bondings with the water molecule. The triades are

aligned to chains along the b direction via T-shaped π-π-interactions. These chains are stacked along the a direction and the resultant layers are packed along the c direction with further T-shaped π-π-interactions between the substructures. Acetone and salicylhydroxamic acid molecules reside in the space between the packed chains. Due to the diffuse solvent molecules in the large cavities especially between different stacks, the SQUEEZE routine had to be applied.[78] According to the elemental analysis, the found electron density and the size of the cavities, the content of the latter can be estimated as 13 acetone and 4 water molecules per asymmetric unit.

Co(II)(Boa)$_2$[12-MC$_{Co(III)N(Shi)}$-4](Pip)$_6$ (3)

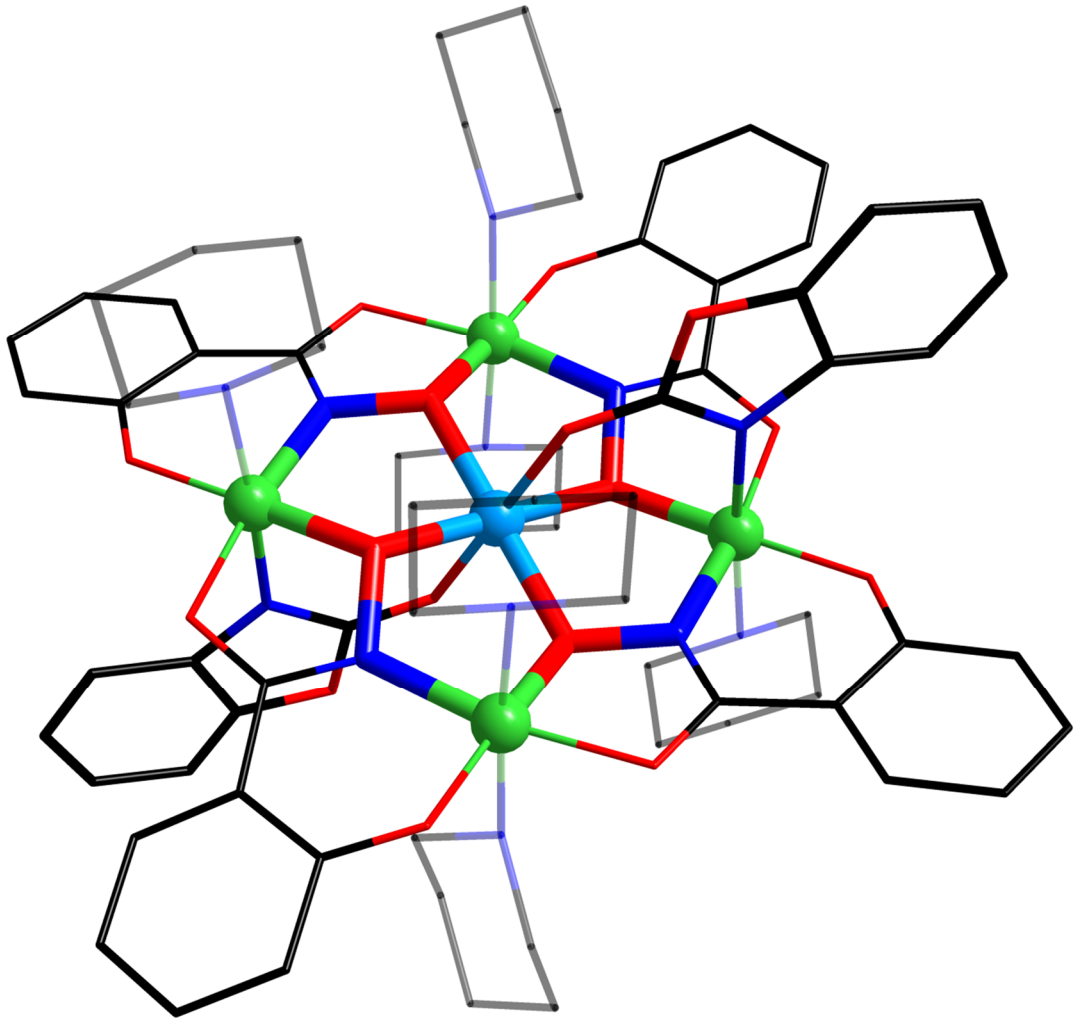

Figure 3 Molecular structure of **3;** color code: green - Co(III), light blue - Co(II), red - O, dark blue - N, black - C

The centrosymmetric molecular structure of **3** represents a regular 12-MC-4 metallacrown which matches the above described general constitution pattern (Fig. 3, S7; Tab. S11, S12). Moreover, the common all-planar arrangement of the salicylhydroximate

ligands is observed. Each of two 2-benzoxazolinonate ligands bind to a Co(III) ion Co1 on opposite sides of the cyclic scaffold via the amide nitrogen donor atom whereas the carbonyl oxygen atoms are coordinated to the Co(II) ion Co3 at the core of the complex. The remaining coordination sites of the octahedral coordination spheres of the metal centers in the ring are occupied by piperidine molecules. As the bridging ligands are attached to different faces of the metallacrown in a trans-anti mode, they reside on opposite vertices of the octahedral arrangement of donor atoms around the central Co(II) ion (Fig S8). The associated axis is significantly elongated because the Co(II)-O distance of the carbonyl oxygen atoms O7 amounts to 2.1771(18) Å whereas the corresponding values of the hydroximate oxygen donor atoms account for Co3-O1 1.9609(17) Å and Co1-O4 1.9409(17) Å, respectively. This finding is also reflected by the calculated high trigonal prismatic measure, which even exceeds with 16.53 the typical range for the coordination spheres of the Co(III) ions and means a coordinate on the shape map of octahedral versus trigonal prismatic measures that is characteristic for the elongation of an octahedron due to the Jahn-Teller effect.[85] Moreover, the elongated axis adopts a skew orientation towards the plane of the metal ions with an angle of 17.39(4)° towards a normal vector of the plane. Nevertheless, a small octahedricity measure of 0.319 is obtained because the two pairs of adjacent salicylhydroximate ligands are each tilted consensually above and below the plane of the cobalt ions with their hydroximate oxygen atoms residing on the corresponding opposite face of the metallacrown. The shape of the basic structural motif can therefore be attributed to the so-called “sofa” configuration.[54]

The complexes in the crystal structure are packed towards layers along the a+b plane and the acetonitrile solvent molecules occupy the remaining cavities in between.

(HPip)(Piv)[Li[Co(II)(μ_2-Piv)$_2$(Piv)[12-MC$_{Co(III)N(Shi)}$-4](Pip)$_5$]]$_2$ (4)

The molecular structure of **4** comprises two inversion-symmetric regular 12-MC-4 metallacrown subunits with the outlined general basic constitution which are connected via a pivalate anion (Fig. 4, S10, S11; Tab. S13, S14). Interacting via hydrogen bonding with the anionic linker, a piperidinium cation preserves the charge balance of the neutral supramolecular structure. Besides two bridging pivalate ligands, each coronate binds another pivalate supporting the peripheral complexation of a lithium ion as anchor for the aforementioned carboxylate linker between the two subunits. The remaining sites of the octahedral coordination spheres of the Co(III) ions in the cyclic scaffolds are saturated by piperidine ligands. Coordinating two adjacent metal ions Co1 and Co2 of the characteristic ring, the two bridging pivalate anions adopt a cis-syn configuration. The associated Co(III) ions are linked by a hydroximate ligand (O1, O2, O3, N1) which is tilted perpendicularly below the face of highest priority and therefore both reveal propeller configuration obeying the same chirality descriptor. Proceeding along the M-O-N

direction, the peripheral phenolate O6 and carbonyl oxygen O8 donor atoms of the adjacent cobalt ion Co3 in the ring additionally bind the attached lithium ion. Moreover, the supplementary pivalate ligand at the face of higher priority bridges the transition and the alkali metal ion. As the two main ligands at the Co(III) ion Co3 are arranged in a transoid orientation, its chirality is attributed to the opposite descriptor of the previous centers Co1 and Co2. Following the taken path around the cyclic host, the linking salicylhydroximate causes a planar configuration of the next trivalent cobalt ion Co4 by an in plane coordination of its iminophenolate moiety (N3, O9) although the carbonyl oxygen O8 represents the vertex of octahedral coordination sphere of the previous Co(III) ion Co3 on the face of lower priority. In accordance with perpendicular (O1, O2, O3, N1) and partial (O7, O8, O9, N3) tilting of the two main ligands, the arrangement of the ring metal ions strongly deviates from planarity and adopts a butterfly-type shape.

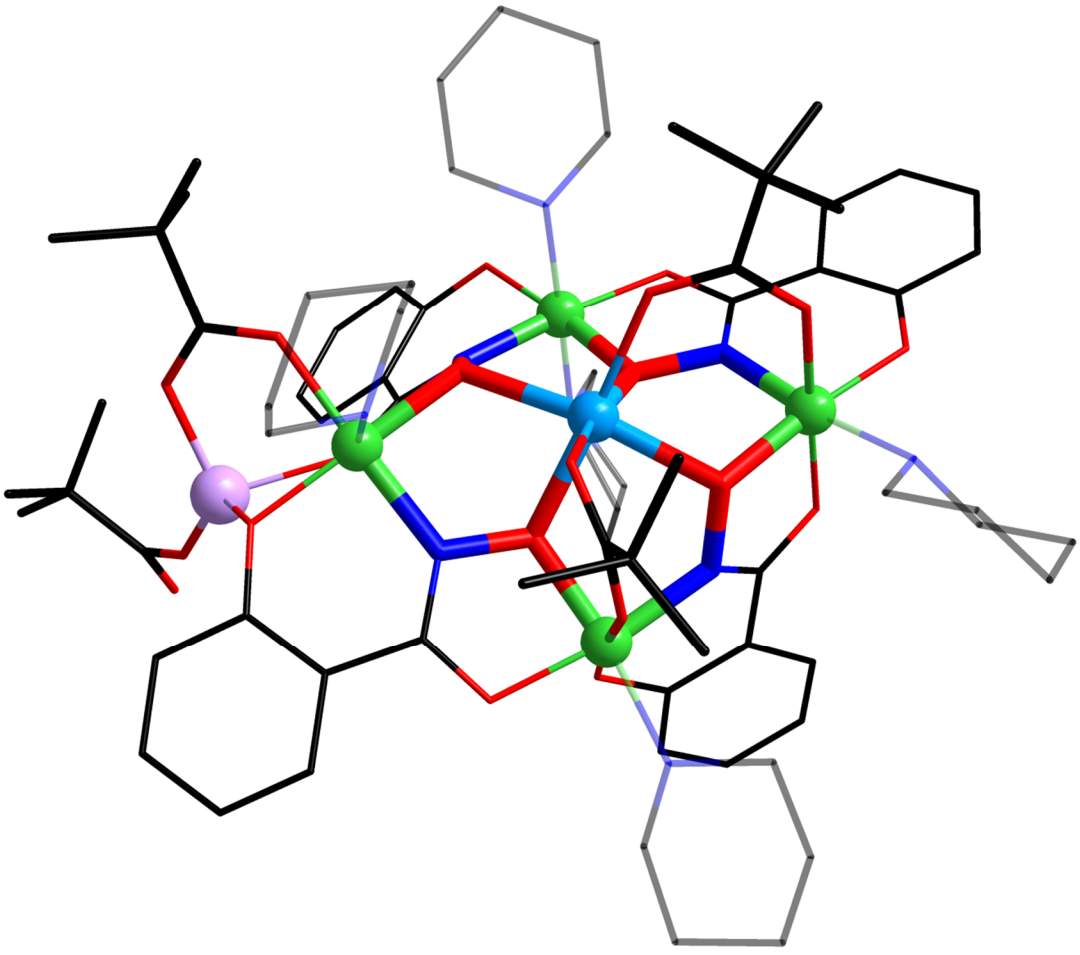

Figure 4 Metallacrown subunit in the molecular structure of **4**; color code: green - Co(III), light blue - Co(II), red - O, dark blue - N, black - C, violet - Li

Hence, the coordination sphere of the central Co(II) ion Co5 is best described as an octahedron but with significant unilateral distortion (Fig. 5). While all angles on one half

of the polyhedron differ only less than 9° from orthogonality, the vertex of the hydroximate oxygen donor atom of the partially tilted main ligand O7 is replaced from its ideal position and therefore gives rise to a pair of large (O7-Co5-O14 101.51(9)°, O7-Co5-O16 106.16(9)°) and smaller cis bond angles (O4-Co5-O7 77.73(9)°, O7-Co5-O10 81.63(9)°) whereas the trans trans angle of the corresponding axis is O1-Co5-O7 159.92(9)°. Moreover, the Co(II)-O distances which are involved in the resultant extended face of the octahedron exceed with Co5-O14 2.085 (3) Å, Co5-O 16 2.113 (3) Å, Co5-O7 2.185 (2) Å all of the remaining bond lengths within in the coordination sphere (Co5-O10 2.024 (2) Å, Co5-O4 2.040 (2) Å, Co5-O1 2.065 (2) Å). The continuous shape calculations support the approach to relate the geometry in a first approximation to the octahedron due to octahedral and trigonal prismatic shape measures of 1.671 and 10.721. However, the significant distortion is also depicted by a generalized coordinate of 30.8% along the minimum distortion interconversion pathway between both polyhedra.

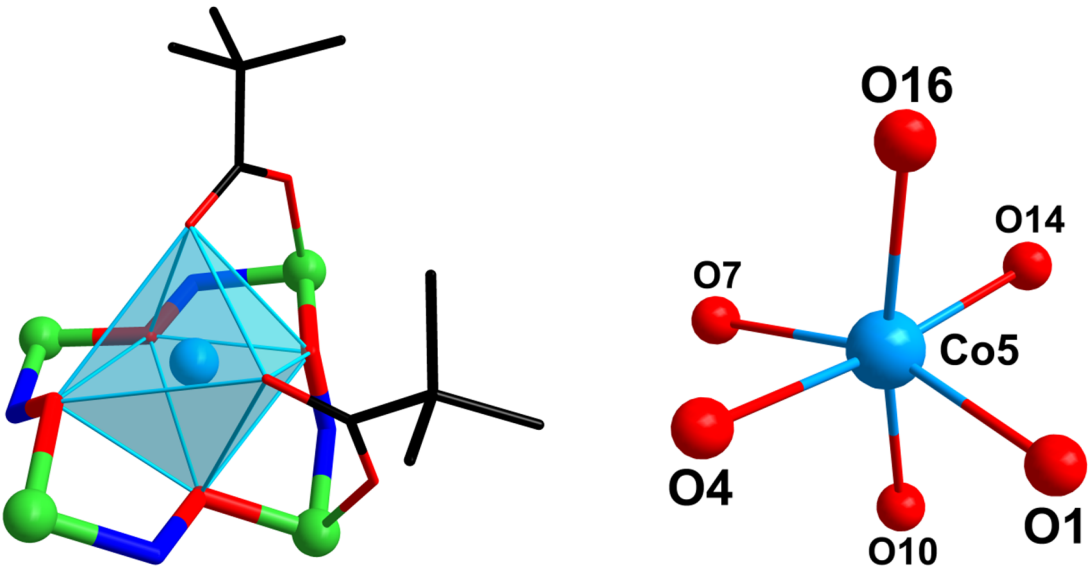

Figure 5 Coordination polyhedron (left) and coordination sphere (right) of the central Co(II) guest ion in **4**; color code: green - Co(III), light blue - Co(II), red - O, dark blue - N, black - C

In the crystal structure of **4**·3MeCN·H_2O, the supramolecular dimers are packed in layers in the a + b plane with Van-der-Waals interactions between the molecules. Along the c direction layers with opposite tilting angles of the complexes are stacked and acetonitrile solvent molecules occupy the cavities inbetween.

Co(II)(Boa)(Piv)[12-MC$_{Co(III)N(Shi)}$-4](Morph)$_5$(MeOH) (5)

The molecular structure of **5** also corresponds to the described general constitution motif of a regular 12-MC-4 metallacrown (Fig. 6, S12; Tab S15, S16). A 2-benzoxazolinonate as well as a pivalate ligand function as bridging ligands and are arranged in a syn-cis mode. Coordinating trans to the amide nitrogen with its carbonyl O2 and trans to the pivalate ligand with the phenolate O3 oxygen donor atom, the linking salicylhydroximate between the corresponding Co(III) ions Co1 and Co2 in the cyclic host is tilted perpendicularly towards the least-square plane of the ring metal ions. By contrast, the three other main ligands all coordinate in plane. The resultant propeller configurations are assigned to the opposite chirality descriptors. Following the cyclic host along the commenced direction, a methanol binds to the next trivalent cobalt ion Co3 whereas all remaining binding sites of the octahedral coordination spheres of the metal centers in the cyclic scaffold are occupied by morpholine molecules.

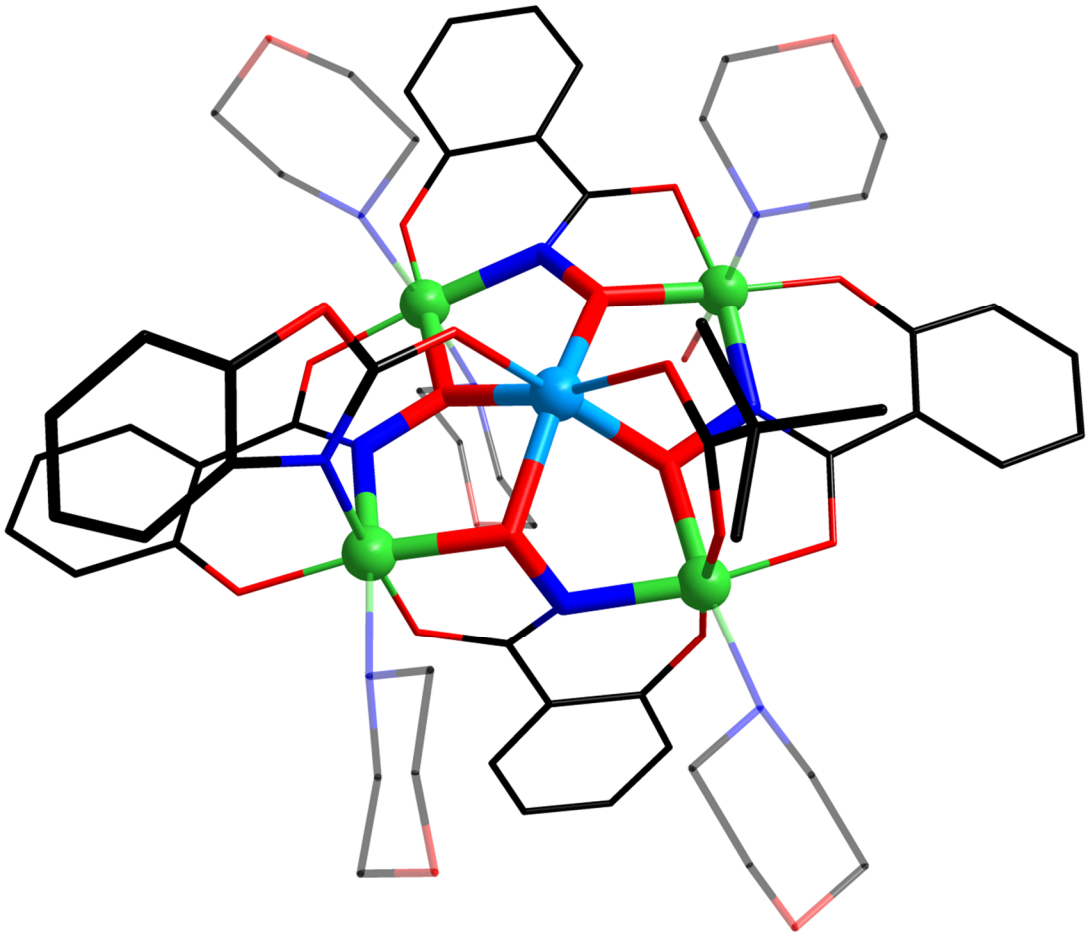

Figure 6 Molecular structure of **5**; color code: green - Co(III), light blue - Co(II), red - O, dark blue - N, black - C

The geometry of the coordination sphere of the elevated central Co(II) ion Co5 is still best described as octahedral in a first approximation(Fig. 7). But although the bond lengths of Co5-O1 2.062(2), Co5-O4 2.094(2), Co5-O7 2.056(2), Co5-O10 2.008(3), Co5-O13 2.112(3) and Co5-O16 2.066(3) Å are limited to a range of moderate extend and the largest interatomic distances belong to donor atoms on opposite vertices, a description as a (tetragonal) distorted octahedron hardly satisfies the actual shape. Consequently, the bond angles within the coordination sphere represent the reason of asymmetry because the values for adjacent as well as for opposite vertices strongly deviate from the ideal 90 and 180° and span large ranges of 76.11(9) - 113.23(10)° and 155.51(10) - 168.52(11)°, respectively. This issue is expressed by octahedral and trigonal prismatic shape measures of 2.935 and 7.750 as well as by the intermediate generalized coordinate for the minimum distortion interconversion pathway of 40.9%.

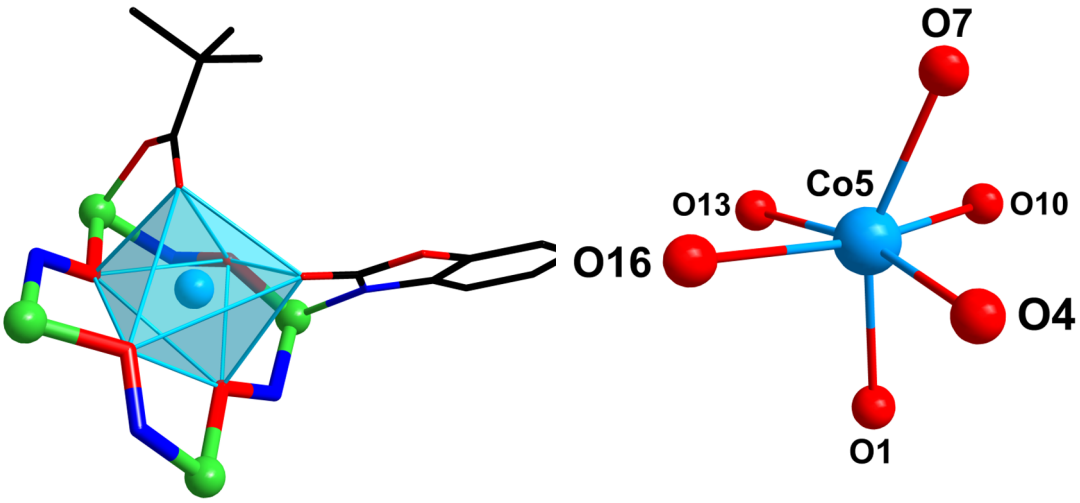

Figure 7 Coordination polyhedron (left) and coordination sphere (right) of the central Co(II) guest ion in **5**; color code: green - Co(III), light blue - Co(II), red - O, dark blue - N, black - C

In the crystal structure of **5**·3.5MeOH·H_2O the metallacrowns are packed in layers along the b + c plane which are stacked along the a axis. A network of methanol and water molecules resides in the cavities and links the clusters with each other by hydrogen bonding.

$Co(II)(Piv)_2[12\text{-}MC_{Co(III)N(Shi)}\text{-}4](Py)_6$ (6)

The arrangement of the cobalt ions and the salicylhydroximate ligands in this complex matches the described general 12-MC-4 pattern concerning its constitution and moreover resembles the configuration of **5**. Thus, one of the main ligand is tilted perpendicularly towards the least square plane of the ring metal ions while the remaining deprotonated moieties of salicylhydroxamic acid chelate the Co(III) ions in-plane trans orien-

tated to each other (Fig. 8, S13; Tab. S17, S18). The relative positions of the two pivalate bridging ions represents a trans-syn mode as one carboxylate binds to Co3 in trans position to the phenolate oxygen donor atom O6 of the tilted main ligand whereas the other pivalate is coordinated to Co1 on the opposite side of the metallacrown. The remaining vertices of the octahedral coordination spheres of the metal centers in the cyclic scaffold are occupied by pyridine ligands. Both centers of chirality Co2 and Co3 are assigned to opposite descriptors.

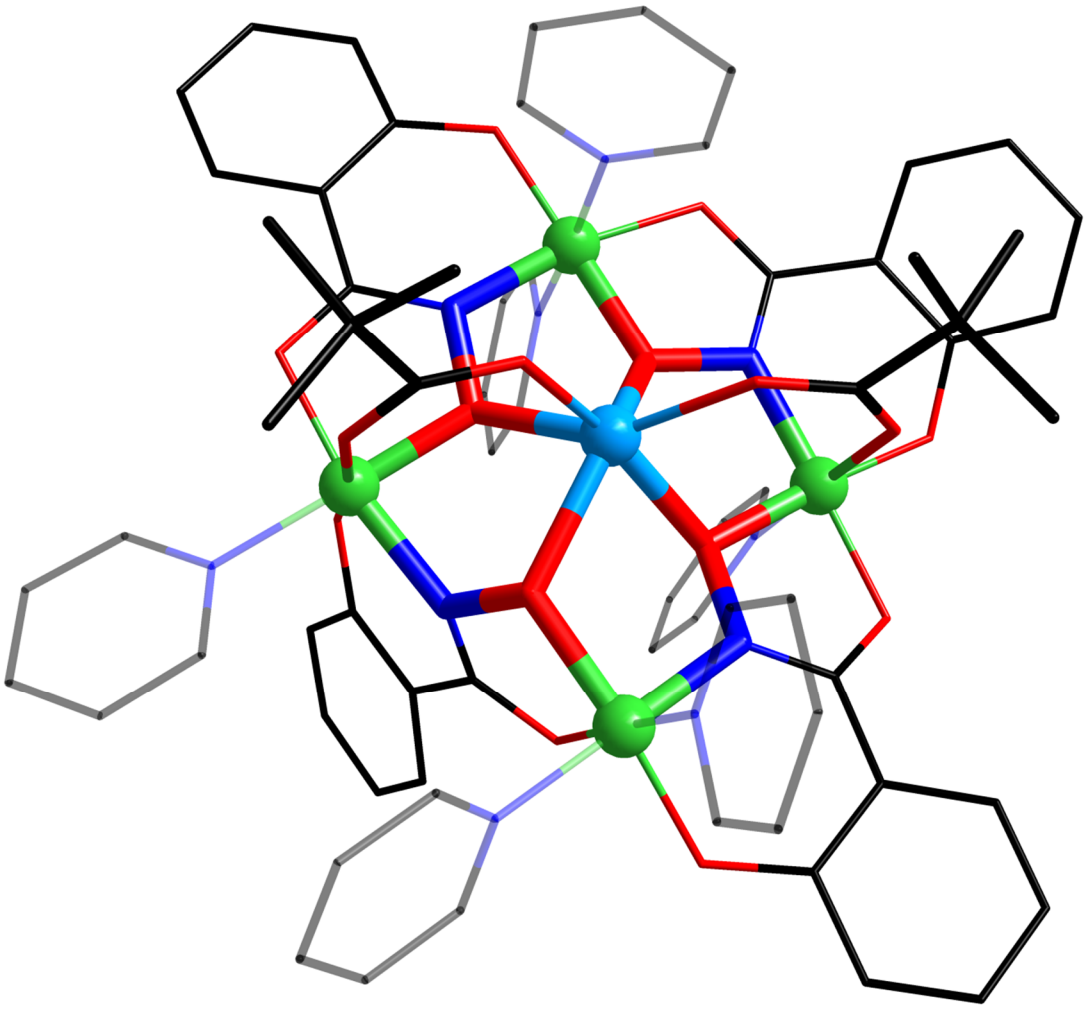

Figure 8 Molecular structure of **6**; color code: green - Co(III), light blue - Co(II), red - O, dark blue - N, black - C

Concerning the elevated divalent cobalt guest ion Co5 at the core of the coronate, all Co-O distances fall into a narrow range around an average value of 2.06 Å except for the slightly enlongated bond of Co5-O4 2.174(3) Å towards the hydroximate oxygen donor atom of the tilted main ligand (Fig. 9). Approaching a trigonal prism, the binding angles can be grouped into three different classes. For the six pairs of donor atoms which reside on same triangular faces of the prism (O1, O10, O14/O4, O7, O16), the

deviations from the ideal O-Co-O angle of 81.8° are found to be smaller than 7° with one exception of O10-Co5-O14 95.08(12)°. The same reference angle is valid for two oxygen atoms on opposite triangular faces sharing the same edge of a rectangular face. Here, the angle values amount to O7-Co5-O10 69.55(11), O1-Co5-O4 80.12(10) and O4-Co5-O7 85.27(11)°. By contrast, angles of remote vertices of O1-Co5-O7 108.35(11), O4-Co5-O14 118.62(12), O10-Co5-O16 125.40(12), O4-Co5-O10 137.19(11), O7-Co5-O14 153.61(13) and O1-Co5-O16 158.26(12)° are observed in comparison with 135.6° for the perfect trigonal prism. These parameters result in trigonal prismatic and octahedral shape measures of 2.941 and 7.823. Thus, they also confirm the present coordination sphere being closer to the general geometry of the trigonal prism than to an octahedron. Moreover, the data are tantamount with a 67.3% completeness of the interconversion along the minimum distortion pathway.

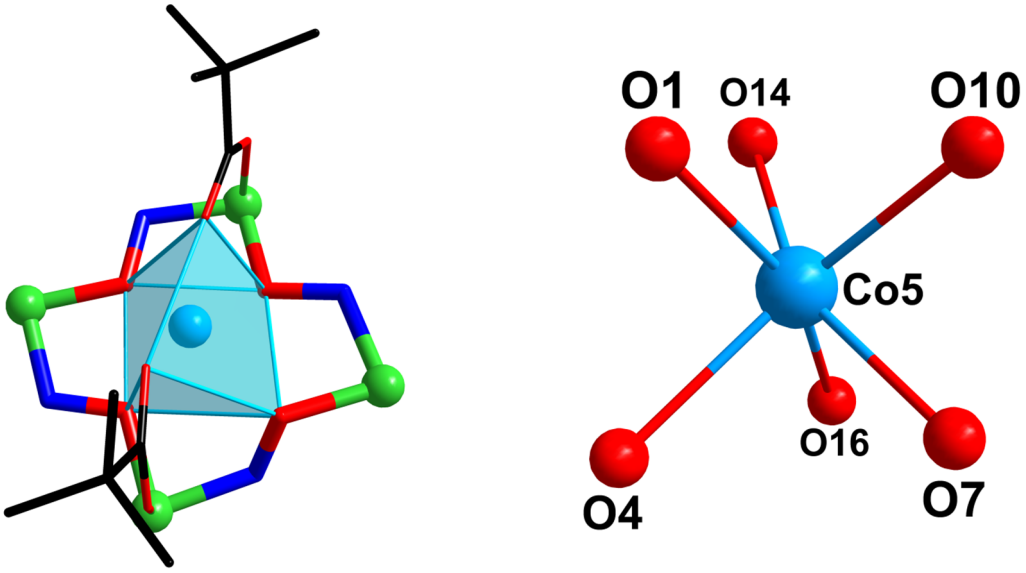

Figure 9 Coordination polyhedron (left) and coordination sphere (right) of the central Co(II) guest ion in **6**; color code: green - Co(III), light blue - Co(II), red - O, dark blue - N, black - C

The packing in the crystal structure of **6**·2.75 MeOH contains the arrangement of layered clusters in planes which are parallel to the one spanned by the a+c and b vectors but do not comprise the origin of the cell. The cavities between the layers are filled with methanol solvent molecules.

$(Co(II)Co(III)(Py)_3(Piv)_2)Co(II)(NO_2)(Piv)(Shi)[12\text{-}MC_{Co(III)N(Shi)}\text{-}4](Py)_4$ (7)

As the crystals of **7**·5.5MeOH·H_2O were obtained from the same reaction as **6**·2.75 MeOH, this pair of structures will be compared in the following. Moreover, correlations between the structural constitutions and configurations of **4** and **7** will be worked out

because both feature the peripheral complexation of an additional cation. Instead of the alkali ion and the pivalate linker, a heterovalent cobalt dimer is attached to the coronate with the support of a fifth salicylhydroximate. The 12-MC-4 subunit of **7** obeys the previously described general constitution pattern and reveals trans-syn arrangement of the bridging ligands in analogy to the molecular structure of **6**. Besides one pivalate ligand, a nitrite anion holds this function by coordinating with its nitrogen atom to the Co(III) ion Co1 of the ring and simultaneously binding with an oxygen donor atom to the Co(II) ion Co5 at the core (Fig. 10, S14; Tab. S19, S20). Therefore, the coordination sphere of the central guest ion is also better described as a trigonal prism rather than an octahedron.

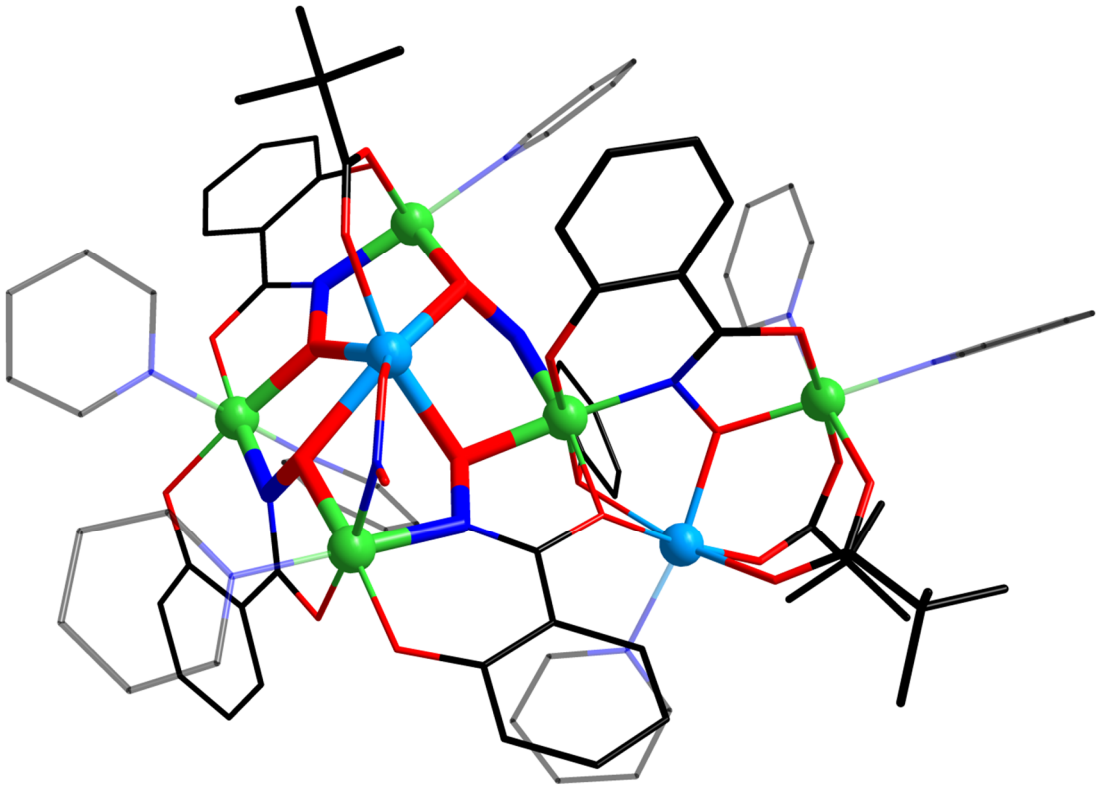

Figure 10 Molecular structure of **7**; color code: green - Co(III), light blue - Co(II), red - O, dark blue - N, black - C

The additional salicylhydroximate ligand forms a six-membered chelate ring including its iminophenolate moiety (O15, N5) and the associated trivalent cobalt ion Co4 of the metallacrown. Both attached phenolate oxygen atoms O9 and O15 are arranged in trans position to each other. The corresponding main ligand which participates in the characteristic cyclic motif of the metallacrown is therefore tilted perpendicularly to the least-square plane of the coronate metal ions. Furthermore, the resultant propeller configuration at Co4 is assigned to the opposite chirality descriptor as the neighbouring metal center Co1 along the M-O-N direction in the ring with the attached nitrite anion and the

second adjacent Co(III) ion Co3 which coordinates the bridging pivalate ligand. The fourth trivalent cobalt ion Co2 in the scaffold reveals a planar arrangement of the coordinating bidental moieties. Hence, the salicylhydroximate which connects it with the Co(III) ion Co1 binding the nitrite ligand features an in-plane coordination via its iminophenolate moiety (O3, N1) whereas the carbonyl oxygen donor atom O2 is attached at the minor priority face. Consequently, this ligand is partially tilted out of the least-square plane of the metal ions although the arrangement of the latter strongly differs from planarity. All remaining octahedral coordination sites of the trivalent cobalt ions in the metallacrown subunit are occupied by pyridine molecules.

The attachment of the heterovalent cobalt dimer involves a facial chelating of the Co(II) ion Co6 via the peripheral carbonyl O11 and phenolate O9 oxygens of the coronate and the hydroximate oxygen O13 of the auxiliary salicylhydroxamic acid trianion. Moreover, the latter also binds the Co(III) ion of the dimer Co7 with both oxygen donor atoms of its hydroximate moiety O13 and O14. In accordance with the oxidation state, the arrangement of the donor atoms around this remote metal center Co7 obeys strictly octahedral geometry. Two further pivalate ligands bridge the heterovalent metal centers Co6 and Co7 and pyridine molecules complete the six-fold coordination in each case.

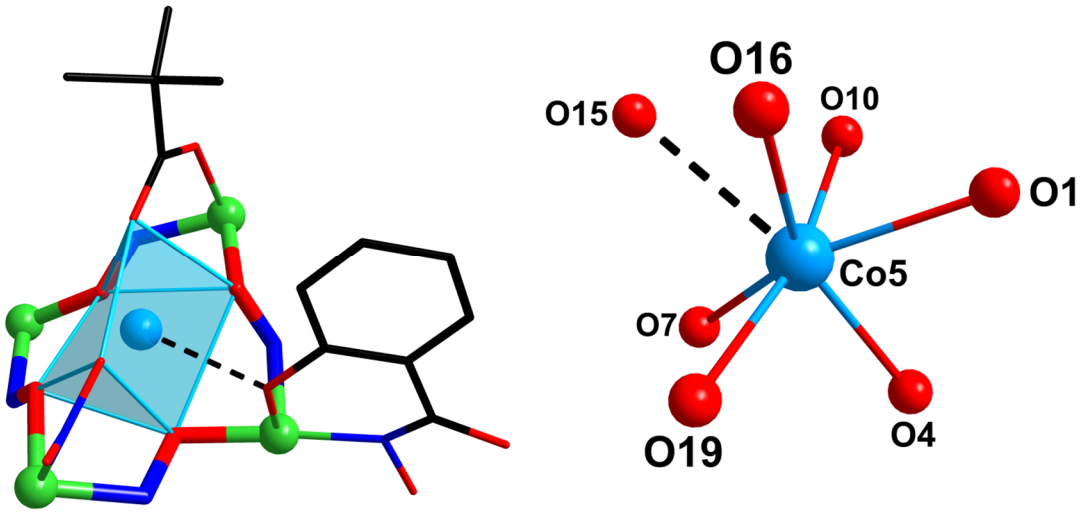

Figure 11 Coordination polyhedron (left) and coordination sphere (right) of the central Co(II) guest ion in **7**; color code: green - Co(III), light blue - Co(II), red - O, dark blue - N, black - C

Taking a closer look at the coordination sphere of the elevated Co(II) guest ion Co5 at the core of the conronate, some differences between the molecular structures of **6** and **7** can be observed although its geometry represents a distorted trigonal prism in both complexes (Fig. 11). In **7**, the average Co(II)-O bond length is slightly increased as the distance to the nitrite anion measures Co5-O16 2.183(3) Å and the other Co(II)-O bonds

on the same virtual triangular face of the trigonal prism are Co5-O1 2.168(2) and Co5-O10 2.104(2) Å. Besides the shortening of the bridging moiety relative to the carboxylate by one atom and the different binding properties of the nitrito ligand, the relatively short interatomic distance of 2.642(2) Å between the Co(II) ion Co5 and the phenolate oxygen O15 of the additional salicylhydroximate ligand represents an evident reason for these findings. The distribution of the value for the angles between the donor atoms of the same triangular face and the central metal ion is also broadened because three of them exceed the satisfied deviation threshold of 7° in **6** from the perfect value of 81.8° with O1-Co5-O10 76.37(8), O4-Co5-O19 89.09(9) and O10-Co5-O16 97.19(9)°. On the contrary, the angles of O1-Co5-O4 76.48(8), O16-Co5-O19 81.73(10) and O7-Co5-O10 89.20(8) for the edge sharing vertices of different triangular faces are in better accordance with the ideal value of 81.8° with a decreased standard deviation compared with the parameters of **6**. The angles for remote oxygen donor atoms however cover with O4-Co5-O10 100.13(8), O1-Co5-O19 116.39(9), O7-Co5-O16 133.63(9), O4-Co5-O16 141.03(10), O1-Co5-O7 150.82(8) and O10-Co5-O19 165.96(9)° a significantly enlarged range around the perfect value of 135.6°. The trigonal prismatic shape measure summarizes this set of parameters with an increased value of 4.077. Simultaneously, the only slight decrease of the octahedral shape measure reflects the broad distribution of the captured values and the resulting asymmetry of the coordination sphere. Thus, no generalized coordinate for the interconversion has been calculated because the deviation from the minimum distortion pathway as its reference exceeded the threshold of 10%.

The cluster in the crystals of **7**·5.5MeOH·H_2O are loosely packed towards straight chains along the a axis and zig-zag chains along the b axis. Large cavities between the compounds host methanol and water solvent molecules which interact with each other and the complexes via hydrogen bonds.

Co(II)(NO_2)(Piv)[12-$MC_{Co(III)N(Shi)}$-4](Pic)$_6$ (8)

In simplified terms, the molecular structure of **8** is obtained from complex **6** via the replacement of the pyridine by 3-picoline ligands and the substitution of one pivalate by a nitrite anion as already observed in the molecular structure of **7**.The constitution of the basic motif, the trans-syn arrangement of the bridging ligands, the perpendicular tilting of a single main ligand towards the minor priority face and the respectively opposite chiralty descriptors for the resultant propeller configurations are retained (Fig. 12, S15; Tab. S21, S22). The exchange of the bridging ligand here concerns Co(III) ion Co1 which adopts a planar configuration of its coordinated bidental moieties. In spite of the shortening of the bridging fragment by one atom relative to the carboxylate, the distorted trigonal prismatic coordination spheres of the central Co(II) ion of **6** and **8** strongly resemble each other. However, small modifications can be determined. The homogeneity in the bond lengths is slightly decreased, as the Co(II)-O distance of the nitrite ligand

accounts for Co5-O13 2.175(2) Å and the bond towards the tilted main ligand is still slightly elongated with Co5-O4 2.137(2) Å (Fig. 13). The pivalate ligand reveals a relatively shortened bond length of Co5-O16 2.008(2) Å.

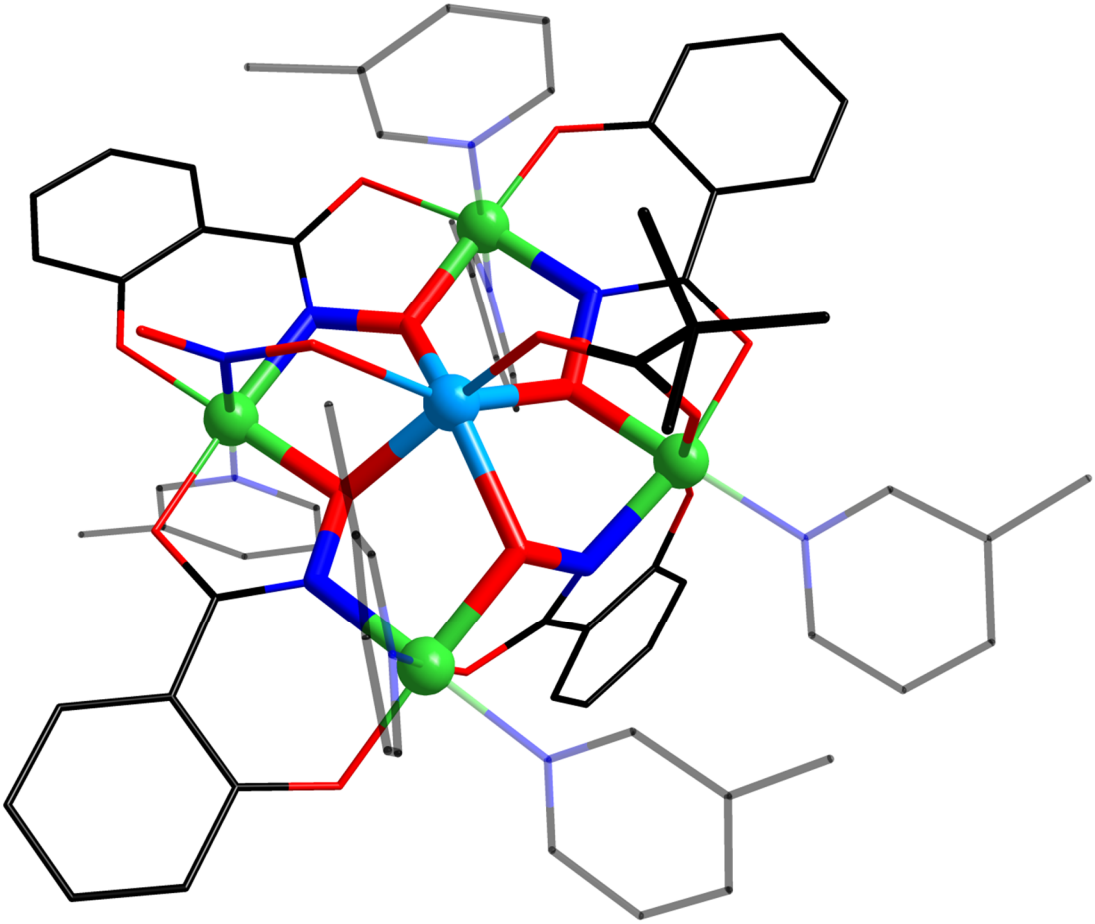

Figure 12 Molecular structure of **8**; color code: green - Co(III), light blue - Co(II), red - O, dark blue - N, black - C

In contrast to this, the bond angles are slightly better in line with the parameters of the perfect trigonal prism. So, the angles for the oxygen atoms within the same triangular face (O1, O10, O13 / O4, O7, O16) and the central Co(II) ion (O1-Co5-O10 77.93(8), O1-Co5-O13 79.96(8), O4-Co5-O7 85.21(7), O4-Co5-O16 88.06(8), O10-Co5-O13 88.65(8), O7-Co5-O16 90.00(9)°) are in better agreement with the ideal value of 81.8°. The same finding holds true for the donor atoms of different triangular faces with a common edge, which show values of O7-Co5-O10 71.75(8), O1-Co5-O4 81.83(8) and O13-Co5-O16 86.32(9)°. Moreover, the minimum and maximum deviation from the reference angle of 135.6° for the divided vertices is reduced in the series O1-Co5-O7 110.84(8), O4-Co5-O13 120.08(8), O10-Co5-O16 121.84(9), O4-Co5-O10 141.09(8), O7-Co5-O13 154.24(8), O1-Co5-O16 155.81(9)°. As the continuous shape measures calculations are more sensitive to the angles, the contradicting results of the bond

lengths and angles give rise to a slightly decreased trigonal prismatic shape measure of 2.902. The insignificantly reduced generalized coordinate of 65.2% for the interconversion pathway on the contrary arises from the simultaneous decline of the octahedral shape measure to 7.359 and the corresponding lower deviation from the minimum distortion pathway.

The complexes in the crystals of **8**·5.75MeOH are packed towards chains along the a axis by S- as well as T-type π- π interactions and by T-type π- π interactions along the b axis. The cavities within and especially in between the resultant layers host methanol molecules, which are linked by hydrogen bonds with each other but also with the clusters.

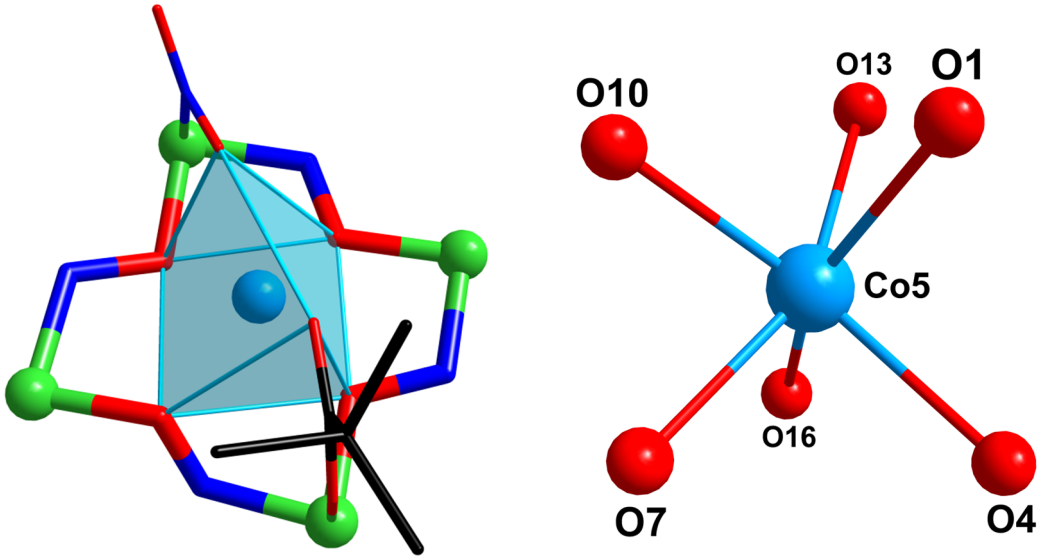

Figure 13 Coordination polyhedron (left) and coordination sphere (right) of the central Co(II) guest ion in **8**; color code: green - Co(III), light blue - Co(II), red - O, dark blue - N, black - C

General remarks concerning the molecular structure

In contrast to the wide-spread existence of metallacrowns based on metals across the periodic system of the elements and the concentrated occurrence of this cluster type for the adjacent 3d metals manganese, iron, nickel and copper, the metallacrown chemistry of cobalt is only very weakly developed. Besides some aza-derivatives,[88–92] just a few 9-MC-3 type and two examples of the same basic inverse 12-MC-4 type complex, which only differ in secondary structural features like the counterion and the residues of carboxylate ligands as well as encapsulated anions, have been hitherto reported. Not even any kind of cobalt complex and hence no metallacrown in particular is known for the pioneering ligand salicylhydroxamic acid in literature up to now although the accessibility of such a species has already been assumed in the early period of metallacrown chemistry.[63] The eight present examples provide a broad structural diversity and each

of these clusters reveals at least unusual or even hitherto unprecedented structural features for 12-MC-4 compounds. As some of these singularities are present in more than one compound and/or are worth to be discussed from a more comprehensive point of view, they have not been dealt with explicitly and set into the context of respective literature in the course of the individual description of the molecular structure.

Although, complex **1** does not obey the general metallacoronate pattern, it might in the style of the "collapsed" metallacrowns[93–98] be named a "nascent" metallacrown. This term however does not refer to an evolutionary view of the cobalt 12-MC-4 compounds but accounts for the fact that a metallacrown fragment can be recognized in the molecular structure as well as a pivalate bridged cobalt dimer, which can be related to the applied precursor compound.

Complex **2** features a vacancy of its core as well as the alternating reversion of the characteristic repetition unit along its cyclic scaffold. In this context, it is worth mentioning that the word "reverse" is here applied purposefully instead of "inverse", as the transposition of the sequences within the constitution of the metallacycle is often accompanied with the encapsulation of anions by the ring metal ions, which project into the central cavity in these cases. Therefore, the term "inverse" has especially been used to characterise the different configuration of the cyclic scaffold and only in second place to describe the changed constitution (Fig. S19).[99,100] So, the first two cobalt metallacrowns were reported as inverse species because they simultaneously reveal the reverse succession and host two anions in central cavity.[60,61] The inverse structures frequently occur for the ligand bis-2-pyridyl ketone oxime for which several mixed ligand clusters with only participation of salicylhydroxamic acid are also known.[56,100-103] However, neither a vacant nor a reverse and/or inverse metallacrown based on the latter ligand have been described in literature for a transition metal yet. Indeed, vacant tin 12-MC-4 compounds have been published which also comprise two perpendicularly tilted main ligands.[104]

The tilting of the main ligands and the corresponding presence of chiral centers with a propeller configuration of the ligands represents a recurring motif for the here described compounds. Apart from **3**, all metallacoronats feature at least one perpendicularly tilted salicylhydroximate ligand. **4** as well as **7** furthermore comprise a particularly tilted one. By contrast, the bidental coordination occurs in-plane and in trans position to each other for the reported transition metal 12-MC-4 metallacrowns of this main ligand.[52,54–59,105,106] The singularity of this structural feature in combination with its numerous presence among the members of this novel class of compounds suggests a causality, which will be discussed.

The great variety of the cobalt metallacrowns regarding the arrangements of the bridging ligands is remarkable as well. The trans-anti mode which is realized in **3** is in general quite rarely observed for 12-MC-4 complexes[101,107–109]and only one description of

a corresponding salicylhydroxamic acid based iron compound is known to date.[53] Moreover, the cis-syn orientation in **4** and **5** was hitherto reserved for a few 12-MC-4 clusters of salicylhydroximate linked trivalent manganese ions which are partly bridged with two alkali ions above and below the actual core of the complex via single, shared donor atom.[55,57] On the contrary, the trans-syn arrangement in **6**, **7** and **8** represents a widely spread motif in literature.[52,56,59,102,103,106]

The possibility of a peripheral, multidental complexation of additional cations presented in **4** and **7** is a further interesting aspect of the cobalt metallacrowns. In general, the majority of 12-MC-4 metallacrown in literature with further attached metal ions to the main ligands of the basic motif are comprised of divalent transition metals ion. While the linkage via a single donor atom is especially known for copper compounds,[110,111] a fused Ni(II) based structure[56,101,102,105] has been observed besides some stacked Cu(II) metallacrowns[112–114] as examples for additional binding of cations above or below the faces. The chelating of metal ions via the peripheral donor atoms in the style of a multidental supramolecular ligand is for instance evident for a zinc metallacrown,[100] a terbium centered zinc metallacryptand,[115] a nickel metallacrown,[116] a family of Ln_8 clusters with a metallacrown core structure[117] and some copper metallacoronates.[54,118,119]

The latter property represents a suitable entrance into the discussion about the reasons for the indicated most singular features of the discovered novel class of cobalt metallacrowns. Analyzing the high frequency of divalent metal ions in expanded coronates, the four key factors negative excess charge, lower local positive charge, flexibility of the coordination number and versatility of the structural configuration can be deduced. The influence of the flexible modification of the molecular configuration on the attachment of cations can be evidently recognized via a comparison of the crystal structures of Cu(II)[12-$MC_{Cu(II)N(Shi)}$-4] compounds. In all cases, the size of the central cavity is enlarged via a slight tilting of the ligands out of the least-square plane of the ring metal ions in order to fit the dimensions of the Cu(II) guest ion. While low interactions with the counter ions causes an opposite tilting of two pairs of adjacent ligand in a “sofa” configuration, a domed shape of the molecule is obtained when the cations are chelated at the periphery.[54]

By contrast, the positive high local and excess charge of the basic constitution pattern in combination with the general need for higher coordination numbers foster the binding of further, partially anionic and/or bridging ligands at the faces of metallacoronats based on trivalent ring metal ions. These hamper the direct access to the donor atoms from the faces and especially rigid bridging ligands reduce the flexibility for the adaption of peripheral sets of binding sites towards possible acceptors of coordinative bonds. Moreover, the attachment of cations in proximity to highly positive charged metal centers is disfavoured due to the Coulomb repulsion. The reason for the unexpectedly distinct ability for peripheral complexation of additional metal ions seems to be closely related

to the phenomenon of the tilted salicylhydroximate ligands, as both features occurred in the molecular structures of **4** and **7** at the same Co(III) ion of the cyclic host. Here, the distance between the carbonyl and the phenolate oxygen as well as the corresponding bite angle of the cobalt coronate as supramolecular ligand is decreased. Hence, the repulsion of the positive charged ring metal ion and the attached cation is reduced by a enlarged distance from each other and the proximity of counter (partial-) charges to the shortest interaction pathway. An additional anionic ligand supports the latter effect and increases the chelat effect of the coordinated moieties. Moreover, the tilting of a main ligand represents the precondition for the cis-syn bridging mode in **4** and **5** as it induces a deformation of cyclic scaffold via an offset of the Co(III) ions and therefore facilitates a sufficient spatial distance of the inner donor atoms of the three-membered linking moieties. Consequently, the two bridged Co(III) ions are linked via a perpendicularly tilted salicylhydroximate ligand in both cases of **4** and **5**. These explanations however directly lead to the question of the reason for the unique flexibility of the arrangement of the main ligands which seems to contradict the strictly octahedral shape of the coordination spheres at the first sight. Actually, both findings share the same origin in the d^6 electronic configuration of the Co(III) ions. The corresponding low-spin configuration yields the maximum stabilization energy for an open d-shell with given octahedral ligand field splitting and features a non-degenerated ground state. Hence, there is ab inito no reason for an energetic disparity of the different binding sites at the Co(III) ion, whereas the Jahn-Teller effect obviously creates a preference of a transoid in-plane coordination of the strongly binding moieties of salicylhydroximate towards Mn(III) and Cu(II), which are to date the most common ring metal ions in 12-MC-4 complexes of this main ligand. Consequently, the possibility for the out-of-plane linkage of the ring metal ions in the cobalt metallacrowns by salicylhydroximate can be rationalized by the fact that there is in first approximation no preference of any pair of the adjacent sites on the vertices of the octahedron. Therefore, the flexibility of the cyclic host arises in simplified terms from the choice of the binding sites but not from the versatility of their relative positions concerning the metal center. The central Co(II) guest ion on the contrary variably adopts different and asymmetric coordination spheres and thus represents the second key to the flexibility of molecular configuration. However, the quest for reasons for the frequent use of these degrees of freedom and the shape of the final results seems to be more complex and its eventual accomplishment might require elaborate theoretic calculations. The variety of structures in spite of the presence of similar reactants already suggests that several different influences might be involved in the shaping of the molecular configuration and that the preference among the different shapes is low. Besides packing effects, electronic, sterical and geometrical influences within in the complex can be taken into account. However, only some of them which appear to be of increased importance will be discussed in more detail. The strong affinity towards a strictly octahedral arrangement of the donor atom Co(III) ions might here also play a

crucial part in the interaction of different influences. It is worth mentioning in that context, that the octahedricity of the cobalt centers with propeller configuration in the metallacoronates with tilted ligands is always greater than of the corresponding in-plane coordinated Co(III) ions. Here, the deviations from the perfect geometry which mainly arise from the low bite angle of the hydroximate group can be compensated more easily by the flexible positioning of the monodentate ligands in the cis orientation. In order to preclude additional sources of strain, the bridged metal ions have been considered in this inquiry. But not only the local effect of the tilting shall be considered but also the influence on the whole assembly might be relevant. So, the rigidity of the coordination geometry might cause a certain degree of ring strain which can be diminished by the incorporation of at least one tilted main ligand into the cyclic scaffold. Although the molecular structures of the present work clearly state the enormous versatility of the central Co(II) ion to adopt different shapes of its coordination geometry, the elevation of the hydroximate oxygen which is implied in the tilting of a main ligand might give a significant contribution to the interplay of influences. The crystal structure of **3**·7MeCN proves the possibility to host the Co(II) guest ion in the actual core of the complex. However, several parameters indicate why this solution is already avoided under slightly different reaction conditions and an out-of-plane coordination is realized in most of the examples. Concerning the Co(II) ion Co3, the axially elongated octahedron with shortened bond lengths in the perpendicular plane represents a quite uncommon setting. Although the parameters might indicate a strong distortion due to the Jahn-Teller effect which is typically observed for Co(II) low-spin complexes, the absence of strongly splitting ligands contradicts this assumption. Instead, the findings seem to be a combination of the weak coordinative properties of the carbonyl oxygen of 2-benzoxazolinone and the limited size of the central cavity. The extraordinarily high octahedral and low trigonal prismatic shape measures of 0.804 and 11.845 for the Co(III) ion Co2 which joins the pairs of oppositely tilted main ligands of the “sofa” configuration suggest in that respect severe obstacles towards a further expansion of the arrangement of donor atoms for this molecular configuration via the tilting of the main ligands. Hence, the trigonal prism represents the simplest counterdraft for a planar cobalt metallacrown with six fold coordination of the elevated Co(II) guest ion as it is observed in the similar case of $Mn(II)(RCOO)_2[12\text{-}MC_{Mn(III)N(Shi)}\text{-}4]$ complexes. Nevertheless, even the cobalt coronates **6**, **7** and **8** with a syn-trans orientation of the bridging ligands contain at least one perpendicularly tilted main ligand. Simultaneously, one of the hydroximate oxygen donor atoms is significantly displaced above the least square plane of the characteristic ring although simple geometric calculations confirm the suitability of the observed range of Co(II)-O bond lengths and the edge length of the hypothetical square arrangement of the inner donor atoms of the cyclic host for the construction of a perfect trigonal prism (Fig. S18). The cause of the avoidance of this ideal geometry might hence be based on its general disadvantageous less convenient splitting of the energy levels of d-

orbitals for the d^7 configuration and a spatial imbalance of the negative charges within the coordination sphere. In that respect, the proximity of the phenolate oxygen of the additional salicylhydroximate in **7** can be interpreted. An analogue increase of the coordination number via a third bridging ligand or the expansion of the ring size by one repetition unit is observed for the manganese metallacrowns. The latter effect is yet always found in combination with the application of aromatic nitrogen ligands. This example furthermore indicates the pronounced importance of the bridging and secondary ligands concerning the constitution and configuration of the metallacrown via their electronic and/or steric influence. For instance, the tilting of the main ligand is accompanied by a deflection of the axis of the octahedron which corresponds to the carbonyl oxygen atom from orthogonality towards the least-square plan of the ring metal ions and therefore the proximity of the secondary ligand in trans position towards the other ligands at the same face is reduced. Additionally, an interaction of the secondary and bridging ligands with each other via hydrogen bonds could be observed in the cases of the incorporation of cyclic aliphatic amines. In the special case of the vacant metallacrown 2, the unshielded Coulomb repulsion between the hydroximate oxygen atoms due to the absence of a central counter charge serves as a probable motivation to avoid planarity.

While the application of ambident bridging ligands for the deformation of coordination polyhedron of the Co(II) guest ion has already been successfully applied, the suitability of the periphaeral complexation of cations for the shaping of the cobalt metallacoronates can be deduced from the present examples. By contrast, the relevance of other effects can only be estimated on the basis of this compilation. The detailed investigation of the relative importance of the different influences represents an interesting issue for further experimental and theoretical research. It will help to gain the precision for the targeted modification of the coordination sphere of the central Co(II) ion via the application of peripheral complexation, secondary, bridging and modified main ligands as synthetic tools for the adjustment of its magnetic properties.

3.5.3 Infrared Spectroscopy

All recorded infrared spectra of the isolated complexes **1**, **2**, **4**, **5** and **8** contained a strong band between 1594 and 1598 cm^{-1} which has been assigned to the stretching vibration of the C=N bond of the salicylhydroximate ligand. Moreover, the corresponding second characteristic band for the N-O stretching vibration has been observed for all clusters except for **2**. However, this deviation is in accordance with the difffernt non-bridging binding mode of the vacant metallacrown. Correspondingly, a shift of this band has also been detected in the vacant tin metallacrowns of salicylhydroximate. Another set of strong bands at 1573-1580 cm^{-1} and 1438-1450 cm^{-1} represents the asymmetric and symmetric stretching vibrations of the carboxylat groups within the compounds. Further bands in the characteristic range of the carbonyl stretching vibrations at 1711

and 1658 cm^{-1} in the spectra of $(\mathbf{2})_3 \cdot H_2Sal \cdot 2OCMe_2 \cdot H_2O$ and $\mathbf{5} \cdot 3.5MeOH \cdot H_2O$ arise from acetone solvent molecules and the 2-benzoxazolinone bridging ligand.

3.5.4 UV-Vis Spectroscopy

The recorded electronic spectra of **1**, **2**, **4**, **6** and **8** resemble each other in their general shape and simultaneously reflect the closer structural relationship between the three Co(II) centered metallacoronats **4**, **6** and **8** although the features are primarily assigned to absorption process which are locate at the Co(III) ions and/or the ligands (Fig. S20; Tab. S44). Apart from one local maximum, the different transitions only appeared as less distinctive shoulders due to the plurality of individual coordination environments within the single complexes. Hence, the characteristic wavelengths were extracted from the obtained data via inflection point analysis using the first and second order derivations. The spectra of **1**, **4**, **6**, **8** each reveal shoulders in the ranges of 325-333, 470-486 and 635-649 nm whereas **2** in principle shares the same sequence of features (337, 423, 616 nm) with a slight blueshift of the wavelength in the visible region. Here, an assignment of the two respective features with lowest energy to d-d transitions from the $^1A_{1g}$ ground state into the excited states of $^1T_{1g}$ and $^1T_{2g}$ term of the Co(III) ions is in good accordance with the related example of a mononuclear trivalent cobalt compound based on benzhydroximate in literature.[120] However, it should be mentioned that the obtained spectra represent a superimposition of the different contributions of the absorption processes located at specific metal centers. Hence, a generalized model might omit hidden features and can be less appropriate for the electronic structure of at least some of the individual cobalt ions. An alternative general interpretation which ascribes the presence of both aforementioned bands to a splitting of the $^1T_{1g}$ terms and includes the infliction point in the near UV-region as a d-d transition between the $^1A_{1g}$ and $^1T_{2g}$ state has been discarded for several reasons.[121,122] The proximity of the ligands within the spectrochemical series in combination with the variety of their relative arrangements in the coordination spheres of the Co(III) ion in the same sample contradicts the corresponding dimension of the assumed splitting. Moreover, the accordance of the absorption feature of **2** and the other complexes around 330 nm suggests an involvement of the salicylhydroximate in the transition rather than a pure localization on the Co(III) ions. A definitive assignment towards a charge-transfer or intraligand band cannot be performed on the basis of the present information. However, the occurrence of absorption characteristics for salicylhydroxamic acid based metallacrowns of different metals like nickel, manganese and copper as well as the energetic proximity of the first absorption maximum of the free ligand supply the latter assumption. Moreover, the spectra weakly indicate another infliction point at 261 nm which represents a ligand centered transition process. The shift of the features in the visible region between **2** and **1**, **4**, **6**, **8** is already detectable by the human eye. While the dissolved sample of the reverse metallacrown

appears dark green, solutions of the latter complexes reveal an orange brown color. As the absorption band of lowest energy can be used for an estimation of the octahedral splitting by adding the Racah parameter C with the value of 3800 cm^{-1} for Co(III) ions,[121,123] the determined value of 616 versus 649, 635, 648 and 646 nm means stronger an average ligand field for the ring metal ions of **2** (Δ_O = 20034 cm^{-1}) compared to the trivalent cobalt ions in **1**, **4**, **6**, **8** (Δ_O = 19209, 19548, 19232, 19280 cm^{-1}). This finding obviously reflects the distinguished coordination spheres of the vacant metallacrown which always comprises two or four nitrogen donor atoms and a non-bridging mode of the hydroximate moiety.

3.5.5 Mass spectrometry

All mass spectra show a complex fragmentation pattern and the intact molecular ion $\{M+H\}^+$ can only be observed in the case of **2**. However, a comprehensive systematic has been to interpret them in a consistent way. Most of the peaks in the high mass range could be assigned to ions which comprise the full scaffold of the cobalt centers and the salicylhydroximate main ligands whereas the anions pivalate, nitrite and 2-benzoxazolinonate as well as the neutral ligands pyridine, 3-picoline, piperidine, morpholine, methanol and water are partially or completely released. The loss of ligands is thereby in general a common phenomenon for ESI MS spectra of Co(III) complexes in literature.[124,125] Although the complex pattern of the mass spectra of the cobalt metallacrowns in the present work are hardly suitable to evaluate the integrity of the clusters in solution, the assignment of the majority of significant peaks to ions with the expected number of metal centers and main ligands strongly indicates a certain stability of the basic motif of the coronates in acetonitrile and methanol. During the following discussion of the obtained data, the observed complex ions will be divided into series of molecules which only differ in the number of amines in order to preserve clarity and comparability but not to rate the binding strength of any ligand type. All assigned peaks in the spectrum of **1** contain the expected five cobalt ions, three salicylhydroximate trianions and the hydroxid ligand. The three peaks at 1608, 1563 and 1545 m/z refer to the complex ions $\{Co_5(Shi)_3(Piv)_5(OH^-)(Pip)_4 + H\}^+$, $\{Co_5(Shi)_3(Piv)_5(OH^-)(Pip)_4 + H\}^+$ and $\{Co_5(Shi)_3(Piv)_5(OH^-)(Pip)_3 + Na\}^+$ with the full number of five pivalate ligands. Moreover, two series of ions comprising four of these carboxylate anions of the general formulae $\{Co_5(Shi)_3(Piv)_4(OH^-)(Pip)_x(H_2O)\}^+$ (x = 3, 4; 1439, 1524 m/z) and $\{Co_5(Shi)_3(Piv)_4(OH^-)(Pip)_4\}^+$ (x = 2, 3, 4; 1336, 1421, 1506) have been identified. Here, the two molecules with three piperidine ligands feature the highest intensity. In both spectra of **2**, a long sequence of equidistant peaks (995, 1074, 1152, 1232, 1311, 1390, 1469 m/z) refers to the complex ions $\{[12\text{-}MC_{Co(III)N(Shi)}\text{-}4](Py)_x + H\}^+$ with x ranging from 2 to 8, the species with five attached pyridine yields the highest count number. Additionally, the three heaviest members of the series can also be found with a

replacement of the associated proton by a sodium ion in the spectrum which has been recorded from a solution in methanol (1333, 1412, 1491 m/z). The spectrum of **4** provides a multitude of peaks, as positive ions can easily be accessed via the successive removal of pivalate ions and an appropriate charging via different cations. Although in general the occurrence of alkali counter ions in mass spectra can originate from the uptake of environmental materials, the frequency of observed complex ions containing lithium is massively raised in the case of **4** and hence the number of peaks is further increased. Therefore, the results will just be summarized at that point and the full list of assigned peaks is available from the supplementary information. Singly positive charged ions can be identified for a series of complexes with the components of the basic coronate subunit motif as well as three pivalate groups which differ in the number of remaining piperidine ligands and in the combination of various counter ions. Here, the most extensive sequence refers to the charged molecules with two associated lithium cations $\{Co(II)(Piv)_3[12\text{-}MC_{Co(III)N(Shi)}\text{-}4](Pip)_x + 2Li\}^+$ (x = 1, 2, 3, 4; 1297, 1382, 1467, 1552 m/z). Additionally, the combination of a proton and a lithium ion as well as a sodium and lithium ion can be recognized for some species of the series. For just two remaining pivalate ions, the most examples are assigned to the formulae $\{Co(II)(Piv)_2[12\text{-}MC_{Co(III)N(Shi)}\text{-}4](Pip)_x + H\}^+$ (x = 2, 3, 4, 5; 1268, 1353, 1438, 1523 m/z) and $\{Co(II)(Piv)_2[12\text{-}MC_{Co(III)N(Shi)}\text{-}4](Pip)_x + Li\}^+$ (x = 2, 3, 4; 1274, 1359, 1444 m/z). Finally, complex ions $\{Co(II)(Piv)[12\text{-}MC_{Co(III)N(Shi)}\text{-}4](Pip)_x\}^+$ (x = 0, 1, 2, 3, 4; 996, 1081, 1166, 1251, 1336 m/z) have been identified besides two methanol adducts $\{Co(II)(Piv)[12\text{-}MC_{Co(III)N(Shi)}\text{-}4](Pip)_x + MeOH\}^+$ (x = 3, 4; 1283, 1368 m/z). The charged molecules $\{Co(II)(Piv)_2[12\text{-}MC_{Co(III)N(Shi)}\text{-}4](Pip)_4 + H\}^+$ and $\{Co(II)(Piv)[12\text{-}MC_{Co(III)N(Shi)}\text{-}4](Pip)_3\}^+$ feature the highest intensities in the spectrum of **4**. Due to the range of different bridging and secondary ligands, the interpretation of the spectra of **5** comprises the consideration of various combinations. The two dominant series $\{Co(II)(Piv)[12\text{-}MC_{Co(III)N(Shi)}\text{-}4](Morph)_x\}^+$ (x = 0, 1, 2, 3, 4; 996, 1083, 1170, 1257, 1344 m/z) and $\{Co(II)(Boa)[12\text{-}MC_{Co(III)N(Shi)}\text{-}4](Morph)_x\}^+$ (x = 0, 1, 2, 3, 4; 1029, 1116, 1203, 1290, 1377 m/z) can be assigned to the respective bridging ligand in the spectrum of the solution in acetonitrile. Moreover, complex ions $\{Co(II)(Boa)(Piv)[12\text{-}MC_{Co(III)N(Shi)}\text{-}4](Morph)_x + H\}^+$ (x = 1, 2 3, 4; 1218, 1305, 1392, 1479 m/z) containing the pivalate as well as the 2-benzoxazolinonate anion. Although, the methanol ligand has vanished in most of the identified ionized clusters, the species $\{Co(II)(Boa)[12\text{-}MC_{Co(III)N(Shi)}\text{-}4](Morph)_xMeOH\}^+$ can be observed in some versions with x = 1, 2, 3 (1148, 1235, 1322, m/z). The peaks in the spectrum of the same sample in methanol resembles these findings and the presence of some additional sodium adducts is evident. A full list of assigned peaks is included in the supplementary information. The same classification of a series of complex ions according to the compilation of the bridging ligands can be conducted for the spectra of **8**. Here, the sequence of peaks for the simultaneous presence of the nitrite and pivalate ligand in the spectrum of the solution in ace-

tonitrile is diversified by the alternation of the cation between a proton in $\{Co(II)(NO_2)(Piv)[12\text{-}MC_{Co(III)N(Shi)}\text{-}4](Pic)_5 + H\}^+$ (x = 1, 2, 3, 4, 5; 1136, 1229, 1322, 1415, 1508 m/z) and a sodium ion in $\{Co(II)(NO_2)(Piv)[12\text{-}MC_{Co(III)N(Shi)}\text{-}4](Pic)_5 + Na\}^+$ (x = 1, 2, 3, 4, 5; 1158, 1251, 1344, 1437, 1530 m/z). Additionally, the individual series of peaks assigned to the carboxylate $\{Co(II)(Piv)[12\text{-}MC_{Co(III)N(Shi)}\text{-}4](Pic)_x\}^+$ (x = 0, 1, 2, 3, 4, 5 ; 996, 1089, 1182, 1275, 1368, 1461 m/z) and the nitrite $\{Co(II)(NO_2)[12\text{-}MC_{Co(III)N(Shi)}\text{-}4](Pic)_x\}^+$ (x =2, 3, 4, 5 ; 1127, 1220, 1313, 1406 m/z) can be identified. Similar results are indicated by the spectrum of the solution in methanol although the resolution was reduced due to the low solubility. The list of assigned peaks is available from the supplementary information.

In summary, the worth of analysis of the compounds via the method mass spectrometry mainly for the present work consists in the complementary evidence for the successful incorporation of some novel or converted building units like the lithium cation, nitrite anion and 2-benzoxazolinate for metallacrown chemistry. Moreover, the similar systematic of the peak patterns, the low frequency of adducts and the lack of agglomerates indicate a certain degree of stability of the coronate including the central guest ion. An evaluation from a chemical point of view on the composition of the obtained fragments hints at the ionization process as the major source of the fragmentation although a previous partial substitution of the secondary and bridging ligand by labile solvent molecules cannot be excluded.

3.5.6 ^{1}H-NMR Spectroscopy

The ^{1}H-NMR spectra of the diamagnetic complexes **1** and **2** reveal signals of the same integral and multiplicity for a respective ligand type which are shifted against each other depending on the individual environments at the binding site.[126] Concerning the aromatic systems, the peak sets of the same ligand species could be subdivided into discrete groups of correlated signals which represent singly distinguishable ligands via two dimensional ^{1}H-^{1}H COSY spectra. The low field region of the ^{1}H-spectrum of **1** contains five distinctive signals of similar integral which correspond to the same number of attached pivalate ligands (δ = 0.48 (s), 0.64 (s), 0.99 (s), 1.16 (s), 1.29 (s) ppm). Moreover, several multiplets in the range between 0.75 and 4.00 ppm arise from the methylene protons of the piperidine ligands (Fig. S21). In the aromatic region a set of partially superimposed doublets and triplets can be observed and can be grouped with the help of the cross-peaks of the two-dimensional NMR experiment into three subsets (δ = 6.46-6.49 (t), 7.00-7.08 (m), 7.11-7.13 (d), 7.45-7.47 (d) ppm), (δ = 6.63-6.68 (m), 6.75-6.77 (d), 6.91-6.96 (m), 7.85-7.87 (d) ppm) and (δ = 6.63-6.68 (m), 6.91-6.96 (m), 7.00-7.08 (m) 8.27-8.29 (m) ppm) for the distinguishable salicylhydroximate ligands (Fig. S22). Signals for the water, hydroxyl and the nitrogen bond hydrogen atom could not be as-

signed unambiguously. Furthermore, the present of few additional peaks with weak intensity in the aromatic region and in proximity to the pivalate signals might indicate minor proton exchange processes. By contrast, the high field region in the spectra of **2** features doublet and triplets for the aromatic protons of the salicylhydroximate ligand as well as for the attached pyridine molecules (Fig. 14; Tab. S46).

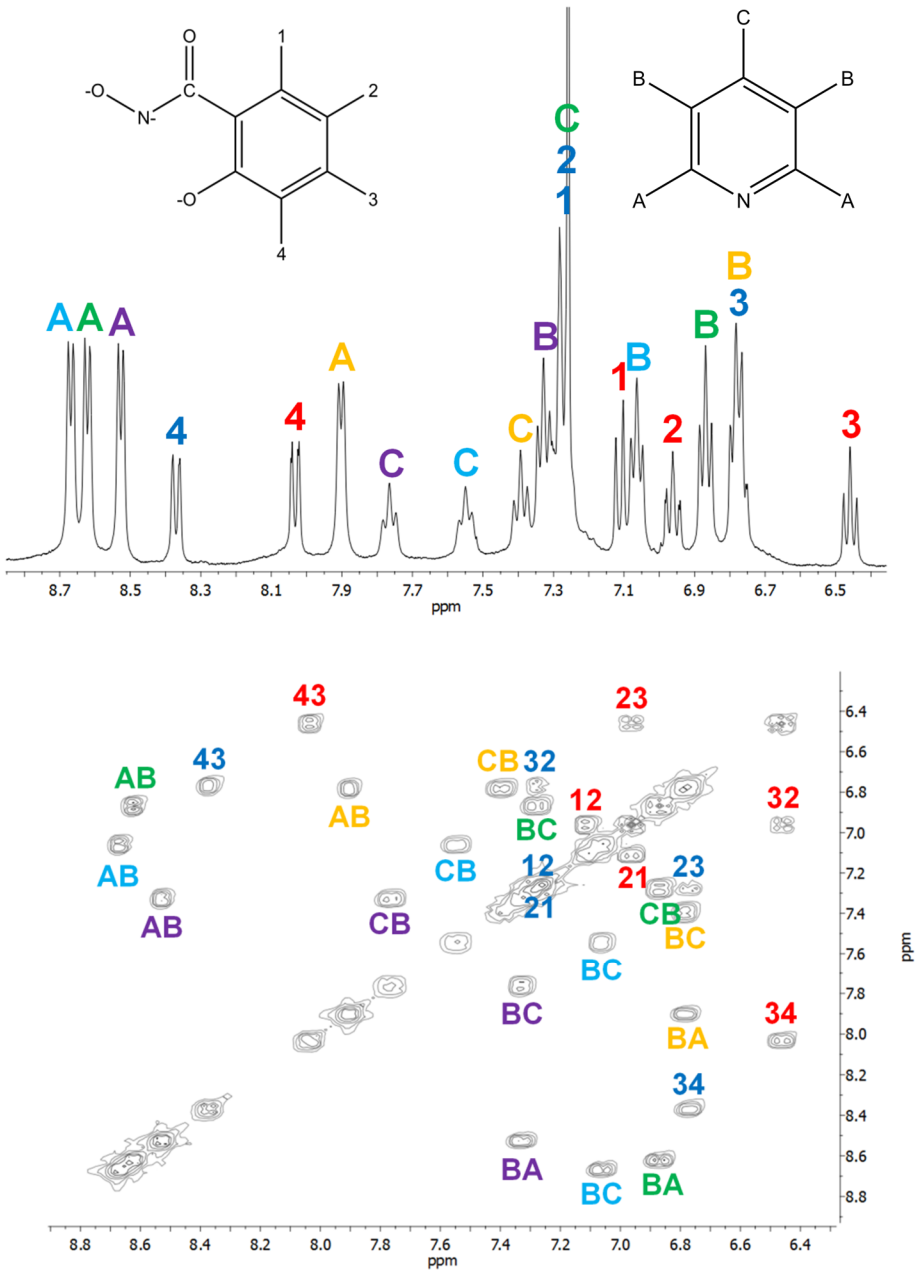

Figure 14 ^{1}H-NMR (top) and ^{1}H-^{1}H COSY (down) spectrum of **2** in chloroform; colored numbers represents assignment of the signal; different colors encode distinguishable ligands, different numbers encode different H-positions

Here, the signals of the pyridine ligands can be easily identified because the protons in ortho- and para-position cause peaks of double intensity indicating a free rotation of this

moiety. Counting the numbers of different signals, only the half amount of protons which might be expected from the crystal structure can be observed at the first sight. However, this finding simply arises from the transfer from pseudo-C_2 symmetry in the solid into a real C_2-symmetry in solution. Hence, four signal groups (δ = 6.75-6.80 (m), 7.37-7.41 (t), 7.90-7.91 (d) ppm), (δ = 6.85-6.89 (t), 7.26-7.30 (m), 8.62-8.63 (d) ppm), (δ = 7.05-7.08 (t), 7.53-7.57 (t), 8.66-8.68 (d) ppm) and (δ = 7.31-7.35 (t), 7.75-7.78 (t), 8.52-8.53 (d) ppm) can be assigned to the four distinguishable pyridine ligands via the ^{1}H-^{1}H COSY spectrum whereas two subsets of peaks (δ = 6.44-6.48 (t), 6.94-6.98 (t), 7.10-7.12 (d), 8.02-8.04 (d) ppm) and (6.75-6.80 (m), 7.26-7.30 (m), 7.26-7.30 (m), 8.36-8.38 (d) ppm) represent the salicylhydroximate main ligands in deuterated chloroform. A complementary ^{1}H spectrum was recorded for a solution in dichlormethane to resolve the multiplet below the signal of the solvent chloroform and is available from the supplementary information (Fig. S23; Tab S47). In summary, the occurrence of distinguishable peak sets and their correlation with the number of ligands clearly prove the integrity of both complexes **1** and **2** in chloroform and dichlormethane respectively.

3.5.7 Magnetic properties

Static magnetism

The temperature dependence of the molar static (dc) susceptibility χ of **4**, **5** and **8** reveals the typical features of samples which are comprised of mononuclear Co(II) high-spin complexes. Due to the partially unquenched orbital moment, the values of the χT product significantly exceed the spin-only value of 1.876 cm^{3}K/mol for a spin of S = 3/2 with a g-factor of g = 2 at room temperature. Moreover, the spin-orbit coupling in combination with the shape of the ligand field can give rise to a strong magnetic anisotropy which causes a deviation from a simple paramagnetic Curie law and is in general observed as a monotonic decrease of the χT product in the course of the cooling of the sample. (Fig. 15)

The χT value of 3.15 cm^{3}K/mol for **4** resembles the reference of 3.37 cm^{3}K/mol for an independent spin and orbital momentum of a ^{4}F ground term.[127] Decreasing with continuously increasing slope in the course of the cooling, the χT curve shape reveals the characteristic behaviour of an isolated six-coordinated Co(II) ion with significant contribution of spin-orbit coupling to the splitting of the $^4T_{1g}$ state.[128–130] At 2 K, lowest temperature of the measurement, the χT product is 2.18 cm^{3}K/mol. The corresponding plot of the χT product versus the temperature T for **5** features a very similar curve shape with benchmark values of 3.03 and 2.26 cm^{3}K/mol at 300 and 2 K, respectively. By contrast, the sample of **8** shows a linear decrease from 3.23 cm^{3}K/mol at room temperature to a value of 2.79 cm^{3}K/mol at 95 K. For lower temperatures, the slope of the χT curve increases continuously and reaches a value of 1.97 cm^{3}K/mol at 2 K. The latter

shape is quite similar to other examples of isolated Co(II) ions with distorted trigonal prismatic coordination sphere.[48]

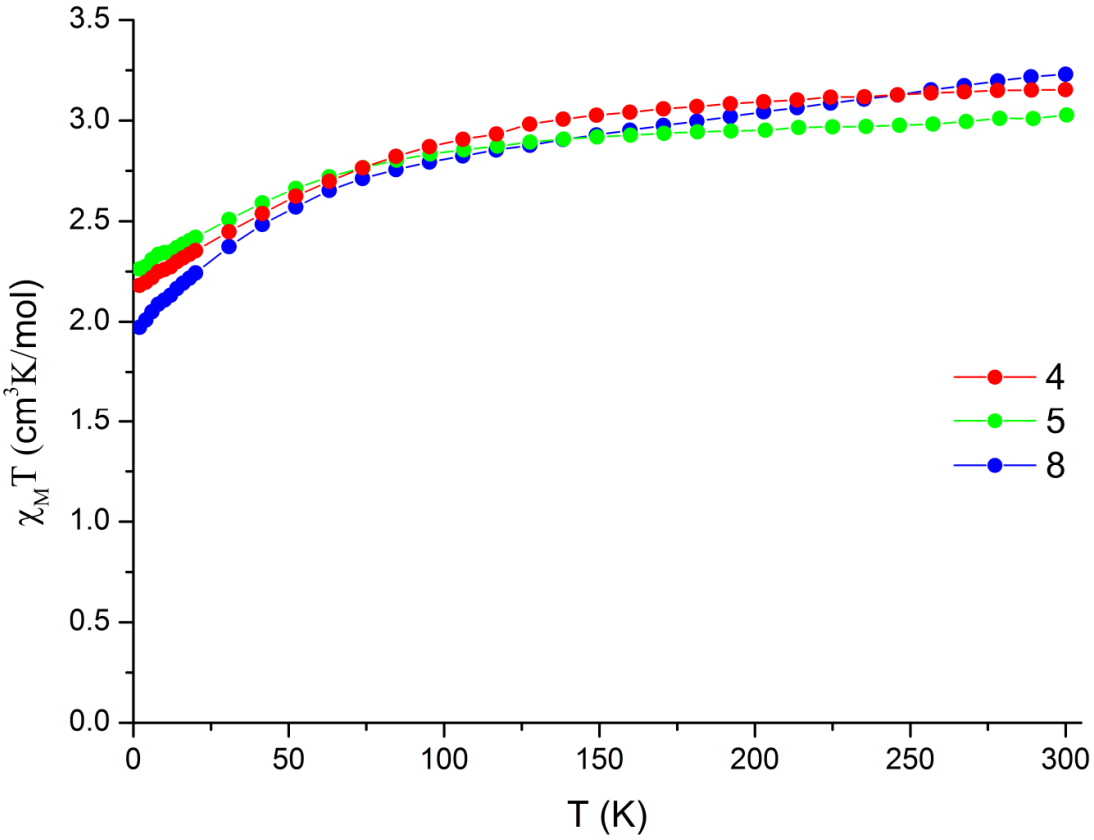

Figure 15 plot of the $\chi_M T$ product versus temperature for **4**, **5** and **8**; solid lines represent guidelines for the eyes

The fitting of temperature dependent susceptibility data of Co(II) is challenging due to the incomplete quenching of the contributions of the orbital momentum. Expressions for six-fold coordinated metal centres have been derived for the model case of an octahedral coordination sphere and have also been adapted for a symmetric tetragonal or trigonal distortion of this reference shape. However, these equations contain an intensive amount of variable parameters and hence can easily cause overparametrization and useless fit results. The coordination spheres of central guest ions at the core of the complexes **4**, **5** and **8** feature pronounced deviations from a perfect regular reference polyhedron. A careful analysis of bond lengths and angles as well as the determination of their position on the shape map of the octahedral and tetragonal shape measures clearly yield that these distortions can neither be projected on a trigonal nor a tetragonal axis of the octahedron. Therefore, the detailed interpretation of the temperature dependent susceptibility of the introduced cobalt metallacrowns is an interesting task of the present and future work and are supported by ab initio calculations as well as experimental in-

vestigations of the electronic structure via complimentary methods like EPR spectroscopy which are already in progress.

The high magnetic anisotropy is also reflected by the recorded magnetization data of all three complexes at low temperatures (Fig. S24, S26, 16). A plot of the reduced magnetization values $M/N_A\mu_B$ versus the ratio of field and temperature H/T does not result in a common master curve for the single measurement series at different temperatures (Fig. S25, S27, S29). Moreover, the corresponding $M/N_A\mu_B$ values of 2.28, 2.23 and 2.17 for **4**, **5** and **8** at a temperature of 2 K and an applied field of 7T come significantly below the saturation magnetization of an isolated S = 3/2 sate with a g-factor of g = 2 according to the Brilloin function but are in good agreement with reported values in literature.[44,46,127]

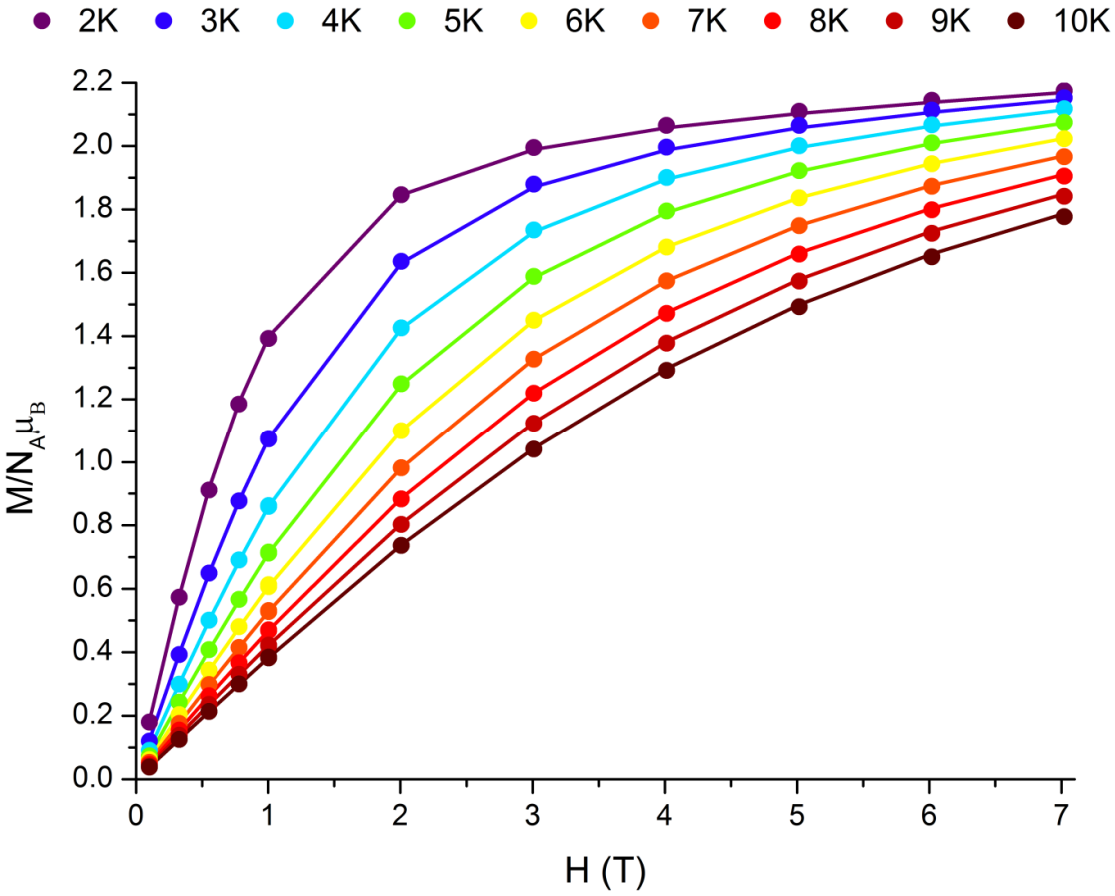

Figure 16 plot of the reduced magnetization versus the applied field for **8**; solid lines represent the best fit results according to an effective spin Hamiltonian with zero-field splitting parameter

The experimental data of **8** could be fitted via an effective spin Hamiltonian which includes a zero field splitting parameter D and an isotropic g-factor (Formula S4). The resultant values of D = -64 cm^{-1} and g = 2.66 did not change significantly when an addi-

tional rhombicity E was introduced into the model (D = -68 cm^{-1}, |E| = 4.3cm^{-1}, g = 2.67) and match the expectations based on magneto-structural correlations (Fig. 16). While Co(II) ions with an octahedral coordination sphere are restricted to a positive sign of the D values, trigonal prismatic divalent cobalt complexes can feature large negative zero field splitting parameters.[48] Corresponding attempts to fit the experimental data of **4** and **5** yielded even higher negative zero field splitting parameters which most likely indicate an inappropriate description of the lowest lying energy levels by the applied model and therefore no relevance is ascribed to without further validation by the ongoing complementary investigations. In summary, a significant amount of magnetic anisotropy has been observed for all three clusters but could only be quantified for complex **8**.

Considering the current findings of mononuclear cobalt compounds with single-molecule magnetic behaviour for both signs of the zero-field splitting parameter, this general observation implies the presence of a possible source for a slow relaxation of magnetization. A detailed model for the order of the different energy levels demands for further elaborate theoretical calculations because Co(II) high-spin ions feature a high sensitivity in their magneto-structural correlations and the corresponding shapes of the coordination spheres in the present cobalt metallacrowns strongly and asymmetrically deviate from simple reference polyhedra which can be descript via less differentiated models. However, these first examples of versatile cobalt coronates represent the promising foundation for a framework which provides a synthetic access for a systematic investigation of the complex dynamic and static magnetism of Co(II) high spin ions. From a static point of view, the detailed understanding of the interplay between static and dynamic phenomena might develope the ac susceptibility measurements as a valuable complementary method to acquire information concerning the lowest lying energy states.

Dynamic magnetism

When a dynamic magnetic field was applied to the sample of **4** no out-of-phase resonance signal could be detected in the absence of an additional static field. By contrast, a corresponding response was obtained for **5** and **8** under zero static field (Fig. S30, S31). However, the height of the causal effective energy barrier to magnetization reversal could not be determined as the measured range of frequencies yielded no maximum for the imaginary component of the susceptibility. In analogy to similar cases of mononuclear single-molecule magnets of cobalt,[38-40,42,44,46] other transition metals[29,31,34] and lanthanides,[131–133] an additional static field of 1500 Oe was applied to all three samples in order to diminish the contributions of quantum tunnelling processes to the relaxation of the magnetization. Indeed, **4**, **5** and **8** reveal frequency-dependent out-of-phase susceptibility signals as characteristic behaviour of single-molecule magnets with peaks at

4.5, 7 and 8.5 K at 1000 Hz (Fig. S34, S35, 17). For all three samples the relaxation times at various temperatures have been analyzed via a generalized Debye model according to the Cole-Cole formalism.[134–137] Here, the isothermal (χ_0) and adiabatic (χ_s) susceptibility as well as the parameter α were obtained by fitting of the experimental data in a Cole-Cole-plot (Fig. S39-S44) of the out-of-phase versus the in-phase-susceptibility (χ'' vs. χ') utilizing formula S5. The corresponding values for α of 0.02-0.15 at 6.1-2.0 K for **4**, 0.02-0.28 at 7.0-2.0 K for **5** and 0.05-0.28 at 9.0-2.0 K for **8** are in good agreement with other cobalt SMMs and simultaneous differentiates the observed phenomena from spin glass behaviour.[44,46,48] Moreover, their proceeding marks the development from an almost exclusive dominance of the thermal relaxation at high temperatures towards an increasing influence of quantum tunnelling processes for the relaxation of the magnetization at low temperatures. Taking the obtained parameters of the Cole-Cole-plot, the temperature dependent relaxation times τ were extracted by fitting the plot of the in-phase susceptibility data versus the frequency (Fig. S47-S49) via formula S6.[136,138]

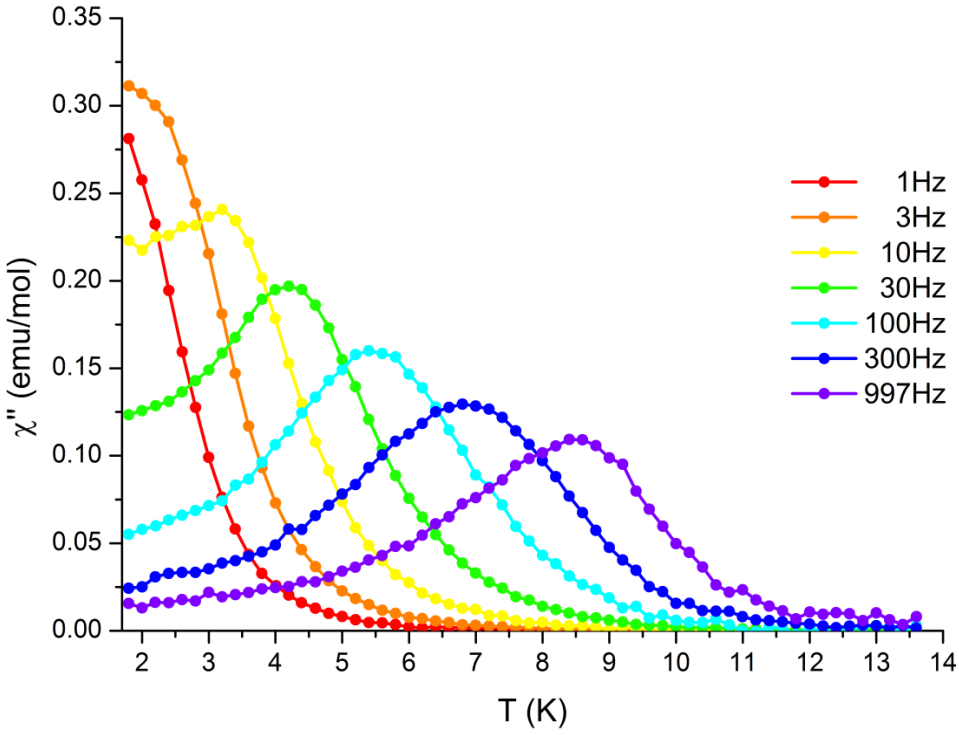

Figure 17 plot of the out-of-phase susceptibility versus temperature under an applied static field of 1500Oe for **8**; solid lines represent guidelines for the eyes

A similar procedure using the out-of-phase susceptibility was checked to yield corresponding results (Fig. 18, S45, S46). The height of the respective energy barriers U_{eff} and the attempt relaxation time τ_0 were than determined via a linear regression of an Arrhenius plot which correlates the natural logarithm of the relaxation time ln(τ) with the reciprocal temperature T^{-1}. However, the gradual decline of the signals in the plot of the out-of-phase susceptibility versus the temperature at lower temperatures already

indicates that the corresponding Orbach process by a thermal activated overcoming of the reversal barrier does not represent the only active relaxation mechanism. Hence, only the high temperature range was taken into account for the fitting according to the Arrhenius equation S7 as the corresponding assumption of a dominant relaxation of the magnetization via the Orbach pathway is most likely fulfilled in this region.[139] The procedure yielded values of 14, 35 and 79 K for the effective energy barrier to magnetization reversal, U_{eff}, and $1.45 \cdot 10^{-5}$, $1.21 \cdot 10^{-6}$ and $1.75 \cdot 10^{-8}$ s for the attempt relaxation time, τ_0, of **4**, **5** and **8** (Fig. 20, S50-S52). Nevertheless, the curvature of the Arrhenius plots already suggests that more types of relaxation processes are involved as the exponential increase of the Orbach relaxation rate with decreasing reciprocal temperature would cause a more sudden angular drop from the temperature independent quantum tunnelling regime.

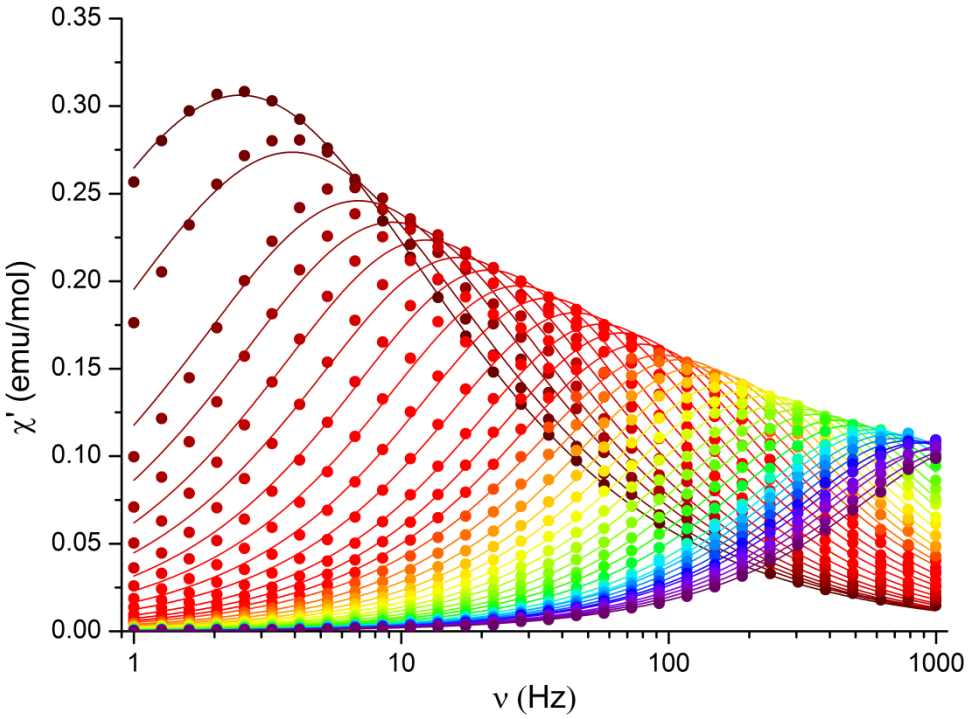

Figure 18 plot of out-of-phase susceptibility versus frequency under an applied static field of 1500Oe for **8**; solid lines represent the best fit results according to a generalized Debye model; color code: red - 2 K, violet - 9 K

In order to obtain more information about the nature of these additional processes, the field dependence of the relaxation time was investigated. For all three complexes an increase of the relaxation time is observed at low field strength which is attributed to the partial suppression of the quantum tunnelling by the lifting of the degeneracy of the coupled states. Moreover, a coexistence and transfer of a fast field suppressed and a slower field induced relaxation can be recognized in the plot of the out-of-phase suscep-

tibility versus the wave frequency of **5** and **8** for low static magnetic fields. Reaching a maximum relaxation time of 0.0014 (1250 Oe), 0.0195 (2500 Oe) and 0.0636 (1500 Oe) at 2 K, the plots of τ versus H_{DC} decline again more slowly at higher fields (Fig. 19, S63, S64). The latter curve shape is assigned to the relaxation via the so-called direct process.[27] This type of spin-lattice relaxation process means a flipping of a magnetic ion by absorption or emission of a phonon which matches the energy difference of the two involved states.[140] The field dependence of its relaxation rate is commonly described with a power factor of 2 for even spins whereas the present Kramer's ions in general feature a H^4 dependence.[141] However, the attempts to fit the field dependent relaxation time at 2 K via combined formula for the quantum tunnelling mechanism and the direct process did not give suitable results. By contrast, a fitting with a power factor of 2 revealed to be suitable to reproduce the curve shape for **8**. Although this abnormal behaviour of Kramer's ions has been reported occasionally in literature,[142] a comprehensive fitting of the temperature dependence of the relaxation time for the whole temperature range on this basis seemed to be too inconclusively.

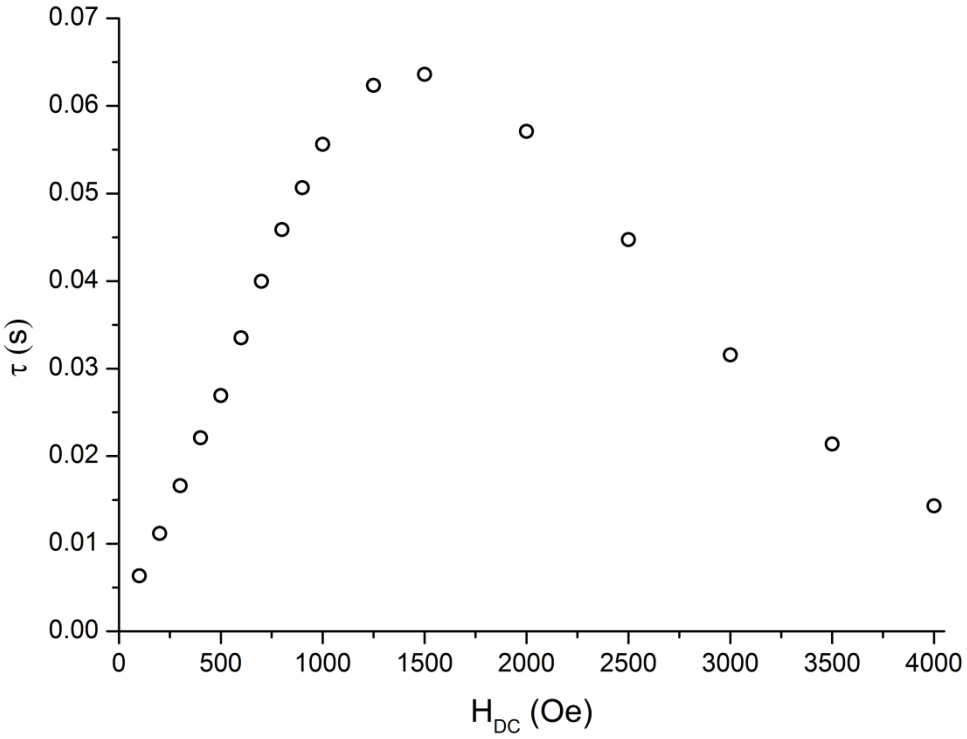

Figure 19 plot of the relaxation time versus the applied magnetic field at a temperature of 2K for **8**

Nevertheless, a significant contribution of the direct process to the curvature of **8** at high temperatures can be excluded by a simple estimation. Even if the full amount of the relaxation rate at 2 K is exclusively attributed to the direct process, its contribution to the experimental relaxation time above 7 K is less than 10% due to the linear depend-

ence from temperature. As the quantum tunnelling mechanism between the ground states is not affected by the temperature, its significance can also be neglected in first approximation for this region. Therefore, the occurrence of another spin-lattice relaxation process to which a high significance is ascribed to in the recent discussion about mononuclear transition metal single-molecule magnets is suggested. The Raman process involves the promotion of the magnetic ion into a virtual excited state by the absorption of a phonon and an immediate decay via the emission of another phonon.[140] Because the abovementioned estimation yields a sufficient separation of the dominant scope of the direct process and quantum tunnelling mechanism at low temperature from the Raman and Arrhenius relaxation regime at high temperatures for **8**, the latter region was fitted between 7 and 9 K by a corresponding two-process model (Formula S11). The results of the fit should be taken carefully as the power factor of the Raman term is only slightly restricted by the present theory and has a strong influence on the final optimized parameters. However, a convincing set of values was obtained for the common T^5 dependence of the Raman relaxation rate.[27,45,48,141] The corresponding constant C of the Raman term accounts for 0.1008 K^5s^{-1} whereas the attempt relaxation time and the energy barrier of the Orbach process amount to $7{,}38 \cdot 10^{-13}$ s and 179 K.

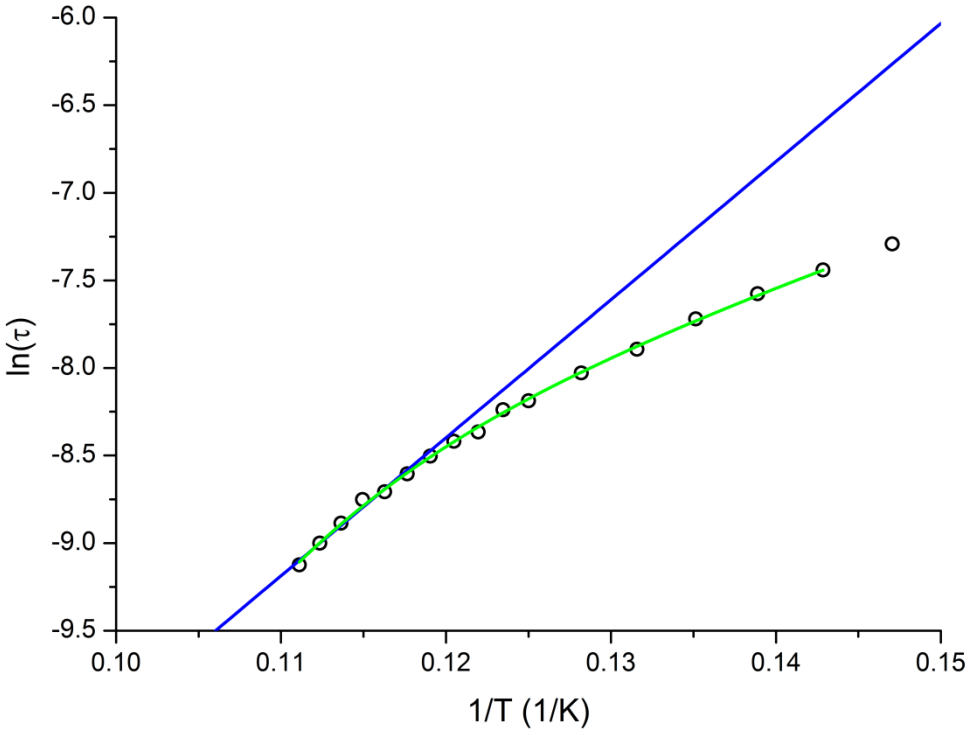

Figure 20 Arrhenius plot of the natural logarithm of the relaxation time versus the reciprocal temperature under an applied static field of 1500Oe for **8;** solid blue line represents the fit result of the high temperature range according to the Arrhenius equation; solid green line represents the fit result of the high temperature range according to a model regarding Orbach and Raman relaxation process

The new value for the energy barrier is significantly higher than the obtained parameter for the simple Arrhenius plot. However, it should be mentioned that the arrangement of the captured data points for the latter processing still indicated curvature and therefore would have yielded even higher energy barriers for a further constrain of the regression range. Moreover, the obtained energy barrier for the two-process model resembles the estimated value for a Kramer's ion based on the determined zero-field splitting parameter 184 K. The fit result furthermore implies a nearly exclusive relaxation via the Raman effect in the temperature range around 7 K. At 2 K its contribution to the sum of relaxation rates still amounts to 21% (Fig. S53, S54). A corresponding implementation of this effect into the aforementioned model for the field dependence at 2 K was applied but did not significantly improve the goodness of the fit result. The Orbach process takes over as dominant relaxation process above 9.4 K according to the parameters of the two-process model of the high temperature regime. It was desisted from a corresponding procedure for the samples of **4** and **5** as the separation of both regimes could not be ensured.

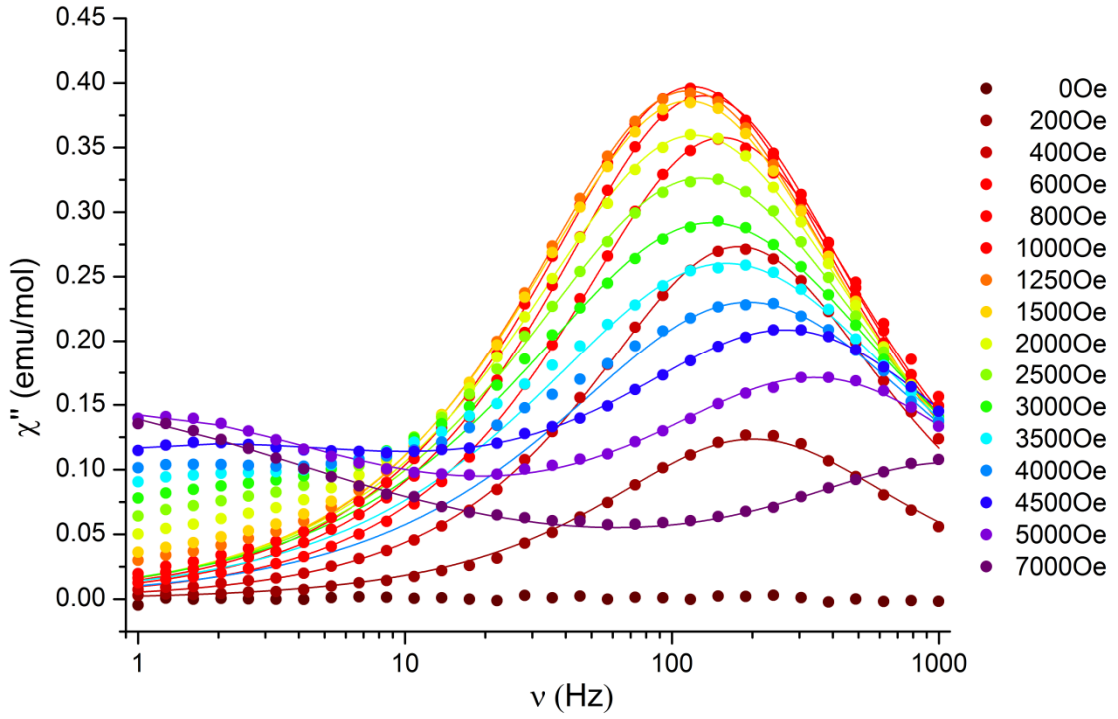

Figure 21 plot of out-of-phase susceptibility versus frequency at a temperature of 2K under different applied magnetic fields for **4**; solid lines represent the best fit results according to a generalized Debye model

A measurement series for the investigation of the field dependence at 5 K for complex **5** however reflects the general presence of the different discussed relaxation processes (Fig. S65-S68). So, the relative influence of the static field on the relaxation rate de-

creases with increasing temperature as quantum tunnelling does not change its rate and the gain of the direct process is overcompensated by Orbach and Raman relaxation. The difference in the temperature dependence of quantum tunnelling and direct process can be recognized from a shift of the magnetic field with maximum relaxation time towards lower values.

The field dependence of the out-of-phase susceptibility of **4** moreover reveals a second peak above 4000 Oe which is already indicated by an offset for lower fields (Fig. 21). Therefore, the frequency dependent in- and out-of-phase susceptibility data were analysed via a concerted fit according to the sum of two generalized Debye functions (Formula S12).[143] The resultant relaxation times for the field enforced second process are more than two magnitudes higher than the corresponding values of the field suppressed case. Similar transfers have been reported previously for mononuclear cobalt[41] and lanthanide complexes.[144] Detailed investigations on the field and temperature dependence of this dualism are in progress and might unveil more information concerning the nature of the respectively involved relaxation mechanisms.

The host of the novel class of cobalt metallacrowns obviously holds a great potential to equip the encapsulated Co(II) guest ion with the feature of single-molecule magnetism. In accordance with similar findings in literature, the shielding effect of the diamagnetic scaffold against magnetic exchange interactions benefits the slow relaxation of the magnetization.[44,48] However, a more unique characteristic of the cobalt coronates is based on their versatility concerning the creation of different coordination spheres of the central divalent cobalt ion. The most singular dualism of preorganization and flexibility creates them a powerful frame to systematically explore the interesting current issue of the static and dynamic magnetism of single Co(II) high spin ions. Here, bridging and secondary ligands as well as attached cations at the periphery represent suitable synthetic tools to tune the magnetic properties via the modification of the overall molecular configuration of the metallacrown. As a first yield of this systematic interface, a series of three novel single-molecule magnets have been obtained which span a large range of the distortion pathway from an octahedral to a trigonal prismatic coordination polyhedron. In the same direction the complexes **4**, **5** and **8** rank with 14, 35 and 79 K in the lower, middle and upper class concerning their height of the energy barrier to magnetization reversal in the context of the present examples of SMMs based on a single Co(II) ion in literature.[35-48,145] Hence, they simultaneously reinforce the promising potential of the trigonal prismatic coordination sphere to yield remarkable energy barriers in a very vivid way (Fig. S69, S70). Moreover, the important influence of the Raman process for the magnetic relaxation could be extracted from the analysis of the dynamic magnetism of **8**. The field induced transfer between different relaxation pathways in **4** furthermore reveals the versatility of the dynamic single-ion magnetism of divalent cobalt which can

be faced with the help of the versatile novel cobalt metallacrowns as systematic molecular interface to the SMM features.

3.6 Conclusions

We here report the synthetic realization and characterization of the first examples of the long-awaited cobalt metallacrowns based on salicylhydroxamic acid. Besides the general rareness of cobalt metallacrowns and the complete absence of cobalt complexes of this ligand, the scope of metallacrown chemistry significantly enlarged as the novel coronates add scarce and completely unprecedented structural features like central vacancy, reverse of the succession of the repetition unit, (semi-) perpendicular out-of-plane tilting of salicylhydroximate and peripheral complexation of additional cations to the repertory of the 12-MC-4 clusters of the mother of all metallacrown ligands. The observed flexibility of the configuration of the cyclic host results in the possibility to create various shapes of coordination polyhedra for the central Co(II) guest ion. This latter feature gains even more functional relevance as the coronates reveal single-molecule magnetic behaviour based on single Co(II) ion at the core of the complexes. Hence, the establishment of three novel magnetic-mononuclear Co(II) SMMs along the distortion pathway from the octahedron to the trigonal prism with low to high energy barriers of 14, 35 and 79 K reinforces the capability of the latter geometry for the achievement of a remarkable extent of this effect and displays the promising potential of the novel cobalt metallacrowns concerning this hot topic of current research. The dualism of preorganization and flexibility of the molecular configuration distinguishes the Co(II)[12MC$_{Co(III)N(Shi)}$-4] compounds as a molecular interface for the systematic investigation and targeted modification of the magnetic properties of single Co(II) ions via the versatile adjustment of their coordination sphere. Here, the bridging and secondary ligands as well as peripherally attached cations have been developed as suitable tools to perform a purposeful shaping of the metallacoronates. Gaining precision in the handling of these tools, the cobalt metallacrowns of salicylhydroxamic acid provide a perfect synthetic access to decode the still challenging issues of the static and dynamic magnetism of Co(II) high-spin ions in cooperation with analytical methods and theoretical calculations.

3.7 Acknowledgement

We are grateful to Regine Jung-Pothmann and Dr. Dieter Schollmeyer for the collection of the X-ray diffraction data and for helpful discussions concerning the refinement of the crystal structures. Marcel Sperner is acknowledged for preparative assistance. Peter Happ is recipient of a fellowship through the Excellence Initiative (DFG/GSC 266).

Moreover, he thanks the German National Academic Foundation (Studienstiftung des deutschen Volkes) for financial support.

3.8 References

[1] M. Murugesu, J. Raftery, W. Wernsdorfer, G. Christou and E.K. Brechin, *Inorg. Chem*, **2004,** *14*, 4203

[2] M. Murugesu, M. Habrych, W. Wernsdorfer, K.A. Abboud and G. Christou, *J. Am. Chem. Soc.*, **2004,** *15*, 4766

[3] A.J. Tasiopoulos, A. Vinslava, W. Wernsdorfer, K.A. Abboud and G. Christou, *Angew. Chem.*, **2004,** *16*, 2169

[4] A.M. Ako, I.J. Hewitt, V. Mereacre, R. Clérac, W. Wernsdorfer, C.E. Anson and A.K. Powell, *Angew. Chem. Int. Ed.*, **2006,** *30*, 4926

[5] T.C. Stamatatos, D. Foguet-Albiol, S.-C. Lee, C.C. Stoumpos, C.P. Raptopoulou, A. Terzis et al., *J. Am. Chem. Soc*, **2007,** *30*, 9484

[6] C.J. Milios, S. Piligkos and E.K. Brechin, *Dalton Trans.*, **2008,** *14*, 1809

[7] R. Inglis, S.M. Taylor, L.F. Jones, G.S. Papaefstathiou, S.P. Perlepes, S. Datta et al., *Dalton Trans.*, **2009,** *42*, 9157

[8] A. Cornia, A.C. Fabretti, P. Garrisi, C. Mortalò, D. Bonacchi, D. Gatteschi et al., *Angew. Chem. Int. Ed.*, **2004,** *9*, 1136

[9] S. Accorsi, A.-L. Barra, A. Caneschi, G. Chastanet, A. Cornia, A.C. Fabretti et al., *J. Am. Chem. Soc.*, **2006,** *14*, 4742

[10] R.W. Saalfrank, A. Scheurer, I. Bernt, F.W. Heinemann, A.V. Postnikov, V. Sch?nemann et al., *Dalton Trans.*, **2006,** *23*, 2865

[11] C. Schlegel, E. Burzurí, F. Luis, F. Moro, M. Manoli, E.K. Brechin et al., *Chem. Eur. J*, **2010,** *33*, 10178

[12] L. Gregoli, C. Danieli, A.-L. Barra, P. Neugebauer, G. Pellegrino, G. Poneti et al., *Chem. Eur. J.*, **2009,** *26*, 6456

[13] O. Waldmann, *Inorg. Chem.*, **2007,** *24*, 10035

[14] E. Ruiz, J. Cirera, J. Cano, S. Alvarez, C. Loose and J. Kortus, *Chem. Commun.*, **2007,** *1*, 52

[15] F. Neese and D.A. Pantazis, *Faraday Discuss.*, **2010**, 229

[16] S. Hill, S. Datta, J. Liu, R. Inglis, C.J. Milios, P.L. Feng et al., *Dalton Trans.*, **2010,** *20*, 4693

[17] C.J. Milios, A. Vinslava, W. Wernsdorfer, S. Moggach, S. Parsons, S.P. Perlepes et al., *J. Am. Chem. Soc.*, **2007,** *10*, 2754

[18] P.-H. Lin, T.J. Burchell, L. Ungur, L.F. Chibotaru, W. Wernsdorfer and M. Murugesu, *Angewandte Chemie*, **2009,** *50*, 9653

[19] I.J. Hewitt, J. Tang, N.T. Madhu, C.E. Anson, Y. Lan, J. Luzon et al., *Angewandte Chemie*, **2010,** *36*, 6496

[20] R.J. Blagg, C.A. Muryn, E.J. L. McInnes, F. Tuna and R.E. P. Winpenny, *Angew. Chem. Int. Ed*, **2011,** *29*, 6530

[21] D.N. Woodruff, R.E. P. Winpenny and R.A. Layfield, *Chem. Rev.*, **2013,** *7*, 5110

[22] N. Ishikawa, M. Sugita, T. Ishikawa, S.-y. Koshihara and Y. Kaizu, *J. Am. Chem. Soc.*, **2003,** *29*, 8694

[23] N. Ishikawa, *Polyhedron*, **2007,** *9-11*, 2147

[24] K. Katoh, H. Isshiki, T. Komeda and M. Yamashita, *Coordination Chemistry Reviews*, **2011,** *17-18*, 2124

[25] C.R. Ganivet, B. Ballesteros, G. de la Torre, J.M. Clemente-Juan, E. Coronado and T. Torres, *Chem. Eur. J.*, **2013,** *4*, 1457

[26] J.D. Rinehart and J.R. Long, *Chem. Sci.*, **2011,** *11*, 2078

[27] J.M. Zadrozny, M. Atanasov, A.M. Bryan, C.-Y. Lin, B.D. Rekken, P.P. Power et al., *Chem. Sci.*, **2012,** *1*, 125

[28] S. Mossin, B.L. Tran, D. Adhikari, M. Pink, F.W. Heinemann, J. Sutter et al., *J. Am. Chem. Soc.*, **2012,** *33*, 13651

[29] A. Grigoropoulos, M. Pissas, P. Papatolis, V. Psycharis, P. Kyritsis and Y. Sanakis, *Inorg. Chem.*, **2013,** *22*, 12869

[30] R. Ishikawa, R. Miyamoto, H. Nojiri, B.K. Breedlove and M. Yamashita, *Inorg. Chem.*, **2013,** *15*, 8300

[31] J. Vallejo, A. Pascual-Álvarez, J. Cano, I. Castro, M. Julve, F. Lloret et al., *Angew. Chem. Int. Ed.*, **2013,** *52*, 14075

[32] D.E. Freedman, W.Hill Harman, T.David Harris, G.J. Long, C.J. Chang and J.R. Long, *J. Am. Chem. Soc*, **2010,** *4*, 1224

[33] W.Hill Harman, T.David Harris, D.E. Freedman, H. Fong, A. Chang, J.D. Rinehart et al., *J. Am. Chem. Soc.*, **2010,** *51*, 18115

[34] P.-H. Lin, N.C. Smythe, S.I. Gorelsky, S. Maguire, N.J. Henson, I. Korobkov et al., *J. Am. Chem. Soc.*, **2011,** *40*, 15806

[35] A. Eichhöfer, Y. Lan, V. Mereacre, T. Bodenstein and F. Weigend, *Inorg. Chem.*, **2014,** *4*, 1962

[36] A. Buchholz, A.O. Eseola and W. Plass, *Comptes Rendus Chimie*, **2012,** *10*, 929

[37] J.M. Zadrozny and J.R. Long, *J. Am. Chem. Soc.*, **2011,** *51*, 20732

[38] J.M. Zadrozny, J. Liu, N.A. Piro, C.J. Chang, S. Hill and J.R. Long, *Chem. Commun.*, **2012,** *33*, 3927

[39] W. Huang, T. Liu, D. Wu, J. Cheng, Z.W. Ouyang and C. Duan, *Dalton Trans.*, **2013,** *43*, 15326

[40] F. Yang, Q. Zhou, Y. Zhang, G. Zeng, G. Li, Z. Shi et al., *Chem. Commun.*, **2013,** *46*, 5289

[41] R. Boča, J. Miklovič and J. Titiš, *Inorg. Chem.*, **2014,** *5*, 2367

[42] T. Jurca, A. Farghal, P.-H. Lin, I. Korobkov, M. Murugesu and D.S. Richeson, *J. Am. Chem. Soc*, **2011,** *40*, 15814

[43] F. Habib, O.R. Luca, V. Vieru, M. Shiddiq, I. Korobkov, S.I. Gorelsky et al., *Angew. Chem. Int. Ed.*, **2013,** *43*, 11290

[44] V. Chandrasekhar, A. Dey, A.J. Mota and E. Colacio, *Inorg. Chem.*, **2013,** *8*, 4554

[45] D. Wu, X. Zhang, P. Huang, W. Huang, M. Ruan and Z.W. Ouyang, *Inorg. Chem.*, **2013,** *19*, 10976

[46] J. Vallejo, I. Castro, R. Ruiz-García, J. Cano, M. Julve, F. Lloret et al., *J. Am. Chem. Soc.*, **2012,** *38*, 15704

[47] E. Colacio, J. Ruiz, E. Ruiz, E. Cremades, J. Krzystek, S. Carretta et al., *Angew. Chem.*, **2013,** *35*, 9300

[48] Y.-Y. Zhu, C. Cui, Y.-Q. Zhang, J.-H. Jia, X. Guo, C. Gao et al., *Chem. Sci.*, **2013,** *4*, 1802

[49] C.J. Milios, A. Vinslava, P.A. Wood, S. Parsons, W. Wernsdorfer, G. Christou et al., *J. Am. Chem. Soc.*, **2007,** *1*, 8

[50] V.L. Pecoraro, A.J. Stemmler, B.R. Gibney, J.J. Bodwin, H. Wang, J.W. Kampf and A. Barwinski, *Metallacrowns: A New Class of Molecular Recognition Agents*, **1996**, In: Kenneth D. Karlin: *Progress in Inorganic Chemistry*, Bd. 45, John Wiley & Sons, Inc (Progress in Inorganic Chemistry), 83

[51] G. Mezei, C.M. Zaleski and V.L. Pecoraro, *Chem. Rev*, **2007,** *11*, 4933

[52] M.Soo Lah and V.L. Pecoraro, *J. Am. Chem. Soc*, **1989,** *18*, 7258

[53] M.Soo Lah and V. Pecoraro, *Comments on Inorg. Chem*, **1990,** *2*, 59

[54] B.R. Gibney, D.P. Kessissoglou, J.W. Kampf and V.L. Pecoraro, *Inorg. Chem*, **1994,** *22*, 4840

[55] B.R. Gibney, H. Wang, J.W. Kampf and V.L. Pecoraro, *Inorg. Chem*, **1996,** *21*, 6184

[56] C. Dendrinou-Samara, G. Psomas, L. Iordanidis, V. Tangoulis and D.P. Kessissoglou, *Chem. Eur. J*, **2001,** *23*, 5041

[57] D.P. Kessissoglou, J.J. Bodwin, J. Kampf, C. Dendrinou-Samara and V.L. Pecoraro, *Inorganica Chimica Acta*, **2002,** *1*, 73

[58] E.S. Koumousi, S. Mukherjee, C.M. Beavers, S.J. Teat, G. Christou and T.C. Stamatatos, *Chem. Commun.*, **2011,** *39*, 11128

[59] C.M. Zaleski, S. Tricard, E.C. Depperman, W. Wernsdorfer, T. Mallah, M.L. Kirk and V.L. Pecoraro, *Inorg. Chem*, **2011,** *22*, 11348

[60] T.C. Stamatatos, S. Dionyssopoulou, G. Efthymiou, P. Kyritsis, C.P. Raptopoulou, A. Terzis et al., *Inorg. Chem.*, **2005,** *10*, 3374

[61] T.C. Stamatatos, C. Papatriantafyllopoulou, E. Katsoulakou, C.P. Raptopoulou and S.P. Perlepes, *Polyhedron*, **2007,** *9-11*, 1830

[62] C.P. Raptopoulou and V. Psycharis, *Inorganic Chemistry Communications*, **2008,** *10*, 1194

[63] M.Soo Lah, M.L. Kirk, W. Hatfield and V.L. Pecoraro, *J. Chem. Soc., Chem. Commun*, **1989,** *21*, 1606

[64] R.H. Blessing, *Acta Crystallogr A Found Crystallogr*, **1995,** *1*, 33

[65] A.L. Spek, *Acta Crystallogr D Biol Crystallogr*, **2009,** *2*, 148

[66] Bruker (2001), SADABS. Madison, Wisconsin, USA: Bruker AXS Inc

[67] A. Altomare, M.Cristina Burla, M. Camalli, G.Luca Cascarano, C. Giacovazzo, A. Guagliardi et al., *J Appl Crystallogr*, **1999,** *1*, 115

[68] G.M. Sheldrick, *Acta Crystallogr A Found Crystallogr*, **2008,** *1*, 112

[69] O.V. Dolomanov, L.J. Bourhis, R.J. Gildea, J.A. K. Howard and H. Puschmann, *J Appl Crystallogr*, **2009,** *2*, 339

[70] Mercury (2001-2013). Cambridge: The Cambridge Crystallographic Data Centre (CCDC)

[71] L.J. Farrugia, *J Appl Crystallogr*, **2012,** *4*, 849

[72] K. Brandenburg (2011), Diamond. Bonn, Germany: Crystal Impact GbR

[73] S.P. Westrip, *J Appl Crystallogr*, **2010,** *4*, 920

[74] G.A. Bain and J.F. Berry, *J. Chem. Educ.*, **2008,** *4*, 532

[75] N.F. Chilton, R.P. Anderson, L.D. Turner, A. Soncini and K.S. Murray, *J. Comput. Chem.*, **2013,** *13*, 1164

[76] MesTreNova (2009). Santiago de Compostela: MESTRELAB RESEARCH

[77] G. Aromí, A.S. Batsanov, P. Christian, M. Helliwell, A. Parkin, S. Parsons et al., *Chem. Eur. J.*, **2003,** *20*, 5142

[78] C.M. Zaleski, J.W. Kampf, T. Mallah, M.L. Kirk and V.L. Pecoraro, *Inorg. Chem*, **2007,** *6*, 1954

[79] L. DuchÃ¡cÌŒkovÃ¡ and J. RoithovÃ¡, *Chem. Eur. J.*, **2009,** *48*, 13399

[80] I. David Brown, Bond Valence Calculator 2.0. online available: http://www.ccp14.ac.uk/solution/bond_valence/

[81] I.David Brown, *Chem. Rev.*, **2009,** *12*, 6858

[82] I. David Brown (2013), Bond valence parameters. online available: http://www.iucr.org/resources/data/datasets/bond-valence-parameters

[83] M. Llunell, D. Casanova and J. Cirera (2013), Shape 2.1. online available: http://www.ee.ub.es/

[84] J. Cirera, E. Ruiz and S. Alvarez, *Organometallics*, **2005,** *7*, 1556

[85] S. Alvarez, D. Avnir, M. Llunell and M. Pinsky, *New J. Chem.*, **2002,** *8*, 996

[86] S.M. Kanowitz and G.J. Palenik, *Inorg. Chem.*, **1998,** *8*, 2086

[87] S. Khanra, M. Helliwell, F. Tuna, E.J. L. McInnes and R.E. P. Winpenny, *Dalton Trans.*, **2009,** *31*, 6166

[88] I. Kim, B. Kwak and M. Soo Lah, *Inorganica Chimica Acta*, **2001,** *1-2*, 12

[89] S. Lin, S.-X. Liu, J.-Q. Huang and C.-C. Lin, *J. Chem. Soc., Dalton Trans.*, **2002,** *8*, 1595

[90] J.Ivar van der Vlugt, S. Demeshko, S. Dechert and F. Meyer, *Inorg. Chem.*, **2008,** *5*, 1576

[91] L.F. Jones, C.A. Kilner and M.A. Halcrow, *Chem. Eur. J.*, **2009,** *18*, 4667

[92] D. Wu, D. Guo, Y. Song, W. Huang, C. Duan, Q. Meng and O. Sato, *Inorg. Chem.*, **2009,** *3*, 854

[93] J.A. Johnson, J.W. Kampf and V.L. Pecoraro, *Angew. Chem. Int. Ed*, **2003,** *5*, 546

[94] M. Alexiou, E. Katsoulakou, C. Dendrinou-Samara, C.P. Raptopoulou, V. Psycharis, E. Manessi-Zoupa et al., *Eur. J. Inorg. Chem.*, **2005,** *10*, 1964

[95] C.-M. Ji, H.-J. Yang, C.-C. Zhao, V. Tangoulis, A.-L. Cui and H.-Z. Kou, *Crystal Growth & Design*, **2009,** *11*, 4607

[96] H.-Z. Kou, G.-Y. An, C.-M. Ji, B.-W. Wang and A.-L. Cui, *Dalton Trans.*, **2010,** *40*, 9604

[97] B. Gole, R. Chakrabarty, S. Mukherjee, Y. Song and P.Sarathi Mukherjee, *Dalton Trans*, **2010,** *41*, 9766

[98] I.A. Golenya, E. Gumienna-Kontecka, A.N. Boyko, M. Haukka and I.O. Fritsky, *Inorg. Chem*, **2012,** *11*, 6221

[99] A.J. Stemmler, J.W. Kampf and V.L. Pecoraro, *Inorg. Chem.*, **1995,** *9*, 2271

[100] M. Alexiou, C. Dendrinou-Samara, C.P. Raptopoulou, A. Terzis and D.P. Kessissoglou, *Inorg. Chem*, **2002,** *18*, 4732

[101] G. Psomas, C. Dendrinou-Samara, M. Alexiou, A. Tsohos, C.P. Raptopoulou, A. Terzis and D.P. Kessissoglou, *Inorg. Chem*, **1998,** *26*, 6556

[102] G. Psomas, A.J. Stemmler, C. Dendrinou-Samara, J.J. Bodwin, M. Schneider, M. Alexiou et al., *Inorg. Chem*, **2001,** *7*, 1562

[103] C. Dendrinou-Samara, L. Alevizopoulou, L. Iordanidis, E. Samaras and D.P. Kessissoglou, *Journal of Inorganic Biochemistry*, **2002,** *1-2*, 89

[104] X.-J. Zhao, Q.-F. Zhang, D.-C. Li, J.-M. Dou and D.-Q. Wang, *Journal of Organometallic Chemistry*, **2010,** *18*, 2134

[105] M. Alexiou, I. Tsivikas, C. Dendrinou-Samara, A.A. Pantazaki, P. Trikalitis, N. Lalioti et al., *Journal of Inorganic Biochemistry*, **2003,** *3-4*, 256

[106] C. Dendrinou-Samara, A.N. Papadopoulos, D.A. Malamatari, A. Tarushi, C.P. Raptopoulou, A. Terzis et al., *Journal of Inorganic Biochemistry*, **2005,** *3*, 864

[107] M. Ullrich, R.J. F. Berger, C. Lustig, R. Fröhlich and N.W. Mitzel, *Eur. J. Inorg. Chem.*, **2006,** *21*, 4219

[108] S. Jana, R. Fröhlich, A. Hepp and N.W. Mitzel, *Organometallics*, **2008,** *6*, 1348

[109] Z. Chen, M. Jia, Z. Zhang and F. Liang, *Crystal Growth & Design*, **2010,** *11*, 4806

[110] M.Soo Lah, B.R. Gibney, D.L. Tierney, J.E. Penner-Hahn and V.L. Pecoraro, *J. Am. Chem. Soc*, **1993,** *13*, 5857

[111] J.J. Bodwin and V.L. Pecoraro, *Inorg. Chem*, **2000,** *16*, 3434

[112] E. Gumienna-Kontecka, I.A. Golenya, N.M. Dudarenko, A. Dobosz, M. Haukka, I.O. Fritsky and J. Swiatek-Kozlowska, *New J. Chem*, **2007,** *10*, 1798

[113] A.V. Pavlishchuk, S.V. Kolotilov, M. Zeller, L.K. Thompson, I.O. Fritsky, A.W. Addison and A.D. Hunter, *Eur. J. Inorg. Chem*, **2010,** *30*, 4851

[114] D. Gaynor, Z.A. Starikova, W. Haase and K.B. Nolan, *J. Chem. Soc., Dalton Trans*, **2001,** *10*, 1578

[115] J. Jankolovits, C.M. Andolina, J.W. Kampf, K.N. Raymond and V.L. Pecoraro, *Angew. Chem. Int. Ed.*, **2011,** *41*, 9660

[116] C.G. Efthymiou, A.A. Kitos, C.P. Raptopoulou, S.P. Perlepes, A. Escuer and C. Papatriantafyllopoulou, *Polyhedron*, **2009,** *15*, 3177

[117] M. Fang, H. Zhao, A.V. Prosvirin, D. Pinkowicz, B. Zhao, P. Cheng et al., *Dalton Trans.*, **2013,** *41*, 14693

[118] J.A. Halfen, J.J. Bodwin and V.L. Pecoraro, *Inorg. Chem*, **1998,** *21*, 5416

[119] A.B. Lago, J. Pasán, L. Cañadillas-Delgado, O. Fabelo, F.J. M. Casado, M. Julve et al., *New J. Chem*, **2011,** *9*, 1817

[120] K. Abu-Dari, S.J. Barclay, P.E. Riley and K.N. Raymond, *Inorg. Chem.*, **1983,** *21*, 3085

[121] Y. Hung, L.Y. Martin, S.C. Jackels, A.Martin Tait and D.H. Busch, *J. Am. Chem. Soc.*, **1977,** *12*, 4029

[122] A.B.P Lever, *Inorganic electronic spectroscopy. 2. Edition,*. **1984**, Elsevier (Studies in physical and theoretical chemistry, 33)

[123] T.J. Hubin, N.W. Alcock, H.J. Clase, L.L. Seib and D.H. Busch, *Inorganica Chimica Acta*, **2002**, 91

[124] T.S. Billson, J.D. Crane, O. Danny Fox and S.L. Heath, *Inorganic Chemistry Communications*, **2000,** *12*, 718

[125] R. Dreos, G. Nardin, L. Randaccio, P. Siega, G. Tauzher and V. Vrdoljak, *Inorganica Chimica Acta*, **2003**, 239

[126] L. Pazderski, J. Toušek, J. Sitkowski, L. Kozerski, R. Marek and E. Szłyk, *Magn. Reson. Chem.*, **2007,** *1*, 24

[127] A. Rodriguez, H. Sakiyama, N. Masciocchi, S. Galli, N. Gálvez, F. Lloret and E. Colacio, *Inorg. Chem.*, **2005,** *23*, 8399

[128] F. Lloret, M. Julve, J. Cano, R. Ruiz-García and E. Pardo, *Inorganica Chimica Acta*, **2008,** *12-13*, 3432

[129] S. Ostrovsky, Z. Tomkowicz and W. Haase, *Coordination Chemistry Reviews*, **2009,** *19-20*, 2363

[130] B. Papánková, R. Boča, Ľ. Dlháň, I. Nemec, J. Titiš, I. Svoboda and H. Fuess, *Inorganica Chimica Acta*, **2010,** *1*, 147

[131] S. Xue, L. Zhao, Y.-N. Guo, R. Deng, Y. Guo and J. Tang, *Dalton Trans*, **2011,** *33*, 8347

[132] J.-L. Liu, K. Yuan, J.-D. Leng, L. Ungur, W. Wernsdorfer, F.-S. Guo et al., *Inorg. Chem.*, **2012,** *15*, 8538

[133] P.-H. Lin, W.-B. Sun, Y.-M. Tian, P.-F. Yan, L. Ungur, L.F. Chibotaru and M. Murugesu, *Dalton Trans.*, **2012,** *40*, 12349

[134] K.S. Cole and R.H. Cole, *J. Chem. Phys.*, **1941,** *4*, 341

[135] C. Dekker, A. Arts, H. de Wijn, A. van Duyneveldt and J. Mydosh, *Phys. Rev. Lett.*, **1988,** *15*, 1780

[136] S.M. J. Aubin, Z. Sun, L. Pardi, J. Krzystek, K. Folting, L.-C. Brunel et al., *Inorg. Chem*, **1999,** *23*, 5329

[137] C. Marcos, A. Argüelles, S.A. Khainakov, J. Rodríguez Fernández and J.A. Blanco, *J. Phys.: Condens. Matter*, **2012,** *34*, 346001

[138] R. Sessoli and A.K. Powell, *Coordination Chemistry Reviews*, **2009,** *19-20*, 2328

[139] D. Gatteschi and R. Sessoli, *Angew. Chem. Int. Ed.*, **2003,** *3*, 268

[140] R.L. Carlin, *Magnetochemistry*, **1986**, Springer Verlag

[141] K.N. Shrivastava, *phys. stat. sol. (b)*, **1983,** *2*, 437

[142] B. Cage and S. Russek, *Rev. Sci. Instrum.*, **2004,** *11*, 4401

[143] Y.-N. Guo, G.-F. Xu, Y. Guo and J. Tang, *Dalton Trans.*, **2011,** *39*, 9953

[144] P.-E. Car, M. Perfetti, M. Mannini, A. Favre, A. Caneschi and R. Sessoli, *Chem. Commun.*, **2011,** *13*, 3751

[145] D.-K. Cao, J.-Q. Feng, M. Ren, Y.-W. Gu, Y. Song and M.D. Ward, *Chem. Commun.*, **2013,** *78*, 8863

3.9 Supplementary Information

3.9.1 Synthesis

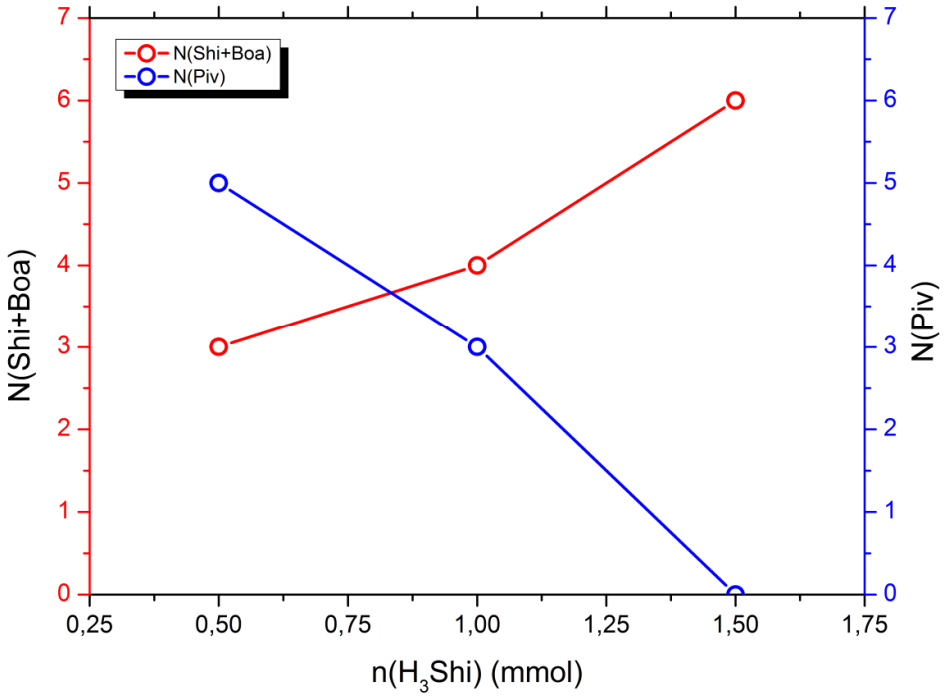

Figure S1 Representation of the numerical correlations between the amounts of added salicylhydroxamic acid to the reaction mixture and the incorporation of pivalate and salicylhydroximate and its rearrangement product 2-benzoxazolinone for the complexe **1**, **4** and **3**

3.9.2 X-Ray Crystallography

Compound	**1**	**2**	**3**	**4**
Formula	$C_{72}H_{113}Co_5N_{10}O_{21}$	$C_{217}H_{188}Co_{12}N_{36}O_{42}$	$C_{86}H_{111}Co_5N_{19}O_{16}$	$C_{152}H_{228}Co_{10}Li_2N_{22}O_{39}$
Formula weight	1749.40	4679.23	1961.59	3590.77
T/K	173	193	173	173
Wavelength/Å	0.71073	0.71073	0.71073	0.71073
Crystal system	triclinic	orthorhombic	monoclinic	monoclinic
Space group	P-1	*Pna*2$_1$	*P*2$_1$/*c*	*P*2$_1$/*c*
a/Å	13.5360 (14)	33.3846(6)	12.4556(8)	16.4058(13)
b/Å	14.4649 (15)	20.5408(4)	14.1543(10)	13.8683(12)
c/Å	22.118 (2)	44.7938(11)	27.0878(18)	37.422(3)
α/°	90.036 (4)	90	90	90
β/°	91.929 (4)	90	95.660(2)	93.758(3)
γ/°	89.563 (4)	90	90	90
V/Å^3	4328.2 (8)	30717.2(11)	4752.3(6)	8495.9(12)
Z	2	4	2	2
δ_{calcd}/gcm^{-3}	1.342	1.012	1.371	1.404
μ/mm^{-1}	1.01	0.688	0.926	1.029
Crystal size/mm	0.68 × 0.21 × 0.03	0.55 × 0.36 × 0.15	0.67 × 0.32 × 0.17	0.58 × 0.37 × 0.02
θ_{max}/°	28.251	28.090	28.182	28.084
Reflns. collected	74478	144482	55742	87482
Indep. Reflns (Rint)	20956 (0.1213)	63935 (0.0901)	11526 (0.0574)	20523 (0.1180)
Data/restrains/ parameters	20956/1029/1330	63935/1542/2945	11526/65/625	20523/693/1270
Goof on F^2	1.004	0.899	1.019	1.037
R$_1$, wR$_2$ (I>2σ(I))	0.0692 0.1601	0.0747 0.1896	0.0414 0.1237	0.0579 0.1087
R$_1$, wR$_2$ (all data)	0.1672 0.2104	0.1399 0.2414	0.0629 0.1320	0.1341 0.1306
Largest diff. peak and hole/e Å^{-3}	0.857/-0.749	0.424/-0.662	0.858/-0.385	0.654/-0.442

Table 1 Crystallographic data and refinement parameter for **1**, **2**, **3** and **4**

Compound	**5**	**6**	**7**	**8**
Formula	$C_{64.50}H_{94}Co_5N_{10}O_{26.50}$	$C_{70.75}H_{75}Co_5N_{10}O_{18.75}$	$C_{90.50}H_{106}Co_7N_{13}O_{29.50}$	$C_{74.75}H_{90}Co_5N_{11}O_{21.75}$
Formula weight	1728.16	1660.08	2260.42	1785.25
T/K	173	173	173	173
Wavelength/Å	0.71073	0.71073	0.71073	0.71073
Crystal system	monoclinic	monoclinic	monoclinic	Triclinic
Space group	*Cc*	$P2_1/n$	$P2_1/c$	P-1
a/Å	23.7782(15)	11.9059(3)	14.6249(7)	13.0028(5)
b/Å	14.1935(10)	15.7265(3)	45.079(2)	14.3466(5)
c/Å	24.8771(16)	39.7489(9)	16.3199(8)	22.4090(8)
α/°	90	90	90	85.7340(11)
β/°	118.027(2)	93.1140(10)	95.577(2)	81.0565(11)
γ/°	90	90	90	89.7543(11)
V/Å^3	7411.3(9)	7431.5(3)	10708.3(9)	4118.0(4)
Z	4	4	4	2
δ_{calcd}/gcm^{-3}	1.549	1.484	1.402	1.440
μ/mm^{-1}	1.182	1.169	1.135	1.063
Crystal size/mm	0.55 × 0.42 × 0.20	0.25 × 0.25 × 0.21	0.74 × 0.67 × 0.61	0.57 × 0.37 × 0.09
θ_{max}/°	28.002	26.427	27.922	28.100
Reflns. collected	63989	64992	154596	74525
Indep. Reflns (Rint)	16286(0.0540)	15223(0.0873)	25610(0.0607)	19900(0.0532)
Data/restrains/ parameters	16286/303/1049	15223/549/1177	25610/792/1661	19900/556/1325
Goof on F^2	1.021	0.933	1.068	1.042
R_1, wR_2 (I>2σ(I))	0.0329	0.0513	0.0507	0.0437
	0.0784	0.1145	0.1406	0.1182
R_1, wR_2 (all data)	0.0361	0.1184	0.0743	0.0764
	0.0796	0.1280	0.1509	0.1367
Largest diff. peak and hole/e Å^{-3}	0.741/-0.488	0.839/-0.523	0.906/-0.559	0.827/-0.364

Table 2 Crystallographic data and refinement parameter for **5**, **6**, **7** and **8**

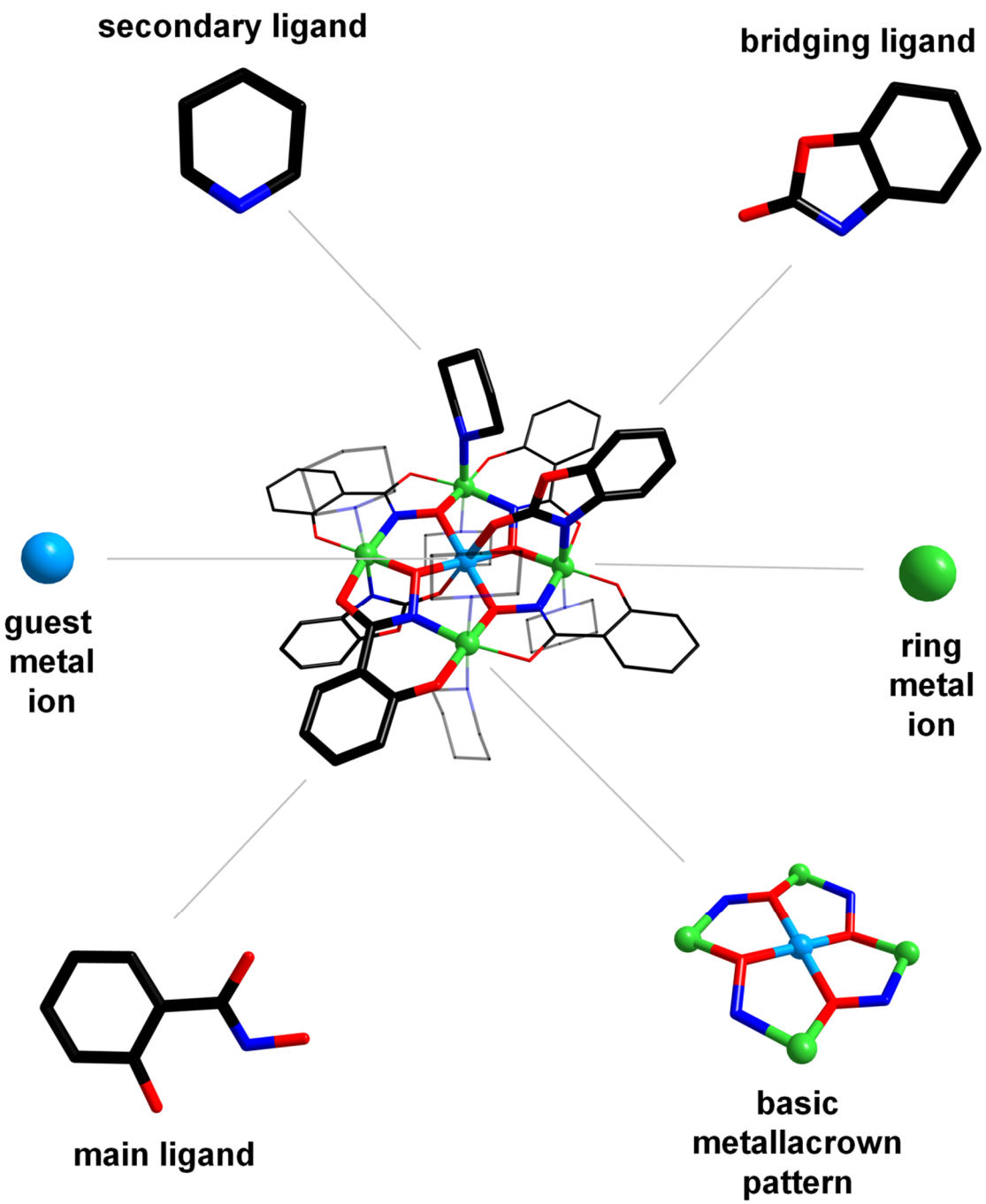

Figure S2 Definition of the functional components of a metallacrown using the example of the molecular structure of **3;** color code: green - Co(III), light blue - Co(II), red - O, dark blue - N, black -C

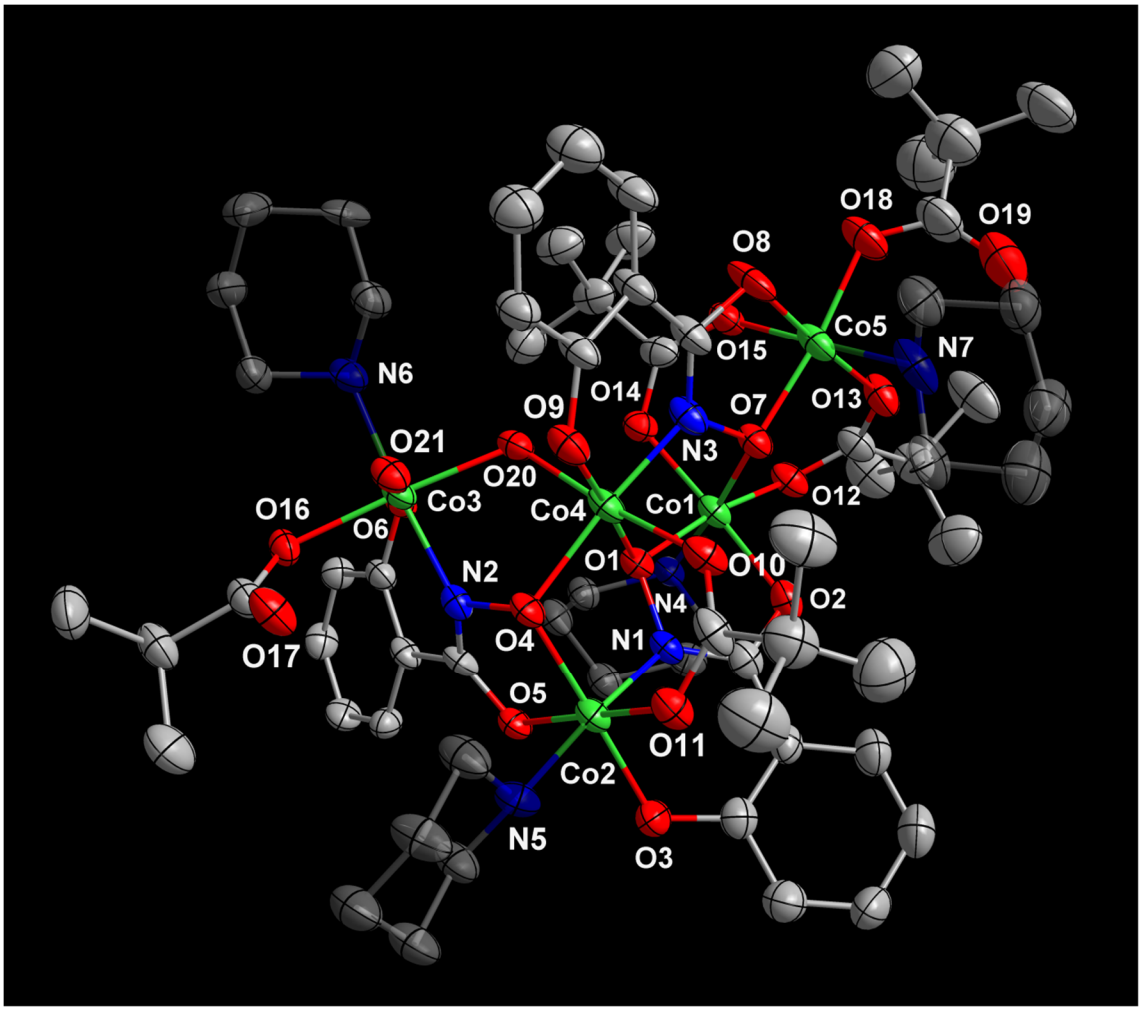

Figure S3 Molecular structure of **1** with numbering scheme and thermal ellipsoids at 50% probability level; color scheme: green - Co(III), red - O, dark blue - N, grey - C

Selected Interatomic Distances (Å) in the Crystal Structure of 1					
Co1–O1	1.904 (4)	Co4–O1	1.908 (4)	Co1···Co2	4.5285(12)
Co1–O2	1.898 (5)	Co4–O4	1.961 (4)	Co1···Co3	5.3437(11)
Co1–O7	1.934 (4)	Co4–O9	1.902 (4)	Co1···Co4	3.2773(12)
Co1–O12	1.927 (4)	Co4–O10	1.938 (5)	Co1···Co5	3.2706(12)
Co1–O14	1.913 (4)	Co4–O20	1.907 (3)		
Co1–N4	2.010 (5)	Co4–N3	1.883 (5)	Co2···Co3	4.5069(13)
				Co2···Co4	3.1555(13)
Co2–O3	1.881 (5)	Co5–O7	1.895 (4)	Co2···Co5	6.8881(14)
Co2–O4	1.911 (4)	Co5–O8	1.876 (5)		
Co2–O5	1.885 (4)	Co5–O13	1.911 (5)	Co3···Co4	3.2494(10)
Co2–O11	1.893 (4)	Co5–O15	1.958 (5)	Co3···Co5	6.9603(13)
Co2–N1	1.883 (5)	Co5–O18	1.905 (5)		
Co2–N5	1.979 (5)	Co5–N7	1.943 (7)	Co4···Co5	4.4958(13)
Co3–O6	1.887 (4)				
Co3–O16	1.915 (4)				
Co3–O20	1.9283 (12)				
Co3–O21	1.943 (4)				
Co3–N2	1.883 (5)				
Co3–N6	2.005 (6)				

Table S3 Selected interatomic distances in the crystal structure of **1**

Selected Angles (°) in the Crystal Structure of 1					
O1–Co1–O2	84.09 (18)	O6–Co3–O16	88.58 (17)	O7–Co5–O8	85.48 (19)
O1–Co1–O7	87.85 (17)	O6–Co3–O20	89.75 (12)	O7–Co5–O13	97.52 (19)
O1–Co1–O12	170.71 (19)	O6–Co3–O21	175.76 (19)	O7–Co5–O15	89.50 (18)
O1–Co1–O14	92.88 (13)	O6–Co3– N2	91.50 (19)	O7–Co5–O18	173.3 (2)
O1–Co1–N4	91.69 (19)	O6–Co3–N6	84.1 (2)	O7–Co5–N7	92.4 (2)
O2–Co1–O7	91.54 (19)	O16–Co3–O20	176.81 (17)	O8–Co5–O13	176.84 (19)
O2–Co1–O12	89.8 (2)	O16–Co3–O21	90.36 (17)	O8–Co5–O15	87.1 (2)
O2–Co1–O14	176.96 (14)	O16–Co3– N2	92.37 (19)	O8–Co5–O18	89.0 (2)
O2–Co1–N4	93.1 (2)	O16–Co3–N6	92.2 (2)	O8–Co5–N7	94.2 (2)
O7–Co1–O12	99.33 (17)	O20–Co3–O21	91.50 (12)	O13–Co5–O15	93.9 (2)
O7–Co1–O14	88.48 (17)	O20–Co3– N2	84.95 (18)	O13–Co5–O18	88.1 (2)
O7–Co1–N4	175.3 (2)	O20–Co3–N6	90.35 (19)	O13–Co5–N7	84.7 (2)
O12–Co1–O14	93.19 (15)	O21–Co3–N2	92.6 (2)	O15–Co5–O18	86.4 (2)
O12–Co1–N4	81.63 (19)	O21–Co3–N6	91.9 (2)	O15–Co5–N7	177.8 (2)
O14–Co1–N4	86.82 (19)	N2–Co3–N6	173.6 (2)	O18–Co5–N7	91.8 (2)
O3–Co2–O4	178.29 (17)	O1–Co4–O4	84.96 (16)	Co1–O1–Co4	118.6 (2)
O3–Co2–O5	92.25 (19)	O1–Co4–O9	177.45 (17)	Co1–O7–Co5	117.4 (2)
O3–Co2–O11	89.1 (2)	O1–Co4–O10	96.59 (19)		
O3–Co2–N1	90.4 (2)	O1–Co4–O20	90.36 (14)	Co2–O4–Co4	109.2 (2)
O3–Co2–N5	86.2 (2)	O1–Co4– N3	89.40 (19)		
O4–Co2–O5	86.09 (18)	O4–Co4–O9	92.53 (17)	Co3–O20–Co4	115.82 (15)
O4–Co2–O11	92.49 (19)	O4–Co4–O10	93.04 (18)		
O4–Co2– N1	90.0 (2)	O4–Co4–O20	91.15 (15)		
O4–Co2–N5	93.5 (2)	O4–Co4– N3	173.7 (2)		
O5–Co2–O11	176.06 (19)	O9–Co4–O10	84.02 (19)		
O5–Co2–N1	90.07 (19)	O9–Co4–O20	89.20 (15)		
O5–Co2–N5	92.4 (2)	O9–Co4– N3	93.1 (2)		
O11–Co2– N1	93.6 (2)	O10–Co4–O20	172.18 (16)		
O11–Co2–N5	84.0 (2)	O10–Co4– N3	84.7 (2)		
N1–Co2–N5	175.9 (2)	O20–Co4– N3	91.80 (19)		

Table S4 Selected angles in the crystal structure of **1**

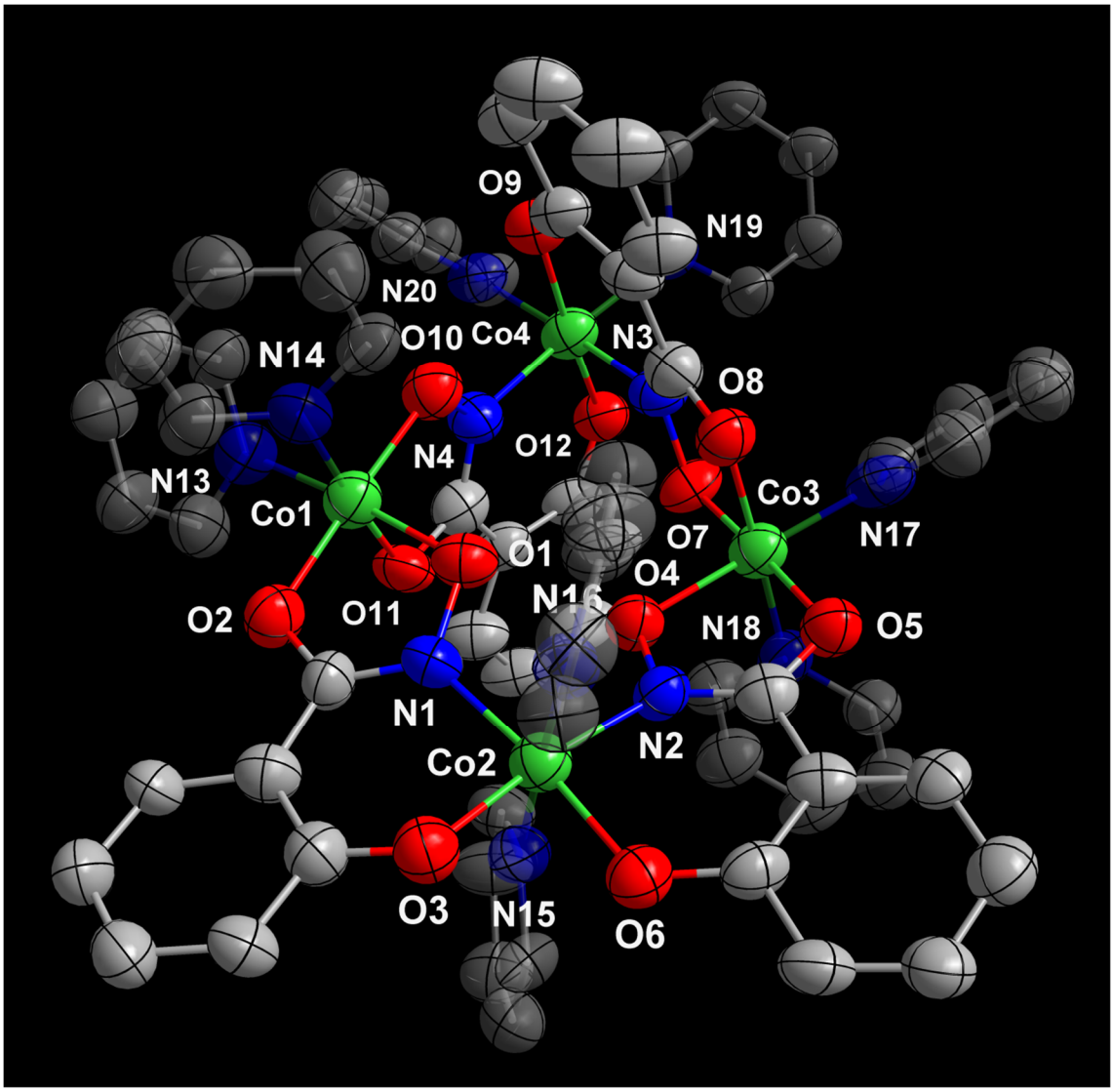

Figure S4 Molecular structure of the first molecule in the asymmetric unit of **2** with numbering scheme and thermal ellipsoids at 50% probability level; color scheme: green - Co(III), red - O, dark blue - N, grey - C

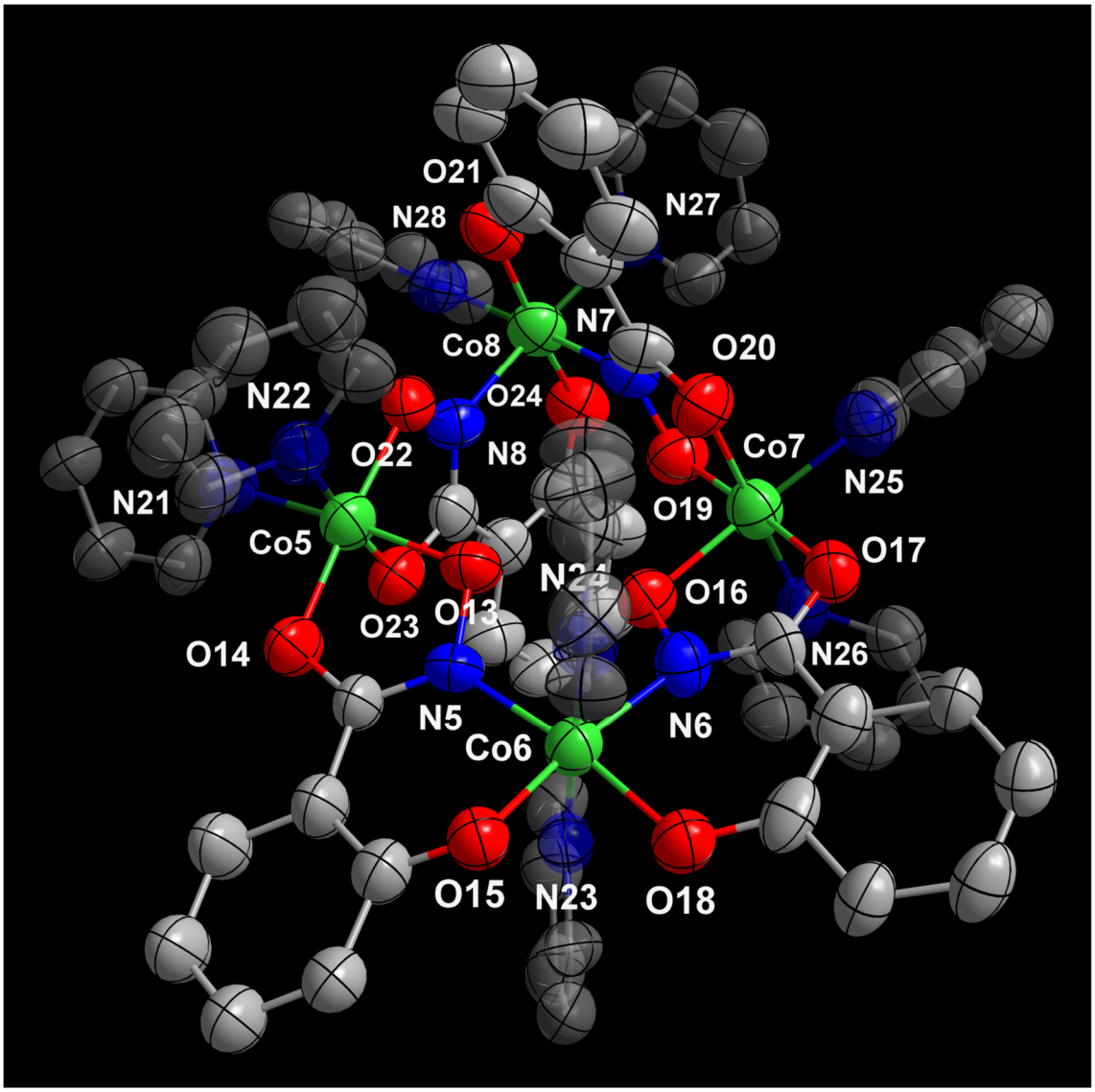

Figure S5 Molecular structure of the second molecule in the asymmetric unit of **2** with numbering scheme and thermal ellipsoids at 50% probability level; color scheme: green - Co(III), red - O, dark blue - N, grey - C

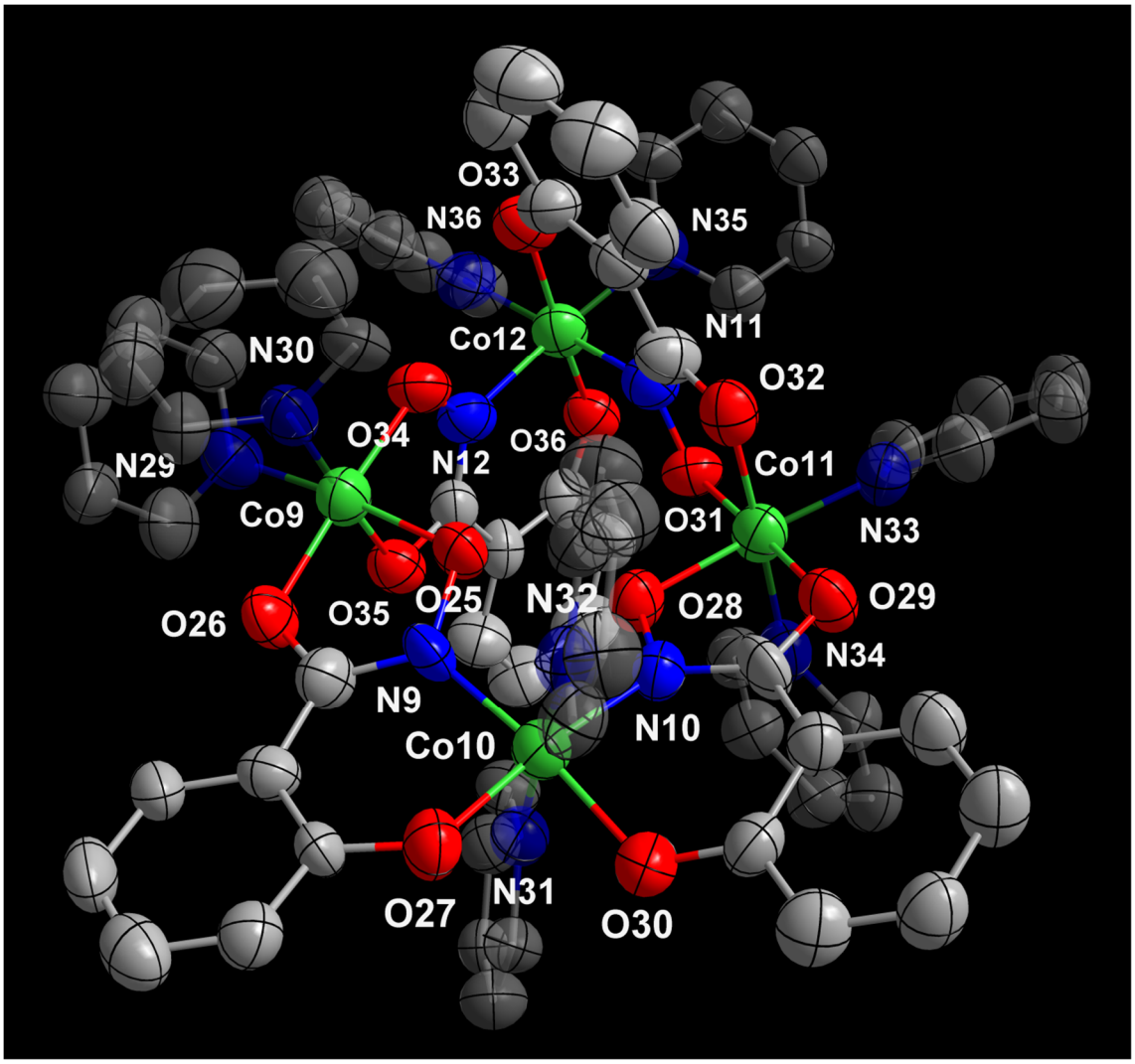

Figure S6 Molecular structure of the third molecule in the asymmetric unit of **2** with numbering scheme and thermal ellipsoids at 50% probability level; color scheme: green - Co(III), red - O, dark blue - N, grey - C

Selected Interatomic Distances (Å) of the first molecule in the Crystal Structure of 2					
Co1–O1	1.915 (8)	Co3–O4	1.935 (7)	Co1···Co2	4.600(4)
Co1–O2	1.866 (8)	Co3–O5	1.896 (8)	Co1···Co4	4.442(4)
Co1–O10	1.858 (8)	Co3–O7	1.805 (8)	Co2···Co3	4.595(4)
Co1–O11	1.864 (9)	Co3–O8	1.869 (8)	Co3···Co4	4.441(4)
Co1–N13	1.914 (10)	Co3–N17	1.916 (11)		
Co1–N14	1.960 (11)	Co3–N18	1.930 (11)	Co1···Co3	5.314(6)
				Co2···Co4	7.3109(17)
Co2–O3	1.892 (6)	Co4–O9	1.885 (8)		
Co2–O6	1.887 (6)	Co4–O12	1.889 (8)		
Co2–N1	1.918 (9)	Co4–N3	1.913 (10)		
Co2–N2	1.920 (9)	Co4–N4	1.878 (9)		
Co2–N15	1.977 (10)	Co4–N19	1.992 (10)		
Co2–N16	1.955 (11)	Co4–N20	1.993 (10)		

Table S5 Selected interatomic distances of the first molecule in the crystal structure of **2**

Selected Interatomic Distances (Å) of the second molecule in the Crystal Structure of 2					
Co5–O13	1.938 (8)	Co7–O16	1.932 (8)	Co5···Co6	4.609(2)
Co5–O14	1.857 (8)	Co7–O17	1.865 (8)	Co5···Co8	4.4.51(5)
Co5–O22	1.868 (8)	Co7–O19	1.844 (9)	Co6···Co7	4.581(5)
Co5–O23	1.839 (9)	Co7–O20	1.875 (9)	Co7···Co8	4.446(3)
Co5–N21	1.912 (11)	Co7–N25	1.931 (10)		
Co5–N22	1.942 (10)	Co7–N26	1.936 (11)	Co5···Co7	5.404(4)
				Co6···Co8	7.250(4)
Co6–O15	1.856 (6)	Co8–O21	1.852 (10)		
Co6–O18	1.869 (6)	Co8–O24	1.889 (10)		
Co6–N5	1.919 (9)	Co8–N7	1.863 (10)		
Co6–N6	1.922 (9)	Co8–N8	1.905 (10)		
Co6–N23	1.960 (10)	Co8–N27	1.998 (11)		
Co6–N24	1.948 (10)	Co8–N28	2.022 (10)		

Table S6 Selected interatomic distances of the second molecule in the crystal structure of **2**

Selected Interatomic Distances (Å) of the third molecule in the Crystal Structure of 2					
Co9–O25	1.950 (7)	Co11–O28	1.919 (8)	Co9···Co10	4.593(5)
Co9–O26	1.883 (8)	Co11–O29	1.879 (8)	Co9···Co12	4.454(3)
Co9–O34	1.836 (8)	Co11–O31	1.830 (8)	Co10···Co11	4.605(3)
Co9–O35	1.848 (8)	Co11–O32	1.861 (9)	Co11···Co12	4.459(6)
Co9–N29	1.893 (10)	Co11–N33	1.916 (10)		
Co9–N30	1.946 (10)	Co11–N34	1.955 (11)	Co9···Co11	5.419(4)
				Co10···Co12	7.253(4)
Co10–O27	1.902 (7)	Co12–O33	1.862 (9)		
Co10–O30	1.882 (8)	Co12–O36	1.868 (9)		
Co10–N9	1.903 (10)	Co12–N11	1.925 (10)		
Co10–N10	1.900 (9)	Co12–N12	1.915 (10)		
Co10–N31	1.970 (10)	Co12–N35	1.960 (11)		
Co10–N32	1.972 (10)	Co12–N36	2.008 (10)		

Table S7 Selected interatomic distances of the third molecule in the crystal structure of **2**

Selected Angles (°) of the first molecule in the Crystal Structure of 2			
O1–Co1–O2	83.9(3)	O4–Co3–O5	84.6(3)
O1–Co1–O10	93.2(3)	O4–Co3–O7	93.3(3)
O1–Co1–O11	88.1(3)	O4–Co3–O8	89.0(3)
O1–Co1–N13	175.2(4)	O4–Co3–N17	175.3(4)
O1–Co1–N14	91.1(4)	O4–Co3–N18	90.1(4)
O2–Co1–O10	177.1(4)	O5–Co3–O7	177.9(4)
O2–Co1–O11	93.3(3)	O5–Co3–O8	92.7(3)
O2–Co1–N13	93.0(4)	O5–Co3–N17	91.3(3)
O2–Co1–N14	89.8(4)	O5–Co3–N18	88.9(4)
O10–Co1–O11	86.7(3)	O7–Co3–O8	87.1(3)
O10–Co1–N13	89.9(4)	O7–Co3–N17	90.7(4)
O10–Co1–N14	90.1(4)	O7–Co3–N18	91.3(4)
O11–Co1–N13	88.5(4)	O8–Co3–N17	88.9(3)
O11–Co1–N14	176.7(4)	O8–Co3–N18	178.1(4)
N13–Co1–N14	92.5(4)	N17–Co3–N18	92.1(4)
O3–Co2–O6	82.20(12)	O9–Co4–O12	170.5(3)
O3–Co2–N1	91.1(3)	O9–Co4–N3	93.5(4)
O3–Co2–N2	172.6(3)	O9–Co4– N4	94.2(4)
O3–Co2–N15	89.7(4)	O9–Co4–N19	88.4(3)
O3–Co2–N16	89.8(4)	O9–Co4–N20	85.0(4)
O6–Co2–N1	173.3(3)	O12–Co4–N3	93.5(4)
O6–Co2–N2	90.4(3)	O12–Co4– N4	92.7(4)
O6–Co2–N15	89.3(4)	O12–Co4–N19	85.1(3)
O6–Co2–N16	89.1(4)	O12–Co4–N20	88.3(4)
N1–Co2–N2	96.3(3)	N3–Co4–N4	85.4(3)
N1–Co2–N15	90.7(4)	N3–Co4–N19	91.5(4)
N1–Co2–N16	90.9(4)	N3–Co4–N20	176.5(4)
N2–Co2–N15	90.4(4)	N4–Co4–N19	176.1(4)
N2–Co2–N16	89.8(4)	N4–Co4–N20	91.5(4)
N15–Co2–N16	178.3(4)	N19–Co4–N20	91.6(3)

Table S8 Selected angles of the first molecule in the crystal structure of **2**

Selected Angles (°) of the second molecule in the Crystal Structure of 2			
O13–Co5–O14	83.2(3)	O16–Co7–O17	83.9(3)
O13–Co5–O22	93.3(3)	O16–Co7–O19	92.4(3)
O13–Co5–O23	89.3(4)	O16–Co7–O20	89.0(4)
O13–Co5–N21	176.2(3)	O16–Co7–N25	175.3(4)
O13–Co5–N22	88.5(4)	O16–Co7–N26	91.0(4)
O14–Co5–O22	176.3(4)	O17–Co7–O19	176.2(4)
O14–Co5–O23	92.6(4)	O17–Co7–O20	92.5(4)
O14–Co5–N21	93.0(3)	O17–Co7–N25	91.6(4)
O14–Co5–N22	89.6(4)	O17–Co7–N26	89.0(4)
O22–Co5–O23	86.2(4)	O19–Co7–O20	86.8(4)
O22–Co5–N21	90.5(3)	O19–Co7–N25	92.1(4)
O22–Co5–N22	91.5(4)	O19–Co7–N26	91.8(4)
O23–Co5–N21	90.4(4)	O20–Co7–N25	90.1(4)
O23–Co5–N22	176.7(4)	O20–Co7–N26	178.6(4)
N21–Co5–N22	92.0(4)	N25–Co7–N26	90.1(4)
O15–Co6–O18	82.22(19)	O21–Co8–O24	170.3(4)
O15–Co6–N5	90.8(3)	O21–Co8–N7	93.4(4)
O15–Co6–N6	171.3(3)	O21–Co8–N8	93.9(4)
O15–Co6–N23	90.9(4)	O21–Co8–N27	88.4(4)
O15–Co6–N24	87.9(3)	O21–Co8–N28	84.9(4)
O18–Co6–N5	172.6(3)	O24–Co8–N7	94.0(4)
O18–Co6–N6	89.8(3)	O24–Co8–N8	93.0(4)
O18–Co6–N23	87.3(3)	O24–Co8–N27	85.2(4)
O18–Co6–N24	90.5(3)	O24–Co8–N28	88.1(4)
N5–Co6–N6	97.3(4)	N7–Co8–N8	86.2(4)
N5–Co6–N23	90.3(4)	N7–Co8–N27	90.3(4)
N5–Co6–N24	91.7(4)	N7–Co8–N28	176.8(4)
N6–Co6–N23	92.1(4)	N8–Co8–N27	175.9(4)
N6–Co6–N24	88.9(4)	N8–Co8–N28	91.3(4)
N23–Co6–N24	177.6(4)	N27–Co8–N28	92.3(4)

Table S9 Selected angles of the second molecule in the crystal structure of **2**

Selected Angles (°) of the third molecule in the Crystal Structure of 2			
O25–Co9–O26	84.0(3)	O28–Co11–O29	83.2(3)
O25–Co9–O34	92.4(3)	O28–Co11–O31	94.0(3)
O25–Co9–O35	88.8(4)	O28–Co11–O32	89.8(3)
O25–Co9–N29	175.0(4)	O28–Co11–N33	175.9(4)
O25–Co9–N30	88.5(4)	O28–Co11–N34	88.9(3)
O26–Co9–O34	176.4(4)	O29–Co11–O31	176.3(4)
O26–Co9–O35	91.9(4)	O29–Co11–O32	91.6(4)
O26–Co9–N29	91.0(4)	O29–Co11–N33	92.8(4)
O26–Co9–N30	88.9(4)	O29–Co11–N34	90.0(4)
O34–Co9–O35	87.2(4)	O31–Co11–O32	85.9(4)
O34–Co9–N29	92.5(4)	O31–Co11–N33	90.0(4)
O34–Co9–N30	91.8(4)	O31–Co11–N34	92.4(4)
O35–Co9–N29	90.5(4)	O32–Co11–N33	91.3(4)
O35–Co9–N30	177.1(4)	O32–Co11–N34	177.8(4)
N29–Co9–N30	92.3(4)	N33–Co11–N34	90.1(4)
O27–Co10–O30	83.2(3)	O33–Co12–O36	170.9(4)
O27–Co10–N9	91.7(3)	O33–Co12–N11	92.1(4)
O27–Co10–N10	171.4(3)	O33–Co12–N12	94.5(4)
O27–Co10–N31	90.2(3)	O33–Co12–N35	87.7(4)
O27–Co10–N32	88.0(4)	O33–Co12–N36	85.7(4)
O30–Co10–N9	173.9(3)	O36–Co12–N11	94.6(4)
O30–Co10–N10	89.1(4)	O36–Co12–N12	92.1(4)
O30–Co10–N31	87.0(3)	O36–Co12–N35	86.1(4)
O30–Co10–N32	90.5(4)	O36–Co12–N36	87.9(4)
N9–Co10–N10	96.2(4)	N11–Co12–N12	85.2(4)
N9–Co10–N31	89.7(4)	N11–Co12–N35	91.5(4)
N9–Co10–N32	92.7(4)	N12–Co12–N35	176.1(4)
N10–Co10–N31	93.2(4)	N11–Co12–N36	176.3(4)
N10–Co10–N32	88.2(4)	N12–Co12–N36	92.0(4)
N31–Co10–N32	177.0(4)	N35–Co12–N36	91.4(4)

Table S10 Selected angles of the third molecule in the crystal structure of **2**

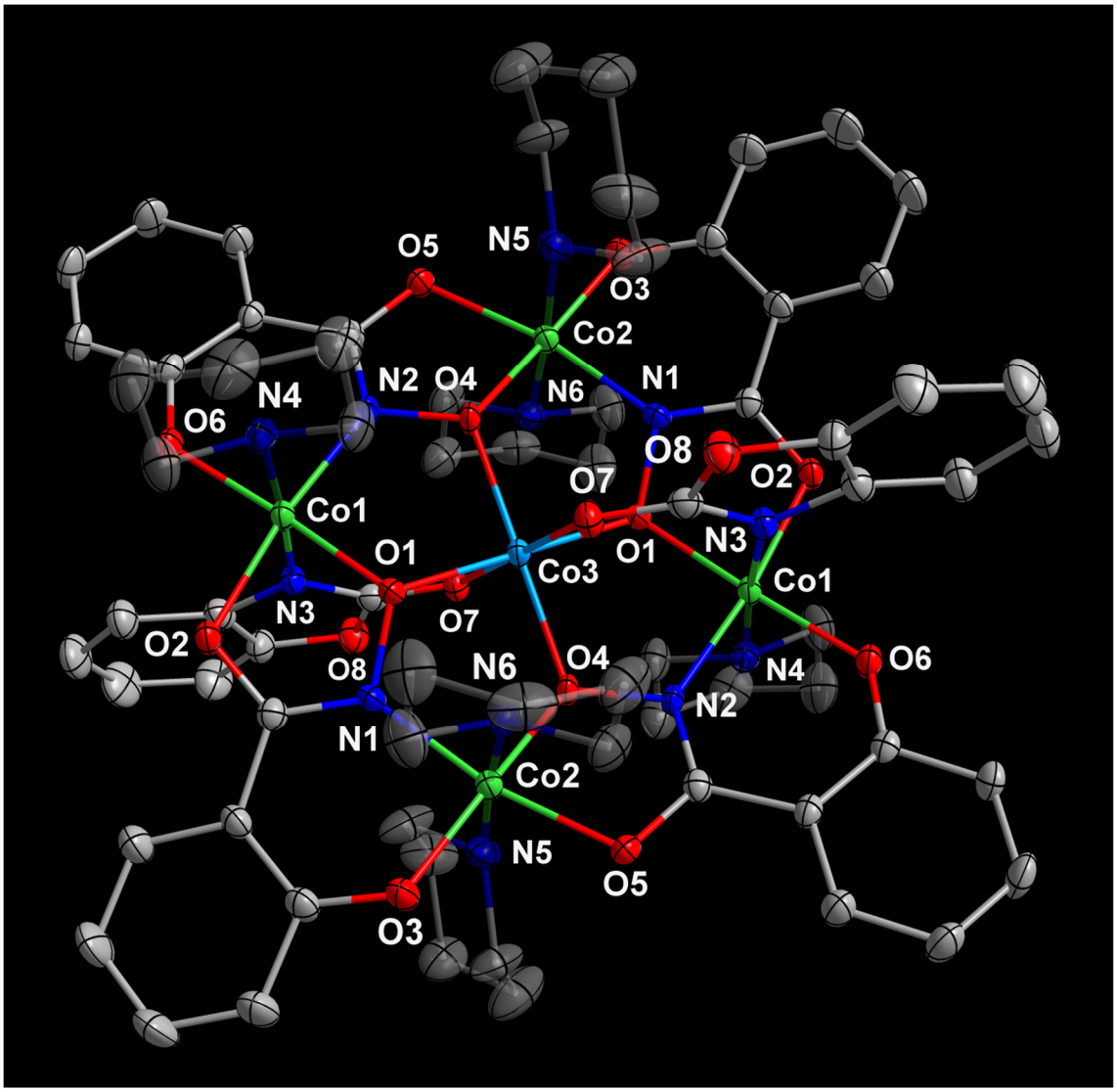

Figure S7 Molecular structure of **3** with numbering scheme and thermal ellipsoids at 50% probability level; color scheme: green - Co(III), light blue - Co(II), red - O, dark blue - N, grey - C

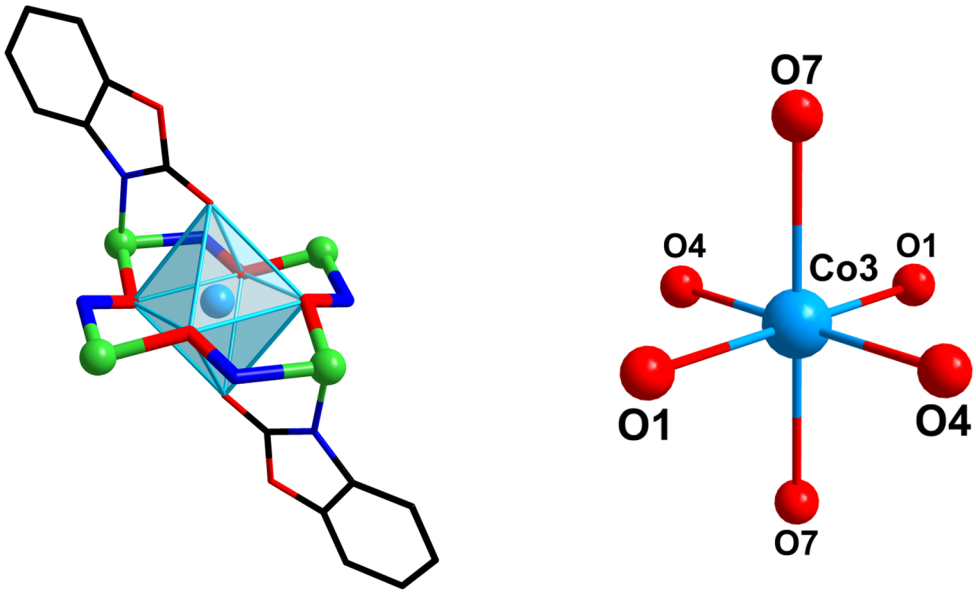

Figure 8 Coordination polyhedron (left) and coordination sphere (right) of the central Co(II) guest ion in **3;** color code: green - Co(III), light blue - Co(II), red - O, dark blue - N, black - C

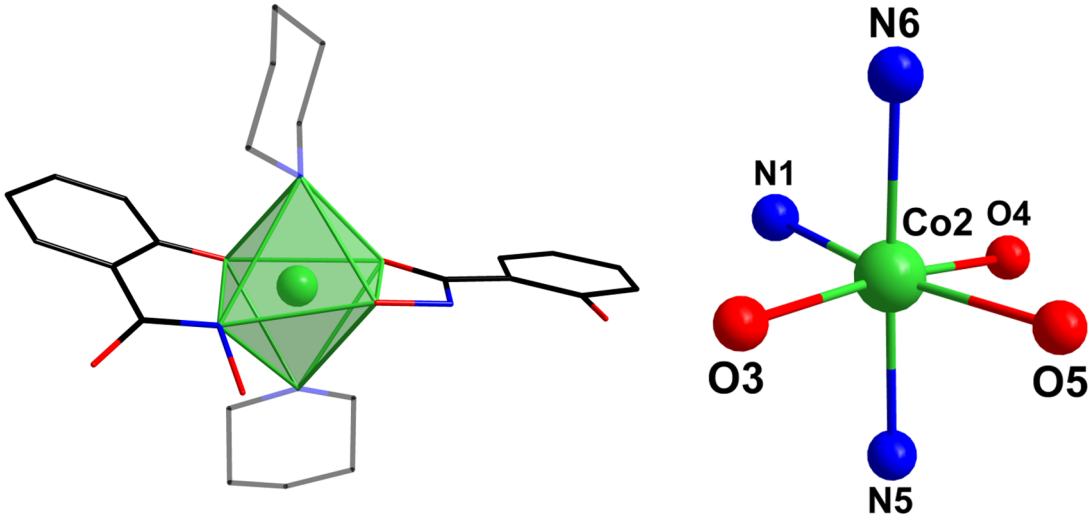

Figure 9 Coordination polyhedron (left) and coordination sphere (right) of the Co(III) ion Co2 in **3;** color code: green - Co(III), red - O, dark blue - N, black - C

Selected Interatomic Distances (Å) in the Crystal Structure of 3			
Co1–O1	1.8901 (17)	Co3–O1	1.9609 (17)
Co1–O2	1.9618 (18)	Co3–O1*	1.9609 (17)
Co1–O6*	1.8763 (18)	Co3–O4	1.9409 (17)
Co1–N2*	1.930 (2)	Co3–O4*	1.9410 (17)
Co1–N3	1.945 (2)	Co3–O7	2.1771 (18)
Co1–N4	1.998 (2)	Co3–O7*	2.1771 (18)
Co2–O3	1.8839 (18)	Co1···Co2	4.5521(6)
Co2–O4	1.8979 (17)	Co1···Co2*	4.5978(7)
Co2–O5	1.9523 (17)		
Co2–N1	1.920 (2)	Co1···Co3	3.1956(4)
Co2–N5	2.014 (2)	Co2···Co3	3.2739(6)
Co2–N6	2.064 (2)		

Table S11 Selected interatomic distances in the crystal structure of **3**

Selected Angles (°) in the Crystal Structure of 3					
O1–Co1–O2	79.85 (7)	O3–Co2–O4	172.72 (8)	O1–Co3–O1*	180.0
O1–Co1– O6*	174.06 (8)	O3–Co2–O5	100.29 (8)	O1–Co3–O4*	90.01 (7)
O1–Co1–N2*	93.81 (8)	O3–Co2–N1	90.33 (8)	O1–Co3–O4	89.99 (7)
O1–Co1–N3	92.91 (8)	O3–Co2–N5	89.03 (9)	O1–Co3–O7	91.64 (7)
O1–Co1–N4	91.35 (8)	O3–Co2–N6	89.27 (9)	O1–Co3–O7*	88.36 (7)
O2–Co1– O6*	95.82 (7)	O4–Co2–O5	80.19 (7)	O4–Co3–O4*	180.0
O2–Co1– N2*	172.78 (8)	O4–Co2–N1	89.71 (8)	O4–Co3–O7	92.28 (7)
O2–Co1– N3	85.64 (8)	O4–Co2–N5	83.76 (9)	O7–Co3–O7*	180.00 (14)
O2–Co1–N4	94.46 (8)	O4–Co2–N6	98.00 (8)		
O6*–Co1–N2*	90.74 (8)	O5–Co2– N1	168.83 (8)	Co1–O1–Co3	112.15 (9)
O6*–Co1–N3	90.80 (8)	O5–Co2–N5	85.48 (9)	Co2–O4–Co3	117.05 (9)
O6*–Co1–N4	84.91 (9)	O5–Co2–N6	90.20 (8)		
N2*–Co1–N3	91.27 (9)	N1–Co2–N5	98.25 (9)		
N2*–Co1–N4	89.12 (9)	N1–Co2–N6	86.46 (9)		
N3–Co1–N4	175.69 (9)	N5–Co2–N6	175.00 (9)		

Table S12 Selected angles in the crystal structure of **3**

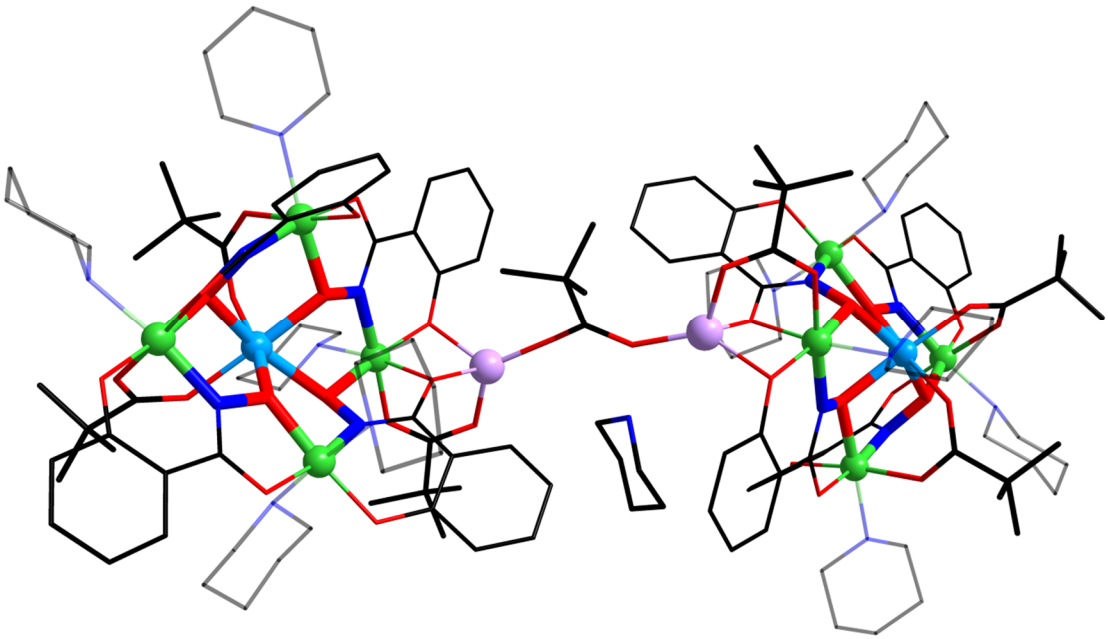

Figure S10 Molecular structure of **4**; color code: green - Co(III), light blue - Co(II), red - O, dark blue - N, black – C, violet - Li

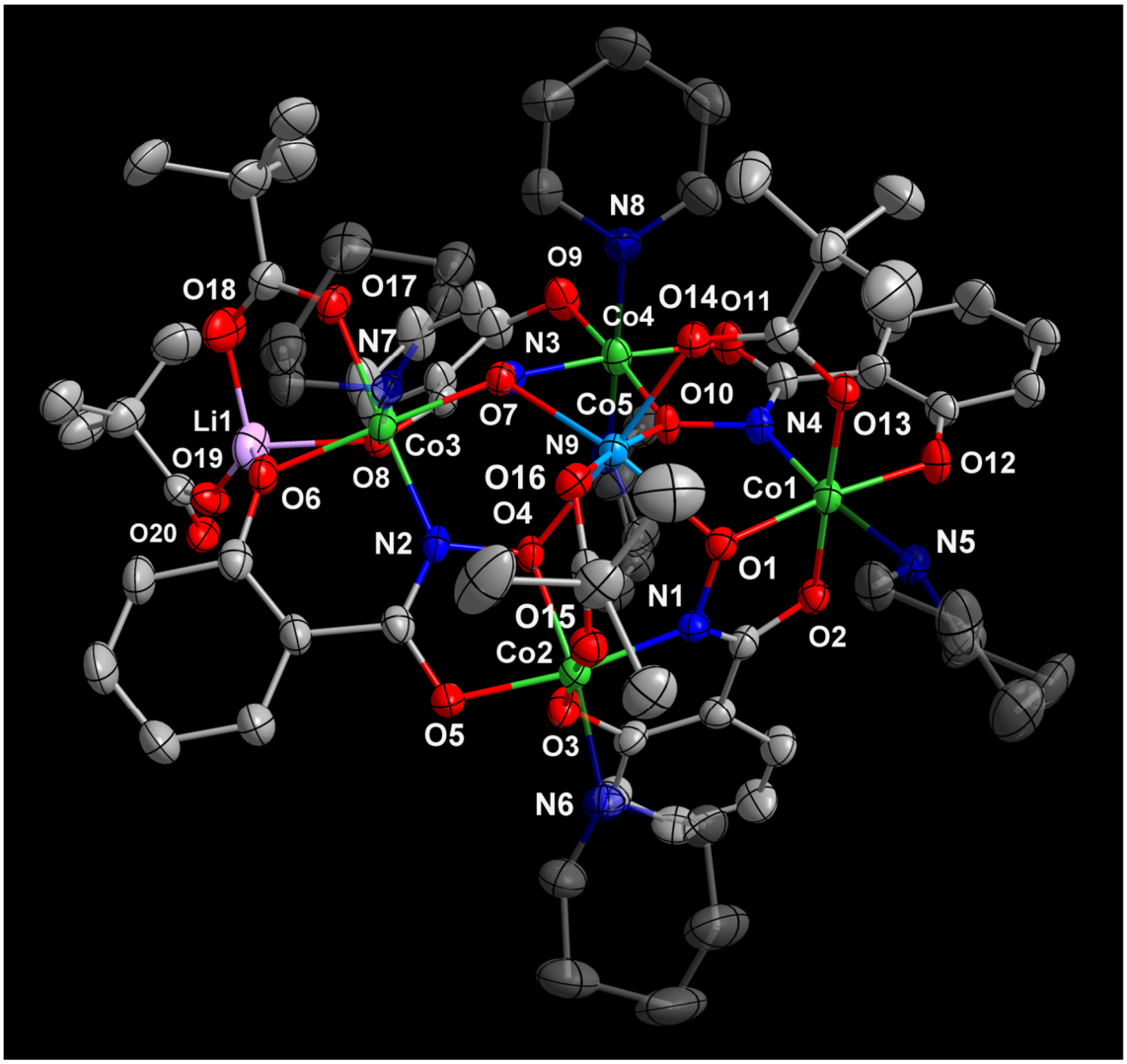

Figure S11 Metallacrown subunit in the molecular structure of **4** with numbering scheme and thermal ellipsoids at 50% probability level; color scheme: green - Co(III), light blue - Co(II), red - O, dark blue - N, grey - C

Selected Interatomic Distances (Å) in the Crystal Structure of 4					
Co1–O1	1.899 (2)	Co4–O9	1.914 (3)	Co1···Co2	4.5372(8)
Co1–O2	1.898 (2)	Co4–O10	1.869 (2)	Co1···Co4	4.5566(11)
Co1–O12	1.893 (2)	Co4–O11	1.919 (3)	Co2···Co3	4.5824(11)
Co1–O13	1.922 (2)	Co4–N3	1.887 (3)	Co3···Co4	4.5228(8)
Co1–N4	1.916 (3)	Co4–N8	2.039 (4)		
Co1–N5	2.000 (3)	Co4–N9	2.017 (3)	Co1···Co3	6.6367(10)
				Co2···Co4	5.6862(10)
Co2–O3	1.893 (3)	Co5–O1	2.065 (2)		
Co2–O4	1.902 (2)	Co5–O4	2.040 (2)	Co1···Co5	3.2776(9)
Co2–O5	1.895 (2)	Co5–O7	2.185 (2)	Co2···Co5	3.2535(9)
Co2–O15	1.941 (3)	Co5–O10	2.024 (2)	Co3···Co5	3.4401(9)
Co2–N1	1.908 (3)	Co5–O14	2.085 (3)	Co4···Co5	3.4481(9)
Co2–N6	1.996 (3)	Co5–O16	2.113 (3)		
				Co3···Li1	2.819 (7)
Co3–O6	1.894 (2)	Li1–O6	2.000 (8)		
Co3–O7	1.910 (2)	Li1–O8	1.981 (7)	Li1···Li1*	5.822(10)
Co3–O8	1.918 (2)	Li1–O18	1.865 (8)		
Co3–O17	1.950 (3)	Li1–O19	1.818 (13)		
Co3–N2	1.931 (3)				
Co3–N7	2.004 (3)				

Table S13 Selected interatomic distances in the crystal structure of **4**

Selected Angles (°) in the Crystal Structure of 4					
O1–Co1–O2	84.69 (10)	O6–Co3–O7	171.45 (11)	O1–Co5–O4	89.80 (9)
O1–Co1–O12	173.63 (11)	O6–Co3–O8	86.33 (11)	O1–Co5–O7	159.92 (9)
O1–Co1–O13	93.80 (10)	O6–Co3–O17	90.50 (11)	O1–Co5–O10	84.83 (9)
O1–Co1–N4	94.01 (11)	O6–Co3–N2	91.28 (12)	O1–Co5–O14	92.62 (9)
O1–Co1–N5	90.14 (12)	O6–Co3–N7	96.12 (12)	O1–Co5–O16	88.64 (9)
O2–Co1– O12	93.44 (11)	O7–Co3–O8	85.11 (10)	O4–Co5–O7	77.73 (9)
O2–Co1–O13	177.07 (11)	O7–Co3–O17	89.25 (10)	O4–Co5–O10	98.65 (10)
O2–Co1–N4	91.65 (12)	O7–Co3–N2	89.33 (11)	O4–Co5–O14	173.47 (10)
O2–Co1–N5	93.85 (12)	O7–Co3–N7	92.37 (11)	O4–Co5–O16	87.18 (10)
O12–Co1–O13	87.79 (11)	O8–Co3–O17	88.39 (11)	O7–Co5–O10	81.63 (9)
O12–Co1–N4	92.13 (12)	O8–Co3–N2	94.01 (11)	O7–Co5–O14	101.51 (9)
O12–Co1–N5	83.90 (12)	O8–Co3–N7	172.74 (12)	O7–Co5–O16	106.16 (9)
O13–Co1– N4	90.96 (12)	O17–Co3– N2	177.10 (11)	O10–Co5–O14	87.61 (11)
O13–Co1–N5	83.63 (12)	O17–Co3–N7	84.77 (12)	O10–Co5–O16	171.21 (9)
N4–Co1–N5	173.39 (13)	N2–Co3–N7	92.77 (13)	O14–Co5–O16	86.81 (10)
O3–Co2–O4	91.23 (11)	O9–Co4–O10	175.43 (12)	Co1–O1–Co5	111.50 (12)
O3–Co2–O5	89.70 (11)	O9–Co4–O11	99.30 (12)	Co2–O4–Co5	111.21 (11)
O3–Co2–O15	173.37 (12)	O9–Co4– N3	89.26 (12)	Co3–O7–Co5	114.13 (12)
O3–Co2–N1	90.48 (12)	O9–Co4–N8	89.96 (14)	Co4–O10–Co5	124.64 (12)
O3–Co2–N6	92.56 (13)	O9–Co4–N9	85.95 (13)		
O4–Co2–O5	83.91 (10)	O10–Co4–O11	83.92 (11)	O6–Li1–O8	81.9 (3)
O4–Co2–O15	95.14 (10)	O10–Co4–N3	87.59 (11)	O6–Li1–O18	96.2 (3)
O4–Co2–N1	87.65 (11)	O10–Co4–N8	93.19 (13)	O6–Li1–O19	136.2 (7)
O4–Co2–N6	170.45 (12)	O10–Co4–N9	90.97 (12)	O8–Li1–O18	99.4 (4)
O5–Co2–O15	89.14 (11)	O11–Co4– N3	171.39 (12)	O8–Li1–O19	116.1 (7)
O5–Co2–N1	171.55 (12)	O11–Co4–N8	91.65 (13)	O18–Li1–O19	117.5 (6)
O5–Co2–N6	87.35 (13)	O11–Co4–N9	87.69 (13)		
O15–Co2– N1	91.63 (12)	N3–Co4–N8	87.37 (13)	Co3–O8–Li1	92.6 (2)
O15–Co2–N6	80.87 (13)	N3–Co4–N9	93.91 (13)	Co3–O6–Li1	92.7 (2)
N1–Co2–N6	101.07 (13)	N8–Co4–N9	175.70 (14)		

Table S14 Selected angles in the crystal structure of **4**

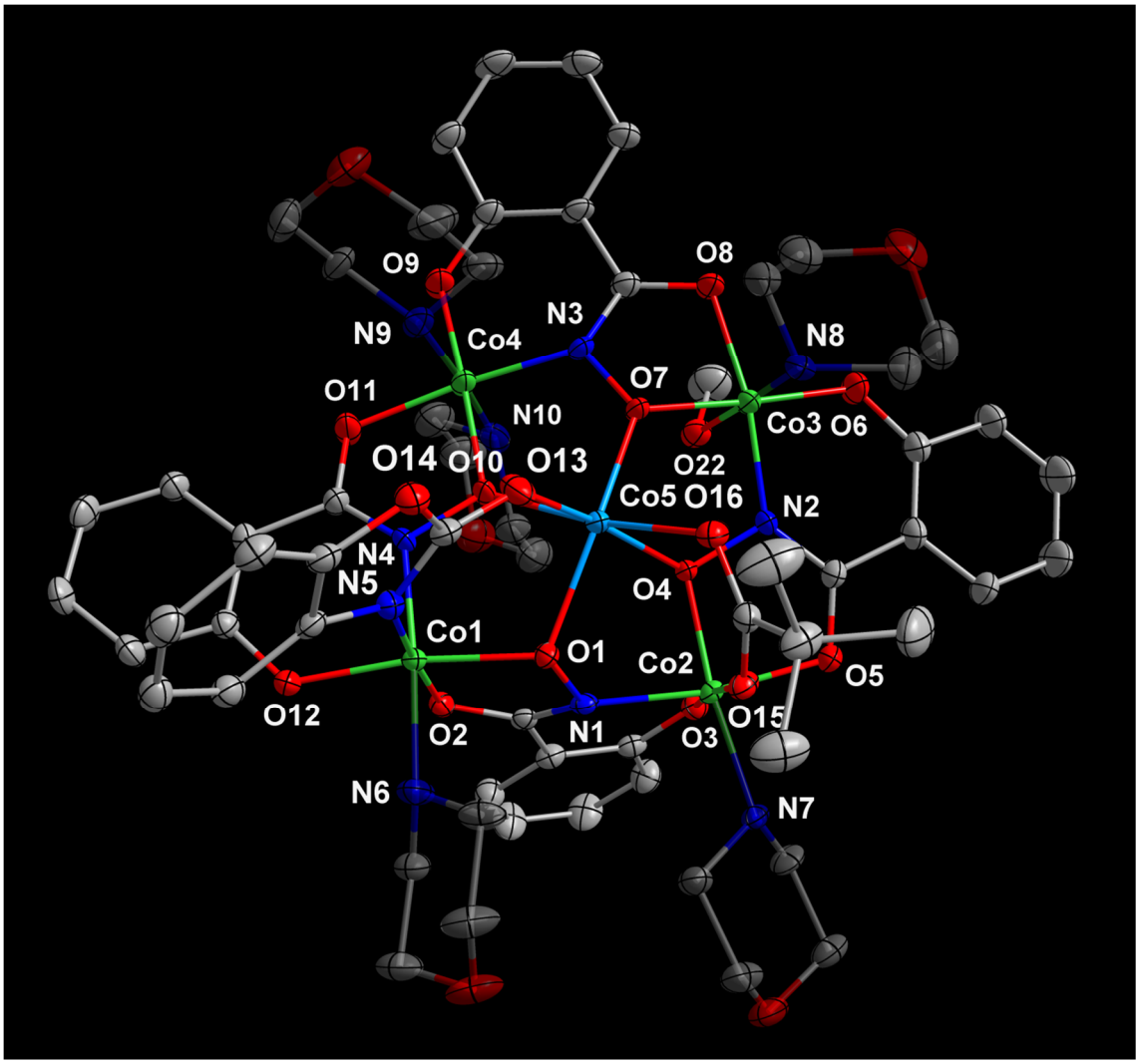

Figure S12 Molecular structure of **5** with numbering scheme and thermal ellipsoids at 50% probability level; color scheme: green - Co(III), light blue - Co(II), red - O, dark blue - N, grey - C

Selected Interatomic Distances (Å) in the Crystal Structure of 5					
Co1–O1	1.919 (2)	Co4–O9	1.881 (3)	Co1···Co2	4.5806(7)
Co1–O2	1.886 (2)	Co4–O10	1.894 (2)	Co1···Co4	4.5804(8)
Co1–O12	1.875 (2)	Co4–O11	1.911 (3)	Co2···Co3	4.4552(8)
Co1–N4	1.924 (3)	Co4–N3	1.890 (3)	Co3···Co4	4.3647(7)
Co1–N5	1.947 (3)	Co4–N9	2.013 (4)		
Co1–N6	2.012 (3)	Co4–N10	2.007 (4)	Co1···Co3	6.5371(7)
				Co2···Co4	6.0274(9)
Co2–O3	1.885 (2)	Co5–O1	2.062 (2)		
Co2–O4	1.869 (2)	Co5–O4	2.094 (2)		
Co2–O5	1.910 (2)	Co5–O7	2.056 (2)	Co1···Co5	3.3124(6)
Co2–O15	1.925 (2)	Co5–O10	2.008 (3)	Co2···Co5	3.2632(8)
Co2–N1	1.935 (3)	Co5–O13	2.112 (3)	Co3···Co5	3.4276(6)
Co2–N7	1.986 (3)	Co5–O16	2.066 (3)	Co4···Co5	3.4513(8)
Co3–O6	1.879 (3)				
Co3–O7	1.864 (2)				
Co3–O8	1.927 (3)				
Co3–O22	1.996 (3)				
Co3–N2	1.872 (3)				
Co3–N8	1.982 (3)				

Table S15 Selected interatomic distances in the crystal structure of **5**

Selected Angles (°) in the Crystal Structure of 5					
O1–Co1– O2	83.41 (10)	O6–Co3– O7	176.98 (11)	O1–Co5–O4	88.04 (9)
O1–Co1– O12	171.20 (10)	O6–Co3–O8	94.16 (11)	O1–Co5– O7	155.51 (10)
O1–Co1–N4	95.20 (11)	O6–Co3–O22	89.48 (12)	O1–Co5– O10	87.32 (9)
O1–Co1–N5	93.49 (11)	O6–Co3– N2	93.25 (12)	O1–Co5–O13	86.10 (9)
O1–Co1–N6	88.53 (12)	O6–Co3–N8	93.50 (13)	O1–Co5–O16	98.40 (10)
O2–Co1– O12	91.21 (10)	O7–Co3–O8	82.84 (10)	O4–Co5– O7	76.11 (9)
O2–Co1–N4	89.78 (12)	O7–Co3–O22	90.62 (11)	O4–Co5– O10	106.11 (10)
O2–Co1–N5	176.75 (11)	O7–Co3–N2	89.78 (11)	O4–Co5–O13	166.08 (10)
O2–Co1–N6	89.52 (11)	O7–Co3–N8	86.39 (12)	O4–Co5– O16	84.14 (10)
O12–Co1–N4	91.73 (11)	O8–Co3–O22	85.57 (12)	O7–Co5–O10	79.49 (10)
O12–Co1–N5	91.98 (11)	O8–Co3– N2	169.82 (12)	O7–Co5–O13	113.23 (10)
O12–Co1–N6	84.44 (12)	O8–Co3–N8	93.88 (12)	O7–Co5–O16	98.41 (10)
N4–Co1–N5	89.55 (13)	O22–Co3– N2	87.53 (12)	O10–Co5–O13	86.24 (11)
N4–Co1–N6	176.10 (12)	O22–Co3– N8	177.00 (12)	O10–Co5–O16	168.52 (11)
N5–Co1–N6	91.36 (12)	N2–Co3–N8	92.63 (13)	O13–Co5–O16	84.24 (11)
O3–Co2– O4	91.01 (11)	O9–Co4–O10	177.12 (13)	Co1–O1–Co5	112.59 (11)
O3–Co2–O5	86.31 (11)	O9–Co4–O11	95.02 (11)	Co2–O4–Co5	110.76 (11)
O3–Co2–O15	172.92 (10)	O9–Co4–N3	91.44 (12)	Co3–O7–Co5	121.89 (12)
O3–Co2–N1	91.29 (11)	O9–Co4–N9	90.09 (14)	Co4–O10–Co5	124.39 (12)
O3–Co2–N7	92.86 (11)	O9–Co4–N10	88.05 (14)		
O4–Co2–O5	85.11 (10)	O10–Co4–O11	82.62 (11)		
O4–Co2–O15	94.49 (10)	O10–Co4– N3	90.97 (11)		
O4–Co2–N1	84.68 (10)	O10–Co4–N9	91.37 (13)		
O4–Co2–N7	172.38 (11)	O10–Co4–N10	90.32 (13)		
O5–Co2–O15	89.72 (11)	O11–Co4– N3	173.39 (12)		
O5–Co2–N1	169.46 (11)	O11–Co4–N9	85.65 (13)		
O5–Co2–N7	88.60 (11)	O11–Co4–N10	90.57 (13)		
O15–Co2–N1	93.66 (11)	N3–Co4–N9	92.94 (13)		
O15–Co2–N7	81.17 (11)	N3–Co4–N10	91.06 (14)		
N1–Co2–N7	101.78 (12)	N9–Co4– N10	175.63 (14)		

Table S16 Selected angles in the crystal structure of **5**

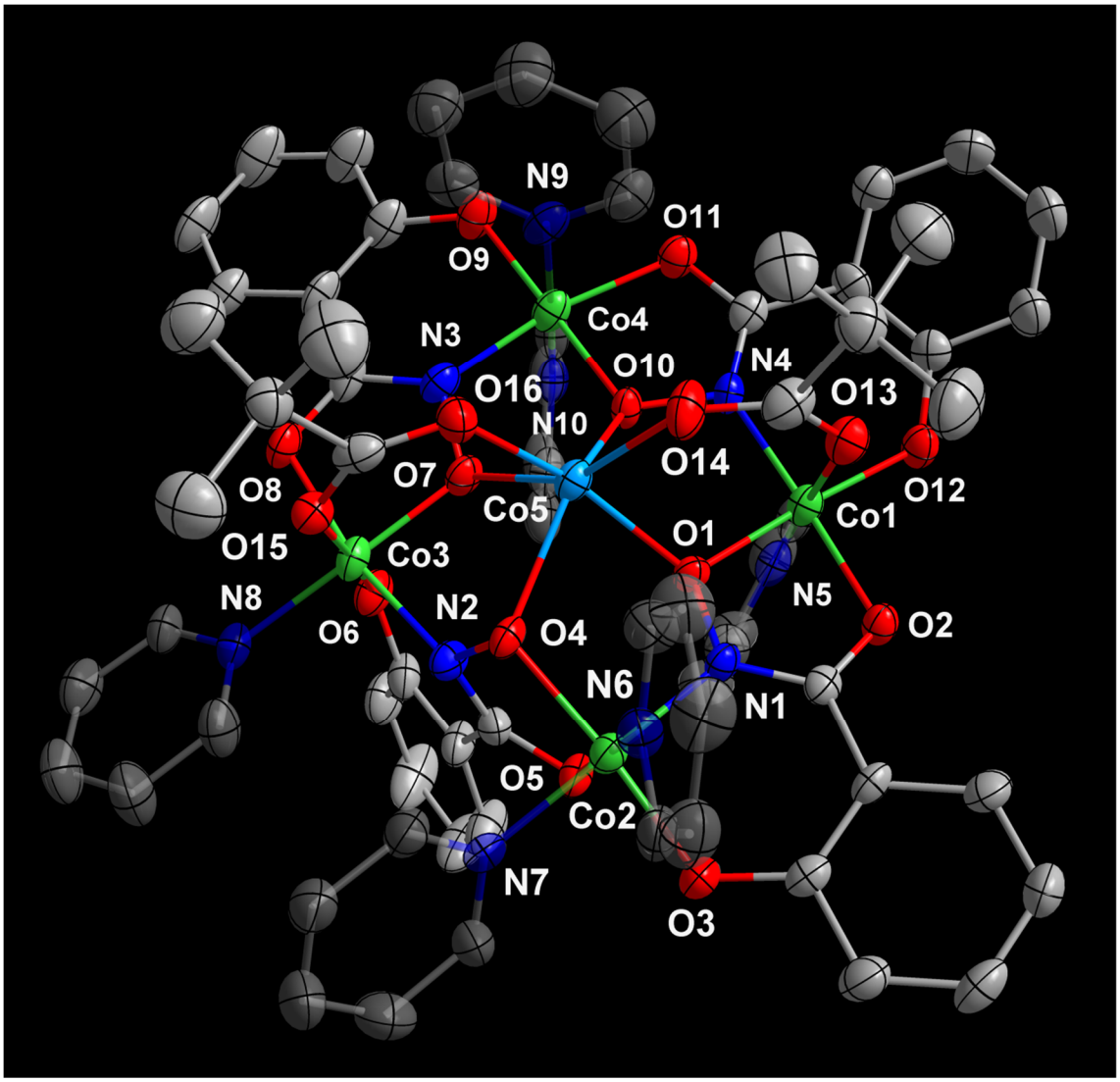

Figure S13 Molecular structure of **6** with numbering scheme and thermal ellipsoids at 50% probability level; color scheme: green - Co(III), light blue - Co(II), red - O, dark blue - N, grey - C

Selected Interatomic Distances (Å) in the Crystal Structure of 6					
Co1–O1	1.880 (3)	Co4–O9	1.886 (3)	Co1···Co2	4.5381(9)
Co1–O2	1.902 (3)	Co4–O10	1.848 (3)	Co1···Co4	4.4420(9)
Co1–O12	1.890 (3)	Co4–O11	1.952 (3)	Co2···Co3	4.5576(10)
Co1–O13	1.901 (3)	Co4–N3	1.872 (4)	Co3···Co4	4.4230(9)
Co1–N4	1.870 (4)	Co4–N9	1.988 (4)		
Co1–N5	1.970 (4)	Co4–N10	1.946 (4)	Co1···Co3	6.0121(9)
				Co2···Co4	6.6048(9)
Co2–O3	1.885 (3)	Co5–O1	2.059 (3)		
Co2–O4	1.916 (3)	Co5–O4	2.174 (3)		
Co2–O5	1.882 (3)	Co5–O7	2.051 (3)		
Co2–N1	1.911 (3)	Co5–O10	2.096 (3)	Co1···Co5	3.3412(9)
Co2–N6	1.953 (4)	Co5–O14	2.058 (3)	Co2···Co5	3.4892(9)
Co2–N7	1.973 (4)	Co5–O16	2.035 (3)	Co3···Co5	3.317(1)
				Co4···Co5	3.3919(10)
Co3–O6	1.875 (3)				
Co3–O7	1.831 (3)				
Co3–O8	1.930 (3)				
Co3–O15	1.924 (3)				
Co3–N2	1.921 (4)				
Co3–N8	1.942 (4)				

Table S17 Selected interatomic distances in the crystal structure of **6**

Selected Angles (°) in the Crystal Structure of 6					
O1–Co1–O2	83.81 (12)	O6–Co3–O7	90.58 (13)	O1–Co5–O4	80.12 (10)
O1–Co1–O12	176.30 (13)	O6–Co3–O8	85.12 (13)	O1–Co5– O7	108.35 (11)
O1–Co1–O13	93.84 (12)	O6–Co3–O15	172.75 (13)	O1–Co5–O10	75.70 (11)
O1–Co1– N4	92.64 (14)	O6–Co3–N2	93.51 (14)	O1–Co5– O14	87.26 (12)
O1–Co1–N5	89.00 (14)	O6–Co3–N8	88.50 (14)	O1–Co5–O16	158.26 (12)
O2–Co1– O12	92.76 (13)	O7–Co3–O8	84.31 (13)	O4–Co5–O7	85.68 (11)
O2–Co1– O13	86.75 (12)	O7–Co3–O15	93.26 (13)	O4–Co5–O10	137.19 (11)
O2–Co1– N4	175.63 (14)	O7–Co3–N2	84.71 (14)	O4–Co5–O14	118.62 (12)
O2–Co1–N5	92.57 (14)	O7–Co3–N8	178.64 (15)	O4–Co5–O16	85.27 (11)
O12–Co1–O13	87.32 (13)	O8–Co3–O15	89.15 (13)	O7–Co5–O10	69.55 (11)
O12–Co1–N4	90.85 (15)	O8–Co3–N2	168.92 (14)	O7–Co5–O14	153.61 (13)
O12–Co1–N5	89.77 (14)	O8–Co3–N8	94.61 (15)	O7–Co5–O16	86.34 (12)
O13–Co1–N4	90.97 (14)	O15–Co3–N2	92.96 (14)	O10–Co5–O14	95.08 (12)
O13–Co1–N5	176.98 (14)	O15–Co3–N8	87.54 (14)	O10–Co5–O16	125.40 (12)
N4–Co1–N5	89.90 (15)	N2–Co3–N8	96.35 (16)	O14–Co5–O16	85.71 (13)
O3–Co2–O4	173.11 (13)	O9–Co4–O10	179.15 (14)	Co1–O1–Co5	116.00 (14)
O3–Co2– O5	89.32 (13)	O9–Co4–O11	97.30 (13)	Co2–O4–Co5	116.97 (13)
O3–Co2–N1	91.75 (14)	O9–Co4–N3	92.75 (15)	Co3–O7–Co5	117.30 (14)
O3–Co2–N6	90.54 (14)	O9–Co4–N9	86.99 (14)	Co4–O10–Co5	118.51 (14)
O3–Co2–N7	88.23 (14)	O9–Co4–N10	89.54 (15)		
O4–Co2– O5	84.52 (12)	O10–Co4–O11	83.36 (12)		
O4–Co2– N1	91.35 (13)	O10–Co4–N3	86.61 (14)		
O4–Co2–N6	95.45 (13)	O10–Co4–N9	92.47 (13)		
O4–Co2–N7	88.50 (14)	O10–Co4–N10	91.01 (14)		
O5–Co2–N1	90.21 (13)	O11–Co4–N3	169.74 (15)		
O5–Co2–N6	176.91 (13)	O11–Co4–N9	90.31 (14)		
O5–Co2–N7	88.15 (15)	O11–Co4–N10	89.55 (14)		
N1–Co2–N6	92.88 (14)	N3–Co4–N9	92.28 (15)		
N1–Co2–N7	178.36 (16)	N3–Co4–N10	88.46 (15)		
N6–Co2–N7	88.76 (15)	N9–Co4–N10	176.48 (15)		

Table S18 Selected angles in the crystal structure of **6**

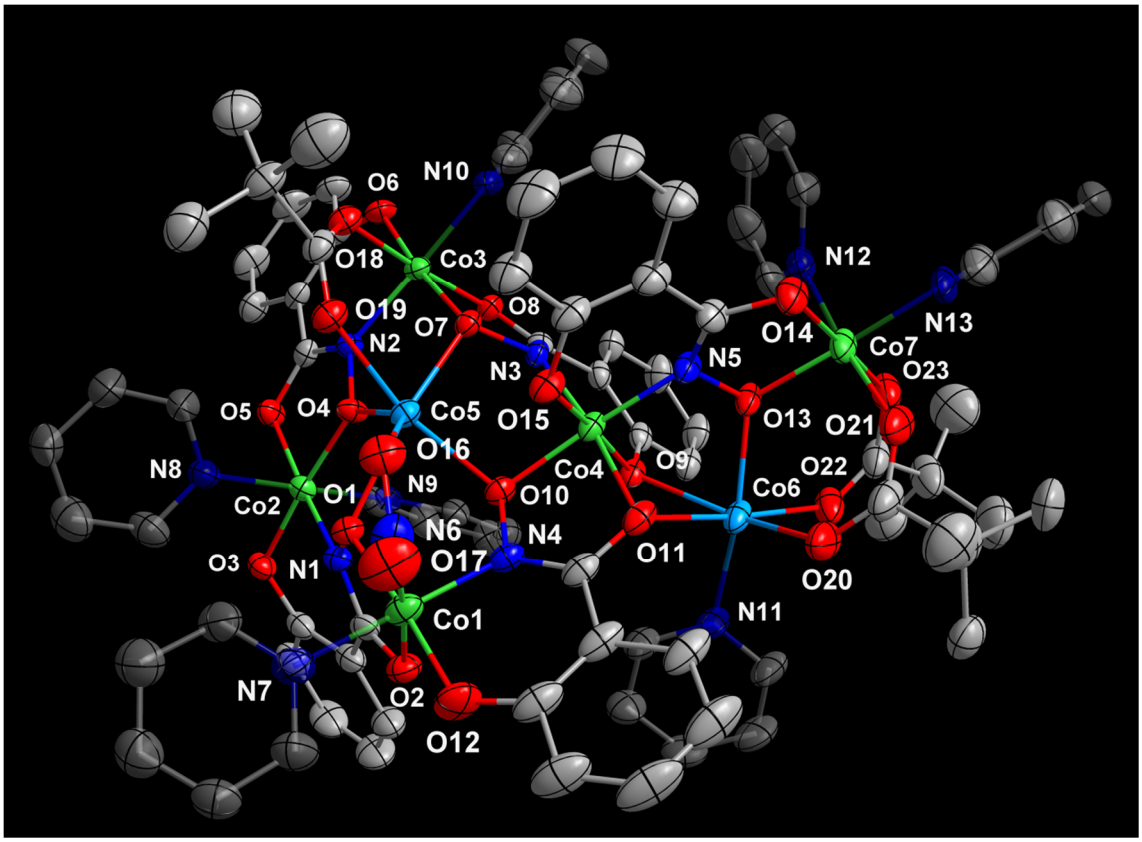

Figure S14 Molecular structure of **7** with numbering scheme and thermal ellipsoids at 50% probability level; color scheme: green - Co(III), light blue - Co(II), red - O, dark blue - N, grey - C

Selected Interatomic Distances (Å) in the Crystal Structure of 7					
Co1–O1	1.881 (2)	Co5–O1	2.168 (2)	Co1···Co2	4.4596(10)
Co1–O2	1.926 (2)	Co5–O4	2.074 (2)	Co1···Co4	4.4782(8)
Co1–O12	1.8706 (7)	Co5–O7	2.055 (2)	Co2···Co3	4.4774(10)
Co1–N4	1.912 (3)	Co5–O10	2.104 (2)	Co3···Co4	4.4761(8)
Co1–N6	1.901 (3)	Co5–O16	2.183 (3)		
Co1–N7	1.982 (3)	Co5–O19	2.092 (2)	Co1···Co3	6.5426(7)
		Co5···O15	2.642(2)	Co2···Co4	5.6555(12)
Co2–O3	1.903 (2)				
Co2–O4	1.862 (2)	Co6–O9	2.181 (2)	Co1···Co5	3.3057(6)
Co2–O5	1.898 (2)	Co6–O11	2.248 (3)	Co2···Co5	3.5292(13)
Co2–N1	1.873 (3)	Co6–O13	2.019 (2)	Co3···Co5	3.3733(7)
Co2–N9	1.953 (3)	Co6–O20	2.003 (3)	Co4···Co5	3.1526(8)
Co2–N8	1.979 (3)	Co6–O22	2.128 (3)		
		Co6–N11	2.066 (3)	Co4···Co6	2.9901(6)
Co3–O6	1.880 (2)				
Co3–O7	1.881 (2)	Co7–O13	1.855 (2)	Co6···Co7	3.4252(10)
Co3–O8	1.892 (2)	Co7–O14	1.891 (3)		
Co3–O18	1.919 (2)	Co7–O21	1.923 (3)	Co1···Co6	6.0473(8)
Co3–N2	1.897 (3)	Co7–O23	1.906 (3)	Co2···Co6	7.8318(10)
Co3–N10	1.975 (3)	Co7–N12	1.943 (3)	Co3···Co6	7.1736(8)
		Co7–N13	1.955 (3)	Co5···Co6	5.9701(8)
Co4–O9	1.931 (2)				
Co4–O10	1.887 (2)			Co1···Co7	8.5956(10)
Co4–O11	1.918 (2)			Co2···Co7	9.9343(11)
Co4–O15	1.880 (2)			Co3···Co7	7.6305(10)
Co4–N3	1.886 (3)			Co4···Co7	4.4601(10)
Co4–N5	1.894 (3)			Co5···Co7	7.4568(10)

Table S19 Selected interatomic distances in the crystal structure of **7**

Selected Angles (°) in the Crystal Structure of 7					
O1–Co1–O2	85.60 (7)	O6–Co3–O7	173.75 (10)	O1–Co5–O4	76.48 (8)
O1–Co1– O12	175.62 (8)	O6–Co3–O8	91.01 (10)	O1–Co5–O7	150.82 (8)
O1–Co1–N4	91.71 (10)	O6–Co3–O18	91.67 (10)	O1–Co5–O10	76.37 (8)
O1–Co1–N6	87.56 (12)	O6–Co3–N2	91.58 (10)	O1–Co5–O16	74.11 (9)
O1–Co1–N7	88.84 (11)	O6–Co3–N10	86.76 (11)	O1–Co5–O19	116.39 (9)
O2–Co1–O12	91.33 (4)	O7–Co3–O8	85.14 (9)	O4–Co5–O7	81.41 (8)
O2–Co1– N4	93.72 (10)	O7–Co3–O18	91.84 (9)	O4–Co5–O10	100.13 (8)
O2–Co1– N6	172.79 (11)	O7–Co3–N2	93.50 (10)	O4–Co5–O16	141.03 (10)
O2–Co1–N7	87.22 (11)	O7–Co3–N10	88.17 (11)	O4–Co5–O19	89.09 (9)
O12–Co1–N4	91.61 (9)	O8–Co3–O18	175.19 (10)	O7–Co5–O10	89.20 (8)
O12–Co1–N6	95.38 (10)	O8–Co3–N2	92.51 (10)	O7–Co5–O16	133.63 (9)
O12–Co1–N7	87.88 (9)	O8–Co3–N10	87.75 (11)	O7–Co5–O19	81.68 (9)
N4–Co1–N6	88.74 (13)	O18–Co3– N2	91.41 (11)	O10–Co5–O16	97.19 (9)
N4–Co1–N7	178.94 (12)	O18–Co3–N10	88.41 (11)	O10–Co5–O19	165.96 (9)
N6–Co1–N7	90.38 (14)	N2–Co3–N10	178.32 (11)	O16–Co5–O19	81.73 (10)
O3–Co2–O4	175.61 (10)	O9–Co4– O10	92.95 (9)	Co1–O1–Co5	109.29 (10)
O3–Co2–O5	96.76 (9)	O9–Co4– O11	84.38 (9)	Co2–O4–Co5	127.35 (11)
O3–Co2– N1	89.49 (10)	O9–Co4– O15	174.80 (10)	Co3–O7–Co5	117.88 (10)
O3–Co2–N8	91.48 (10)	O9–Co4– N3	92.04 (10)	Co4–O10–Co5	104.21 (9)
O3–Co2–N9	86.32 (10)	O9–Co4– N5	90.26 (10)	Co4–O15···Co5	86.675
O4–Co2–O5	84.98 (9)	O10–Co4–O11	84.03 (10)		
O4–Co2–N1	88.93 (10)	O10–Co4–O15	84.24 (10)		
O4–Co2–N8	92.65 (10)	O10–Co4– N3	88.22 (10)		
O4–Co2–N9	89.69 (10)	O10–Co4–N5	173.09 (11)		
O5–Co2–N1	173.44 (10)	O11–Co4–O15	90.97 (10)		
O5–Co2–N8	86.75 (10)	O11–Co4– N3	171.27 (10)		
O5–Co2–N9	88.77 (10)	O11–Co4– N5	90.21 (11)		
N1–Co2–N8	91.11 (11)	O15–Co4–N3	92.24 (10)		
N1–Co2–N9	93.63 (11)	O15–Co4–N5	92.08 (11)		
N8–Co2–N9	174.75 (11)	N3–Co4–N5	97.78 (11)		

Table S20 Selected angles in the crystal structure of **7**

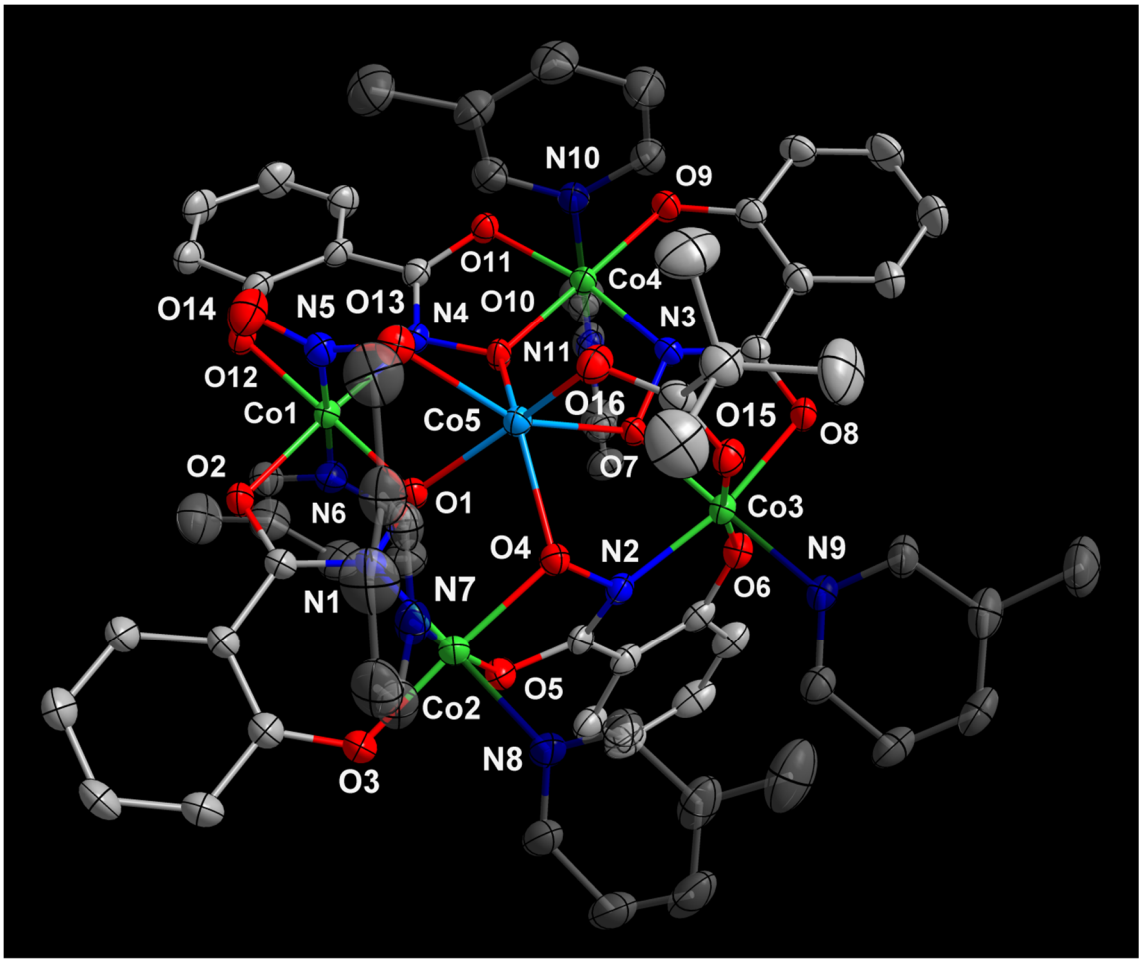

Figure S15 Molecular structure of **8** with numbering scheme and thermal ellipsoids at 50% probability level; color scheme: green - Co(III), light blue - Co(II), red - O, dark blue - N, grey - C

Selected Interatomic Distances (Å) in the Crystal Structure of 8					
Co1–O1	1.889 (2)	Co4–O9	1.890 (2)	Co1···Co2	4.5355(6)
Co1–O2	1.914 (2)	Co4–O10	1.862 (2)	Co1···Co4	4.4881(6)
Co1–O12	1.883 (2)	Co4–O11	1.942 (2)	Co2···Co3	4.5257(6)
Co1–N4	1.888 (2)	Co4–N3	1.880 (2)	Co3···Co4	4.4380(6)
Co1–N5	1.933 (3)	Co4–N10	1.992 (3)		
Co1–N6	1.963 (3)	Co4–N11	1.948 (3)	Co1···Co3	6.1305(6)
				Co2···Co4	6.5649(6)
Co2–O3	1.881 (2)	Co5–O1	2.068 (2)		
Co2–O4	1.904 (2)	Co5–O4	2.137 (2)	Co1···Co5	3.2559(6)
Co2–O5	1.892 (2)	Co5–O7	2.073 (2)	Co2···Co5	3.4412(6)
Co2–N1	1.908 (2)	Co5–O10	2.028 (2)	Co3···Co5	3.2900(6)
Co2–N7	1.956 (3)	Co5–O13	2.175 (2)	Co4···Co5	3.3795(6)
Co2–N8	1.970 (3)	Co5–O16	2.008 (2)		
Co3–O6	1.885 (2)				
Co3–O7	1.8326 (19)				
Co3–O8	1.928 (2)				
Co3–O15	1.932 (2)				
Co3–N2	1.914 (2)				
Co3–N9	1.952 (2)				

Table S21 Selected interatomic distances in the crystal structure of **8**

Selected Angles (°) in the Crystal Structure of 8					
O1–Co1–O2	84.07 (9)	O6–Co3–O7	92.24 (9)	O1–Co5–O4	81.83 (8)
O1–Co1–O12	177.82 (10)	O6–Co3–O8	84.44 (10)	O1–Co5–O7	110.84 (8)
O1–Co1– N4	91.20 (9)	O6–Co3–O15	170.15 (9)	O1–Co5–O10	77.93 (8)
O1–Co1–N5	88.17 (10)	O6–Co3–N2	92.84 (10)	O1–Co5–O13	79.96 (8)
O1–Co1–N6	91.15 (10)	O6–Co3–N9	89.25 (10)	O1–Co5–O16	155.81 (9)
O2–Co1–O12	94.53 (9)	O7–Co3–O8	84.68 (8)	O4–Co5–O7	85.21 (7)
O2–Co1– N4	175.07 (10)	O7–Co3–O15	93.73 (9)	O4–Co5– O10	141.09 (8)
O2–Co1–N5	88.12 (10)	O7–Co3–N2	82.43 (9)	O4–Co5–O13	120.08 (8)
O2–Co1–N6	89.52 (10)	O7–Co3–N9	178.35 (10)	O4–Co5– O16	88.06 (8)
O12–Co1–N4	90.16 (9)	O8–Co3–O15	88.30 (9)	O7–Co5– O10	71.75 (8)
O12–Co1–N5	90.12 (10)	O8–Co3– N2	166.71 (10)	O7–Co5–O13	154.24 (8)
O12–Co1–N6	90.51 (10)	O8–Co3–N9	94.76 (10)	O7–Co5– O16	90.00 (9)
N4–Co1–N5	90.37 (11)	O15–Co3–N9	84.70 (10)	O10–Co5–O13	88.65 (8)
N4–Co1–N6	91.95 (11)	O15–Co3– N2	95.72 (10)	O10–Co5–O16	121.84 (9)
N5–Co1–N6	177.60 (11)	N2–Co3–N9	98.22 (11)	O13–Co5–O16	86.32 (9)
O3–Co2–O4	176.43 (10)	O9–Co4–O10	178.43 (10)	Co1–O1–Co5	110.65 (9)
O3–Co2–O5	93.61 (11)	O9–Co4–O11	97.79 (9)	Co2–O4–Co5	116.63 (10)
O3–Co2–N1	90.18 (10)	O9–Co4– N3	92.55 (10)	Co3–O7–Co5	114.65 (10)
O3–Co2–N7	90.43 (12)	O9–Co4–N10	88.57 (10)	Co4–O10–Co5	120.59 (10)
O3–Co2–N8	89.45 (11)	O9–Co4–N11	89.02 (10)		
O4–Co2–O5	83.55 (9)	O10–Co4–O11	82.76 (8)		
O4–Co2–N1	91.93 (9)	O10–Co4–N3	86.98 (9)		
O4–Co2–N7	92.28 (10)	O10–Co4–N10	89.97 (10)		
O4–Co2–N8	88.20 (10)	O10–Co4–N11	92.48 (10)		
O5–Co2–N1	89.02 (10)	O11–Co4– N3	169.26 (10)		
O5–Co2–N7	174.83 (10)	O11–Co4–N10	90.23 (9)		
O5–Co2–N8	86.29 (11)	O11–Co4–N11	86.54 (10)		
N1–Co2–N7	94.18 (11)	N3–Co4–N10	92.97 (10)		
N1–Co2–N8	175.27 (12)	N3–Co4–N11	90.72 (10)		
N7–Co2–N8	90.54 (12)	N10–Co4–N11	175.68 (10)		

Table S22 Selected angles in the crystal structure of **8**

Bond Valence Sum Analysis

The Bond Valence Sum (BVS) Analysis is a widespread tool in coordination chemistry to assign the oxidation states of metal ions and is based on the bond valence model.[1,2] It utilizes the correlation between the bond length R and bond valence v between two atoms or ions i and j, which can be expressed via the bond valence parameters R_0 and b and the empirical formula 1.[3,4]

$$v_{ij} = \exp((R_0 - R_{ij})/b) \qquad (S1)$$

The valence V of an atom or ion is calculated by summing up the bond valences according to formula 2 and is than equated to its oxidation state z.[5,6]

$$z_i = V_i = \sum_j^N v_{ij} \qquad (S2)$$

Moreover the BVS analysis has been frequently applied to determine the protonation state of oxygen ligands. Here, the ligands are assigned as hydroxid or oxo-group when the bond valence sum is close to 1 or 2, respectively. For BVS values significantly below 1 the presence of a water ligand is confirmed.[7,8]

In the present work, the following BVS parameters have been applied to the program Bond Valence Calculator 2.0.[9,10]

Bond Type	**b**	**R_0**
Co(II)-O	0.37	1.692
Co(III)-O	0.37	1.637
Co(II)-N	0.37	1.650
Co(III)-N	0.37	1.750

Metal Ion	Bond	Length (Å)	Assumption Co(II) Bond Valence		Assumption Co(III) Bond Valence		Assignment
Co1	Co1-O1	1.904	0.564	**Sum**	0.486	**Sum**	**Co(III)**
	Co1-O2	1.898	0.573	**3.118**	0.494	**2.857**	
	Co1-O7	1.933	0.521	**Difference**	0.449	**Difference**	
	Co1-O12	1.927	0.530	**1.118**	0.457	**0.143**	
	Co1-O14	1.912	0.552		0.476		
	Co1-N4	2.010	0.378		0.495		
Co2	Co2-O3	1.882	0.598	**Sum**	0.516	**Sum**	**Co(III)**
	Co2-O4	1.911	0.553	**3.271**	0.477	**3.243**	
	Co2-O5	1.885	0.594	**Difference**	0.512	**Difference**	
	Co2-O11	1.893	0.581	**1.271**	0.501	**0.243**	
	Co2-N1	1.883	0.533		0.698		
	Co2-N5	1.978	0.412		0.540		
Co3	Co3-O6	1.888	0.589	**Sum**	0.507	**Sum**	**Co(III)**
	Co3-O16	1.915	0.547	**3.089**	0.472	**3.073**	
	Co3-O20	1.928	0.528	**Difference**	0.455	**Difference**	
	Co3-O21	1.943	0.507	**1.089**	0.437	**0.073**	
	Co3-N2	1.883	0.533		0.698		
	Co3-N6	2.004	0.384		0.503		
Co4	Co4-O1	1.907	0.559	**Sum**	0.482	**Sum**	**Co(III)**
	Co4-O4	1.961	0.483	**3.214**	0.417	**3.009**	
	Co4-O9	1.903	0.565	**Difference**	0.487	**Difference**	
	Co4-O10	1.938	0.514	**1.214**	0.443	**0.009**	
	Co4-O20	1.907	0.559		0.482		
	Co4-N3	1.883	0.533		0.698		
Co5	Co5-O7	1.895	0.578	**Sum**	0.498	**Sum**	**Co(III)**
	Co5-O8	1.877	0.607	**3.240**	0.523	**2.996**	
	Co5-O13	1.911	0.553	**Difference**	0.477	**Difference**	
	Co5-O15	1.957	0.489	**1.240**	0.421	**0.004**	
	Co5-O18	1.906	0.561		0.483		
	Co5-N7	1.943	0.453		0.594		

Table S23 Results of the Bond Valence Sum Analysis for the assignment of oxidation states of cobalt ions in **1**

Oxygen Atom	Bond	Length (Å)	Bond Valence	Sum	Assignment
O20	O20-Co3	1.928	0.455	**0.937**	**OH^-**
	O20-Co4	1.907	0.482		
O21	O21-Co3	1.943	0.437	**0.437**	**H_2O**

Table S24 Results of the Bond Valence Sum Analysis for the assignment of protonation states of oxygen-sites in **1**

Metal Ion	Bond	Length (Å)	Assumption Co(II) Bond Valence		Assumption Co(III) Bond Valence		Assignment
Co1	Co1-O1	1.916	0.546	**Sum**	0.470	**Sum**	**Co(III)**
	Co1-O2	1.866	0.625	**3.367**	0.539	**3.317**	
	Co1-O10	1.857	0.640	**Difference**	0.552	**Difference**	
	Co1-O11	1.863	0.630	**1.367**	0.543	**0.317**	
	Co1-N13	1.913	0.491		0.644		
	Co1-N14	1.958	0.435		0.570		
Co2	Co2-O3	1.893	0.581	**Sum**	0.501	**Sum**	**Co(III)**
	Co2-O6	1.886	0.592	**2.989**	0.510	**3.391**	
	Co2-N1	1.918	0.485	**Difference**	0.635	**Difference**	
	Co2-N2	1.920	0.482	**0.989**	0.632	**0.391**	
	Co2-N15	1.978	0.412		0.540		
	Co2-N16	1.956	0.437		0.573		
Co3	Co3-O4	1.935	0.519	**Sum**	0.447	**Sum**	**Co(III)**
	Co3-O5	1.897	0.575	**3.405**	0.495	**3.363**	
	Co3-O7	1.806	0.735	**Difference**	0.633	**Difference**	
	Co3-O8	1.868	0.621	**1.405**	0.536	**0.363**	
	Co3-N17	1.916	0.487		0.638		
	Co3-N18	1.931	0.468		0.613		
Co4	Co4-O9	1.884	0.595	**Sum**	0.513	**Sum**	**Co(III)**
	Co4-O12	1.890	0.586	**3.007**	0.505	**3.410**	
	Co4-N3	1.912	0.493	**Difference**	0.645	**Difference**	
	Co4-N4	1.879	0.539	**1.007**	0.706	**0.410**	
	Co4-N19	1.990	0.399		0.523		
	Co4-N20	1.993	0.396		0.519		

Table S25 Results of the Bond Valence Sum Analysis for the assignment of oxidation states of cobalt ions of the first molecule in **2**

Metal Ion	Bond	Length (Å)	Assumption Co(II) Bond Valence		Assumption Co(III) Bond Valence		Assignment
Co5	Co5-O13	1.936	0.517	**Sum**	0.446	**Sum**	**Co(III)**
	Co5-O14	1.855	0.644	**3.395**	0.555	**3.350**	
	Co5-O22	1.870	0.618	**Difference**	0.533	**Difference**	
	Co5-O23	1.839	0.672	**1.395**	0.579	**0.350**	
	Co5-N21	1.913	0.491		0.644		
	Co5-N22	1.943	0.453		0.594		
Co6	Co6-O15	1.856	0.642	**Sum**	0.553	**Sum**	**Co(III)**
	Co6-O18	1.870	0.618	**3.103**	0.533	**3.501**	
	Co6-N5	1.920	0.482	**Difference**	0.632	**Difference**	
	Co6-N6	1.923	0.478	**1.103**	0.627	**0.501**	
	Co6-N23	1.958	0.435		0.570		
	Co6-N24	1.947	0.448		0.587		
Co7	Co7-O16	1.932	0.523	**Sum**	0.451	**Sum**	**Co(III)**
	Co7-O17	1.865	0.627	**3.354**	0.540	**3.309**	
	Co7-O19	1.844	0.663	**Difference**	0.572	**Difference**	
	Co7-O20	1.875	0.610		0.526	**0.309**	
	Co7-N25	1.929	0.470		0.616		
	Co7-N26	1.936	0.462		0.605		
Co8	Co8-O21	1.851	0.651	**Sum**	0.561	**Sum**	**Co(III)**
	Co8-O24	1.890	0.586	**3.054**	0.505	**3.447**	
	Co8-N7	1.865	0.559	**Difference**	0.733	**Difference**	
	Co8-N8	1.904	0.503	**1.054**	0.660	**0.447**	
	Co8-N27	2.000	0.388		0.509		
	Co8-N28	2.021	0.367		0.481		

Table S26 Results of the Bond Valence Sum Analysis for the assignment of oxidation states of cobalt ions of the second molecule in **2**

Metal Ion	Bond	Length (Å)	Assumption Co(II) Bond Valence		Assumption Co(III) Bond Valence		Assignment
Co9	Co9-O25	1.950	0.498	**Sum**	0.429	**Sum**	**Co(III)**
	Co9-O26	1.884	0.595	**3.393**	0.513	**3.358**	
	Co9-O34	1.836	0.678	**Difference**	0.584	**Difference**	
	Co9-O35	1.849	0.654	**1.393**	0.564	**0.358**	
	Co9-N29	1.893	0.519		0.679		
	Co9-N30	1.946	0.449		0.589		
Co10	Co10-O27	1.904	0.564	**Sum**	0.486	**Sum**	**Co(III)**
	Co10-O30	1.883	0.597	**3.012**	0.514	**3.426**	
	Co10-N9	1.902	0.506	**Difference**	0.663	**Difference**	
	Co10-N10	1.901	0.507	**1.012**	0.665	**0.426**	
	Co10-N31	1.971	0.420		0.550		
	Co10-N32	1.973	0.418		0.547		
Co11	Co11-O28	1.921	0.539	**Sum**	0.464	**Sum**	**Co(III)**
	Co11-O29	1.878	0.605	**3.395**	0.521	**3.341**	
	Co11-O31	1.829	0.691	**Difference**	0.595	**Difference**	
	Co11-O32	1.860	0.635	**1.395**	0.547	**0.341**	
	Co11-N33	1.916	0.487		0.638		
	Co11-N34	1.955	0.439		0.575		
Co12	Co12-O33	1.862	0.632	**Sum**	0.544	**Sum**	**Co(III)**
	Co12-O36	1.869	0.620	**3.030**	0.534	**3.409**	
	Co12-N11	1.924	0.477	**Difference**	0.625	**Difference**	
	Co12-N12	1.914	0.490	**1.030**	0.642	**0.409**	
	Co12-N35	1.961	0.431		0.565		
	Co12-N36	2.008	0.380		0.498		

Table S27 Results of the Bond Valence Sum Analysis for the assignment of oxidation states of cobalt ions of the third molecule in **2**

Metal Ion	Bond	Length (Å)	Assumption Co(II) Bond Valence		Assumption Co(III) Bond Valence		Assignment
Co1	Co1-O1	1.890	0.586	**Sum**	0.505	**Sum**	**Co(III)**
	Co1-O2	1.962	0.482	**2.986**	0.415	**3.161**	
	Co1-O6	1.876	0.608	**Difference**	0.524	**Difference**	
	Co1-N2	1.930	0.469	**0.986**	0.615	**0.161**	
	Co1-N3	1.945	0.451		0.590		
	Co1-N4	1.998	0.390		0.512		
Co2	Co2-O3	1.884	0.595	**Sum**	0.513	**Sum**	**Co(III)**
	Co2-O4	1.898	0.573	**2.846**	0.494	**2.983**	
	Co2-O5	1.952	0.495	**Difference**	0.427	**Difference**	
	Co2-N1	1.920	0.482	**0.846**	0.632	**0.017**	
	Co2-N5	2.014	0.374		0.490		
	Co2-N6	2.064	0.327		0.428		
Co3	Co3-O1	1.961	0.483	**Sum**	0.417	**Sum**	**Co(II)**
	Co3-O1	1.961	0.483	**2.526**	0.417	**2.177**	
	Co3-O4	1.941	0.510	**Difference**	0.440	**Difference**	
	Co3-O4	1.941	0.510	**0.526**	0.440	**0.823**	
	Co3-O7	2.177	0.270		0.232		
	Co3-O7	2.177	0.270		0.232		

Table S28 Results of the Bond Valence Sum Analysis for the assignment of oxidation states of cobalt ions ion **3**

Metal Ion	Bond	Length (Å)	Assumption Co(II) Bond Valence		Assumption Co(III) Bond Valence		Assignment
Co1	Co1-O1	1.899	0.572	**Sum**	0.493	**Sum**	**Co(III)**
	Co1-O2	1.898	0.573	**3.139**	0.494	**3.099**	
	Co1-O12	1.893	0.581	**Difference**	0.501	**Difference**	
	Co1-O13	1.922	0.537	**1.139**	0.463	**0.099**	
	Co1-N4	1.915	0.489		0.640		
	Co1-N5	2.000	0.388		0.509		
Co2	Co2-O3	1.893	0.581	**Sum**	0.501	**Sum**	**Co(III)**
	Co2-O4	1.902	0.567	**3.125**	0.489	**3.092**	
	Co2-O5	1.895	0.578	**Difference**	0.498	**Difference**	
	Co2-O15	1.941	0.510	**1.125**	0.440	**0.092**	
	Co2-N1	1.908	0.498		0.652		
	Co2-N6	1.997	0.391		0.513		
Co3	Co3-O6	1.895	0.578	**Sum**	0.498	**Sum**	**Co(III)**
	Co3-O7	1.910	0.555	**3.028**	0.478	**2.992**	
	Co3-O8	1.917	0.544	**Difference**	0.469	**Difference**	
	Co3-O17	1.950	0.498	**1.028**	0.429	**0.008**	
	Co3-N2	1.931	0.468		0.613		
	Co3-N7	2.003	0.385		0.505		
Co4	Co4-O9	1.914	0.549	**Sum**	0.473	**Sum**	**Co(III)**
	Co4-O10	1.869	0.620	**2.956**	0.534	**3.107**	
	Co4-O11	1.919	0.541	**Difference**	0.467	**Difference**	
	Co4-N3	1.887	0.527	**0.956**	0.691	**0.107**	
	Co4-N8	2.040	0.349		0.457		
	Co4-N9	2.017	0.371		0.486		
Co5	Co5-O1	2.065	0.365	**Sum**	0.315	**Sum**	**Co(II)**
	Co5-O4	2.040	0.390	**2.093**	0.336	**1.804**	
	Co5-O7	2.185	0.264	**Difference**	0.227	**Difference**	
	Co5-O10	2.024	0.408	**0.093**	0.351	**1.196**	
	Co5-O14	2.085	0.346		0.298		
	Co5-O16	2.113	0.321		0.276		

Table S29 Results of the Bond Valence Sum Analysis of for the assignment of oxidation states of cobalt ions in **4**

Metal Ion	Bond	Length (Å)	Assumption Co(II) Bond Valence		Assumption Co(III) Bond Valence		Assignment
Co1	Co1-O1	1.919	0.541	**Sum**	0.467	**Sum**	**Co(III)**
	Co1-O2	1.886	0.592	**3.044**	0.510	**3.207**	
	Co1-O12	1.875	0.610	**Difference**	0.526	**Difference**	
	Co1-N4	1.924	0.477	**1.044**	0.625	**0.207**	
	Co1-N5	1.947	0.448		0.587		
	Co1-N6	2.012	0.376		0.493		
Co2	Co2-O3	1.885	0.594	**Sum**	0.512	**Sum**	**Co(III)**
	Co2-O4	1.868	0.621	**3.169**	0.536	**3.119**	
	Co2-O5	1.910	0.555	**Difference**	0.478	**Difference**	
	Co2-O15	1.925	0.533	**1.169**	0.459	**0.119**	
	Co2-N1	1.935	0.463		0.607		
	Co2-N7	1.986	0.403		0.528		
Co3	Co3-O6	1.879	0.603	**Sum**	0.520	**Sum**	**Co(III)**
	Co3-O7	1.864	0.628	**3.158**	0.541	**3.150**	
	Co3-O8	1.927	0.530	**Difference**	0.457	**Difference**	
	Co3-O22	1.996	0.440	**1.158**	0.379	**0.150**	
	Co3-N2	1.872	0.549		0.719		
	Co3-N8	1.982	0.408		0.534		
Co4	Co4-O9	1.881	0.600	**Sum**	0.517	**Sum**	**Co(III)**
	Co4-O10	1.893	0.581	**3.013**	0.501	**3.171**	
	Co4-O11	1.911	0.553	**Difference**	0.477	**Difference**	
	Co4-N3	1.889	0.524	**1.013**	0.687	**0.171**	
	Co4-N9	2.014	0.374		0.490		
	Co4-N10	2.007	0.381		0.499		
Co5	Co5-O1	2.062	0.368	**Sum**	0.317	**Sum**	**Co(II)**
	Co5-O4	2.094	0.337	**2.190**	0.291	**1.888**	
	Co5-O7	2.056	0.374	**Difference**	0.322	**Difference**	
	Co5-O10	2.008	0.426	**0.190**	0.367	**1.112**	
	Co5-O13	2.112	0.321		0.277		
	Co5-O16	2.066	0.364		0.314		

Table S30 Results of the Bond Valence Sum Analysis for the assignment of oxidation states of cobalt ions in **5**

Metal Ion	Bond	Length (Å)	Assumption Co(II) Bond Valence		Assumption Co(III) Bond Valence		Assignment
Co1	Co1-O1	1.880	0.602	**Sum**	0.519	**Sum**	**Co(III)**
	Co1-O2	1.901	0.568	**3.297**	0.490	**3.278**	
	Co1-O12	1.890	0.586	**Difference**	0.505	**Difference**	
	Co1-O13	1.900	0.570	**1.297**	0.491	**0.278**	
	Co1-N4	1.870	0.552		0.723		
	Co1-N5	1.971	0.420		0.550		
Co2	Co2-O3	1.885	0.594	**Sum**	0.512	**Sum**	**Co(III)**
	Co2-O4	1.916	0.546	**3.090**	0.470	**3.270**	
	Co2-O5	1.882	0.598	**Difference**	0.516	**Difference**	
	Co2-N1	1.911	0.494	**1.090**	0.647	**0.270**	
	Co2-N6	1.953	0.441		0.578		
	Co2-N7	1.973	0.418		0.547		
Co3	Co3-O6	1.874	0.611	**Sum**	0.527	**Sum**	**Co(III)**
	Co3-O7	1.831	0.687	**3.293**	0.592	**3.257**	
	Co3-O8	1.930	0.526	**Difference**	0.453	**Difference**	
	Co3-O15	1.924	0.534	**1.293**	0.460	**0.257**	
	Co3-N2	1.921	0.481		0.630		
	Co3-N8	1.942	0.454		0.595		
Co4	Co4-O9	1.885	0.594	**Sum**	0.512	**Sum**	**Co(III)**
	Co4-O10	1.849	0.654	**3.144**	0.564	**3.338**	
	Co4-O11	1.952	0.495	**Difference**	0.427	**Difference**	
	Co4-N3	1.871	0.550	**1.144**	0.721	**0.338**	
	Co4-N9	1.988	0.401		0.526		
	Co4-N10	1.946	0.449		0.589		
Co5	Co5-O1	2.059	0.371	**Sum**	0.320	**Sum**	**Co(II)**
	Co5-O4	2.174	0.272	**2.125**	0.234	**1.831**	
	Co5-O7	2.051	0.379	**Difference**	0.327	**Difference**	
	Co5-O10	2.096	0.336	**0.125**	0.289	**1.169**	
	Co5-O14	2.058	0.372		0.321		
	Co5-O16	2.035	0.396		0.341		

Table S31 Results of the Bond Valence Sum Analysis for the assignment of oxidation states of cobalt ions in **6**

Metal Ion	Bond	Length (Å)	Assumption Co(II) Bond Valence		Assumption Co(III) Bond Valence		Assignment
Co1	Co1-O1	1.881	0.600	**Sum**	0.517	**Sum**	**Co(III)**
	Co1-O2	1.926	0.531	**3.154**	0.458	**3.349**	
	Co1-O12	1.871	0.616	**Difference**	0.531	**Difference**	
	Co1-N4	1.912	0.493	**1.154**	0.645	**0.349**	
	Co1-N6	1.902	0.506		0.663		
	Co1-N7	1.982	0.408		0.534		
Co2	Co2-O3	1.903	0.565	**Sum**	0.487	**Sum**	**Co(III)**
	Co2-O4	1.862	0.632	**3.169**	0.544	**3.359**	
	Co2-O5	1.898	0.573	**Difference**	0.494	**Difference**	
	Co2-N1	1.873	0.547	**1.169**	0.717	**0.359**	
	Co2-N8	1.979	0.411		0.539		
	Co2-N9	1.953	0.441		0.578		
Co3	Co3-O6	1.880	0.602	**Sum**	0.519	**Sum**	**Co(III)**
	Co3-O7	1.881	0.600	**3.254**	0.517	**3.221**	
	Co3-O8	1.892	0.582	**Difference**	0.502	**Difference**	
	Co3-O18	1.919	0.541	**1.254**	0.467	**0.221**	
	Co3-N2	1.897	0.513		0.672		
	Co3-N10	1.975	0.415		0.544		
Co4	Co4-O9	1.931	0.524	**Sum**	0.452	**Sum**	**Co(III)**
	Co4-O10	1.887	0.590	**3.305**	0.509	**3.317**	
	Co4-O11	1.918	0.543	**Difference**	0.468	**Difference**	
	Co4-O15	1.880	0.602	**1.305**	0.519	**0.317**	
	Co4-N3	1.886	0.528		0.692		
	Co4-N5	1.894	0.517		0.678		
Co5	Co5-O1	2.168	0.276	**Sum**	0.238	**Sum**	**Co(II)**
	Co5-O4	2.074	0.356	**1.939 (2.016)**	0.307	**1.671 (1.737)**	
	Co5-O7	2.056	0.374	**Difference**	0.322	**Difference**	
	Co5-O10	2.104	0.328	**0.061 (0.016)**	0.283	**1.329 (1.263)**	
	Co5-O16	2.183	0.265		0.229		
	Co5-O19	2.092	0.339		0.292		
	Co5 O15	2.642	0.077		0.066		

Table S32 Results of the Bond Valence Sum Analysis for the assignment of oxidation states of cobalt ions of the metallacrown subunit in **7**

Metal Ion	Bond	Length (Å)	Assumption Co(II) Bond Valence		Assumption Co(III) Bond Valence		Assignment
Co6	Co6-O9	2.181	0.267	**Sum**	0.230	**Sum**	**Co(II)**
	Co6-O11	2.248	0.223	**1.967**	0.192	**1.841**	
	Co6-O13	2.019	0.413	**Difference**	0.356	**Difference**	
	Co6-O20	2.003	0.431	**0.033**	0.372	**1.159**	
	Co6-O22	2.128	0.308		0.265		
	Co6-N11	2.066	0.325		0.426		
Co7	Co7-O13	1.855	0.644	**Sum**	0.555	**Sum**	**Co(III)**
	Co7-O14	1.891	0.584	**3.216**	0.503	**3.171**	
	Co7-O21	1.922	0.537	**Difference**	0.463	**Difference**	
	Co7-O23	1.906	0.561	**1.216**	0.483	**0.171**	
	Co7-N12	1.943	0.453		0.594		
	Co7-N13	1.956	0.437		0.573		

Table S33 Results of the Bond Valence Sum Analysis for the assignment of oxidation states of cobalt ions of the dimer attached to the periphery of the metallacrown subunit in **7**

Metal Ion	Bond	Length (Å)	Assumption Co(II) Bond Valence		Assumption Co(III) Bond Valence		Assignment
Co1	Co1-O1	1.889	0.587	**Sum**	0.506	**Sum**	**Co(III)**
	Co1-O2	1.914	0.549	**3.153**	0.473	**3.354**	
	Co1-O12	1.883	0.597	**Difference**	0.514	**Difference**	
	Co1-N4	1.888	0.526	**1.153**	0.689	**0.354**	
	Co1-N5	1.933	0.465		0.610		
	Co1-N6	1.963	0.429		0.562		
Co2	Co2-O3	1.881	0.600	**Sum**	0.517	**Sum**	**Co(III)**
	Co2-O4	1.904	0.564	**3.104**	0.486	**3.284**	
	Co2-O5	1.892	0.582	**Difference**	0.502	**Difference**	
	Co2-N1	1.908	0.498	**1.104**	0.652	**0.284**	
	Co2-N7	1.955	0.439		0.575		
	Co2-N8	1.970	0.421		0.552		
Co3	Co3-O6	1.885	0.594	**Sum**	0.512	**Sum**	**Co(III)**
	Co3-O7	1.833	0.683	**3.260**	0.589	**3.228**	
	Co3-O8	1.928	0.528	**Difference**	0.455	**Difference**	
	Co3-O15	1.932	0.523	**1.260**	0.451	**0.228**	
	Co3-N2	1.914	0.490		0.642		
	Co3-N9	1.952	0.442		0.579		
Co4	Co4-O9	1.890	0.586	**Sum**	0.505	**Sum**	**Co(III)**
	Co4-O10	1.862	0.632	**3.106**	0.544	**3.295**	
	Co4-O11	1.942	0.509	**Difference**	0.439	**Difference**	
	Co4-N3	1.880	0.537	**1.106**	0.704	**0.295**	
	Co4-N10	1.993	0.396		0.519		
	Co4-N11	1.948	0.447		0.586		
Co5	Co5-O1	2.069	0.361	**Sum**	0.311	**Sum**	**Co(II)**
	Co5-O4	2.137	0.300	**2.119**	0.259	**1.826**	
	Co5-O7	2.073	0.357	**Difference**	0.308	**Difference**	
	Co5-O10	2.028	0.403	**0.119**	0.348	**1.174**	
	Co5-O13	2.175	0.271		0.234		
	Co5-O16	2.008	0.426		0.367		

Table S34 Results of the Bond Valence Sum Analysis for the assignment of oxidation states of cobalt ions in **8**

Continuous Shape Measures Calculation

Continuous Shape Measures Calculations were performed with the help of the program Shape 2.1 as they provide an established way to quantify the deviation of the shape of the coordination sphere surrounding a metal ion from an ideal polyhedron.[11-13] Therefore, the Continuous Shape Measure (S) of a structure is defined as its minimized distance to a perfect reference shape of appropriate size and orientation. A corresponding mathematical description is given in formula 2 with $\overrightarrow{Q_i}$, $\overrightarrow{Q_0}$ and $\overrightarrow{P_i}$ representing the position vectors of the vertices and the center mass of the analyzed structure Q and the position vectors of the vertices of the compared ideal reference shape P.

$$S_Q(P) = min \frac{\sum_{i=1}^{N} \left|\overrightarrow{Q_i} - \overrightarrow{P_i}\right|^2}{\sum_{i=1}^{N} \left|\overrightarrow{Q_i} - \overrightarrow{Q_0}\right|^2} \cdot 100 \qquad \textit{(S3)}$$

The shapes of the coordination spheres of all cobalt ions have been compared with the following polyhedrons with six vertices.

Code	**Point Group**	**Polyhedron**
HP-6	D_{6h}	Hexagon
PPY-6	C_{5v}	Pentagonal pyramid
OC-6	O_h	Octahedron
TPR-6	D_{3h}	Trigonal prism
JPPY-6	C_{5v}	Johnson pentagonal pyramid J2

Moreover, the Shape 2.1 program offers measures to evaluate intermediate shaped structures concerning their proceeding along the minimal interconversion distortion pathway between two reference shapes.[14,15] Here, the generalized coordinates along the minimal distortion path from the perfect octahedron HP-6 (0%) to the ideal trigonal prism TPR-6 (100%) were calculated as long as the deviation from the pathway Δ(path) remained below the threshold of 10%.[16]

Metal Ion	Continuous Shape Measures					Minimal Distortion Path Analysis	
	S(HP-6)	S(PPY-6)	S(OC-6)	S(TPR-6)	S (JPPY-6)	Δ(Path)	Gen.Coord.
Co1	31.295	26.280	**0.425**	**14.013**	29.631	6.5	**15.5**
Co2	32.115	28.513	**0.180**	**15.444**	32.031	5.9	**10.1**
Co3	32.282	27.970	**0.201**	**15.092**	31.875	5.3	**10.6**
Co4	31.961	26.172	**0.357**	**13.909**	29.816	4.9	**14.2**
Co5	30.346	27.820	**0.279**	**15.155**	30.893	7.4	**12.5**

Table S36 Results of the Continuous Shape Measures Calculations for the cobalt ions in **1**

Metal Ion	Continuous Shape Measures					Minimal Distortion Path Analysis	
	S(HP-6)	S(PPY-6)	S(OC-6)	S(TPR-6)	S (JPPY-6)	Δ(Path)	Gen.Coord.
Co1	31.673	27.733	**0.197**	**15.145**	31.526	5.4	**10.5**
Co2	33.106	28.550	**0.215**	**15.277**	32.459	6.3	**11.0**
Co3	31.950	28.486	**0.152**	**15.309**	32.194	4.6	**9.3**
Co4	32.452	26.972	**0.311**	**14.003**	30.506	4.2	**13.2**
Co5	31.669	28.455	**0.185**	**15.578**	32.306	6.5	**10.2**
Co6	33.312	27.596	**0.299**	**14.520**	31.488	5.7	**13.0**
Co7	31.608	28.517	**0.158**	**15.355**	31.868	5.0	**9.4**
Co8	32.776	26.729	**0.345**	**13.897**	30.280	4.6	**13.9**
Co9	32.203	28.732	**0.139**	**15.590**	32.611	5.1	**8.8**
Co10	33.114	27.848	**0.236**	**14.854**	31.421	5.4	**11.5**
Co11	31.271	28.526	**0.192**	**15.622**	31.941	6.8	**10.4**
Co12	32.811	26.935	**0.325**	**13.848**	30.426	4.0	**13.5**

Table S37 Results of the Continuous Shape Measures Calculations for the cobalt ions in **2**

Metal Ion	Continuous Shape Measures					Minimal Distortion Path Analysis	
	S(HP-6)	S(PPY-6)	S(OC-6)	S(TPR-6)	S (JPPY-6)	Δ(Path)	Gen.Coord.
Co1	31.076	25.990	**0.445**	**14.301**	29.643	7.9	**15.8**
Co2	31.683	25.561	**0.804**	**11.845**	29.227	4.7	**21.3**
Co3	31.930	29.269	**0.319**	**16.530**	32.367	12.7	**-**

Table S38 Results of the Continuous Shape Measures Calculations for the cobalt ions in **3**

Metal Ion	Continuous Shape Measures					Minimal Distortion Path Analysis	
	S(HP-6)	S(PPY-6)	S(OC-6)	S(TPR-6)	S (JPPY-6)	Δ(Path)	Gen.Coord.
Co1	31.539	27.480	**0.272**	**14.933**	30.816	6.5	**12.4**
Co2	31.299	25.829	**0.582**	**13.669**	29.377	8.0	**18.1**
Co3	32.954	27.142	**0.307**	**14.368**	30.622	5.4	**13.1**
Co4	31.049	27.166	**0.483**	**13.409**	30.565	5.5	**16.5**
Co5	29.051	20.969	**1.671**	**10.721**	24.315	9.9	**30.8**

Table S39 Results of the Continuous Shape Measures Calculations for the cobalt ions in **4**

Metal Ion	Continuous Shape Measures					Minimal Distortion Path Analysis	
	S(HP-6)	S(PPY-6)	S(OC-6)	S(TPR-6)	S (JPPY-6)	Δ(Path)	Gen.Coord.
Co1	32.330	27.322	**0.274**	**14.600**	31.014	5.4	**12.4**
Co2	30.746	26.441	**0.650**	**13.709**	29.804	9.1	**19.2**
Co3	31.580	27.046	**0.302**	**14.886**	30.548	7.0	**13.0**
Co4	31.733	27.139	**0.273**	**14.980**	30.690	6.7	**12.4**
Co5	28.606	17.627	**2.935**	**7.750**	21.125	7.8	**40.9**

Table S40 Results of the Continuous Shape Measures Calculations for the cobalt ions in **5**

Metal Ion	Continuous Shape Measures					Minimal Distortion Path Analysis	
	S(HP-6)	S(PPY-6)	S(OC-6)	S(TPR-6)	S (JPPY-6)	Δ(Path)	Gen.Coord.
Co1	30.986	27.156	**0.185**	**14.962**	30.671	4.5	**10.2**
Co2	32.314	28.708	**0.142**	**15.833**	32.144	6.0	**8.9**
Co3	32.709	26.982	**0.454**	**14.150**	30.878	7.5	**16.0**
Co4	32.069	27.380	**0.372**	**14.331**	30.905	6.6	**14.5**
Co5	33.131	15.496	**7.823**	**2.941**	19.804	8.1	**67.3**

Table S41 Results of the Continuous Shape Measures Calculations for the cobalt ions in **6**

Metal Ion	Continuous Shape Measures					Minimal Distortion Path Analysis	
	S(HP-6)	S(PPY-6)	S(OC-6)	S(TPR-6)	S (JPPY-6)	Δ(Path)	Gen.Coord.
Co1	32.532	28.426	**0.161**	**15.056**	32.058	4.1	**9.5**
Co2	32.156	27.146	**0.302**	**13.667**	30.701	2.9	**13.1**
Co3	32.692	28.874	**0.109**	**15.689**	32.405	4.5	**7.8**
Co4	32.162	27.336	**0.271**	**14.381**	31.276	4.6	**12.4**
Co5	27.306	14.140	**7.431**	**4.077**	16.976	13.7	-
Co6	29.325	19.625	**2.519**	**10.167**	23.696	14.8	-
Co7	31.287	27.884	**0.215**	**14.833**	31.451	4.8	**11.0**

Table S42 Results of the Continuous Shape Measures Calculations for the cobalt ions in **7**

Metal Ion	Continuous Shape Measures					Minimal Distortion Path Analysis	
	S(HP-6)	S(PPY-6)	S(OC-6)	S(TPR-6)	S (JPPY-6)	Δ(Path)	Gen.Coord.
Co1	32.000	28.869	**0.116**	**15.666**	32.404	4.6	**8.1**
Co2	31.898	28.594	**0.160**	**15.528**	32.269	5.6	**9.5**
Co3	32.559	26.269	**0.699**	**13.258**	29.857	8.3	**19.9**
Co4	32.281	26.455	**0.384**	**13.685**	30.049	4.6	**14.7**
Co5	33.409	16.719	**7.359**	**2.902**	21.083	5.8	**65.2**

Table S43 Results of the Continuous Shape Measures Calculations for the cobalt ions in **8**

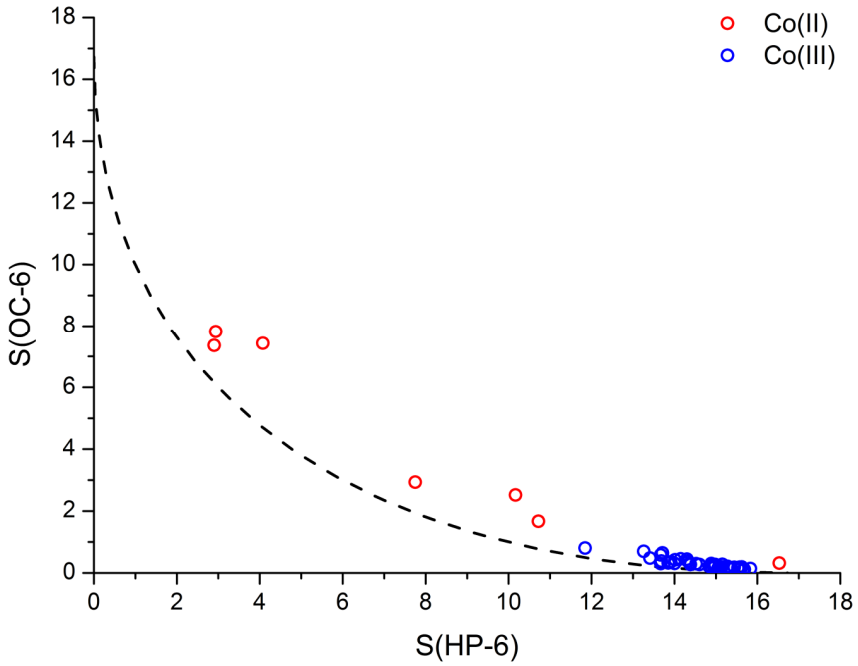

Figure S16 Shape map of the coordination spheres of all cobalt ions of the present work for the interconversion from ideal octahedron and trigonal prism; color code: red – Co(II), blue – Co(III), black dashed line – minimum distortion path between ideal octahedron and trigonal prism

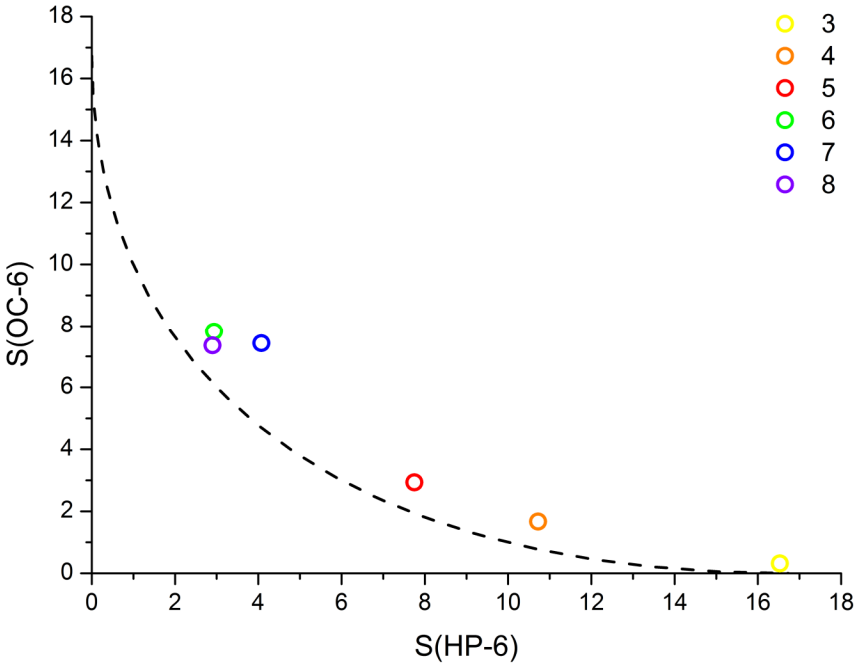

Figure S17 Shape map of the coordination spheres of all Co(II) guest ions of the present work for the interconversion from ideal octahedron and trigonal prism; colors - compound code, black dashed line - minimum distortion path between ideal octahedron and trigonal prism

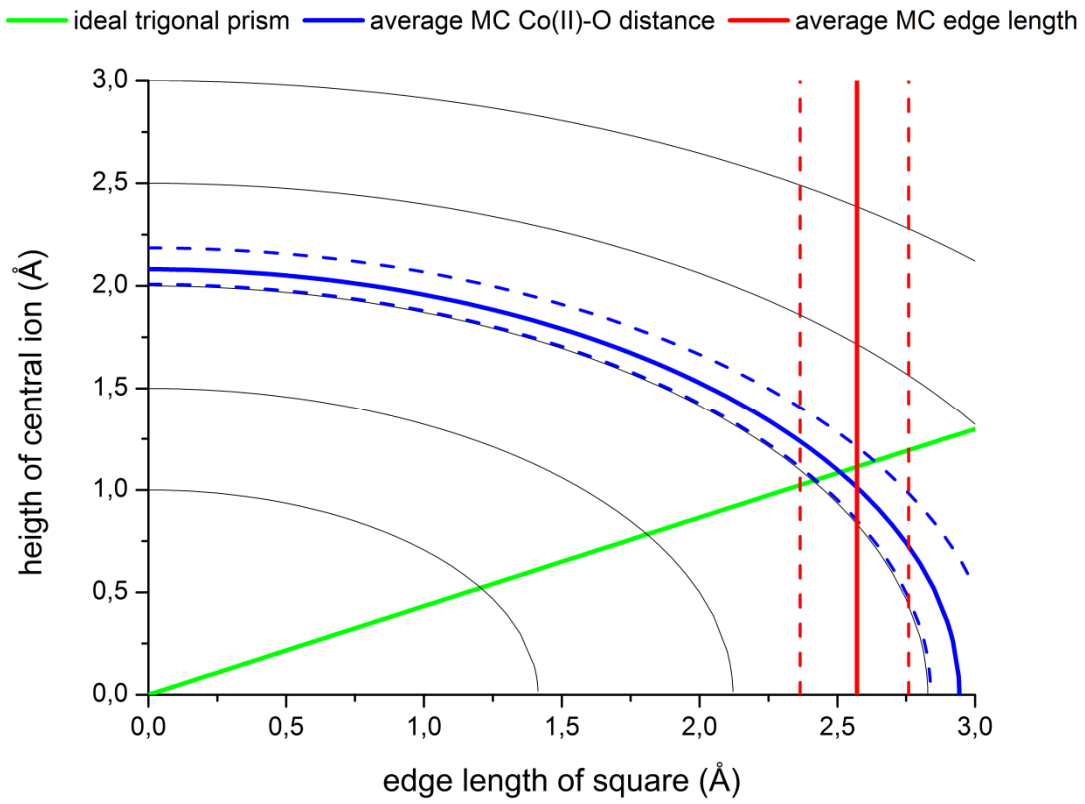

Figure S18 Representation of the calculations concerning the geometric matching of the estimated size of the square formed by the hydroximate oxygen donor atoms and average Co(II)-O bond length for the construction of a perfect trigonal prism with the theoretical elevation height of the central ion above the ground square as reference ; arcs represent the height of the Co(II) ion as the upper vertex of a tetragonal pyramid with different edge lengths (grey - 1, 1.5, 2, 2.5, 3 Å; red – average experimental Co(II)-O distance) in dependence of the edge length of the base square; green line marks the height of the central Co(II) ion in a perfect trigonal prism in dependence of the edge length; red line illustrates the average interatomic distance between adjacent, non-tilted hydroximate oxygen donor atoms; dashed lines mark the minimum and maximum deviation within the selected data compilation

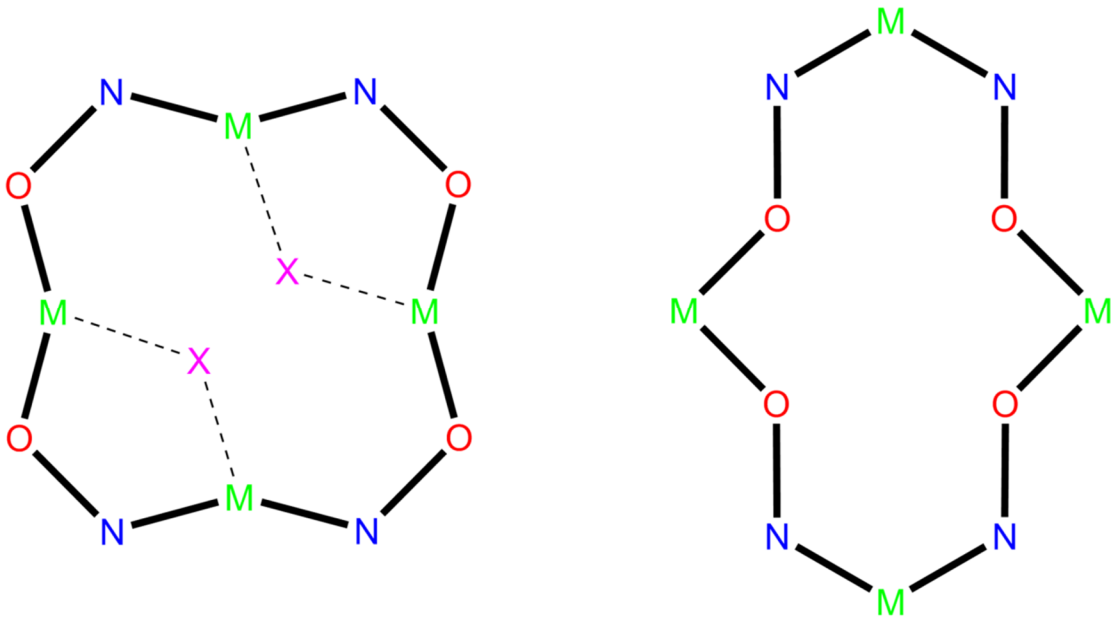

Figure S19 Structure formulae of an inverse metallacrown and the vacant reverse metallacrown **2**

3.9.3 UV-Vis Spectroscopy

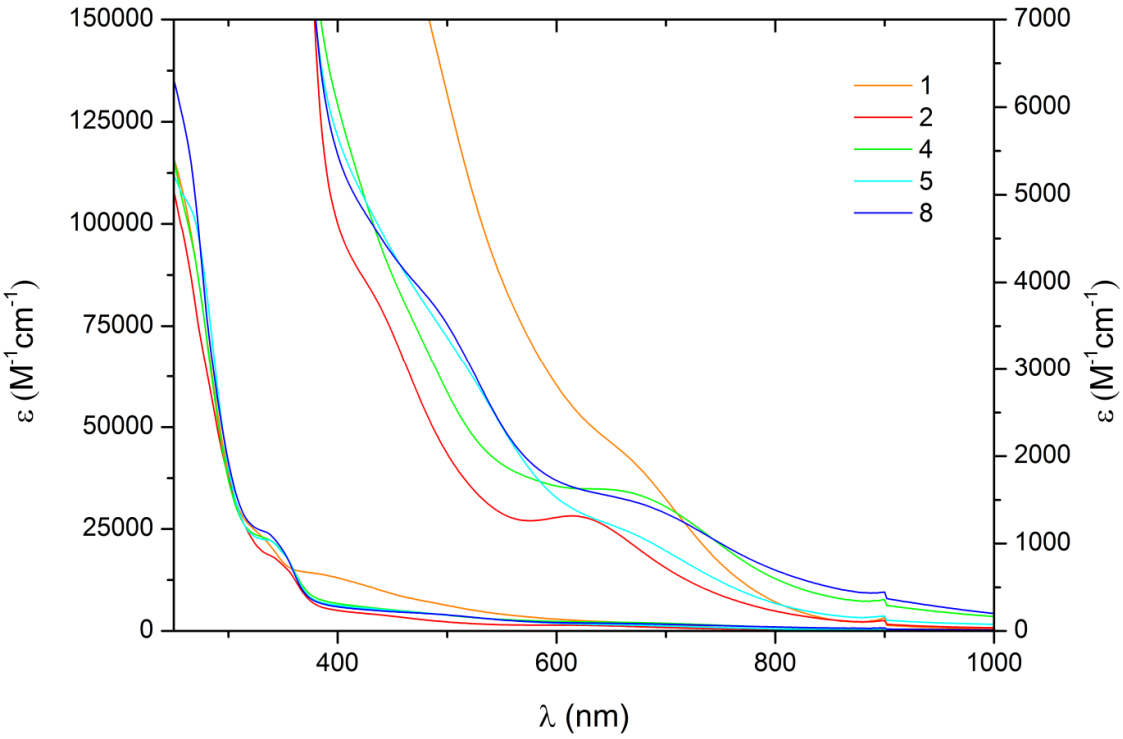

Figure S20 UV-Vis spectra of **1**,**2**,**4**,**5** and **8**; spectrum of **4** has been renormalized on one metallacrown subunit

Complex	$\lambda_{inf,1}$ (nm)	$\lambda_{inf,2}$ (nm)	$\lambda_{inf,3}$ (nm)	$\lambda_{inf/max,4}$ (nm)
1		325	484	649
2		337	423	594
4	261	331	470	635
5	261	333	486	648
8		331	471	646

Table S44 Observed infliction point and maxima in the UV-Vis spectra of **1**,**2**,**4**,**5** and **8**

3.9.4 ESI Mass Spectrometry

1: m/z (methanol)

1608 $\{Co_5(Shi)_3(Piv)_5(OH^-)(Pip)_4 + H\}^+$

1563 $\{Co_5(Shi)_3(Piv)_5(OH^-)(Pip)_3(H_2O) + Na\}^+$

1545 $\{Co_5(Shi)_3(Piv)_5(OH^-)(Pip)_3 + Na\}^+$

1524 $\{Co_5(Shi)_3(Piv)_4(OH^-)(Pip)_4(H_2O)\}^+$

1506 $\{Co_5(Shi)_3(Piv)_4(OH^-)(Pip)_4\}^+$

1439 $\{Co_5(Shi)_3(Piv)_4(OH^-)(Pip)_3(H_2O)\}^+$

1421 $\{Co_5(Shi)_3(Piv)_4(OH^-)(Pip)_3\}^+$

1336 $\{Co_5(Shi)_3(Piv)_4(OH^-)(Pip)_2\}^+$

2: m/z (acetonitrile)

1469 $\{ [12\text{-}MC_{Co(III)N(Shi)}\text{-}4](Py)_8 + H\}^+$

1390 $\{ [12\text{-}MC_{Co(III)N(Shi)}\text{-}4](Py)_7 + H\}^+$

1311 $\{ [12\text{-}MC_{Co(III)N(Shi)}\text{-}4](Py)_6 + H\}^+$

1232 $\{ [12\text{-}MC_{Co(III)N(Shi)}\text{-}4](Py)_5 + H\}^+$

1152 $\{ [12\text{-}MC_{Co(III)N(Shi)}\text{-}4](Py)_4 + H\}^+$

1074 $\{ [12\text{-}MC_{Co(III)N(Shi)}\text{-}4](Py)_3 + H\}^+$

995 $\{ [12\text{-}MC_{Co(III)N(Shi)}\text{-}4](Py)_2 + H\}^+$

2: m/z (methanol)

1491 { [12-$MC_{Co(III)N(Shi)}$-4](Py)$_8$ + Na}$^+$

1469 { [12-$MC_{Co(III)N(Shi)}$-4](Py)$_8$ + H}$^+$

1412 { [12-$MC_{Co(III)N(Shi)}$-4](Py)$_7$ + Na}$^+$

1390 { [12-$MC_{Co(III)N(Shi)}$-4](Py)$_7$ + H}$^+$

1333 { [12-$MC_{Co(III)N(Shi)}$-4](Py)$_6$ + Na}$^+$

1311 { [12-$MC_{Co(III)N(Shi)}$-4](Py)$_6$ + H}$^+$

1232 { [12-$MC_{Co(III)N(Shi)}$-4](Py)$_5$ + H}$^+$

1152 { [12-$MC_{Co(III)N(Shi)}$-4](Py)$_4$ + H}$^+$

1074 { [12-$MC_{Co(III)N(Shi)}$-4](Py)$_3$ + H}$^+$

995 { [12-$MC_{Co(III)N(Shi)}$-4](Py)$_2$ + H}$^+$

4: m/z (methanol)

1552 $\{Co(II)(Piv)_3[12\text{-}MC_{Co(III)N(Shi)}\text{-}4](Pip)_4 + 2Li\}^+$

1523 $\{Co(II)(Piv)_2[12\text{-}MC_{Co(III)N(Shi)}\text{-}4](Pip)_5 + H\}^+$

1467 $\{Co(II)(Piv)_3[12\text{-}MC_{Co(III)N(Shi)}\text{-}4](Pip)_3 + 2Li\}^+$

1461 $\{Co(II)(Piv)_3[12\text{-}MC_{Co(III)N(Shi)}\text{-}4](Pip)_3 + H + Li\}^+$

1444 $\{Co(II)(Piv)_2[12\text{-}MC_{Co(III)N(Shi)}\text{-}4](Pip)_4 + Li\}^+$

1438 $\{Co(II)(Piv)_2[12\text{-}MC_{Co(III)N(Shi)}\text{-}4](Pip)_4 + H\}^+$

1398 $\{Co(II)(Piv)_3[12\text{-}MC_{Co(III)N(Shi)}\text{-}4](Pip)_2 + Na + Li\}^+$

1382 $\{Co(II)(Piv)_3[12\text{-}MC_{Co(III)N(Shi)}\text{-}4](Pip)_2 + 2Li\}^+$

1376 $\{Co(II)(Piv)_3[12\text{-}MC_{Co(III)N(Shi)}\text{-}4](Pip)_2 + H + Li\}^+$

1375 $\{Co(II)(Piv)_2[12\text{-}MC_{Co(III)N(Shi)}\text{-}4](Pip)_3 + Na\}^+$

1368 $\{Co(II)(Piv)[12\text{-}MC_{Co(III)N(Shi)}\text{-}4](Pip)_4 + MeOH\}^+$

1359 $\{Co(II)(Piv)_2[12\text{-}MC_{Co(III)N(Shi)}\text{-}4](Pip)_3 + Li\}^+$

1353 $\{Co(II)(Piv)_2[12\text{-}MC_{Co(III)N(Shi)}\text{-}4](Pip)_3 + H\}^+$

1336 $\{Co(II)(Piv)[12\text{-}MC_{Co(III)N(Shi)}\text{-}4](Pip)_4\}^+$

1297 $\{Co(II)(Piv)_3[12\text{-}MC_{Co(III)N(Shi)}\text{-}4](Pip)_1 + 2Li\}^+$

1290 $\{Co(II)(Piv)_2[12\text{-}MC_{Co(III)N(Shi)}\text{-}4](Pip)_2 + Na\}^+$

1283 $\{Co(II)(Piv)[12\text{-}MC_{Co(III)N(Shi)}\text{-}4](Pip)_3 + MeOH\}^+$

1274 $\{Co(II)(Piv)_2[12\text{-}MC_{Co(III)N(Shi)}\text{-}4](Pip)_2 + Li\}^+$

1268 $\{Co(II)(Piv)_2[12\text{-}MC_{Co(III)N(Shi)}\text{-}4](Pip)_2 + H\}^+$

1251 $\{Co(II)(Piv)[12\text{-}MC_{Co(III)N(Shi)}\text{-}4](Pip)_3\}^+$

1204 $\{Co(II)(Piv)_2[12\text{-}MC_{Co(III)N(Shi)}\text{-}4](Pip)_1 + Na\}^+$

1189 $\{Co(II)(Piv)_2[12\text{-}MC_{Co(III)N(Shi)}\text{-}4](Pip)_1 + Li\}^+$

1166 $\{Co(II)(Piv)[12\text{-}MC_{Co(III)N(Shi)}\text{-}4](Pip)_2\}^+$

1081 $\{Co(II)(Piv)[12\text{-}MC_{Co(III)N(Shi)}\text{-}4](Pip)_1\}^+$

996 $\{Co(II)(Piv)[12\text{-}MC_{Co(III)N(Shi)}\text{-}4]\}^+$

5: m/z (acetonitrile)

1479 {Co(II)(Boa)(Piv)[12-MC$_{Co(III)N(Shi)}$-4](Morph)$_4$ + H}$^+$

1392 {Co(II)(Boa)(Piv)[12-MC$_{Co(III)N(Shi)}$-4](Morph)$_3$ + H}$^+$

1377 {Co(II)(Boa)[12-MC$_{Co(III)N(Shi)}$-4](Morph)$_4$}$^+$

1344 {Co(II)(Piv)[12-MC$_{Co(III)N(Shi)}$-4](Morph)$_4$}$^+$

1322 {Co(II)(Boa)[12-MC$_{Co(III)N(Shi)}$-4](Morph)$_3$MeOH}$^+$

1305 {Co(II)(Boa)(Piv)[12-MC$_{Co(III)N(Shi)}$-4](Morph)$_2$ + H}$^+$

1290 {Co(II)(Boa)[12-MC$_{Co(III)N(Shi)}$-4](Morph)$_3$}$^+$

1257 {Co(II)(Piv)[12-MC$_{Co(III)N(Shi)}$-4](Morph)$_3$}$^+$

1235 {Co(II)(Boa)[12-MC$_{Co(III)N(Shi)}$-4](Morph)$_2$MeOH}$^+$

1218 {Co(II)(Boa)(Piv)[12-MC$_{Co(III)N(Shi)}$-4](Morph) + H}$^+$

1203 {Co(II)(Boa)[12-MC$_{Co(III)N(Shi)}$-4](Morph)$_2$}$^+$

1170 {Co(II)(Piv)[12-MC$_{Co(III)N(Shi)}$-4](Morph)$_2$}$^+$

1148 {Co(II)(Boa)[12-MC$_{Co(III)N(Shi)}$-4](Morph)MeOH}$^+$

1116 {Co(II)(Boa)[12-MC$_{Co(III)N(Shi)}$-4](Morph)}$^+$

1083 {Co(II)(Piv)[12-MC$_{Co(III)N(Shi)}$-4](Morph)}$^+$

1029 {Co(II)(Boa)[12-MC$_{Co(III)N(Shi)}$-4]}$^+$

996 {Co(II)(Piv)[12-MC$_{Co(III)N(Shi)}$-4]}$^+$

5: m/z (methanol)

1392 {Co(II)(Boa)(Piv)[12-MC$_{Co(III)N(Shi)}$-4](Morph)$_3$ + H}$^+$

1359 {Co(II)(Boa)(Piv)[12-MC$_{Co(III)N(Shi)}$-4](Morph)$_2$ (MeOH)+ Na}$^+$

1327 {Co(II)(Boa)(Piv)[12-MC$_{Co(III)N(Shi)}$-4](Morph)$_2$ + Na}$^+$

1322 {Co(II)(Boa)[12-MC$_{Co(III)N(Shi)}$-4](Morph)$_3$MeOH}$^+$

1290 {Co(II)(Boa)[12-MC$_{Co(III)N(Shi)}$-4](Morph)$_3$}$^+$

1272 {Co(II)(Boa)(Piv)[12-MC$_{Co(III)N(Shi)}$-4](Morph) (MeOH)+ Na}$^+$

1257 {Co(II)(Piv)[12-MC$_{Co(III)N(Shi)}$-4](Morph)$_3$}$^+$

1240 {Co(II)(Boa)(Piv)[12-MC$_{Co(III)N(Shi)}$-4](Morph) + Na}$^+$

1203 {Co(II)(Boa)[12-MC$_{Co(III)N(Shi)}$-4](Morph)$_2$}$^+$

1170 {Co(II)(Piv)[12-MC$_{Co(III)N(Shi)}$-4](Morph)$_2$}$^+$

1153 {Co(II)(Boa)(Piv)[12-MC$_{Co(III)N(Shi)}$-4] + Na}$^+$

1116 {Co(II)(Boa)[12-MC$_{Co(III)N(Shi)}$-4](Morph)}$^+$

1083 {Co(II)(Piv)[12-MC$_{Co(III)N(Shi)}$-4](Morph)}$^+$

1029 {Co(II)(Boa)[12-MC$_{Co(III)N(Shi)}$-4]}$^+$

996 {Co(II)(Piv)[12-MC$_{Co(III)N(Shi)}$-4]}$^+$

8: m/z (acetonitrile)

1530 $\{Co(II)(NO_2)(Piv)[12\text{-}MC_{Co(III)N(Shi)}\text{-}4](Pic)_5 + Na\}^+$

1508 $\{Co(II)(NO_2)(Piv)[12\text{-}MC_{Co(III)N(Shi)}\text{-}4](Pic)_5 + H\}^+$

1461 $\{Co(II)(Piv)[12\text{-}MC_{Co(III)N(Shi)}\text{-}4](Pic)_5\}^+$

1437 $\{Co(II)(NO_2)(Piv)[12\text{-}MC_{Co(III)N(Shi)}\text{-}4](Pic)_4 + Na\}^+$

1415 $\{Co(II)(NO_2)(Piv)[12\text{-}MC_{Co(III)N(Shi)}\text{-}4](Pic)_4 + H\}^+$

1406 $\{Co(II)(NO_2)[12\text{-}MC_{Co(III)N(Shi)}\text{-}4](Pic)_5\}^+$

1368 $\{Co(II)(Piv)[12\text{-}MC_{Co(III)N(Shi)}\text{-}4](Pic)_4\}^+$

1344 $\{Co(II)(NO_2)(Piv)[12\text{-}MC_{Co(III)N(Shi)}\text{-}4](Pic)_3 + Na\}^+$

1322 $\{Co(II)(NO_2)(Piv)[12\text{-}MC_{Co(III)N(Shi)}\text{-}4](Pic)_3 + H\}^+$

1313 $\{Co(II)(NO_2)[12\text{-}MC_{Co(III)N(Shi)}\text{-}4](Pic)_4\}^+$

1275 $\{Co(II)(Piv)[12\text{-}MC_{Co(III)N(Shi)}\text{-}4](Pic)_3\}^+$

1251 $\{Co(II)(NO_2)(Piv)[12\text{-}MC_{Co(III)N(Shi)}\text{-}4](Pic)_2 + Na\}^+$

1229 $\{Co(II)(NO_2)(Piv)[12\text{-}MC_{Co(III)N(Shi)}\text{-}4](Pic)_2 + H\}^+$

1220 $\{Co(II)(NO_2)[12\text{-}MC_{Co(III)N(Shi)}\text{-}4](Pic)_3\}^+$

1182 $\{Co(II)(Piv)[12\text{-}MC_{Co(III)N(Shi)}\text{-}4](Pic)_2\}^+$

1158 $\{Co(II)(NO_2)(Piv)[12\text{-}MC_{Co(III)N(Shi)}\text{-}4](Pic) + Na\}^+$

1136 $\{Co(II)(NO_2)(Piv)[12\text{-}MC_{Co(III)N(Shi)}\text{-}4](Pic) + H\}^+$

1127 $\{Co(II)(NO_2)[12\text{-}MC_{Co(III)N(Shi)}\text{-}4](Pic)_2\}^+$

1089 $\{Co(II)(Piv)[12\text{-}MC_{Co(III)N(Shi)}\text{-}4](Pic)\}^+$

996 $\{Co(II)(Piv)[12\text{-}MC_{Co(III)N(Shi)}\text{-}4]\}^+$

8: m/z (methanol)

1275 $\{Co(II)(Piv)[12\text{-}MC_{Co(III)N(Shi)}\text{-}4](Pic)_3\}^+$

1251 $\{Co(II)(NO_2)(Piv)[12\text{-}MC_{Co(III)N(Shi)}\text{-}4](Pic)_2 + Na\}^+$

1229 $\{Co(II)(NO_2)(Piv)[12\text{-}MC_{Co(III)N(Shi)}\text{-}4](Pic)_2 + H\}^+$

1220 $\{Co(II)(NO_2)[12\text{-}MC_{Co(III)N(Shi)}\text{-}4](Pic)_3\}^+$

1182 $\{Co(II)(Piv)[12\text{-}MC_{Co(III)N(Shi)}\text{-}4](Pic)_2\}^+$

1089 $\{Co(II)(Piv)[12\text{-}MC_{Co(III)N(Shi)}\text{-}4](Pic)\}^+$

996 $\{Co(II)(Piv)[12\text{-}MC_{Co(III)N(Shi)}\text{-}4]\}^+$

3.9.5 ^{1}H-Nuclear Resonance Spectroscopy

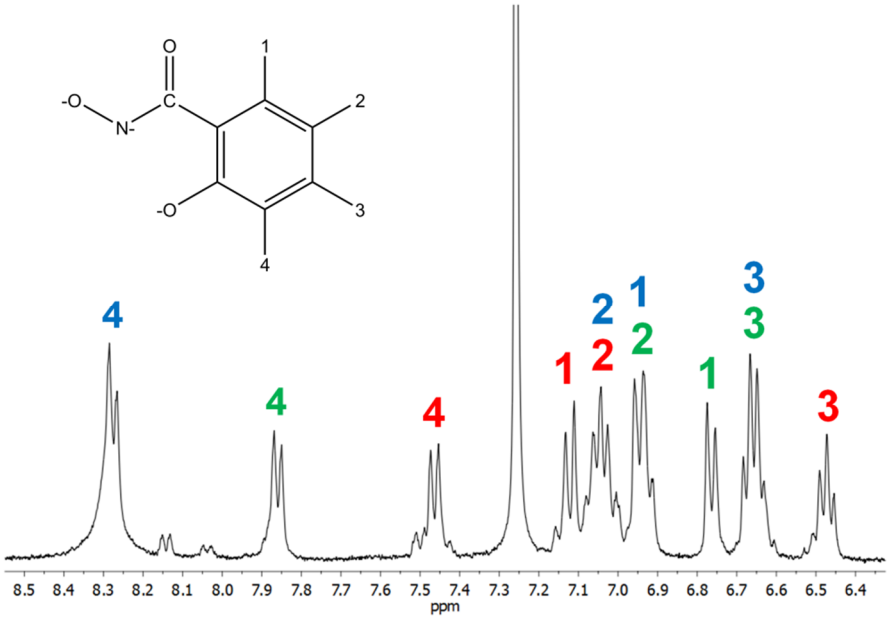

Figure 21 ^{1}H-NMR spectrum of **1** in chloroform; colored numbers represents assignment of the signal; different colors encode distinguishable ligands, different numbers encode different H-positions

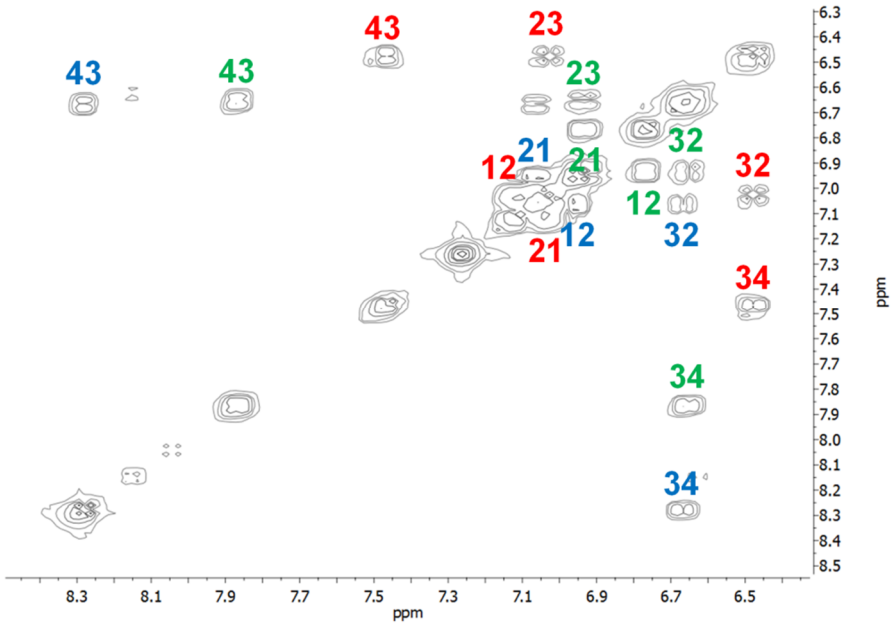

Figure 22 ^{1}H-^{1}H Cosy NMR spectrum of **1** in chloroform; colored numbers represents assignment of the signal; different colors encode distinguishable ligands, different numbers encode different H-positions

δ (ppm)	Multiplicity	Assignment	Equivalent Protons
0.48	s	Piv	9
0.64	s	Piv	9
0.99	s	Piv	9
1.16	s	Piv	9
1.29	s	Piv	9
0.75-4.00	m	Pip	
6.46-6.49	t	Shi-H3	1
6.63-6.68	m	Shi-H3	1
		Shi-H3	1
6.75-6.77	d	Shi-H1	1
6.91-6.96	m	Shi-H2	1
		Shi-H1	1
7.00-7.08	m	Shi-H2	1
		Shi-H2	1
7.11-7.13	d	Shi-H1	1
7.45-7.47	d	Shi-H4	1
7.85-7.87	d	Shi-H4	1
8.27-8.29	m	Shi-H4	1

Table 45 Assignment of the signals in the ^{1}H-NMR spectrum of **1** in chloroform

δ (ppm)	Multiplicity	Assignment	Equivalent Protons
6.44-6.48	t	Shi-3	2
6.75-6.80	m	Shi-3	2
		Py-B	4
6.85-6.89	t	Py-B	4
6.94-6.98	t	Shi-2	2
7.05-7.08	t	Py-B	4
7.10-7.12	d	Shi-1	2
7.26-7.30	m	Shi-1	2
		Shi-2	2
		Py-C	2
7.31-7.35	t	Py-B	4
7.37-7.41	t	Py-C	2
7.53-7.57	t	Py-C	2
7.75-7.78	t	Py-C	2
7.90-7.91	d	Py-A	4
8.02-8.04	d	Shi-4	2
8.36-8.38	d	Shi-4	2
8.52-8.53	d	Py-A	4
8.62-8.63	d	Py-A	4
8.66-8.68	d	Py-A	4

Table S46 Assignment of the signals in the ^{1}H-NMR spectrum of **2** in dichlormethan

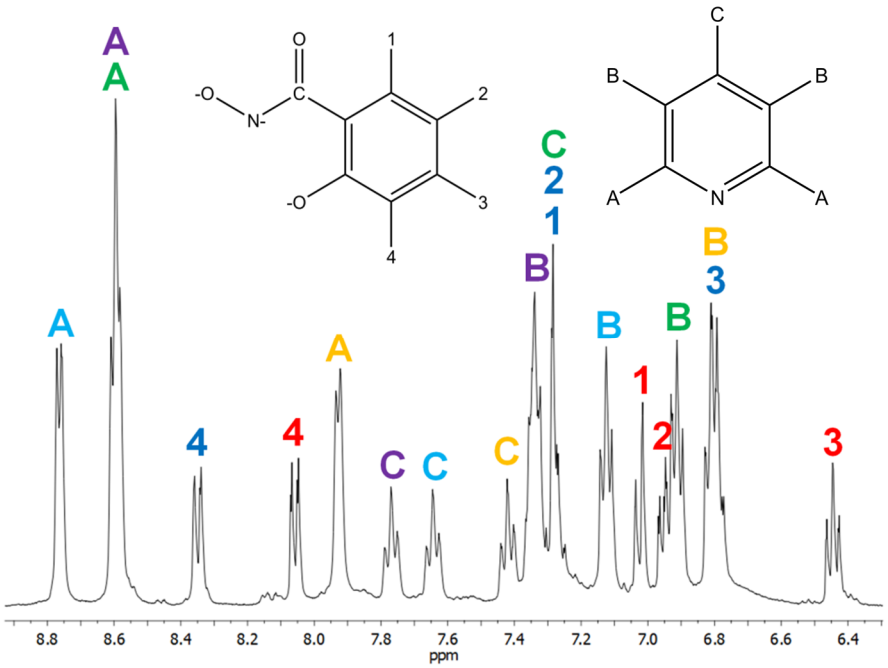

Figure 23 ^{1}H-NMR spectrum of **2** in dichlormethane; colored numbers represents assignment of the signal; different colors encode distinguishable ligands, different numbers encode different H-positions

δ (ppm)	Multiplicity	Assignment	Equivalent Protons
6.43-6.47	t	Shi-3	2
6.77-6.83	m	Shi-3	2
		Py-B	4
6.90-6.93	t	Py-B	4
6.94-6.97	d	Shi-2	2
7.02-7.04	d	Shi-1	2
7.11-7.14	t	Py-B	4
7.26-7.30	m	Shi-1	2
		Shi-2	2
		Py-C	2
7.32-7.36	m	Py-B	4
7.40-7.44	t	Py-C	2
7.63-7.66	t	Py-C	2
7.75-7.78	t	Py-C	2
7.92-7.93	d	Py-A	4
8.06-8.07	d	Shi-4	2
8.34-8.36	d	Shi-4	2
8.58-8.61	m	Py-A	4
		Py-A	4
8.76-8.77	d	Py-A	4

Table S47 Assignment of the signals in the ^{1}H-NMR spectrum of **2** in dichlormethane

3.9.6 Static Magnetism

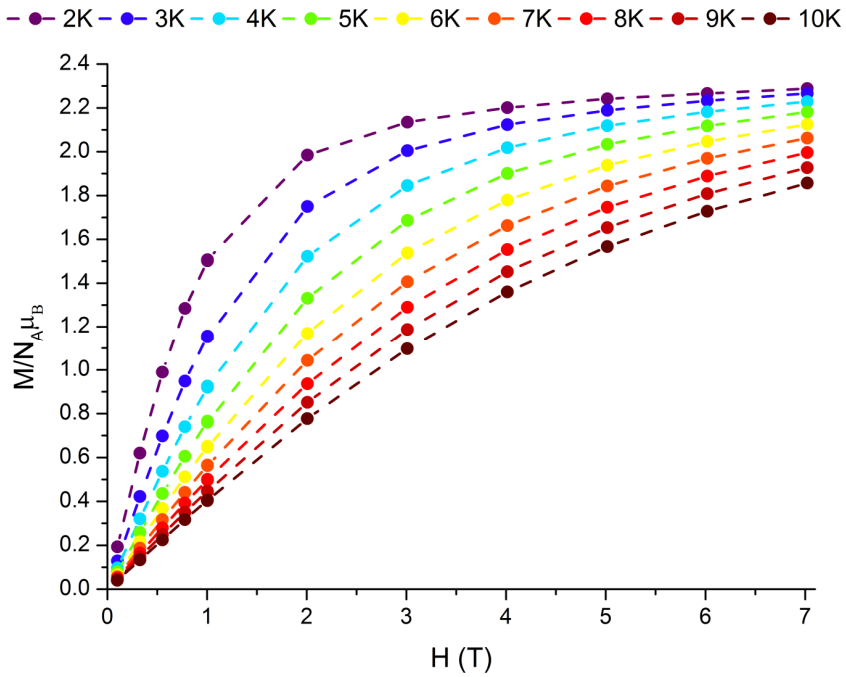

Figure S24 plot of the reduced magnetization versus the applied field for **4**; dashed lines represent guidelines for the eyes

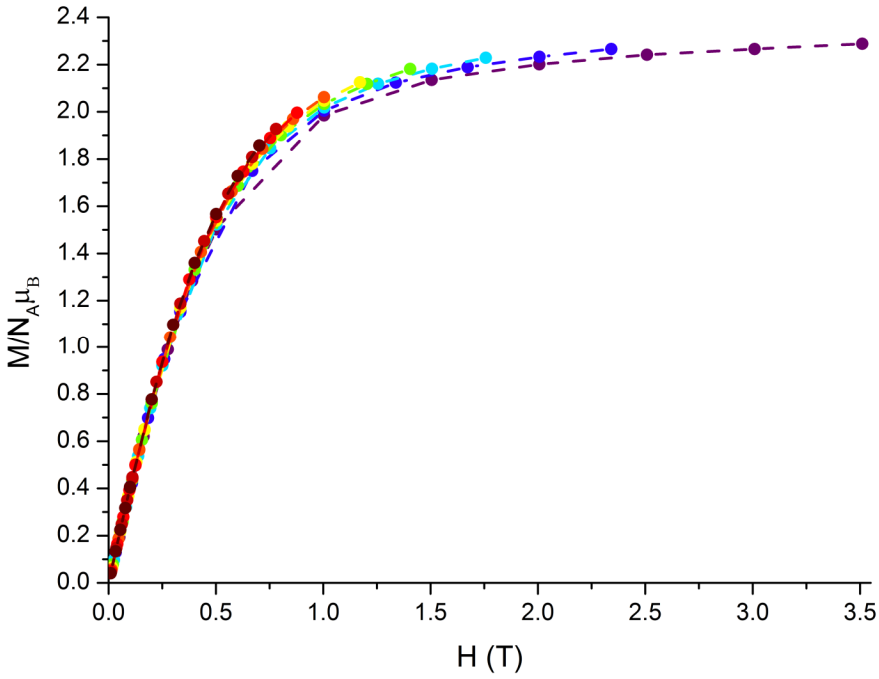

Figure S25 plot of the reduced magnetization versus the ratio of applied field and temperature for **4**; dashed lines represent guidelines for the eyes

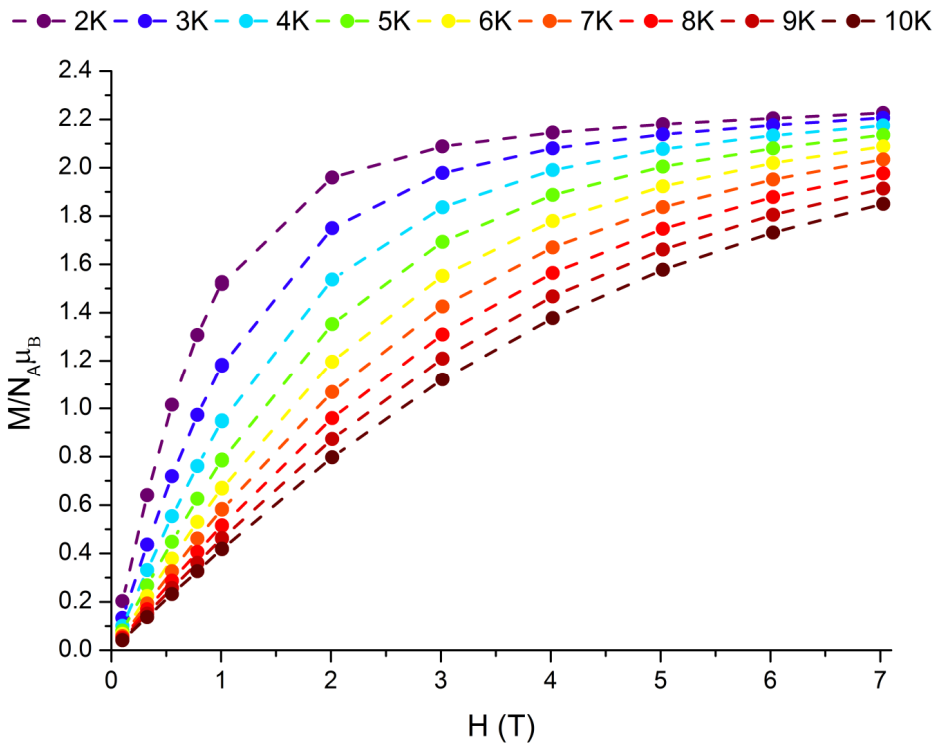

Figure S26 plot of the reduced magnetization versus the applied field for **5**; dashed lines represent guidelines for the eyes

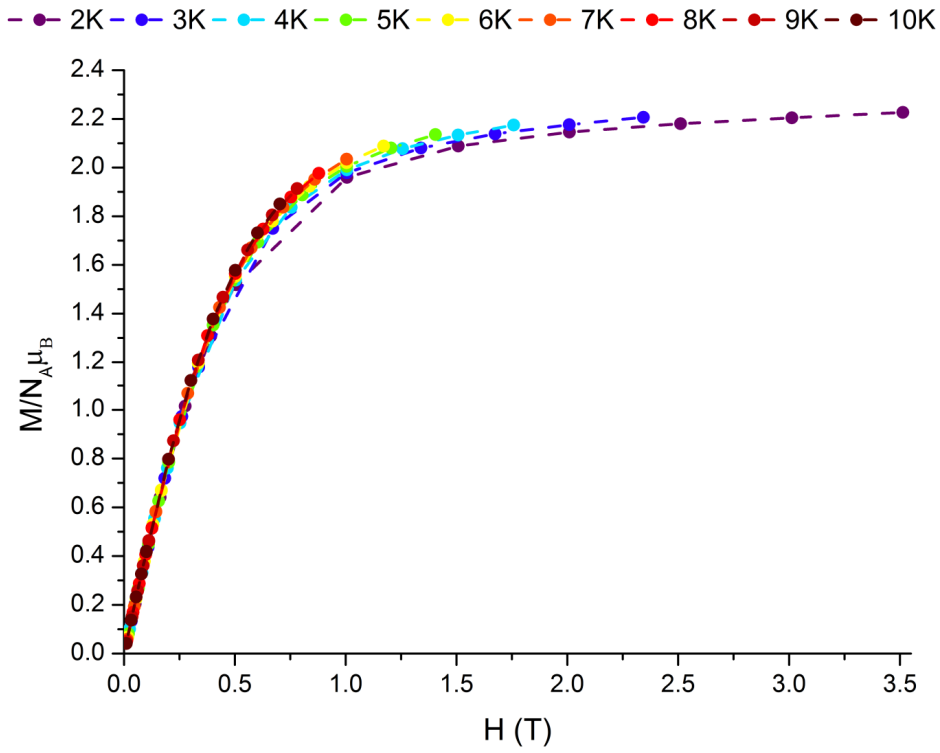

Figure S27 plot of the reduced magnetization versus the ratio of applied field and temperature for **5**; dashed lines represent guidelines for the eyes

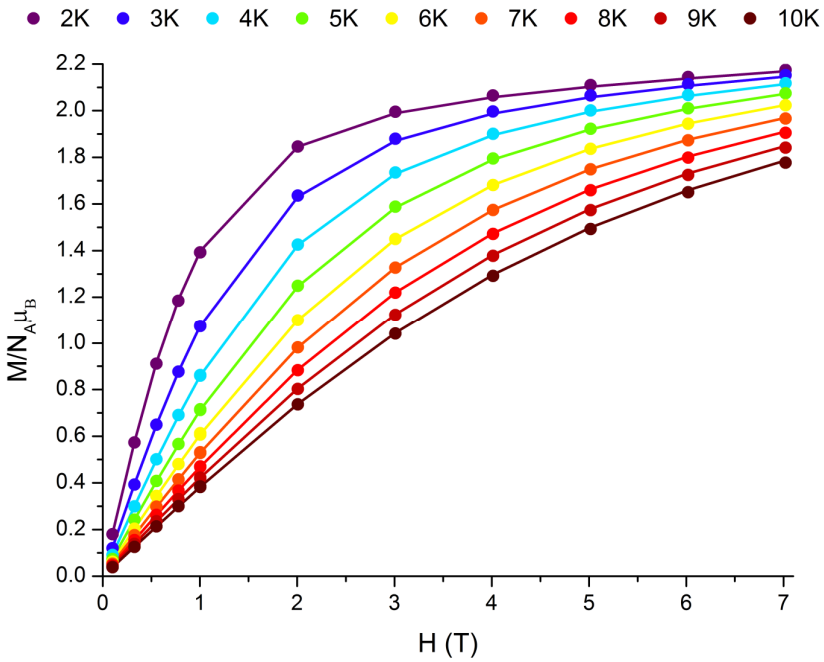

Figure S28 plot of the reduced magnetization versus the applied field for **8**; solid lines represent the best fit results according to an effective spin Hamiltonian with zero-field splitting parameter

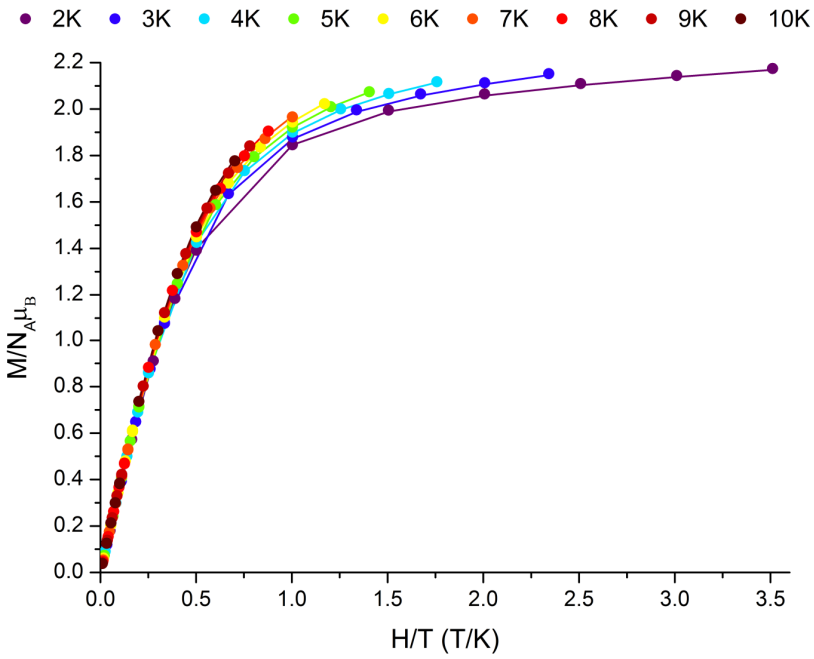

Figure S29 plot of the reduced magnetization versus the ratio of applied field and temperature for **8**; solid lines represent the best fit results according to an effective spin Hamiltonian with zero-field splitting parameter

$$\hat{H} = D\hat{S}_z^2 + E\left(\hat{S}_x^2 - \hat{S}_z^2\right) + g_{iso}\mu_B\hat{S}H \qquad \text{(S4)}$$

3.9.7 Dynamic Magnetism

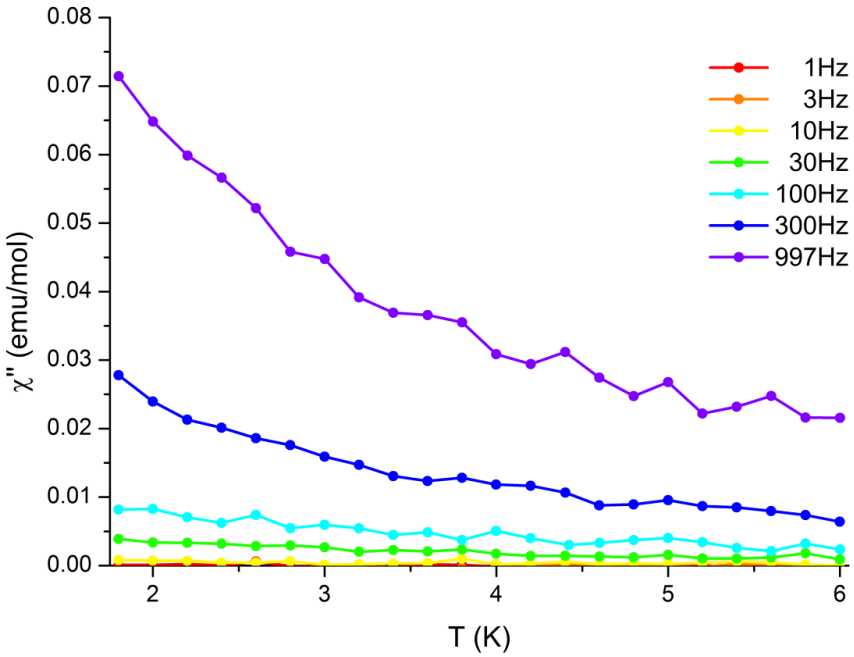

Figure S30 plot of the out-of-phase susceptibility versus temperature under zero applied static field for **5**; solid lines represent guidelines for the eyes

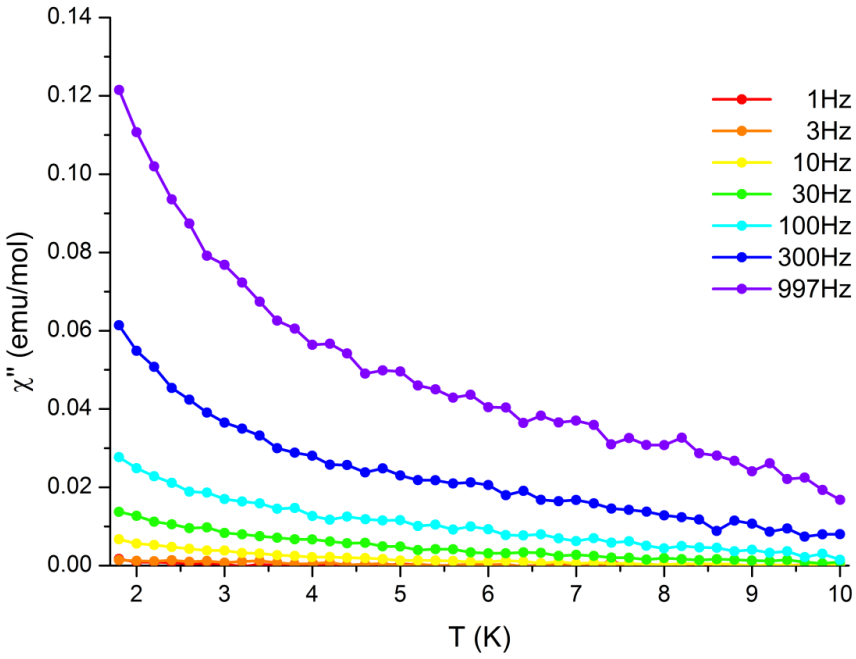

Figure S31 plot of the out-of-phase susceptibility versus temperature under zero applied static field for **8**; solid lines represent guidelines for the eyes

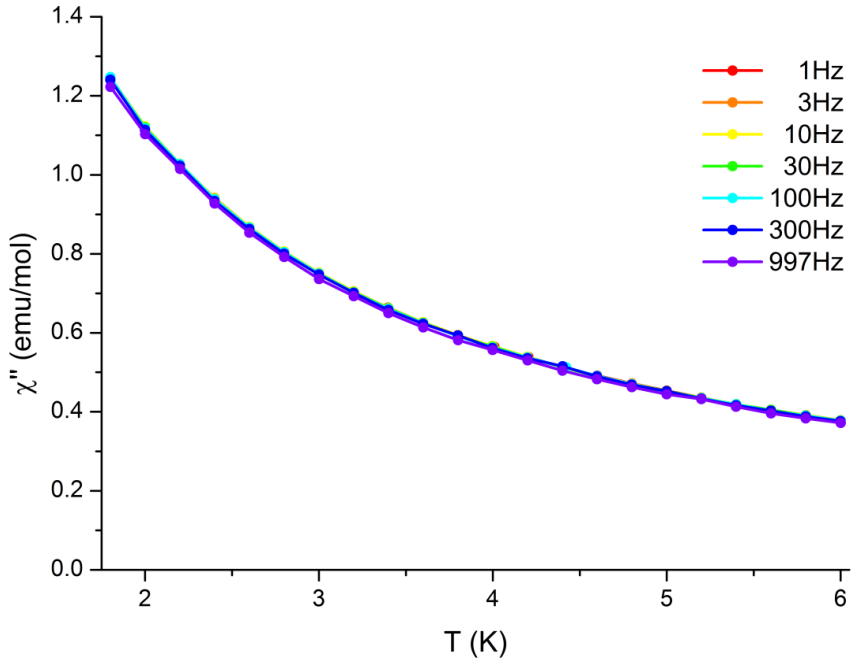

Figure S32 plot of the in-phase susceptibility versus temperature under zero applied static field for **5**; solid lines represent guidelines for the eyes

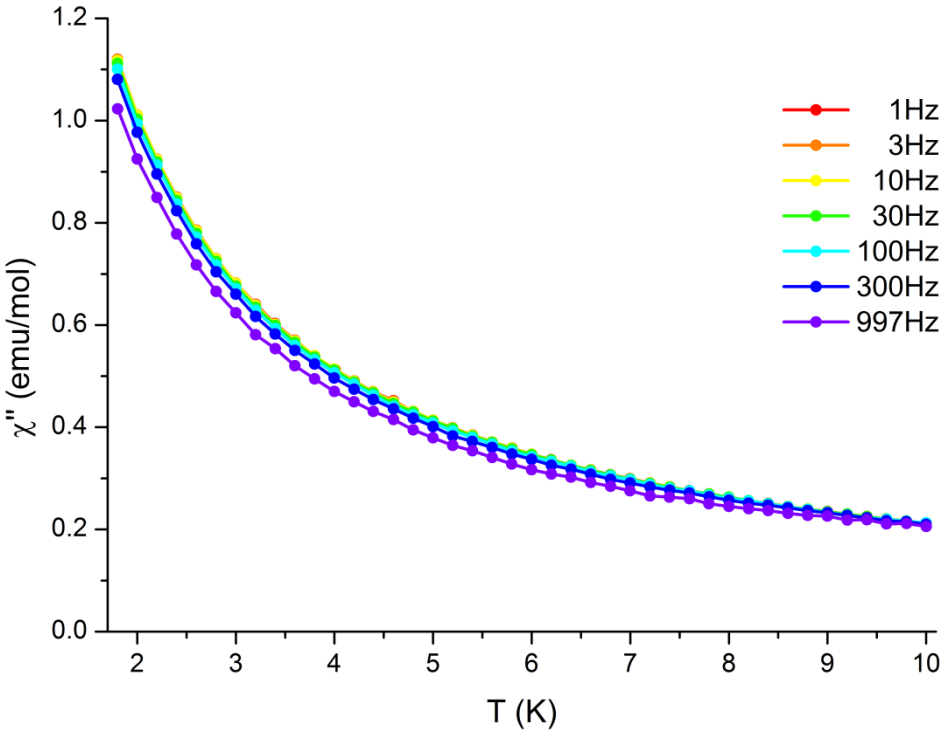

Figure S33 plot of the in-phase susceptibility versus temperature under zero applied static field for **8**; solid lines represent guidelines for the eyes

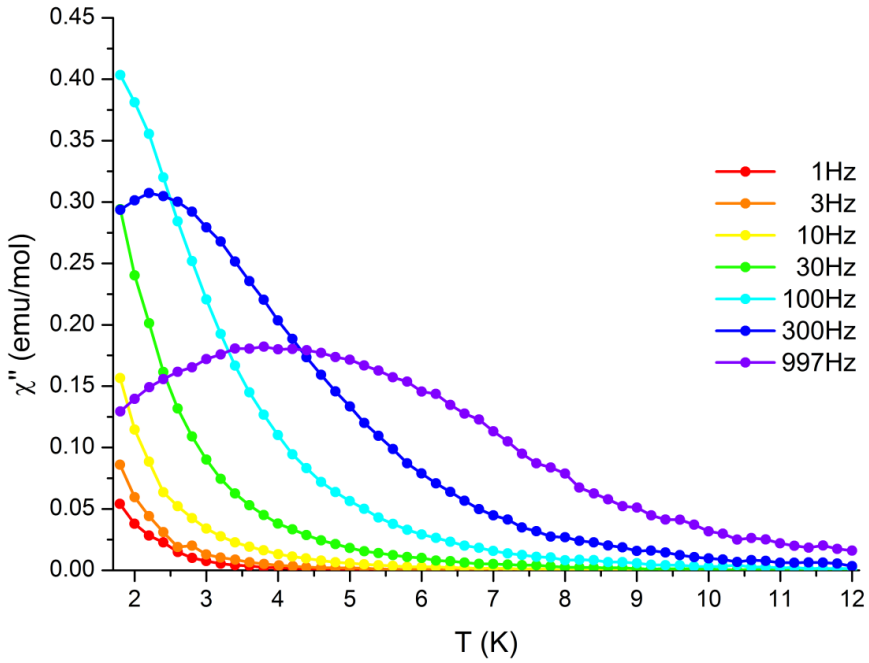

Figure S34 plot of the out-of-phase susceptibility versus temperature under an applied static field of 1500Oe for **4**; solid lines represent guidelines for the eyes

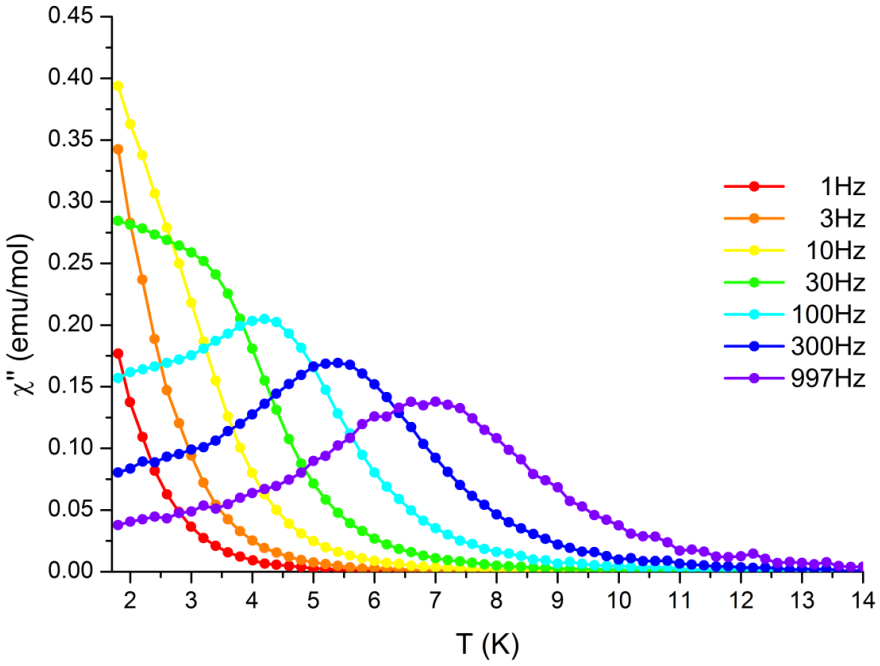

Figure S35 plot of the out-of-phase susceptibility versus temperature under an applied static field of 1500Oe for **5**; solid lines represent guidelines for the eyes

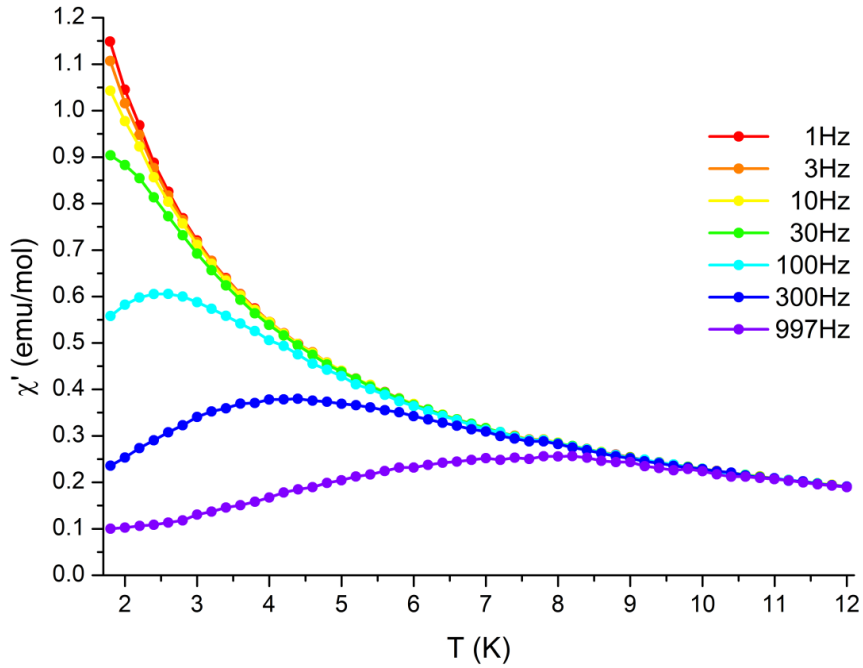

Figure S36 plot of the in susceptibility versus temperature under an applied static field of 1500Oe for **4**; solid lines represent guidelines for the eyes

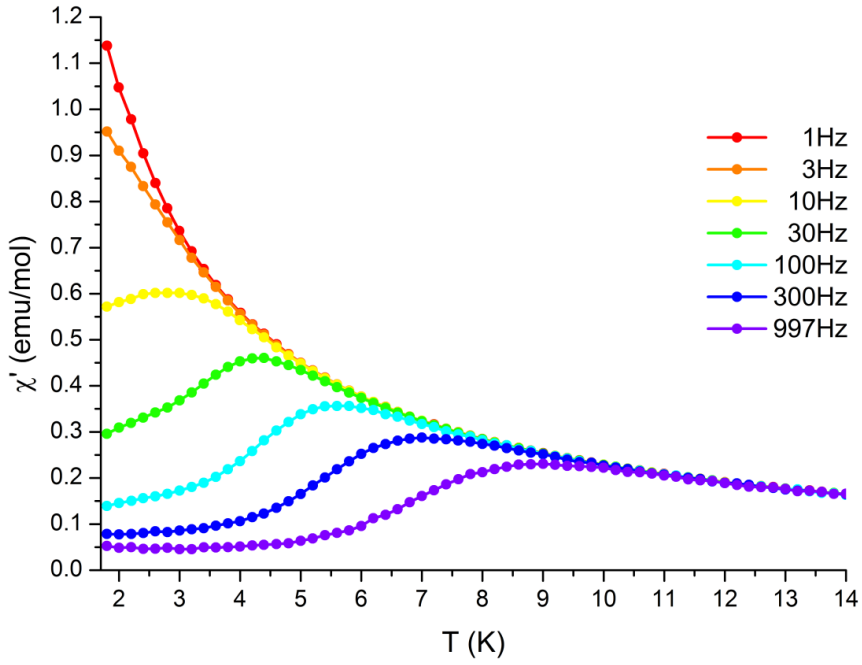

Figure S37 plot of the in susceptibility versus temperature under an applied static field of 1500Oe for **5**; solid lines represent guidelines for the eyes

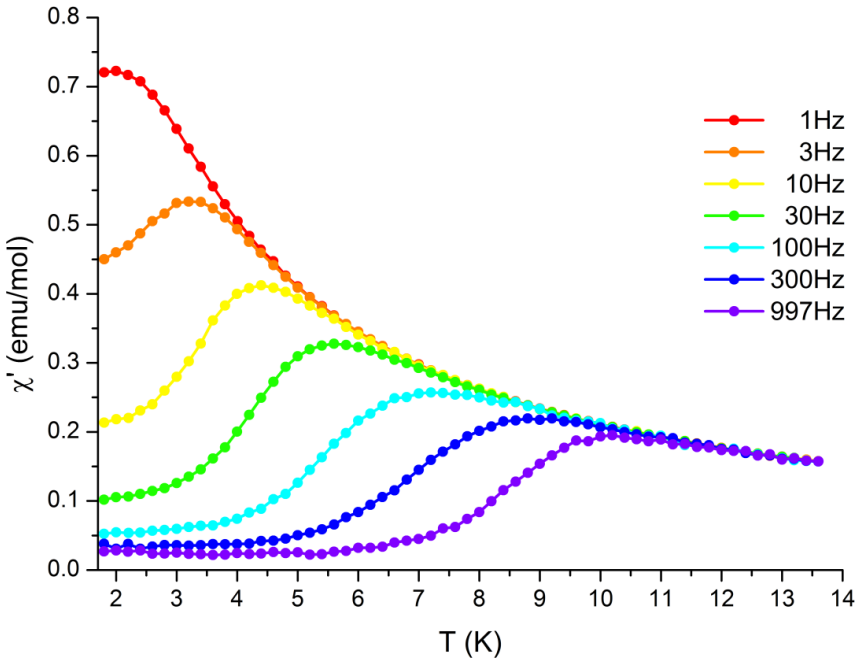

Figure S38 plot of the in susceptibility versus temperature under an applied static field of 1500Oe for **8**; solid lines represent guidelines for the eyes

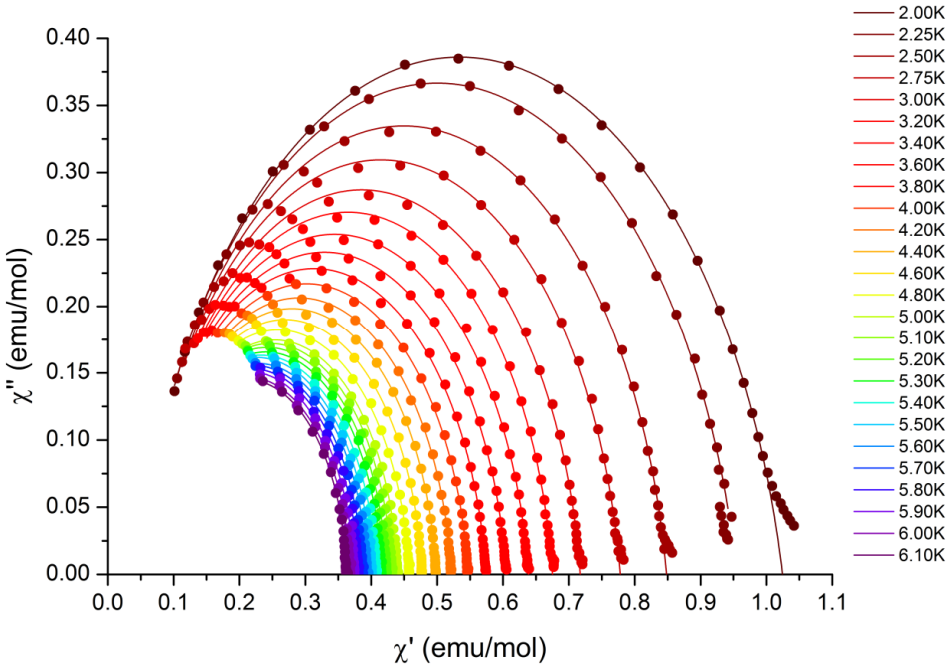

Figure S39 Cole-Cole plot of in- and out-of-phase susceptibility under an applied static field of 1500Oe for **4**; solid lines represent the best fit results according to a generalized Debye model

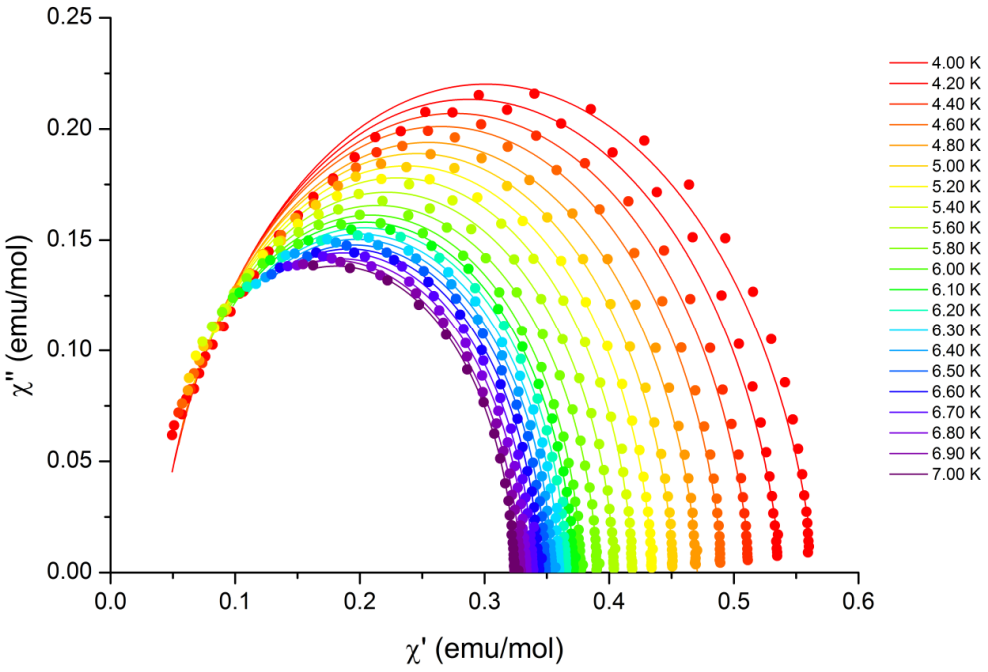

Figure S40 Cole-Cole plot of in- and out-of-phase susceptibility under an applied static field of 1500Oe for **4**; solid lines represent the best fit results according to a generalized Debye model

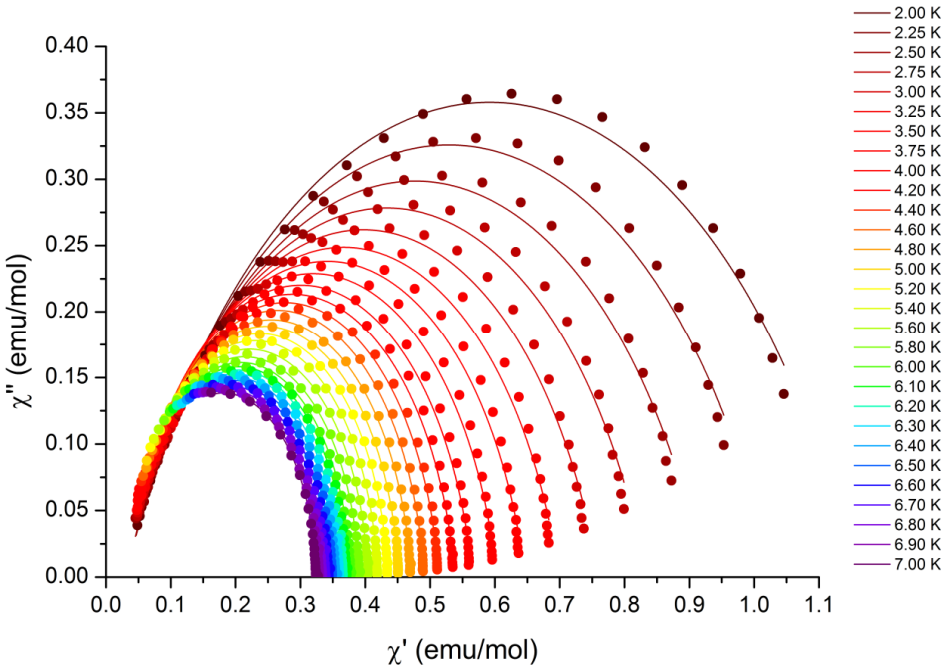

Figure S41 Cole-Cole plot of in- and out-of-phase susceptibility under an applied static field of 1500Oe for **5**; solid lines represent the best fit results according to a generalized Debye model

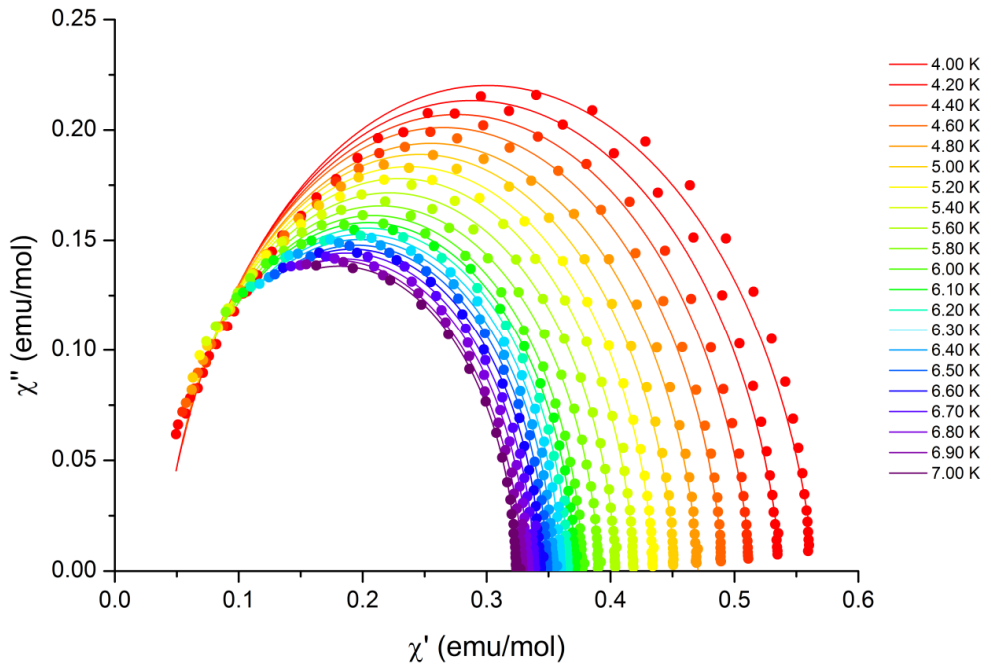

Figure S42 Cole-Cole plot of in- and out-of-phase susceptibility under an applied static field of 1500Oe for **5**; solid lines represent the best fit results according to a generalized Debye model

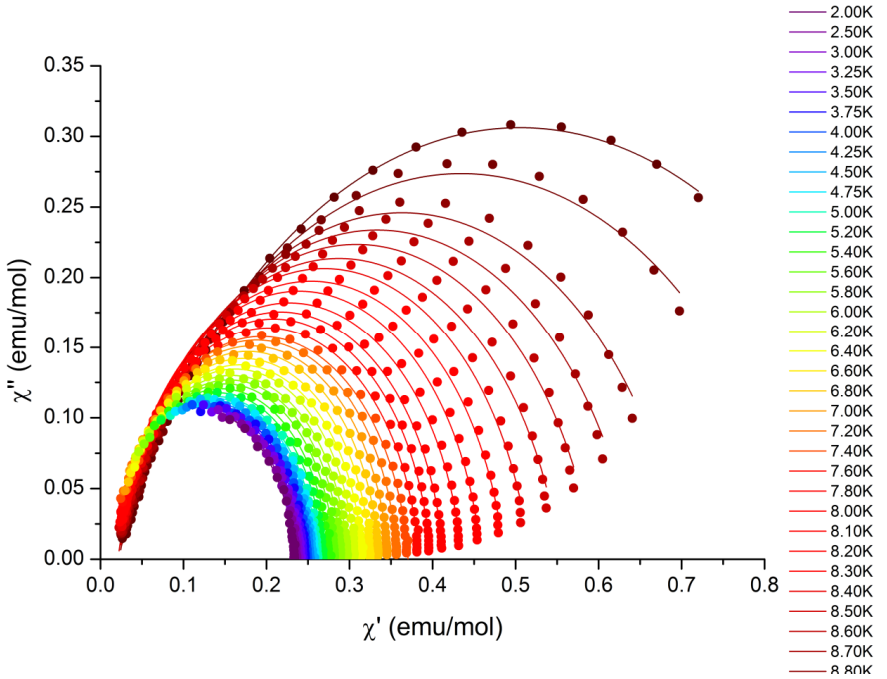

Figure S43 Cole-Cole plot of in- and out-of-phase susceptibility under an applied static field of 1500Oe for **8**; solid lines represent the best fit results according to a generalized Debye model

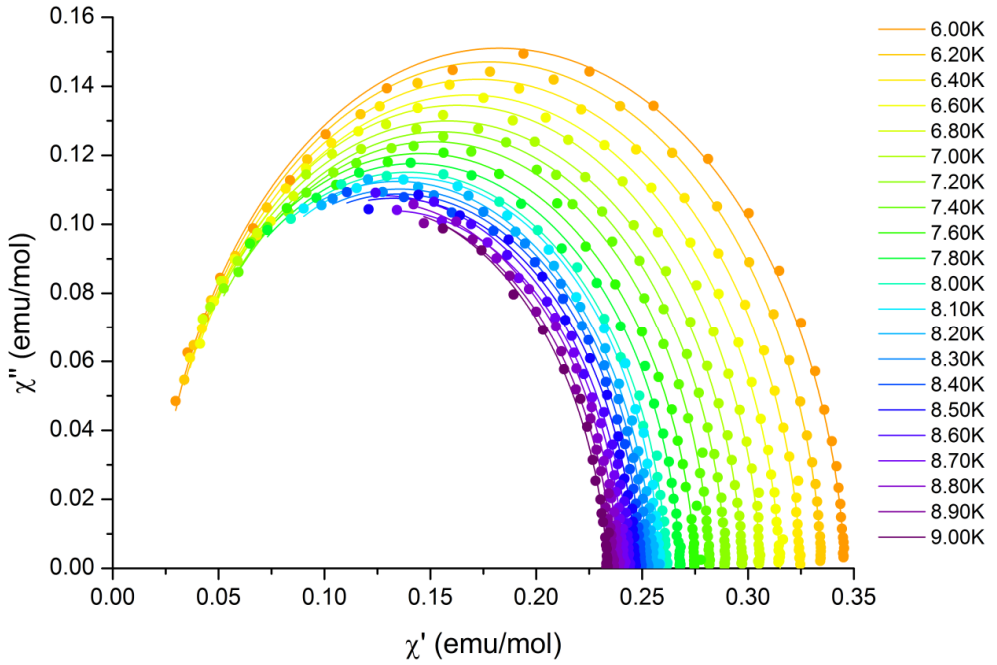

Figure S44 Cole-Cole plot of in- and out-of-phase susceptibility under an applied static field of 1500Oe for **8**; solid lines represent the best fit results according to a generalized Debye model

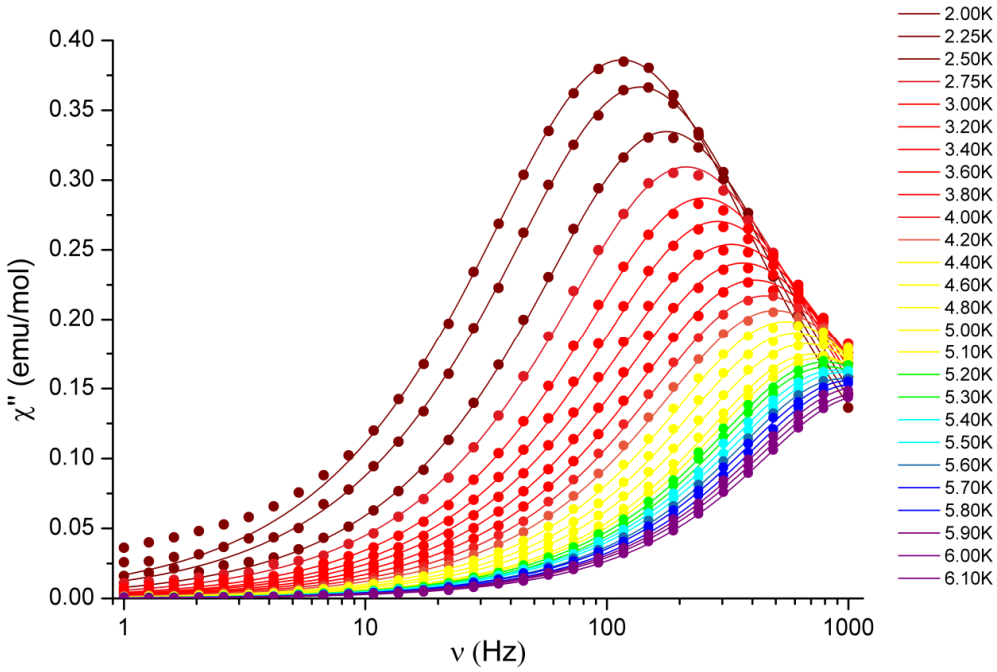

Figure S45 plot of out-of-phase susceptibility versus frequency under an applied static field of 1500Oe for **4**; solid lines represent the best fit results according to a generalized Debye model

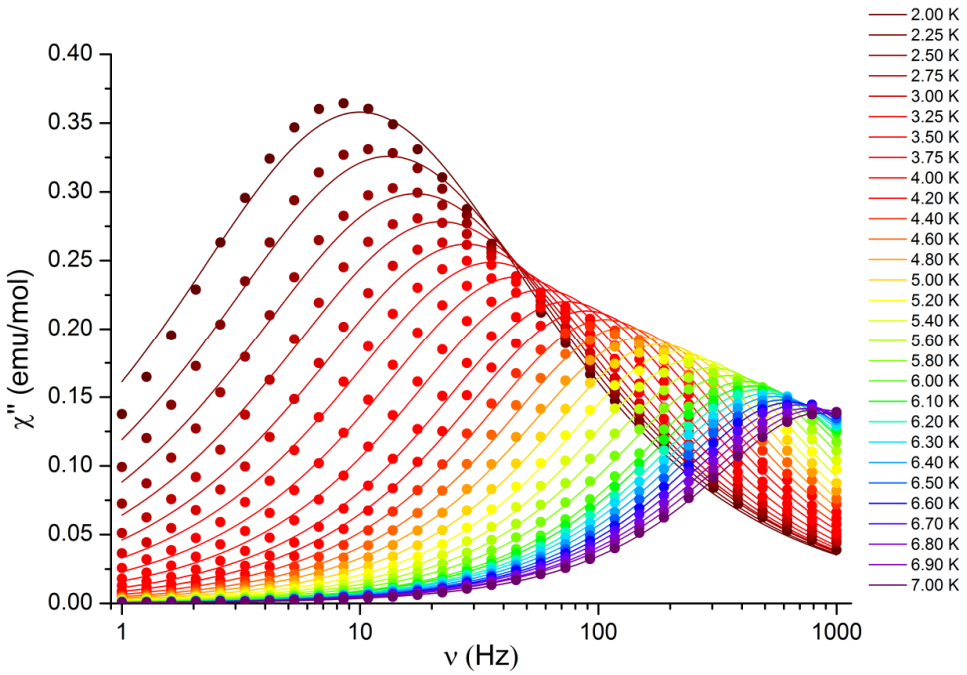

Figure S46 plot of out-of-phase susceptibility versus frequency under an applied static field of 1500Oe for **5**; solid lines represent the best fit results according to a generalized Debye model

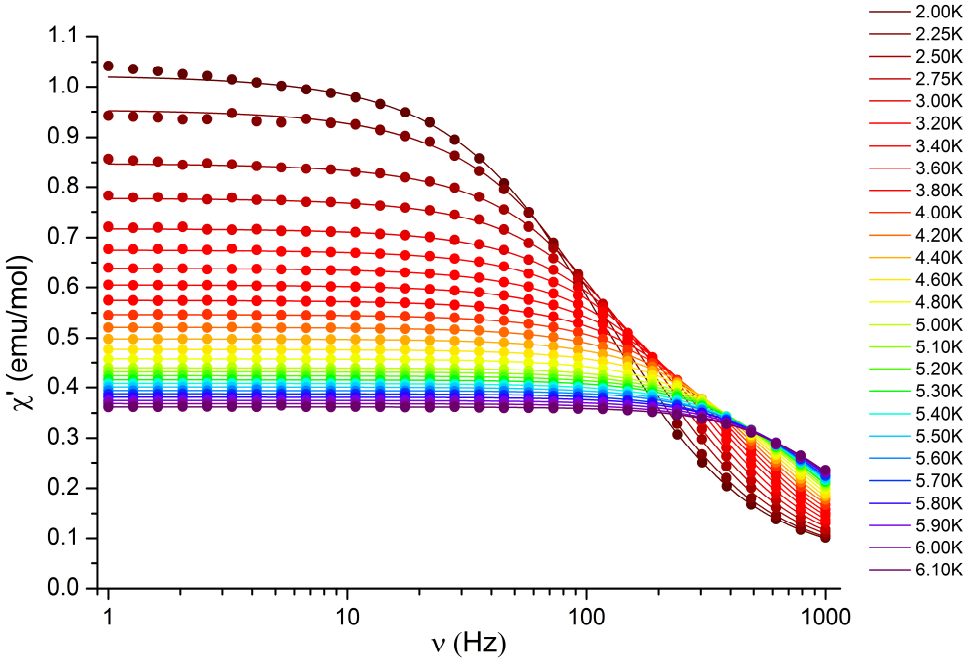

Figure S47 plot of in-phase susceptibility versus frequency under an applied static field of 1500Oe for **4**; solid lines represent the best fit results according to a generalized Debye model

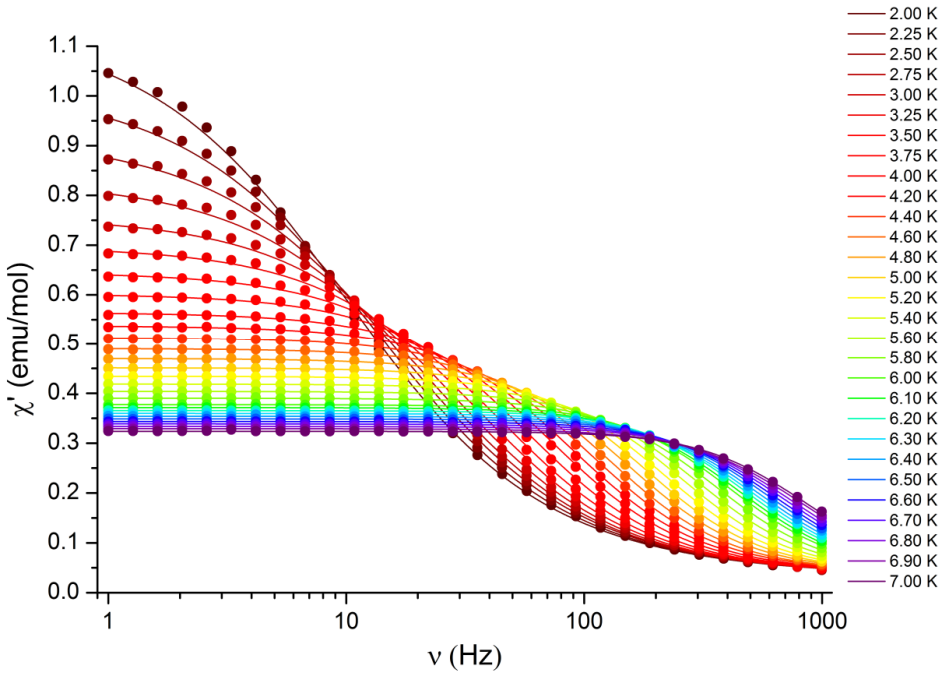

Figure S48 plot of in-phase susceptibility versus frequency under an applied static field of 1500Oe for **5**; solid lines represent the best fit results according to a generalized Debye model

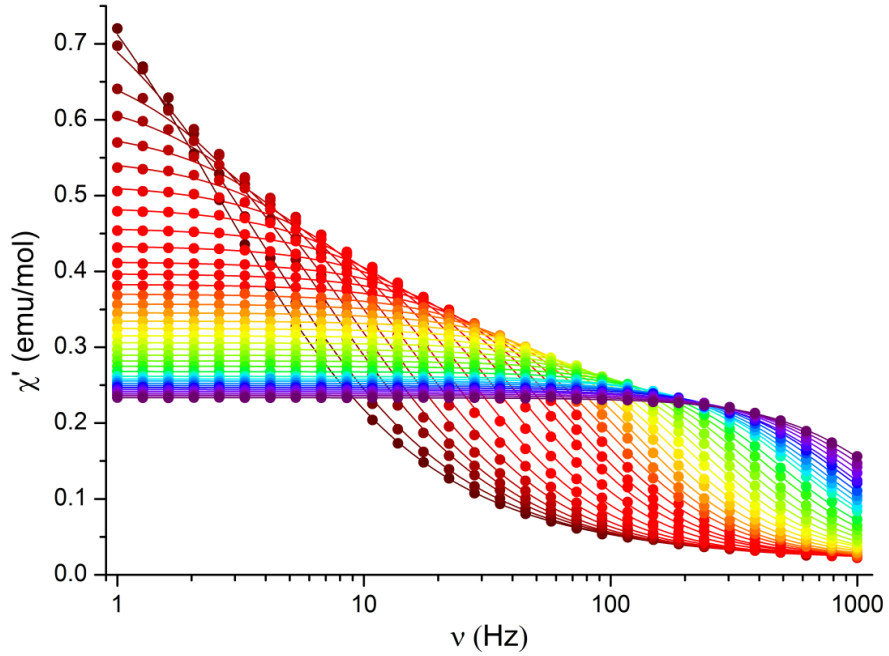

Figure S49 plot of in-phase susceptibility versus frequency under an applied static field of 1500Oe for **8**; solid lines represent the best fit results according to a generalized Debye model

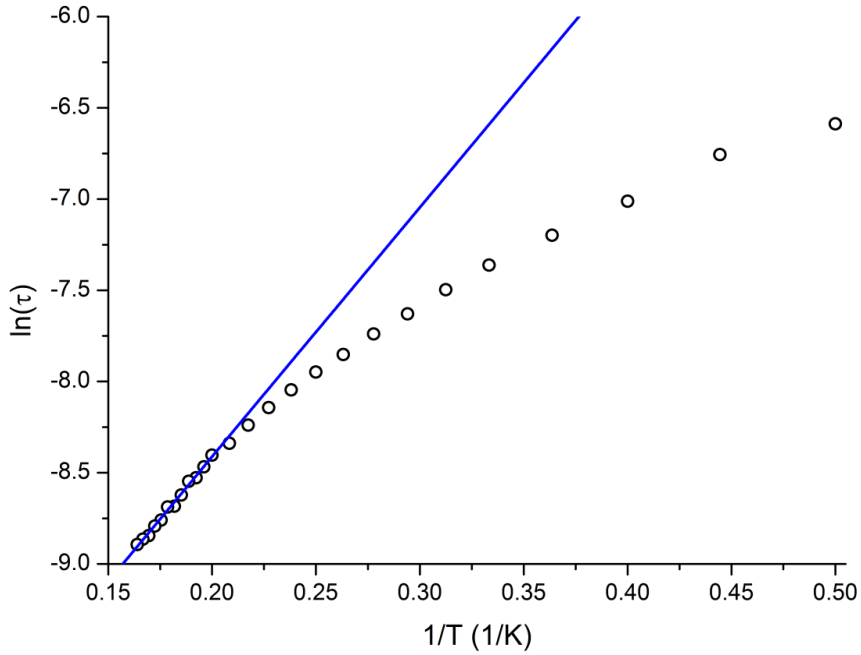

Figure S50 Arrhenius plot of the natural logarithm of the relaxation time versus the reciprocal temperature under an applied static field of 1500Oe for **4;** solid line represents the fit result of the high temperature range according to the Arrhenius equation

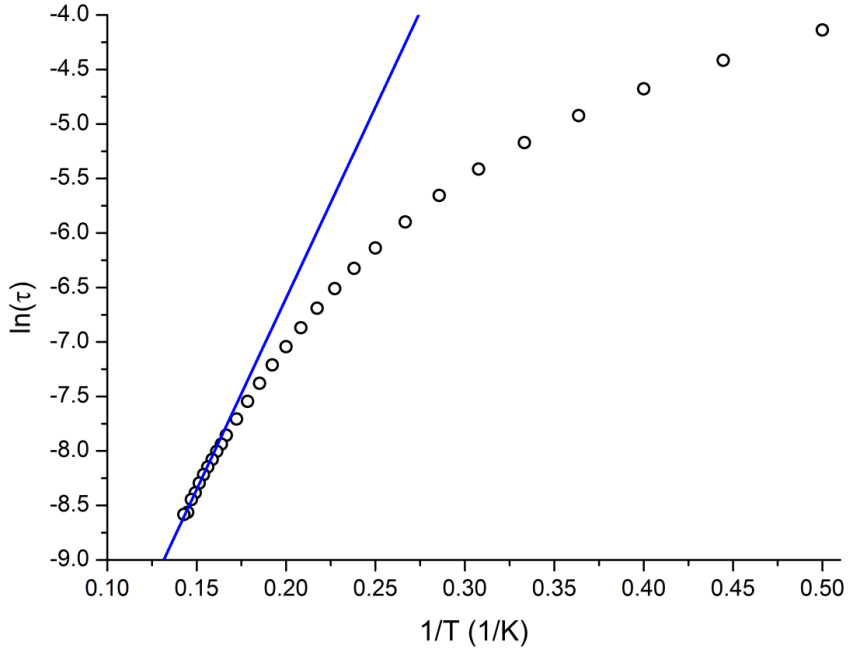

Figure S51 Arrhenius plot of the natural logarithm of the relaxation time versus the reciprocal temperature under an applied static field of 1500Oe for **5;** solid line represents the fit result of the high temperature range according to the Arrhenius equation

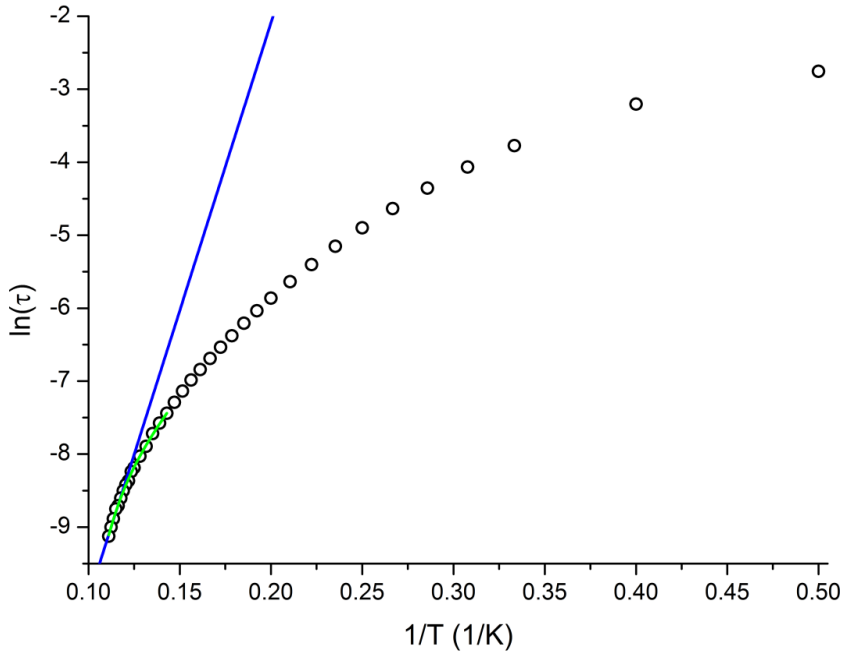

Figure S52 Arrhenius plot of the natural logarithm of the relaxation time versus the reciprocal temperature under an applied static field of 1500Oe for **8;** solid blue line represents the fit result of the high temperature range according to the Arrhenius equation; solid green line represents the fit result of the high temperature range according to a model regarding Orbach and Raman relaxation process

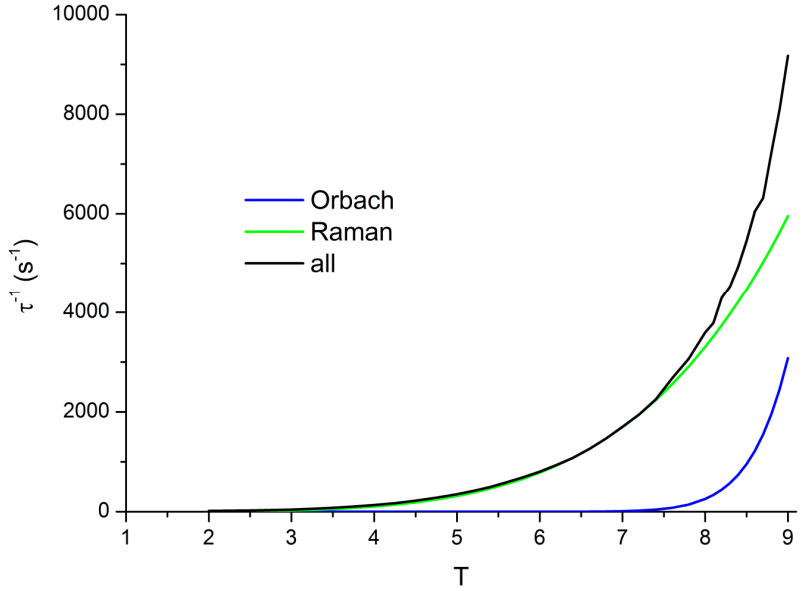

Figure S53 plot of relaxation rate versus the temperature from experimental data under an applied static field of 1500Oe for **8** and for the corresponding calculated contributions of Orbach and Raman relaxation according to the fit result of the high temperature data of the relaxation times

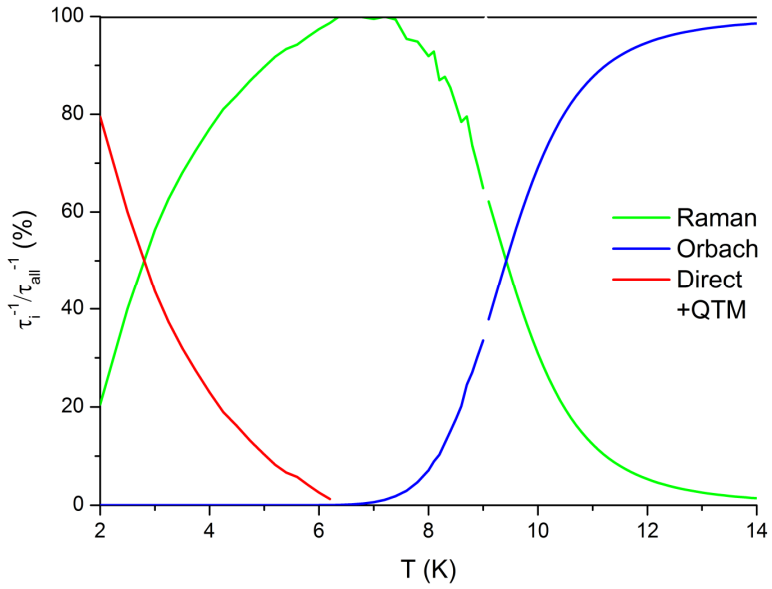

Figure S54 plot of the relative contributions of Orbach, Raman and remaining relaxation process to the overall relaxation rate based on the fit of the high temperature data of the relaxation time according to a model regarding Orbach and Raman relaxation of the experimental data under an applied static field of 1500Oe for **8;** relative values above 9.1K were calculated using the optimized fit parameters of Orbach and Raman relaxation and setting their sum equal to the overall relaxation rate

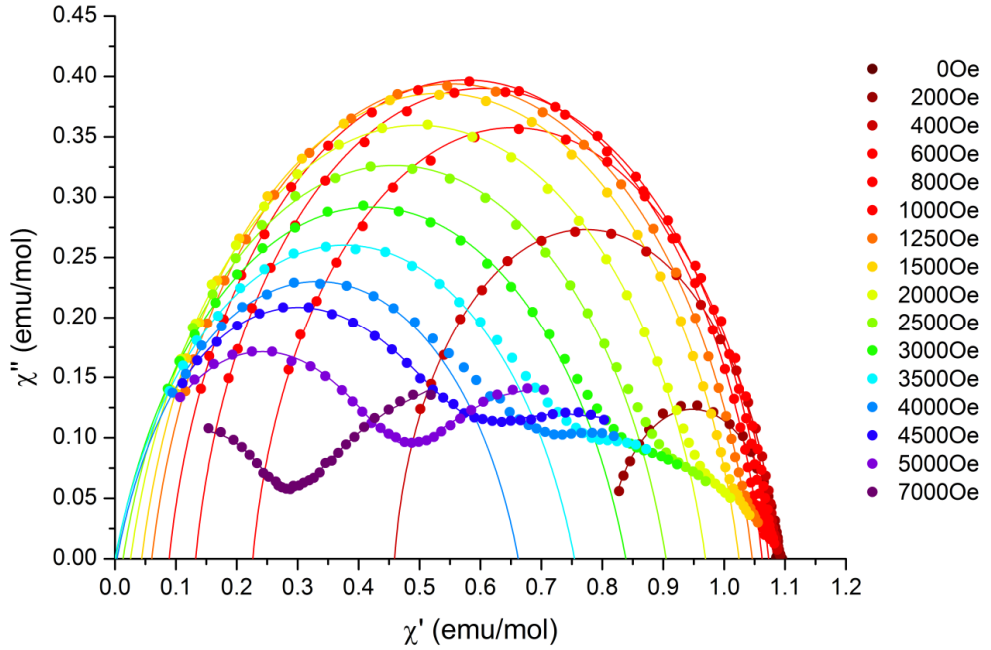

Figure S55 Cole-Cole plot of in- and out-of-phase susceptibility at a temperature of 2K under different applied magnetic fields for **4**; solid lines represent the best fit results according to a generalized Debye model

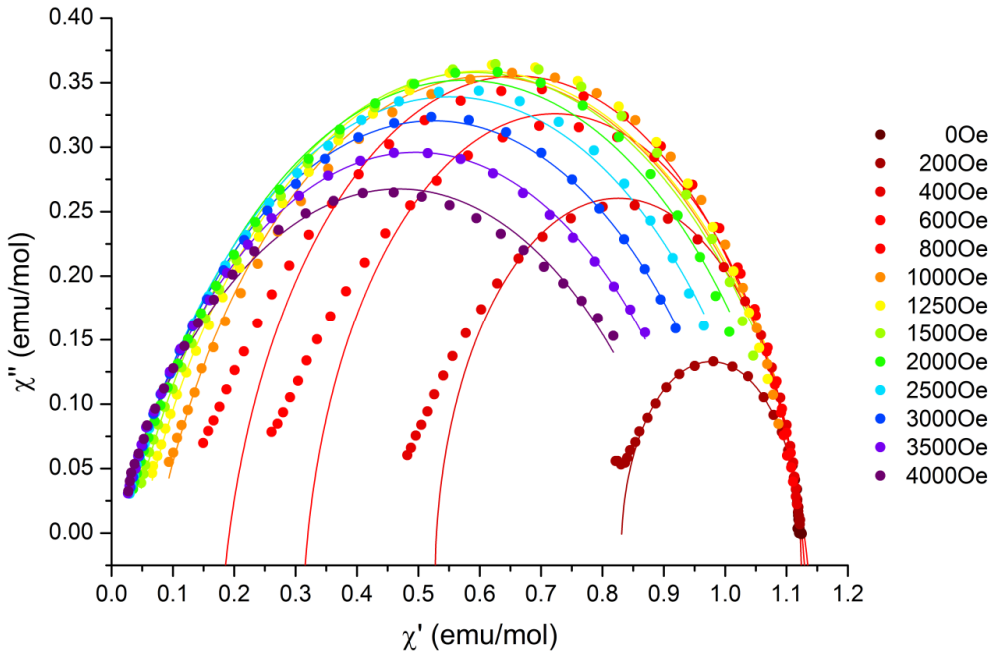

Figure S56 Cole-Cole plot of in- and out-of-phase susceptibility at a temperature of 2K under different applied magnetic fields for **5**; solid lines represent the best fit results according to a generalized Debye model

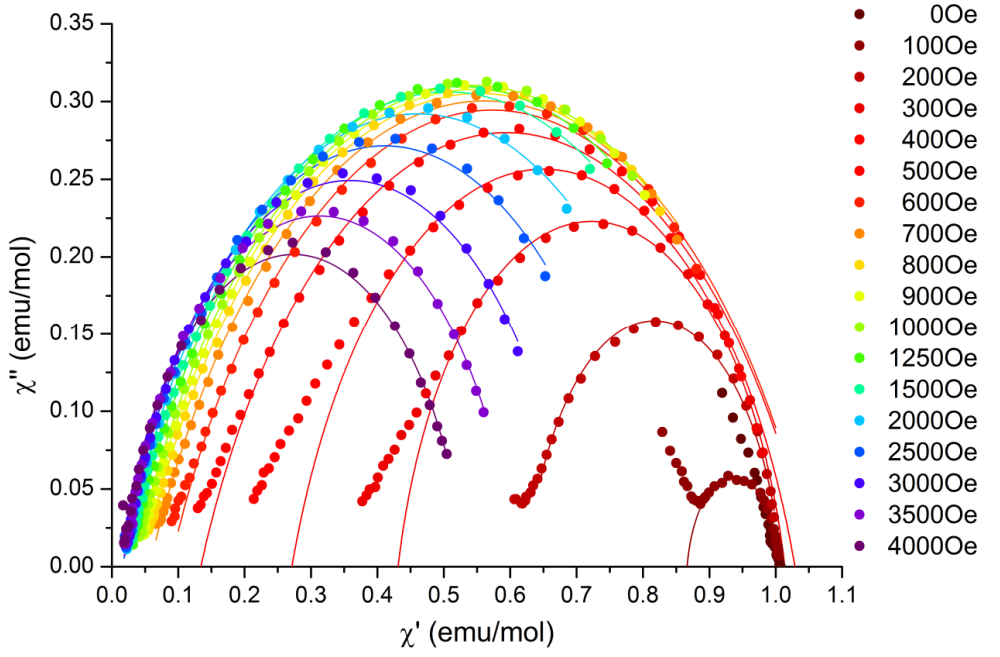

Figure S57 Cole-Cole plot of in- and out-of-phase susceptibility at a temperature of 2K under different applied magnetic fields for **8**; solid lines represent the best fit results according to a generalized Debye model

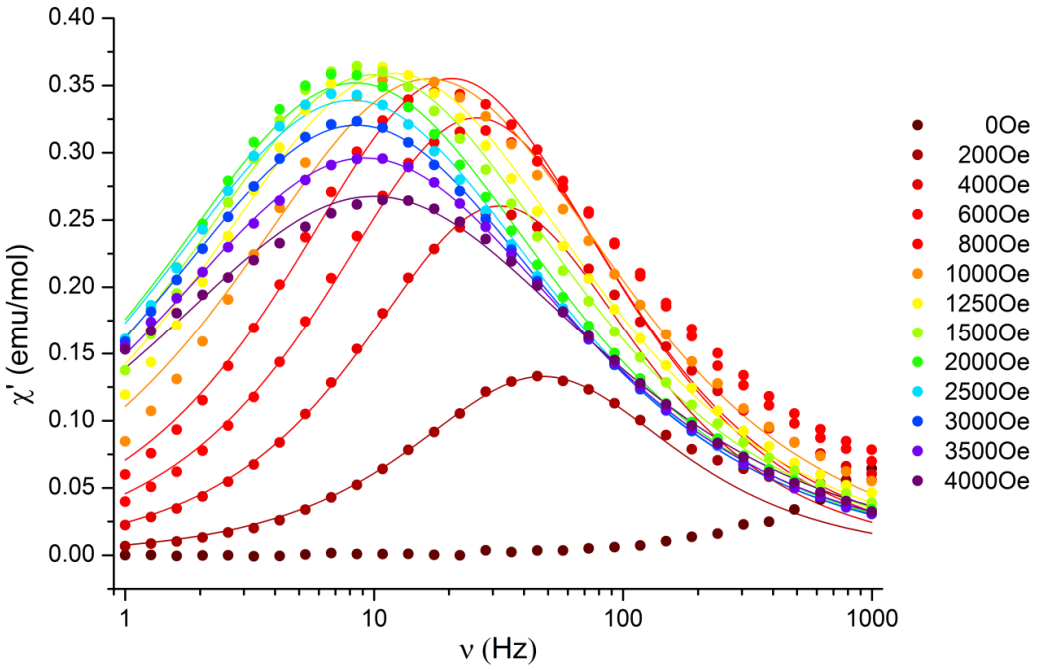

Figure S58 plot of out-of-phase susceptibility versus frequency at a temperature of 2K under different applied magnetic fields for **5**; solid lines represent the best fit results according to a generalized Debye model

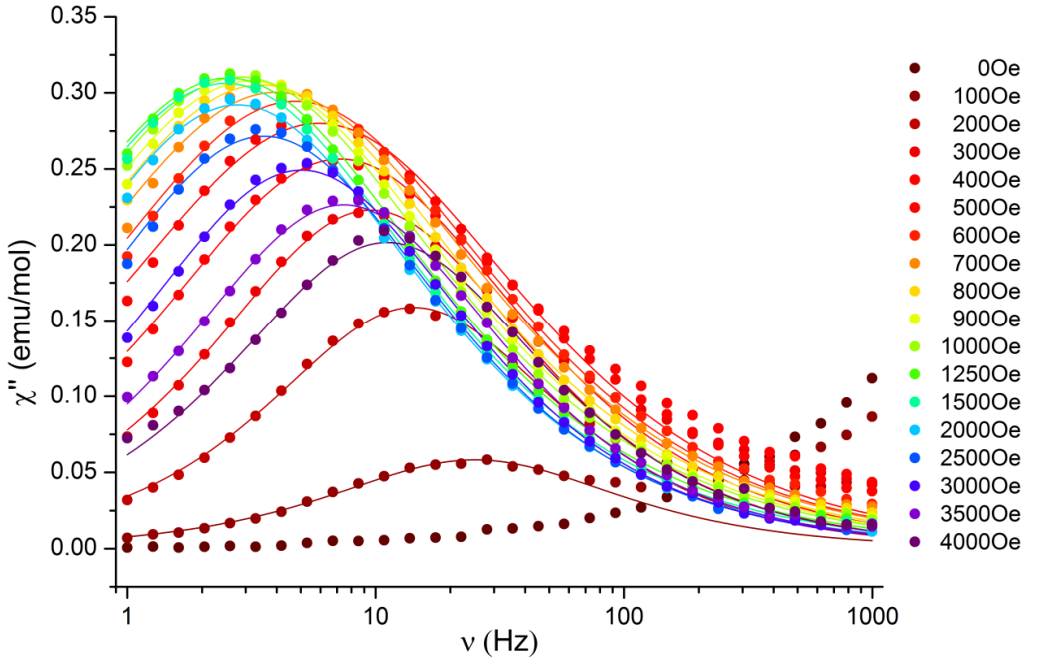

Figure S59 plot of out-of-phase susceptibility versus frequency at a temperature of 2K under different applied magnetic fields for **8**; solid lines represent the best fit results according to a generalized Debye model

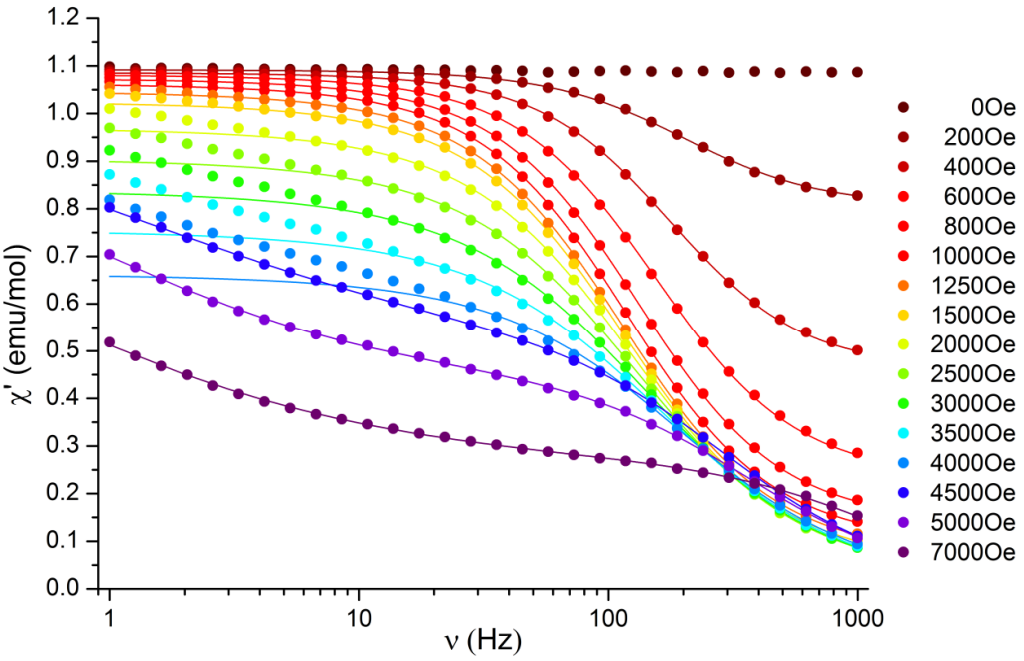

Figure S60 plot of in-phase susceptibility versus frequency at a temperature of 2K under different applied magnetic fields for **4**; solid lines represent the best fit results according to a generalized Debye model

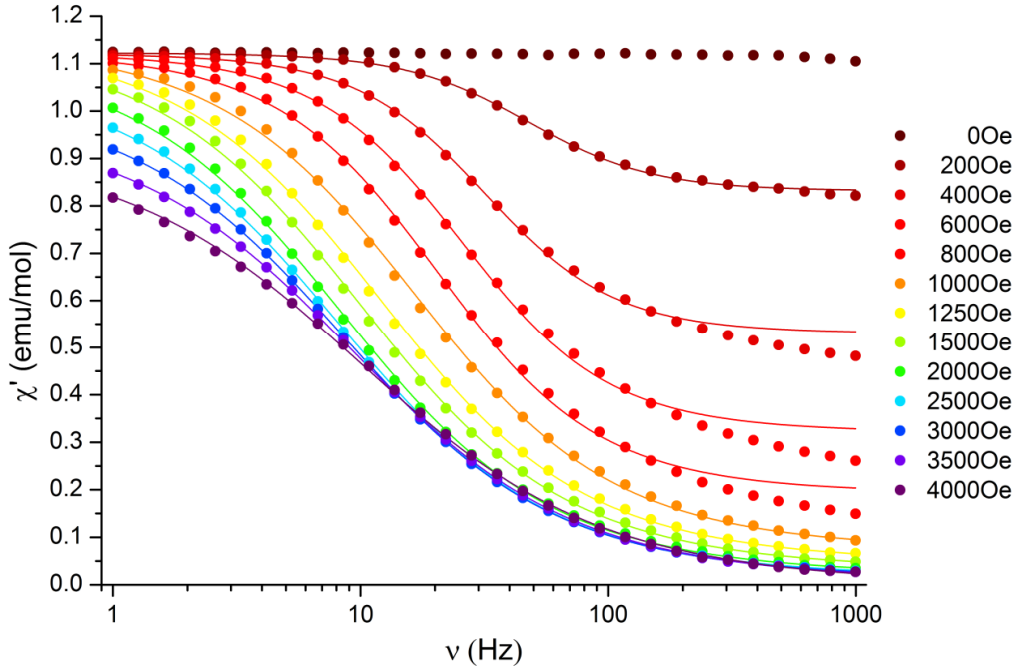

Figure S61 plot of in-phase susceptibility versus frequency at a temperature of 2K under different applied magnetic fields for **5**; solid lines represent the best fit results according to a generalized Debye model

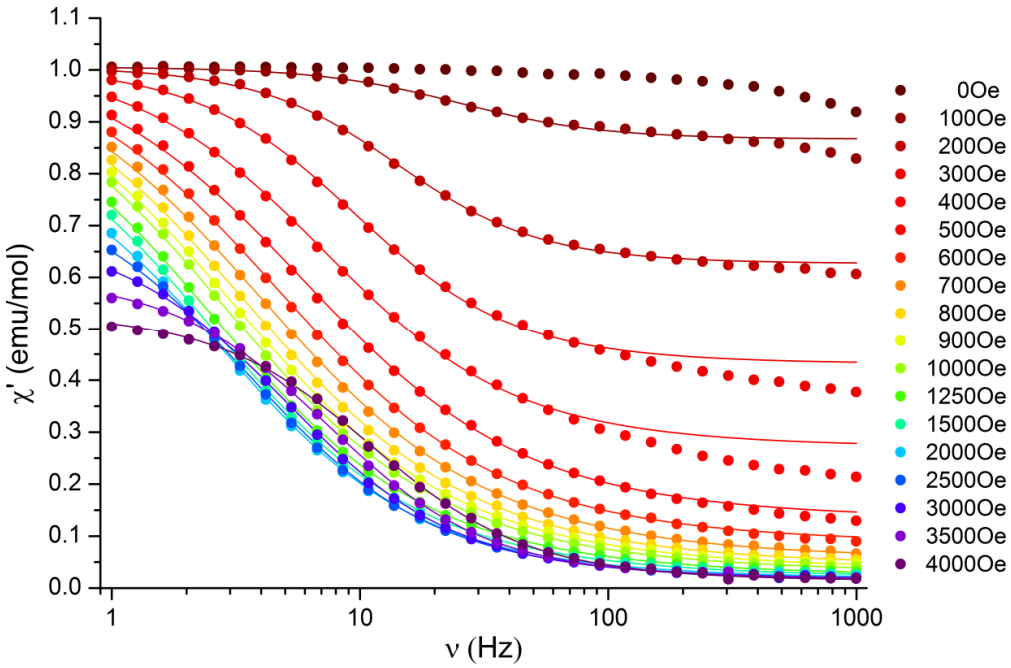

Figure S62 plot of in-phase susceptibility versus frequency at a temperature of 2K under different applied magnetic fields for **8**; solid lines represent the best fit results according to a generalized Debye model

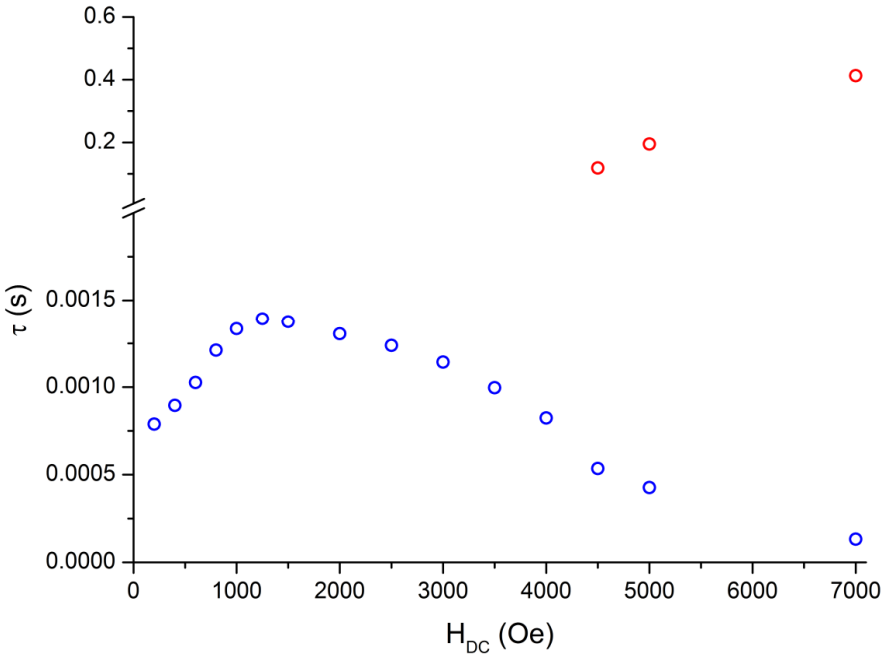

Figure S63 plot of the relaxation time versus the applied magnetic field at a temperature of 2K for **4**

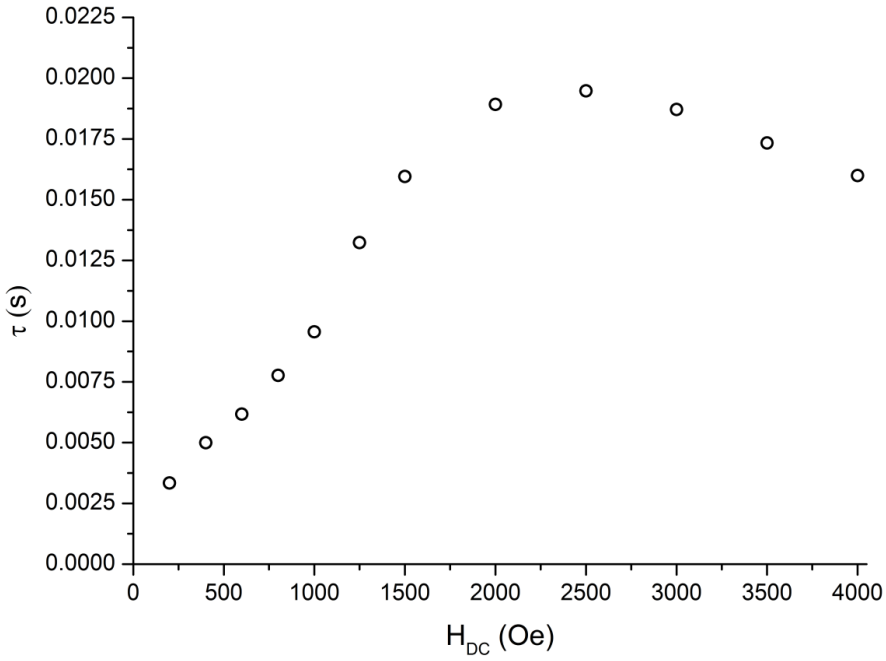

Figure S64 plot of the relaxation time versus the applied magnetic field at a temperature of 2K for **5**

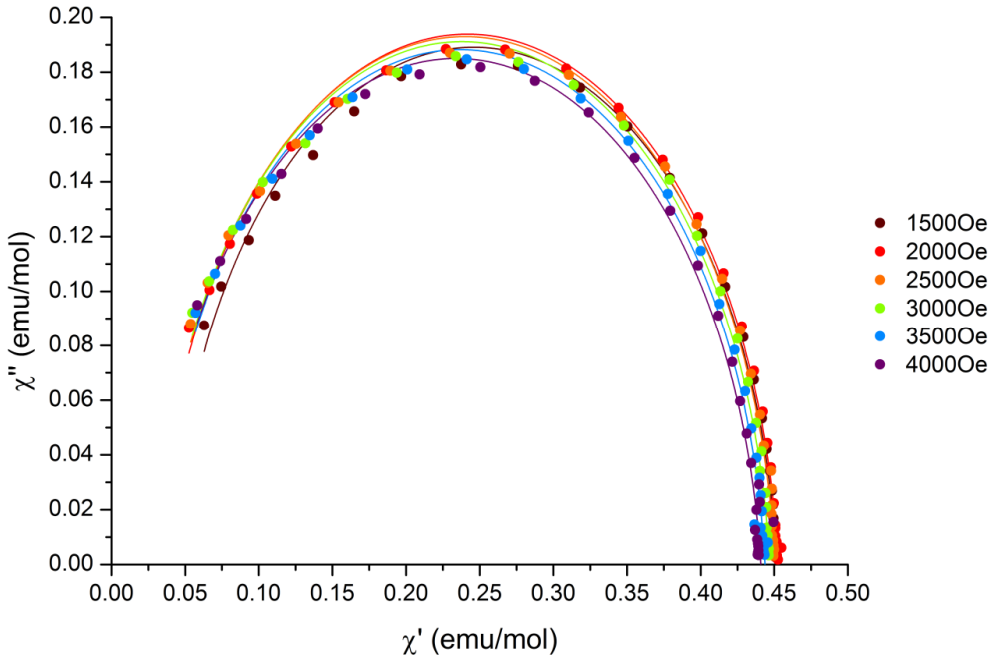

Figure S65 Cole-Cole plot of in- and out-of-phase susceptibility at a temperature of 5K under different applied magnetic fields for **5**; solid lines represent the best fit results according to a generalized Debye model

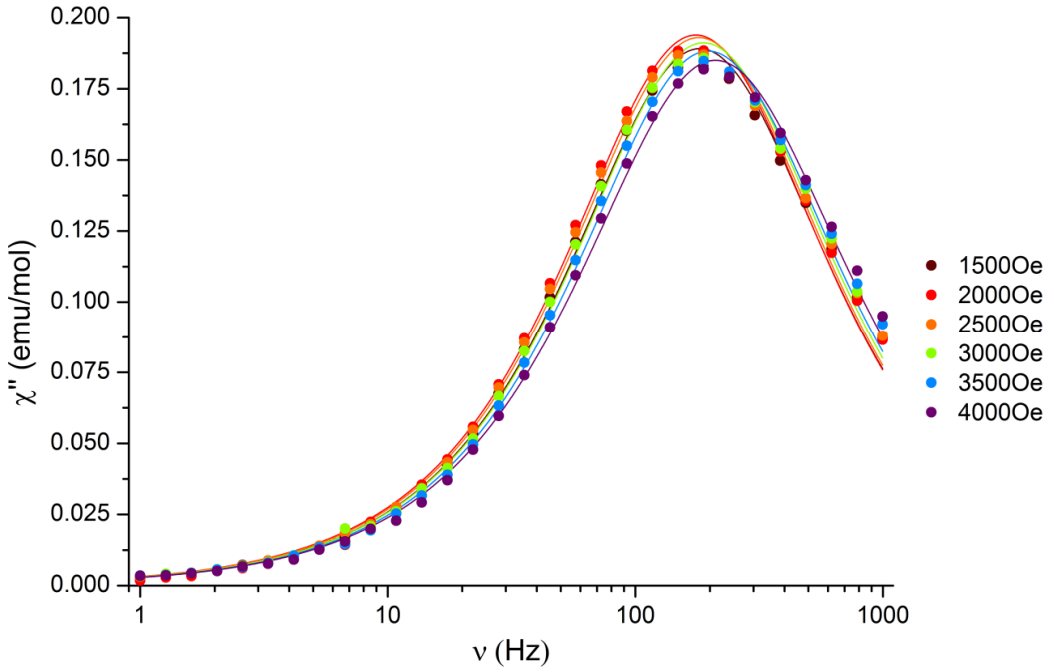

Figure S66 plot of out-of-phase susceptibility versus frequency at a temperature of 5K under different applied magnetic fields for **5**; solid lines represent the best fit results according to a generalized Debye model

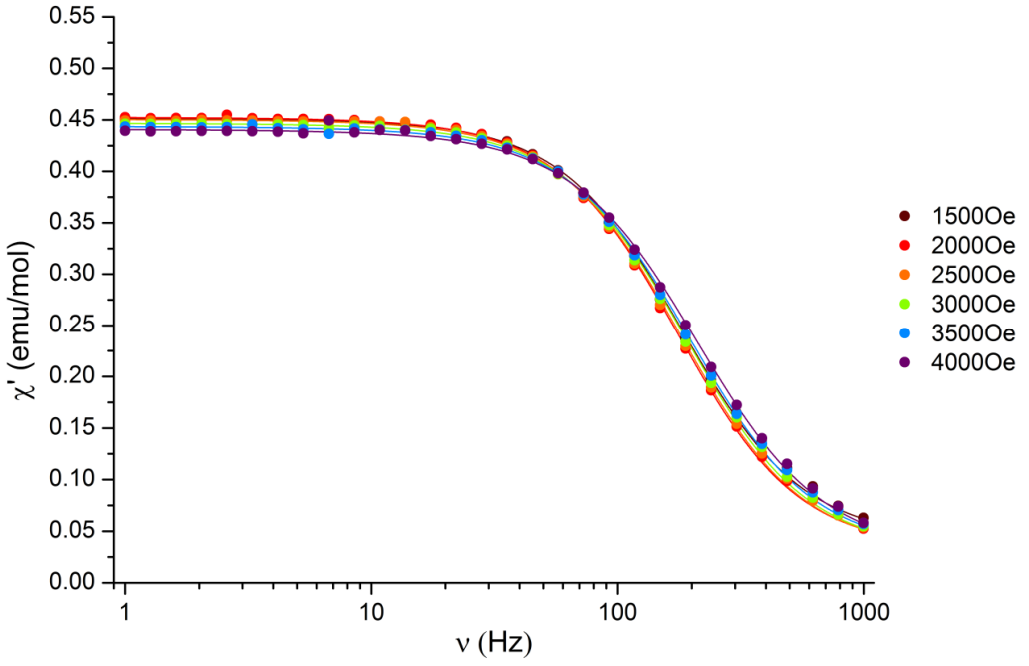

Figure S67 plot of in-phase susceptibility versus frequency at a temperature of 5K under different applied magnetic fields for **5**; solid lines represent the best fit results according to a generalized Debye model

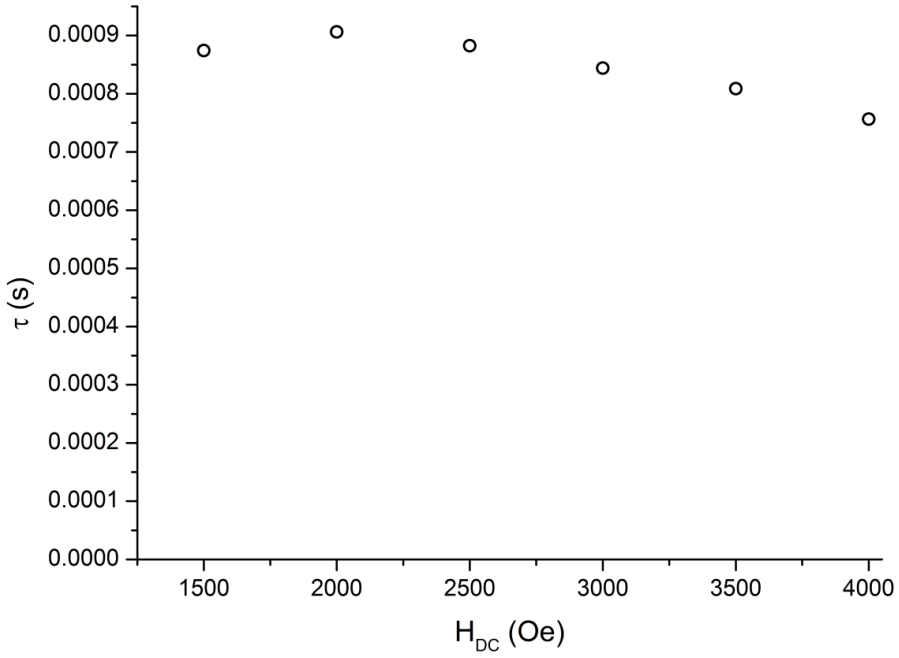

Figure S68 plot of the relaxation time versus the applied magnetic field at a temperature of 5K for **5**

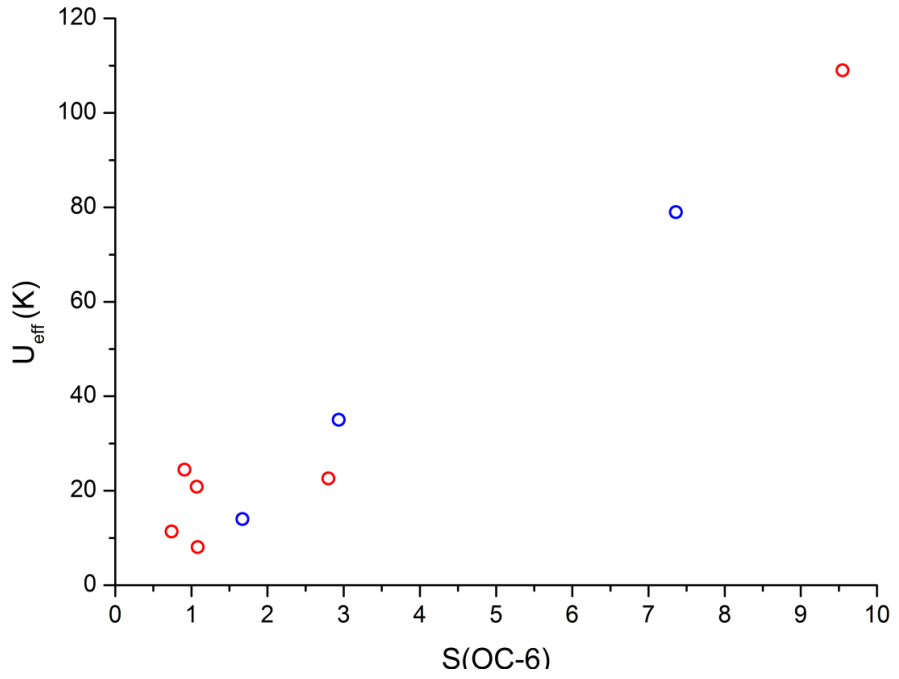

Figure S69 comprehensive plot of the height of the effective energy barrier versus the octahedral shape measure for current examples of mononuclear sixfold coordinated Co(II) SMMs; color code: red - literature, blue - present work

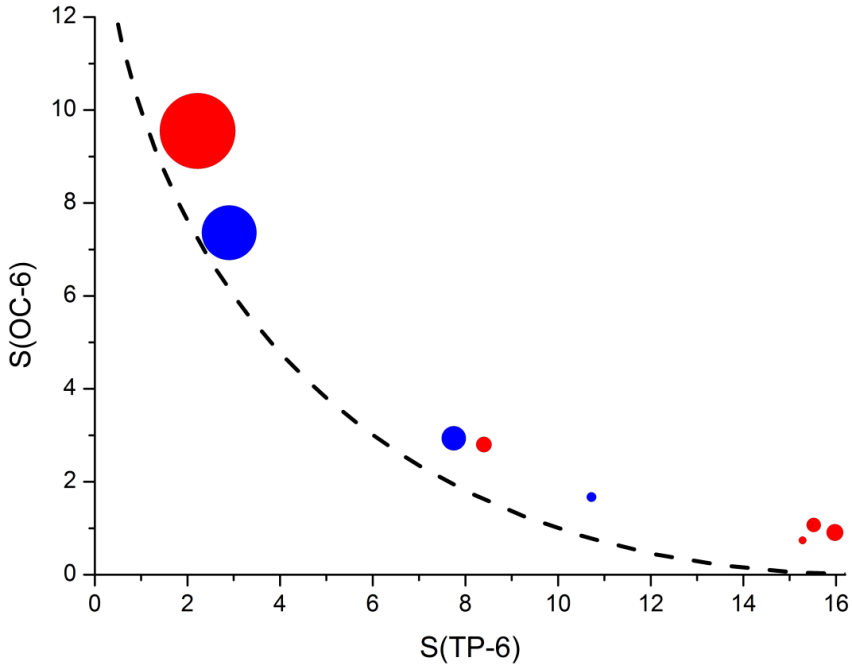

Figure S70 comprehensive plot of the height of the effective energy barrier on the shape map for the interconversion from ideal octahedron and trigonal prism for current examples of mononuclear sixfold coordinated Co(II) SMMs; radii of the data points are proportional to the effective energy barrier; color code: red - literature, blue - present work, black dashed line - minimum distortion path between ideal octahedron and trigonal prism

$$\chi''(\chi') = -\frac{\chi_0 - \chi_S}{2 \cdot \tan(\frac{\pi}{2} \cdot (1-a))} + \sqrt{(\chi' - \chi_S)(\chi_0 - \chi') + \frac{(\chi_0 - \chi_S)^2}{4tan^2(\frac{\pi}{2} \cdot (1-a))}} \quad \text{(S5)}$$

$$\chi'(\omega) = \chi_S + (\chi_0 - \chi_S) \cdot \frac{1 + (\omega\tau)^{1-\alpha} \cdot \sin(\alpha \cdot \frac{\pi}{2})}{1 + 2 \cdot (\omega\tau)^{1-\alpha} \cdot \sin(\alpha \cdot \frac{\pi}{2})(\omega\tau)^{2(1-\alpha)}} \quad \text{(S6)}$$

$$\ln(\tau) = \ln(\tau_0) \cdot -\frac{U_{eff}}{k} \cdot (\frac{1}{T}) \quad \text{(S7)}$$

$$\tau^{-1} = A \cdot H^4 \cdot T + \frac{B_1}{1 + B_2 \cdot H_2} \quad \text{(S8)}$$

$$\tau^{-1} = A \cdot H^4 \cdot T + \frac{B_1}{1 + B_2 \cdot H_2} + C \cdot T^n \quad \text{(S9)}$$

$$\tau^{-1} = A \cdot H^4 \cdot T + \frac{B_1}{1 + B_2 \cdot H_2} + C \cdot T^n + \tau_0^{-1} \cdot \exp(-\frac{U_{eff}}{kT}) \quad \text{(S10)}$$

$$\tau^{-1} = C \cdot T^n + \tau_0^{-1} \cdot \exp(-\frac{U_{eff}}{kT}) \quad \text{(S11)}$$

$$\chi'(\omega) - i \cdot \chi''(\omega) = \chi_{S1} + \chi_{S2} + \frac{\chi_{01} - \chi_{S1}}{1 + (i \cdot \omega\tau_1)^{(1-\alpha_1)}} + \frac{\chi_{02} - \chi_{S2}}{1 + (i \cdot \omega\tau_2)^{(1-\alpha_2)}} \quad \text{(S12)}$$

3.9.8 References

[1] D.I. Brown, *The chemical bond in inorganic chemistry. The bond valence model*, **2006**, Oxford University Press (Oxford Science publications, 12)

[2] I.David Brown, *Chem. Rev.*, **2009,** *12*, 6858

[3] M. O'Keefe and N.E. Brese, *J. Am. Chem. Soc.*, **1991,** *9*, 3226

[4] I.D. Brown and D. Altermatt, *Acta Crystallogr B Struct Sci*, **1985,** *4*, 244

[5] S.M. Kanowitz and G.J. Palenik, *Inorg. Chem.*, **1998,** *8*, 2086

[6] R.M. Wood and G.J. Palenik, *Inorg. Chem.*, **1998,** *16*, 4149

[7] X.-Y. Zhang, C.J. O'Connor, G.B. Jameson and M.T. Pope, *Inorg. Chem.*, **1996,** *1*, 30

[8] S. Khanra, M. Helliwell, F. Tuna, E.J. L. McInnes and R.E. P. Winpenny, *Dalton Trans.*, **2009,** *31*, 6166

[9] I. David Brown (2013), Bond valence parameters. Online verfügbar unter http://www.iucr.org/resources/data/datasets/bond-valence-parameters

[10] I. David Brown, Bond Valence Calculator 2.0. Online verfügbar unter http://www.ccp14.ac.uk/solution/bond_valence/

[11] M. Pinsky and D. Avnir, *Inorg. Chem.*, **1998,** *21*, 5575

[12] J. Cirera, E. Ruiz and S. Alvarez, *Organometallics*, **2005,** *7*, 1556

[13] M. Llunell, D. Casanova and J. Cirera (2013), Shape 2.1. Online verfügbar unter http://www.ee.ub.es/

[14] D. Casanova, J. Cirera, M. Llunell, P. Alemany, D. Avnir and S. Alvarez, *J. Am. Chem. Soc.*, **2004,** *6*, 1755

[15] J. Cirera, E. Ruiz and S. Alvarez, *Chem. Eur. J.*, **2006,** *11*, 3162

[16] S. Alvarez, D. Avnir, M. Llunell and M. Pinsky, *New J. Chem.*, **2002,** *8*, 996

4 Conclusion and Outlook

The achieved results of the two here described sub-projects of heterometallic and heterovalent cobalt metallacoronates provide significant contributions to the areas of metallacrown chemistry as well as single-molecule magnetism based on virtually magnetically isolated transition metal ions and have simultaneously proven the high capability of both new developed strategies to exploit the distinguished features of 12-MC-4 transition metal complexes for the research on single-molecule magnets.

The first 3d heterometallic 12-MC-4 metallacoronate $Cu(II)(DMF)_2Cl_2[12\text{-}MC_{Fe(III)N(Shi)}\text{-}4](DMF)_4$ has been designed according to a novel magnetic director approach and synthetically realized. Causing a high-spin ground state of approximately S = 11/2, the new developed concept accomplishes its intension to overcome the common mutual cancelation of the spins in 12-MC-4 complexes and therefore achieves the fulfillment of an essential requirement for SMM behavior. Here, the central Cu(II) ion as the magnetic director enforces a more parallel alignment of the high single-ion spins of Fe(III) ions in the cyclic host via strong antiferromagnetic interactions. The still missing signs of slowed relaxation might be triggered for the concrete example via a additional synthetic manipulation of the molecular configuration and the coordination environment of the Fe(III) ions. For that purpose, these measures provide the potential to fine-tune the energetic order and separation of the spin states and especially achieve a negative magnetic anisotropy as second necessary condition. The exchange of the ring metal ions by species which are more capable for strong single-ion contributions to the magnetic anisotropy like Mn(III) ions remains a promising task for future work. However, the novel developed magnetic director approach has clearly revealed its general potential to overcome the intrinsic handicap of the connectivity pattern of the coupling pathways in the 12-MC-4 clusters and to attain a high-spin ground state in spite of antiferromagnetic coupling. Therefore, it represents a uniquely targeted procedure to turn 12-MC-4 metallacoronates and other pseudo-star-shaped complexes into novel multinuclear single-molecule magnets with valuable features for current issues in SMM research.

On the other side, the first cobalt complexes of the pioneering ligand salicylhydroxamic acid have been established and the richness of the chemistry of this compounds class has been explored with the help of eight varied examples. In that respect, rare or completely unknown structural features have been observed like central vacancy, reverse of the sequence of the characteristic repetition units, perpendicular and partial tilting of salicylhydroximate ligands out of the least-square plane of the metal ions, variable arrangement of the bridging ligands relative to each and the complexation of additional cations via peripheral donor atoms of the metallacoronate as supramolecular ligand.

These singularities can be ascribed to combination of a non-degeneracy of the d^6 low spin ground state in an octahedral environment for the Co(III) ions in the ring and the flexibility of the central Co(II) guest ion concerning the shape of its coordination sphere. Due to the simultaneous discovery of the single-molecule magnetic behavior of some examples of the Co[12-$MC_{Co(III)N(Shi)}$-4] compounds based on the virtually magnetically isolated Co(II) ion at the core, the recognized structural versatility is assigned to an even greater functional relevance. As the static and dynamic magnetic properties of divalent high-spin cobalt ions are strongly correlated with their coordinative environment, the opportunity of a precise synthetic control over the shape of the coordination spheres in the novel cobalt coronates provides a unique foundation for their systematic investigation and optimization. For that purpose, the bridging and secondary ligand as well as the peripheral attached additional cations have been identified and applied as synthetic tools for the engineering of the magnetism of the central guest ion via its coordination sphere. The cyclic scaffold of the new cobalt metallacrowns has hence established as a versatile interface to SMM features based on a virtually magnetically isolated Co(II) ion by the realization of three novel single-molecule magnets with energy barriers of 14, 35 and 79 K. While the effects of quantum tunneling and the direct process are evident from the field dependence of the relaxation times at low temperatures, a significant importance of the Raman relaxation process was determined at moderate to high temperatures for a sample of Co(II)(NO_2)(Piv)[12-$MC_{Co(III)N(Shi)}$-4](Pic)$_6$. Not until the highest relevant temperatures above 9K for the applied measurement setup, the Orbach process takes over as dominant relaxation mechanism for this compound of the series with the highest energy barrier. Furthermore, a field induced transfer from a faster to a by magnitudes slower relaxation pathway can be observed for the SMM with the smallest barrier and its investigation represents an interesting task for future work. Magneto-structural correlations reveal an increase of the height of the energy barrier along the interconversion pathway from an octahedral to a trigonal prismatic coordination sphere and therefore confirm the potential of the latter shape for the creation of high-performance single-molecule magnets. These findings indicate the high capability of the here developed platform for the establishment and refinement of a comprehensive model of the single-molecule magnetism of virtually magnetically isolated Co(II) ions as a current hot topic in magneto-chemical.

Giving a final outlook beyond the above outlined great scopes of the two basic strategies, the first steps towards the exploration of an ilk of next generation metallacrown ligands are depicted in the following. These provide additional donor atoms which are linked to the actual main ligand fragment via flexible spacer groups like alkyl chains. Due to its less preorganization, the upgrade does not prevent the formation of the basic metallacrown motif but hold the potential to control the selectivity for different guest ions as well as their number and position, the selection of secondary ligands, the molec-

ular configuration of the cyclic host, the attachment of additional cations and the intermolecular linkage. In that respect, the change of the amount of anionic charges, steric effects and the degree of spatial flexibility in dependence of the spacer represent the envisioned effective forces of the interference. Some of these aspects can be recognized from a first example of an early stage result. So, an anthranilhydroxamic acid armed with an ethyl-spacered carboxylic acid moiety has been prepared and applied for the evolution of a heterometallic metallacrown. While the regular cyclic host is formed by the rigid donor sets and Cu(II) ions, the flexibly associated carboxylate groups in cooperation with the charge balance give rise to a complexation of two Mn(II) guest ions above and below the least-square plane of the metal ions because the spacer admits two of these moieties to function as monodentate bridging ligands. Simultaneously, the peripheral scaffold significantly deviates from planarity and the guest ions are only coordinated by three of the central hydroximate oxygen donor atoms each. The remaining spacered moieties additionally link the coronate with adjacent clusters. Hence, this exemple demonstrates the enhanced control of the shaping via next generation ligands and distinguishes the latter as powerful upgrade of the capability of metallacrowns for the targeted generation of advanced magnetic materials.

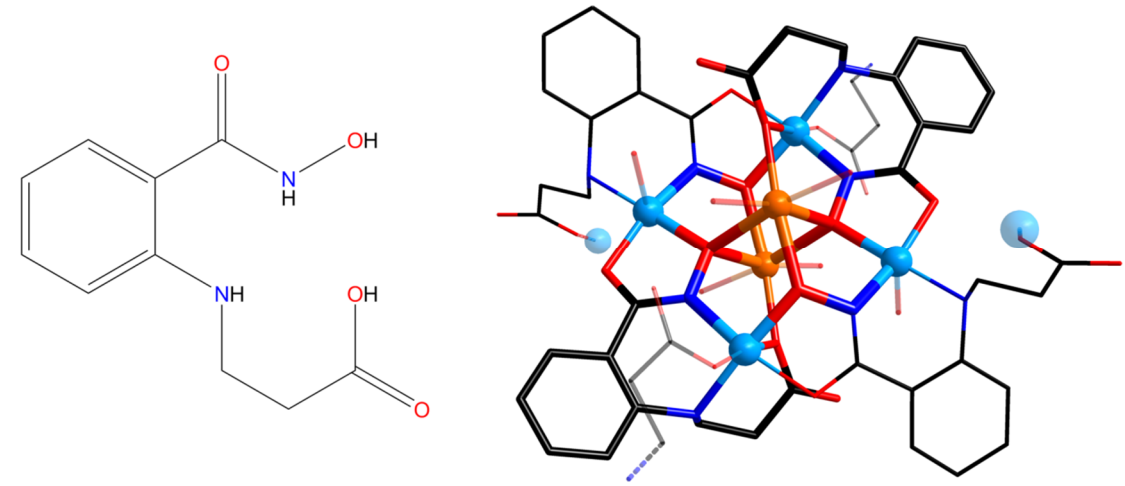

Figure 1 anthranilhydroxamic acid armed with an additional ethyl-spacered carboxylic acid as example of a next generation metallacrown ligand (left) and molecular structure of a first corresponding heterometallic metallacoronate (right); color code: light blue - Cu(II), orange - Mn(II), red - O, dark blue - N, black - C